

DISS. ETH NO 28661

**Chemical and Compositional Effects in  
Electroreduction of CO<sub>2</sub> over Cu-Based Catalysts**

A thesis submitted to attain the degree of  
DOCTOR OF SCIENCES of ETH ZURICH

(Dr. sc. ETH Zurich)

Presented by

Florentine Louise Petronella Veenstra

MSc in Chemistry

University of Amsterdam, The Netherlands

Born on 22 November 1990

Citizen of Amsterdam, The Netherlands

Accepted on the recommendation of

Prof. Dr. Javier Pérez-Ramírez

Dr. Antonio José Martín

Prof. Dr. Chih-Jen Shih

2022





~ to my Sunshine ~

Proof that it is never too late to find your way,  
strive for excellence in every aspect of life and maintaining your uncompromised self.

~ in memory of Tine ~

Time, you can always make it for the important things.



# Acknowledgement

**Benjamin**, you have been my family, support, and partner throughout this crazy journey over the past decade. I have enjoyed chasing your big dreams and making them our reality. With Lausanne and a growing family being the next stop on our journey, I cannot but feel blessed to share every sunshine and rainy cloud with you. Our little sunshine, **Lawrence**, gave us purpose and kicked our ambition into overdrive; anything I do next is for him.

**Javier**, thank you for giving me the opportunity to work, learn and improve under your guidance. You raised my bar and taught me what excellence in attitude, research and communication looks like. **Antonio**, as my second PI you were always ready to make time for me to have conversations, providing support and challenging me intellectually. It was both a blessing and a challenge to share the office with you, and I hope we will stay in touch.

I am tremendously grateful for the many collaborators with whom I shared so many precious moments. In the first years of my doctoral studies, I worked closely with **Norbert** which resulted in the type of work that I now wish I could do all over again. It were always crazy hours to communicate with **Sergio**, in Spain and **Louisa**, calling in from Singapore. Over the different time-zones, we got to work on some impressive collaborations that turned out quite nicely. However, it is too bad that I never got to visit NUS, in Singapore or the ICIQ facilities in Spain. Furthermore, during the past year, I got to work on a scale-up projects with the people of Julich in Germany and hope to work on many more projects with them. **Therese**, **Tsveti**, **Daniel** and **Joachim**, thank you for the great time last Fall. I also thank my colleagues at aCe for the great times in the lab and the few parties, I will never forget newyears with **Matthias S.** or the crazy evenings in the lab with **Ali**. Thank you both for an unforgettable experience. I had the pleasure of working with a couple of students, who were absolutely brilliant! Big thank you to: **David**, **Arjun**, **Georgios** and **James**. Many thanks to the staff of the glassblowers at University of Zurich, and to **Jean-Pierre**, **Roland** and **Joel** from the ICB workshop. They were always ready to support me with last minute quick fixes and in the 'oh help it broke' moments. Their support was invaluable, as was the support from **Rene** for the NMR methodologies and all Dutch chatting that needed to happen.

My start at ETHZ was also the start of my journey at AVETH. 3 months into the job and I met **Alina** who introduced me to the peer-to-peer counselling. As counsellor I got to work with inspiring people; **Anne, Ed, Alok, Betty,** and **Linda** whom each went above and beyond for each other, the community and me. When I became a coordinator, I got further involved with AVETH leadership and the different offices within ETH that provide support. I learned a lot from my friends; **Mark, Claire, Viki, Deepak, Rosa** and **Konstantinos**. I might have lost my mind in the long days in the lab during my second and third year at ETH if it wasn't for this crazy bunch. Once I transitioned into AVETH presidency, I got to extend the working together to the different DAs, the different working groups within ETH and the core team at ETH Circle. **Victoria** and **Claudine**, thank you for the many research, brainstorming and organizational meetings in service of our mentorship program at ETHZ. I am so glad to have met you and the wonderful people from the ETH Circle. While it was probably only suppose to be a part-time volunteering job, AVETH took over all of my spare time, and I regret nothing. **Niko, Cyprien** and **Michèle**, I am glad I found so much support in you. **Niroshan, Jake, Maxim** and **Sandro**, I had the best times with Telejob on the MEM's, the late night drinks, skiing and retreat. Oh.. and we obviously also did some things for telejob and poly-E-fair, but that was mostly you guys. Thank you for allowing me to tag along for the ride.

Zurich was loads of fun with the hockeying, swimming, floating, shopping, travelling, hiking and skiing. I should give a huge shout out to my hockey girls (**Neva, Dawn, Natasha, Nathi, Carmen, Carine, Jasmin, Prisca, Ambre, Jildau, Janina**) from RedSox, with whom I have played and chirped, many many many nights over the past 4 years. In my first year here, I got to join the guys **Julian, Weida** and **Xavier** from my corridor for swimming, and Wednesday drink nights. You guys were brilliant and made me feel at home in ICB and Zurich. Lucky for me I had some true friends from Amsterdam (**Cleopatra, Krista, Jorien, Yorik, Camiel, Sjoerd, Niels, Tessa, Lausa**) visiting me over these years, and hopefully they will stay in my life for many more years. Lucky for me, **Roberto** and **Katja** made the same move from Amsterdam to Zurich, and hopefully all our other friends who are like family from Amsterdam (**Hernan, Bruno, Tomislav, Dasha**) will also follow. This way, we can recreate a warm, kind and ambitious environment for **Lawrence** to grow up in, with the many uncles and aunties.

Mijn familie zal altijd een speciaal plekje in mijn hart hebben, mijn broertje (**Philip**) zusje (**Belle**) en hun partners (**Mijke en Jessey**) en mijn ouders (**Roelof-Rinse** en **Jessie**). Dankjulliewel voor de eindeloze steun en de vele bezoeken, kaartjes en lieve whatsapp berichtjes. Amsterdam voelde nooit ver weg met alle lieve aandacht van de VanderLinden-Clan (**Bert, Marijn, Tanneke, Henk, Joep, Manon, Roel, Caro, Jip, Belle, Noud, Cato, Ot, Kato, Britt, Tijl, Huub**) en de Veenstra familie (**Jo-Anne, Rene, Matthieu, Myrthe, Rogier, Quinten, James, Charlie**). I am intensely grateful to have my extended family (**Cordelia, Jack, Jasper** and **Rose**) so close to me and growing by the year. I can't wait for the kids to grow up together and for us to become neighbours someday.

The mentors that gave me support when I needed it the most, without whom I would have never gotten this far. **John van der Toorn**, who gave me another change to prove to myself I can be a student again at the age of 22. **Gadi Rothenberg**, who directed my focus toward a world greater than Amsterdam and supported my move toward ETH Zurich. **Sarah Springman**, who gave me a role model, a critical conversationalist and above all a support to dream big and remain me. **Tine Verheij**, my godmother, my example, my guardian, the strength in my backbone and the voice in my head to never back down and always move forwards. You will never leave me.



# Table of Contents

Acknowledgement	iii
Table of Contents	vii
Summary	ix
Zusammenfassung	xiii
Samenvatting	xvii
Author Contributions	xxi
1. Introduction	1
2. Nitride-Derived Copper Modified with Indium as a Selective and Highly Stable Catalyst for the Electroreduction of Carbon Dioxide	13
3. Selectivity Patterns in the Electrocatalytic Reduction of CO <sub>2</sub> Revealed by Laser-Microstructured Copper	35
4. Mechanistic Routes toward C <sub>3</sub> Products in Copper-Catalyzed CO <sub>2</sub> Electroreduction	59
5. Electrochemical Reduction of Carbon Dioxide to 1-Butanol on Oxide-Derived Copper	79
6. Conclusions and Outlook	97
Bibliography	103
Appendix A Annexes	115
Appendix B List of Publications and Presentations	203
Appendix C Curriculum Vitae	207









## Summary

It is of the utmost importance to close the carbon cycle converting carbon dioxide ( $\text{CO}_2$ ) into value added compounds. This work focuses on the electrocatalytic  $\text{CO}_2$  reduction ( $\text{eCO}_2\text{R}$ ) toward multicarbon products. As of yet, copper (Cu) is the only heterogeneous electrocatalyst that is able to reach higher carbon ( $\text{C}_{2+}$ ) compounds with potentially practical rates. With a catalyst that can produce such a great variety of 17 of them, understanding selectivity drivers is crucial to direct this catalytic process toward desired products (*e.g.* fuel or intermediate). The effect that the composition or nanostructuring of the catalyst has to the selectivity pattern attracts most attention and is intensively studied. Nonetheless, the effect of local chemical environment, despite being known for decades, has only been recently targeted. Most mechanistic investigations have explored routes towards  $\text{C}_2$  products, while the formation of  $\text{C}_{3+}$  compounds remain almost uncharted. A lack of fundamental understanding prevents from developing strategies to maximize productivities for long chain products. Most understanding efforts have been driven by DFT in view of the lack of model systems enabling experimental studies under relevant operation conditions.

This work first develops tools towards model electrocatalysts enabling fundamental insights relevant for the design of practical systems. The potential use of model systems was exemplified by rationalizing the excellent performance of a newly developed indium-modified copper nitride catalyst. Indium-modified copper nitride was identified as a selective and stable electrocatalyst for CO production. With a Faradaic efficiency ( $FE$ ) of 80% at 0.50 V overpotential for at least 50 h, in stark contrast to the very limited stability of the benchmark  $\text{In}_2\text{O}_3/\text{Cu}_2\text{O}$ . Microfabricated systems allowed to correlate activity with highly stable indium-copper interfaces. In contrast, fast diffusion of indium resulted in rapidly evolving interfaces in the case of the system based on oxide-derived Cu (OD-Cu). A metastable nitrogen species acting as diffusion barrier observed by spectroscopic means was proposed as the underlying cause. These observations were confirmed in tests with catalysts in powder form. This work thus reveals the stabilizing properties of nitride-derived copper (ND-Cu) toward high-performance multicomponent catalysts and illustrates the value of microfabrication to develop model systems free of operation conditions gaps.

Microfabrication could also be used to probe chemical environment. The impact of the (electro)chemical environment on the selectivity pattern was quantified by using microstructured Cu electrodes prepared by ultra-short pulse laser ablation. Regularly distributed micro-probes were created and their product distributions assessed at distinct overpotentials. The regular geometry enabled the accurate simulation of the local pH and CO<sub>2</sub> concentration. Selectivity maps useful for mechanistic and applied studies emerged. They revealed clear patterns for C<sub>1</sub>-C<sub>3</sub> products, suggesting untried insights, such as the presence of two reaction mechanisms for 1-propanol. The effect on the selectivity pattern of operating parameters, such as mass transport and electrolyte composition, was also predicted by these maps.

Aiming at disclosing routes toward C<sub>3</sub> products, the formation mechanism toward main C<sub>3</sub> products was explored. A divide – and – conquer strategy was devised to explain the formation of the C<sub>3</sub> backbone and elucidate the mechanism responsible for the formation of the main C<sub>3</sub> products by combining network graphs, DFT, and experiments to prune the network including 700 intermediates and 2266 transition states and benchmark the identified pathway. Our approach concluded that the most frequently reported products, propionaldehyde and 1-propanol, originate from the coupling of CH<sub>2</sub>CH\* with C(H)O\*. While the highly valued propylene and 1-propanol share common intermediates, the former is barely produced due to the unfavorable formation of allyl alkoxy, whose crucial role was confirmed experimentally. On the light of these results, tailoring selective routes towards C<sub>3</sub> products might be possible.

Exploring the formation of longer products was aimed for, in order to reach products associated to higher market value. The first direct electroreduction of CO<sub>2</sub> to 1-butanol was reported in alkaline electrolyte on Cu gas diffusion electrode with *FE* of 0.056%, partial current density of -0.080 mA cm<sup>-2</sup> at -0.48 V *vs.* RHE. Electrolysis of possible molecular intermediates, coupled with DFT, indicate that CO<sub>2</sub> first electroreduced to acetaldehyde – a key C<sub>2</sub> intermediate to 1-butanol. Acetaldehyde then undergoes a base-catalyzed aldol condensation to give crotonaldehyde via electrochemical promotion by the catalyst surface. Crotonaldehyde is subsequently electroreduced to 1-butanal, and then to 1-butanol.

In a broad context, the results point to the relevance of coupling chemical and electrochemical processes for the synthesis of higher molecular weight products from CO<sub>2</sub>. Overall, this thesis provides a deepened understanding into the mechanistic pathways toward C<sub>2+</sub> products from eCO<sub>2</sub>R. Initially, microfabrication is introduced as a multipurpose tool to study the effects of catalyst composition, nanostructuring and local environment to the product selectivity. In it, the optimal conditions are revealed for the production of complex products and suggested the existence of two mechanisms for 1-propanol formation. Secondly, the mechanistic pathways have been revealed towards more abundant C<sub>3</sub> products and disclosing why propylene, the C<sub>3</sub> equivalent to the very favored ethylene, is not observed. Finally, the palette of products was extended to C<sub>4</sub> oxygenates, setting the limit of copper chemistry toward implementation of one-step processes.



## Zusammenfassung

Es ist von größter Bedeutung, den Kohlenstoffkreislauf zu schließen, indem Kohlendioxid ( $\text{CO}_2$ ) in wertschöpfend veredelt wird. Diese Arbeit konzentriert sich auf die elektrokatalytische  $\text{CO}_2$ -Reduktion ( $\text{eCO}_2\text{R}$ ) zu Mehrkohlenstoffprodukten. Bislang ist Kupfer (Cu) der einzige heterogene Elektrokatalysator, der in der Lage ist, höhere Kohlenstoffprodukte ( $\text{C}_{2+}$ ) mit relevanten Reaktionsraten zu erzeugen. Bei einem Katalysator, der eine so große Vielfalt an Verbindungen herstellen kann, ist das Verständnis von selektivitätsbedingenden Faktoren von entscheidender Bedeutung, um diesen katalytischen Prozess auf die gewünschten Produkte (z. B. Kraftstoffe oder Zwischenprodukte) auszurichten. Die Zusammensetzung oder Nanostrukturierung des Katalysators und dessen Einfluss auf das Selektivitätsmuster werden am intensivsten untersucht. Die Auswirkung der lokalen chemischen Umgebung ist zwar seit Jahrzehnten bekannt, wurde jedoch erst kürzlich untersucht. Obwohl mechanistischen Untersuchungen die Bildung von  $\text{C}_2$ -Produkten weitgehend erforscht haben, ist die Bildung von  $\text{C}_{3+}$ -Verbindungen nahezu unbekannt ist. Ein Mangel an grundlegendem Verständnis verhindert die Entwicklung von Strategien zur Maximierung der Produktivität langkettiger Produkte. Die meisten Bemühungen um ein besseres Verständnis wurden durch DFT vorangetrieben, da es keine Modellsysteme gibt, die experimentelle Studien unter relevanten Betriebsbedingungen ermöglichen.

In dieser Arbeit werden zunächst Werkzeuge für Modellelektrokatalysatoren entwickelt, die grundlegende Erkenntnisse für die Entwicklung praktischer Systeme ermöglichen. Der potenzielle Nutzen von Modellsystemen wurde anhand der hervorragenden Leistung eines neu entwickelten, mit Indium modifizierten Kupfernitriddkatalysators veranschaulicht. Indium-modifiziertes Kupfernitridd wurde als selektiver und stabiler Elektrokatalysator für die CO-Produktion identifiziert. Mit einer Faradäischen Effizienz (FE) von 80% bei einer Überspannung von 0,50 V für mindestens 50 Stunden steht er in starkem Kontrast zu der sehr begrenzten Stabilität des Referenzmaterials  $\text{In}_2\text{O}_3/\text{Cu}_2\text{O}$ . Mikrometergenau gefertigte Systeme ermöglichten es, die Aktivität mit der Bildung von hochstabilen Indium-Kupfer-Grenzflächen zu korrelieren. Im Gegensatz dazu führte die schnelle Diffusion von Indium im Falle des Systems auf der Basis von oxidischem Cu (OD-Cu) zu sich schnell degradierenden Grenzflächen. Als Ursache wurde eine metastabile Stickstoffspezies vorgeschlagen, die als Diffusionsbarriere fungiert und mit spektroskopischen



Techniken beobachtet wurde. Diese beziehen sich auf Katalysatoren in weit anwendungsnäherer Pulverform. Somit zeigt diese Arbeit die stabilen Eigenschaften von Kupfer aus Nitriden (ND-Cu) im Vergleich zu leistungsstarken Mehrkomponenten-Katalysatoren und veranschaulicht den Mehrwert der Mikrofabrikation zur Entwicklung von Modellsystemen.

Die Mikrofabrikation könnte auch zur Untersuchung der chemischen Umgebung genutzt werden. Die Auswirkungen der (elektro-)chemischen Umgebung auf das Selektivitätsmuster wurden mit Hilfe von mikrostrukturierten Cu-Elektroden quantifiziert, die durch Ultrakurzpuls-Laserablation hergestellt wurden. Es wurden regelmäßig verteilte Mikrosonden an der Oberfläche der Cu-Elektroden erzeugt und die entstehende  $e\text{CO}_2\text{R}$ -Produktverteilungen bei unterschiedlichen Überspannungen untersucht. Die regelmäßige Geometrie ermöglichte die genaue Simulation des lokalen pH-Werts und der  $\text{CO}_2$ -Konzentration. Es entstanden Selektivitätskarten, die für mechanistische und angewandte Studien nützlich sind. Sie enthüllten klare Regionen mit bevorzugter Bildung von  $\text{C}_1$ - $\text{C}_3$ -Produkten, die auf bisher unerprobte Erkenntnisse hindeuten, wie z. B. das Vorhandensein von zwei Reaktionsmechanismen für 1-Propanol. Die Auswirkungen von Betriebsparametern wie Massentransport und Elektrolytzusammensetzung auf das Selektivitätsmuster wurden durch diese Karten ebenfalls vorhergesagt.

Mit dem Ziel, Reaktionsrouten zu  $\text{C}_3$ -Produkten aufzuzeigen, wurde der Bildungsmechanismus für die wichtigsten  $\text{C}_3$ -Produkte untersucht. Es wurde eine Strategie des Teilens und Eroberns entwickelt, um die Bildung des  $\text{C}_3$ -Grundgerüsts zu erklären und den für die Bildung der wichtigsten  $\text{C}_3$ -Produkte verantwortlichen Mechanismus aufzuklären. Indem Netzwerkgraphen, DFT und Experimente kombiniert wurden, konnte ein Netzwerk mit 700 Zwischenstufen und 2266 Übergangszuständen zerlegt und nach vielversprechenden Wegen durchsucht werden. Unser Ansatz ergab, dass die am häufigsten berichteten Produkte, Propionaldehyd und 1-Propanol, durch die Kopplung von  $\text{CH}_2\text{CH}^*$  mit  $\text{C}(\text{H})\text{O}^*$  entstehen. Während das hochgeschätzte Propylen und 1-Propanol gemeinsame Zwischenprodukte aufweisen, wird ersteres aufgrund der ungünstigen Bildung von Allylalkoxy, dessen entscheidende Rolle experimentell bestätigt wurde, kaum hergestellt. Auf der Grundlage dieser Ergebnisse ergibt sich die Möglichkeit selektive Katalysatoren für  $\text{C}_3$ -Produkten zu entwickeln.

Die Bildung längerkettiger Produkte ist aufgrund des höheren Marktwertes stets erwünscht. In dieser Arbeit wurde die erste direkte Elektroreduktion von  $\text{CO}_2$  zu 1-Butanol in einem alkalischen Elektrolyten an einer Cu-Gasdiffusionselektrode mit einem  $FE$  von 0,056% und einer Stromdichte von  $-0,080 \text{ mA cm}^{-2}$  bei  $-0,48 \text{ V}$  gegen RHE beobachtet. Die Elektrolyse relevanter molekularer Zwischenprodukte, gekoppelt mit DFT-Untersuchungen, zeigen, dass  $\text{CO}_2$  zunächst zu Acetaldehyd elektroreduziert wird - einem wichtigen  $\text{C}_2$ -Zwischenprodukt zu 1-Butanol. Acetaldehyd durchläuft dann eine basenkatalysierte Aldolkondensation zu Crotonaldehyd elektrochemisch durch die Katalysatoroberfläche gefördert. Crotonaldehyd wird anschließend elektroreduziert zu 1-Butanal und schliesslich zu 1-Butanol.

In einem breiteren Kontext weisen die Ergebnisse auf die Bedeutung der Kopplung chemischer und elektrochemischer Prozesse für die Synthese von Produkten mit höherem Molekulargewicht aus  $\text{CO}_2$  hin. Insgesamt bietet diese Arbeit ein vertieftes Verständnis der mechanistischen Wege zu  $\text{C}_{2+}$ -Produkten aus  $\text{eCO}_2\text{R}$ . Zunächst wird die Mikrofabrikation als Mehrzweckwerkzeug eingeführt, um die Auswirkungen der Katalysatorzusammensetzung, der Nanostrukturierung und der lokalen Umgebung auf die Produktselektivität zu untersuchen. Darin werden die optimalen Bedingungen für die Herstellung komplexer Produkte aufgezeigt und die Existenz zweier Mechanismen für die Bildung von 1-Propanol vorgeschlagen. Zweitens wurden die mechanistischen Wege zu reichlich verwendeten  $\text{C}_3$ -Produkten aufgezeigt und erklärt, warum Propylen, das  $\text{C}_3$ -Äquivalent zum sehr beliebten Ethylen, nicht beobachtet wird. Schließlich wurde die Palette der Produkte auf  $\text{C}_4$ -Oxygenate erweitert, wodurch die Grenzen der Kupferchemie in Richtung der Umsetzung von 1-Stufen-Prozessen verschoben wurden.



# Samenvatting

Het is van het grootste belang de koolstof cirkel te sluiten door koolstofdioxide ( $\text{CO}_2$ ) om te zetten in producten met industriële waarde. Dit werk richt zich op de elektrokatalytische  $\text{CO}_2$  reductie ( $\text{eCO}_2\text{R}$ ) naar hogere koolstof houdende producten. Tot nu toe is koper ( $\text{Cu}$ ) de enige heterogene elektrokatalysator die in staat is om hogere koolstofverbindingen ( $\text{C}_{2+}$ ) te bereiken met potentieel praktische snelheden.  $\text{Cu}$  is de enige katalysator met een groot bereik (17 producten dusver) en dus is het begrijpen van selectiviteitsbepalende factoren van cruciaal belang om dit katalytische proces in de richting van gewenste producten (bv. brandstof of tussenproduct) te sturen. Het effect dat de samenstelling of nanostructurering van de katalysator heeft op het selectiviteitspatroon trekt de meeste aandacht en is altijd intensief bestudeerd. Het effect van de lokale chemische omgeving is echter, ondanks het feit dat dit al tientallen jaren bekend is, pas recentelijk onder de loep genomen. De meeste mechanistische onderzoeken hebben routes naar  $\text{C}_2$  producten onderzocht, terwijl de vorming van  $\text{C}_{3+}$  verbindingen nog vrijwel onbekend is. Een gebrek aan fundamenteel begrip verhindert de ontwikkeling van strategieën om de productiviteit van  $\text{C}_{2+}$  producten te maximaliseren. De meeste pogingen om dit te begrijpen zijn gebaseerd op DFT, gezien het gebrek aan modelsystemen die experimentele studies onder relevante werkingsomstandigheden mogelijk zouden kunnen maken.

Dit werk ontwikkelt eerst instrumenten voor model systemen die fundamentele inzichten mogelijk maken, relevant voor het ontwerp van praktische systemen. Het potentiële gebruik van modelsystemen werd geïllustreerd door het rationaliseren van de uitstekende prestaties van een nieuw ontwikkelde met indium gemodificeerde kopernitride katalysator. Indium-gemodificeerd kopernitride werd geïdentificeerd als een selectieve en stabiele elektrokatalysator voor  $\text{CO}$  productie. Met een Faradaiische efficiëntie ( $FE$ ) van 80% bij 0,50 V overpotentiaal gedurende ten minste 50 uur, in schril contrast met de zeer beperkte stabiliteit van de benchmark  $\text{In}_2\text{O}_3/\text{Cu}_2\text{O}$ . Micro-gefabriceerde systemen toegestaan om de activiteit correleren met zeer stabiele indium-koper interfaces. Snelle diffusie van indium daarentegen resulteerde in snel evoluerende interfaces in het geval van het systeem op basis van oxide-afgeleid  $\text{Cu}$  ( $\text{OD-Cu}$ ). Een metastabiele stikstofsoort die als diffusiebarrière fungeert, waargenomen door spectroscopische middelen, werd voorgesteld als de onderliggende oorzaak. Deze waarnemingen werden bevestigd in proeven met katalysatoren in

poedervorm. Dit werk onthult dus de stabiliserende eigenschappen van nitride-afgeleid koper (ND-Cu) in de richting van hoogwaardige multicomponent katalysatoren en illustreert de waarde van microfabricage om modelsystemen te ontwikkelen die vrij zijn van hiaten in de bedrijfsomstandigheden.

Microfabricage kan ook worden gebruikt om chemische omgevingen te onderzoeken. De invloed van de (elektro)chemische omgeving op het selectiviteitspatroon werd gekwantificeerd door gebruik te maken van microgestructureerde Cu-elektroden, geprepareerd door ultrakorte puls laser ablatie. Regelmatig verdeelde micro-sondes werden gecreëerd en hun productdistributies werden beoordeeld bij verschillende overpotentialen. De regelmatige geometrie maakte de nauwkeurige simulatie van de lokale pH en CO<sub>2</sub> concentratie mogelijk. Selectiviteitskaarten die nuttig zijn voor mechanistische en toegepaste studies kwamen naar voren. Zij vertoonden duidelijke patronen voor C<sub>1</sub>-C<sub>3</sub> producten en suggereerden niet eerder geteste inzichten, zoals de aanwezigheid van twee reactiemechanismen voor 1-propanol. Het effect op het selectiviteitspatroon van bedrijfsparameters, zoals massatransport en elektrolytsamenstelling, werd ook door deze kaarten voorspeld.

Met het oog op het blootleggen van routes naar C<sub>3</sub> producten, werd het vormingsmechanisme naar de belangrijkste C<sub>3</sub> producten onderzocht. Er werd een verdeel-en-heers strategie ontwikkeld om de vorming van de C<sub>3</sub> ruggengraat te verklaren en het mechanisme op te helderen dat verantwoordelijk is voor de vorming van de belangrijkste C<sub>3</sub> producten door netwerkgrafieken, DFT en experimenten te combineren om het netwerk met 700 tussenproducten en 2266 overgangstoestanden te ontleden en de geïdentificeerde route te benchmarken. Onze benadering leidde tot de conclusie dat de meest gerapporteerde producten, propionaldehyde en 1-propanol, ontstaan uit de koppeling van CH<sub>2</sub>CH\* met C(H)O\*. Hoewel het zeer gewaardeerde propyleen en 1-propanol gemeenschappelijke tussenproducten hebben, wordt het eerste nauwelijks geproduceerd als gevolg van de ongunstige vorming van allylalkoxy, waarvan de cruciale rol experimenteel werd bevestigd. In het licht van deze resultaten is het wellicht mogelijk selectieve routes naar C<sub>3</sub> producten te ontwikkelen.

Er werd gestreefd naar de vorming van langere producten, om producten met een hogere marktwaarde te verkrijgen. De eerste directe elektrolyse van CO<sub>2</sub> tot 1-butanol werd gerapporteerd in alkalische elektrolyt op Cu-gasdiffusie-elektrode met *FE* van 0,056%, partiële stroomdichtheid van -0,080 mA cm<sup>-2</sup> bij -0,48 V *vs.* RHE. Elektrolyse van mogelijke moleculaire tussenproducten, gekoppeld aan DFT, geven aan dat CO<sub>2</sub> eerst geëlektrolyseerd wordt tot acetaldehyde - een belangrijk C<sub>2</sub> tussenproduct voor 1-butanol. Acetaldehyde ondergaat vervolgens een base-gekatalyseerde aldolcondensatie om crotonaldehyde te geven via elektrochemische promotie door het katalysatoroppervlak. Crotonaldehyde wordt vervolgens geëlektrolyseerd tot 1-butanol, en vervolgens tot 1-butanol.

In een brede context wijzen de resultaten op de relevantie van de koppeling van chemische en elektrochemische processen voor de synthese van producten met een hoger moleculair gewicht uit CO<sub>2</sub>. In het algemeen verschaft dit proefschrift een dieper inzicht in de mechanistische paden naar C<sub>2+</sub> producten uit eCO<sub>2</sub>R. In eerste instantie wordt microfabricage geïntroduceerd als een multifunctioneel instrument om de effecten van katalysatorsamenstelling, nanostructurering en lokale omgeving op de productselectiviteit te bestuderen. Hierin worden de optimale condities onthuld voor de productie van complexe producten en wordt het bestaan van twee mechanismen voor de vorming van 1-propanol gesuggereerd. Ten tweede zijn de mechanistische routes onthuld naar meer overvloedige C<sub>3</sub> producten en is onthuld waarom propeen, het C<sub>3</sub> equivalent van het zeer favoriete ethyleen, niet wordt waargenomen. Tenslotte werd het palet van producten uitgebreid tot C<sub>4</sub> oxygenaten, waarmee de grens van de koperchemie werd verlegd naar de implementatie van 1-stap-processen.



## Author Contributions

Collaborations with experts in different fields were developed to achieve the aims of this thesis, which was supervised by Prof. Dr. Javier Pérez-Ramírez and Dr. Antonio J. Martín. In view of experiments, Florentine L.P. Veenstra synthesized and evaluated catalytic materials and was responsible for their characterization by different methods. She analyzed and quantified the gaseous products using gas chromatography and the liquid products using Nuclear Magnetic Resonance (NMR) spectroscopy. She was supported by Dr. René Verel throughout the work for NMR method development. She was supported by the core team of FIRST (Chapter 2) for training of clean room procedures. Dr. Norbert Ackerl (Chapter 3) created the laser-ablated copper foil catalysts. Dr. Louisa Ting from the group of Prof. Dr. B.S. Yeo from NUS (Singapore) (Chapter 4 and 5) contributed to the experimental activities. X-ray photoelectron spectroscopy measurements were performed by Dr. Simon Büchele and microscopy imaging were performed by Dr. Antonio J. Martín. In view of simulations, COMSOL was performed by Florentine L.P. Veenstra with the support of Dr. Antonio J. Martín (Chapter 3) and all Density Functional Theory and Graph Network simulations were performed by the group of Prof. Dr. Nuria Lopez from ICIQ (Spain): Dr. Sergio Pablo-García (Chapter 4 and 5), Dr. Federico Dattila (Chapter 4), Dr. Rodrigo García-Muelas (Chapter 4 and 5). Their input on the interpretation of the corresponding analysis was key to the insights gained in this thesis.





# Chapter 1

## Introduction

### 1.1. The Carbon Cycle

In nature, reduction of carbon dioxide (CO<sub>2</sub>) through photosynthesis is mostly in equilibrium to the oxidation of carbon compounds in cellular respiration. While humanity increased its oxidation of carbon compounds through increased industrialization over the last centuries, we are yet to balance it by reduction of CO<sub>2</sub>. This imbalance has become a significant perturbation to Earth's natural carbon cycle and is the motivation to today's climate change agenda<sup>[1]</sup> and the birth of the Paris agreement.<sup>[2]</sup> There are three main strategies to reduce net CO<sub>2</sub> emissions: decarbonization of energy sources, Carbon Capture and Storage (CCS) and Carbon Capture and Utilization (CCU). Decarbonization is referring to the decoupling of economic growth from energy consumption and CO<sub>2</sub> emissions.<sup>[3,4]</sup> This strategy, while being pursued heavily by private investment, is still limited in terms of scalability, versatility and energy storage capability.<sup>[5,6]</sup> CCS would allow for the net production of CO<sub>2</sub> in industry but aims to prevent its release to the atmosphere (by storing safely underground).<sup>[7-9]</sup> This strategy demands that the cost of emitting CO<sub>2</sub> needs to rise higher than the costs of separation and storage, but the geological storage capacity is limited and therefore this is not a sustainable pathway.<sup>[8]</sup> CCU is the strategy of CO<sub>2</sub> conversion toward more reduced products. This approach would require the transfer of electrons to carbon, making the oxidation state (+4) more negative. The stability of CO<sub>2</sub> makes this transfer demanding, therefore, conversion of CO<sub>2</sub> requires efficient catalysts to lower the energy barrier. This reaction can be facilitated through photo-, thermo- or electrocatalysis. The conversion of CO<sub>2</sub> using water as the proton source is depicted in **Eq. 1**, and the one using hydrogen (H<sub>2</sub>)<sup>[10]</sup> is depicted in **Eq. 2**.



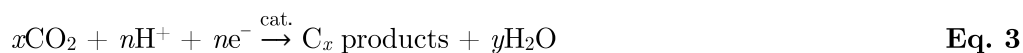
In photocatalysis, this conversion in **Eq. 1** is referred to as CO<sub>2</sub> fixation and is currently limited by; low catalytic performance, frequent use of sacrificial agents, low energy density of sunlight,

and the complexity of achieving multicarbon ( $C_{2+}$ ) products due to the monometallic nature of homogeneous catalysts.<sup>[11]</sup> In thermocatalysis (**Eq. 2**),  $CO_2$  is hydrogenated mostly towards  $C_1$  compounds (*e.g.* carbon monoxide, methane, methanol), requiring multi-step processes to achieve appreciable rates towards complex products,<sup>[12]</sup> based on producing  $H_2 + CO$  or synthetic gas (syngas) as an intermediate step.<sup>[13–15]</sup> In order for  $CO_2$  hydrogenation by the above reactions to be a renewable process, the hydrogen must come from water splitting using renewable energy or biomass gasification.

In electrochemistry the conversion mentioned in **Eq. 1** is referred to as electrocatalytic  $CO_2$  reduction ( $eCO_2R$ ), using water in excess as source of electrons ( $e^-$ ) and protons ( $H^+$ ) and as supporting electrolyte enabling charge transfer of present cations. This reaction can be integrated with a renewable energy source, such as wind and solar,<sup>[16–18]</sup> making it a desirable strategy to close the carbon cycle.

## 1.2. The Electrocatalytic $CO_2$ Reduction

The  $eCO_2R$  converts either dissolved  $CO_2$  in aqueous electrolyte or a stream of gaseous  $CO_2$  (in gas diffusion electrode (GDE) configuration) toward carbon products that are either gaseous or liquid. Gaseous products are commonly detected by gas chromatography (GC) or GC connected to mass spectrometry (GC-MS) and liquid products are sampled from the electrolyte and quantified by nuclear magnetic resonance (NMR) spectroscopy or headspace high performance liquid chromatography (headspace HPLC). **Eq. 3** shows a general form of the reaction at the cathodic side, needing protonated medium and the equivalent number of electrons enabling the conversion on a catalytic surface. The competing reaction to the  $eCO_2R$  is the hydrogen evolution reaction (HER, **Eq. 4**). Both **Eq. 3** and **Eq. 4** are cathodic half reactions that require an anodic half reaction to close the charge balance, which is usually the oxygen evolution reaction (OER) as depicted in **Eq. 5**.



Hori *et al.*<sup>[19]</sup> were the first on reporting the eCO<sub>2</sub>R reaction in 1985 on polycrystalline metal electrodes. This and subsequent studies, utilizing basically the same methods,<sup>[20–22]</sup> led to a classification of metal electrodes into four groups.<sup>[23]</sup> The first group produces mainly formate (HCOO<sup>-</sup>) and is composed of Pb, Hg, Tl, In, Sn, Cd, and Bi. The second group produces mainly carbon monoxide (CO) and is composed of Au, Ag, Zn, and Pd. The third group almost exclusively prefers HER over eCO<sub>2</sub>R; Ni, Fe, Pt, and Ti. The fourth group only shows one member able to produce a variety of C<sub>2+</sub> products with substantial Faradaic efficiency (*FE*); Cu. Even discussed in more detail below, the unique ability of Cu may be due to the fact that it is the only metal that has a slight negative adsorption energy for CO\* but a positive adsorption energy for H\*.<sup>[24]</sup> Hori *et al.*<sup>[25]</sup> continued their work on constant-potential electrolysis (CO<sub>2</sub> saturated 0.1 M potassium bicarbonate (KHCO<sub>3</sub>) at pH of 6.8) and found a variety of products formed in the potential range of -0.40 V to -1.05 V *vs.* reverse hydrogen electrode (RHE). Later, Kuhl *et al.*<sup>[26]</sup> drew similar conclusions in their electrolysis experiments in the potential range between -0.60 V and -1.20 V *vs.* RHE and, using more sensitive product detection techniques for liquid products, they observed a total of 16 products. Based on the demonstrated versatility of copper, many more studies since then have targeted selectivity enhancement for specific products and increased to 17 the palette of reported products reaching up to C<sub>3</sub> compounds. Among other contributions, this thesis expands the scope of products up to C<sub>4</sub>. A comprehensive overview of all products reaching C<sub>3</sub> compounds reported thus far for eCO<sub>2</sub>R can be observed in **Figure 1.1a**, with the highest *FE* values reported per product. **Figure 1.1b** is adapted from Nitopi *et al.*<sup>[27]</sup>, showing a simplified mapping of the energetics of more relevant CO<sub>2</sub> electroreduction products. The approximate market price of selected CO<sub>2</sub> reduction products are depicted and represented versus their specific energy content. The marker size indicates the (logarithmic) size of the global market, which spans more than 4 orders of magnitude. All quantities are normalized to the mass of carbon.

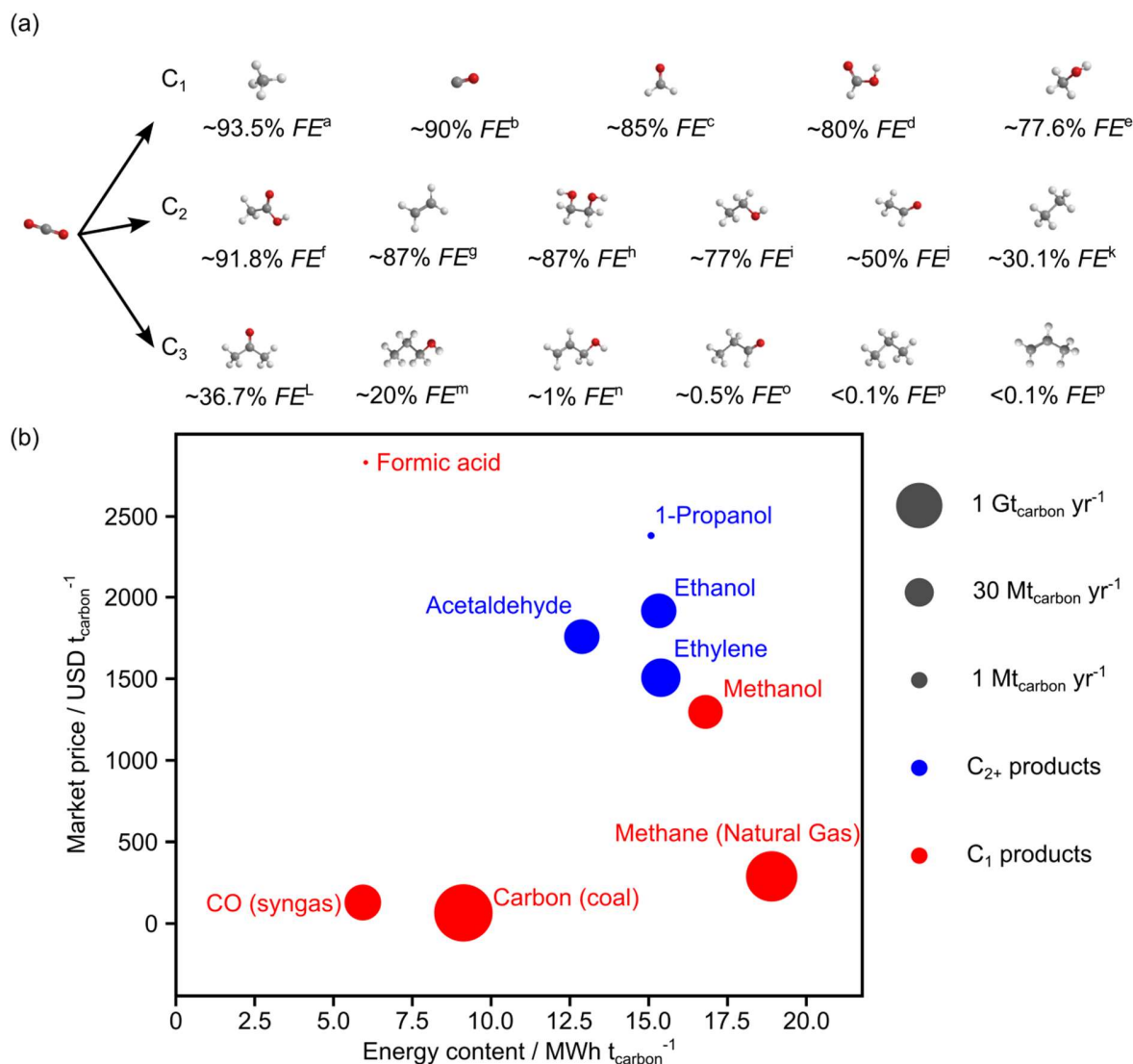


**Figure 1.1.** (a) Electrocatalytic CO<sub>2</sub> reduction products, highest *FE* reported. a,<sup>[28]</sup> b,<sup>[29]</sup> c,<sup>[30]</sup> d,<sup>[31]</sup> e,<sup>[32]</sup> f,<sup>[33]</sup> g,<sup>[34]</sup> h,<sup>[35]</sup> i,<sup>[36]</sup> j,<sup>[37]</sup> k,<sup>[35]</sup> l,<sup>[38]</sup> m,<sup>[39]</sup> n,<sup>[40]</sup> o,<sup>[25]</sup> p.<sup>[41]</sup> (b) Market price of selected CO<sub>2</sub> recycling products as a function of energy content adapted from Nitopi *et al.*<sup>[27]</sup>

The ability to reduce CO<sub>2</sub> to complex and valuable hydrocarbons, aldehydes, and alcohols is thus of great interest; as a result, there has been much work done in the field to better understand the reactivity of Cu and how it can be tuned to achieve greater selectivity, stability, and efficiency. To favor one of the reported products,<sup>[26]</sup> variations in the composition and nanostructuring of Cu electrodes have been largely explored. For example, numerous p- and d-block elements have been used as modifiers or as alloying agents.<sup>[27,31]</sup> The structure sensitivity of eCO<sub>2</sub>R has been demonstrated, opening the door for nanostructuring efforts in catalyst design of Cu materials.<sup>[27]</sup>

Remarkably, Cu oxide as the catalyst precursor shows distinctive catalytic performance to metallic Cu, despite its (almost) complete reduction under operation conditions.<sup>[42]</sup> This so-called oxide-derived Cu (OD-Cu) exhibits lower overpotentials towards complex products in general than its pristine metallic counterpart.<sup>[25]</sup> The next section discusses these aspects in more detail.

### 1.3. Selectivity Drivers

As mentioned, 17 products ranging from C<sub>1</sub> to C<sub>3</sub> have been reported thus far for the eCO<sub>2</sub>R over Cu-based catalysts as depicted in **Figure 1.1a**. In general terms, it can be claimed that there is a moderate understanding of the influence of catalyst composition to the selectivity of C<sub>1</sub> products and how surface nanostructuring affects the selectivity patterns in complex product formation (**Figure 1.2a**). Regarding the latter, electrocatalytic properties can be altered by nanostructuring due to higher occurrence of undercoordinated sites, preferential faceting, and re-adsorption of products.<sup>[43–45]</sup> Among available strategies to achieve nanostructuring, a commonly used one is anodic treatment or in-situ electrochemical oxidation–reduction treatment which would result in formation of nanostructures on the surface of polycrystalline Cu.<sup>[46–49]</sup> OD-Cu material from copper(I)oxide films, prepared by electrodeposition or hydrothermal synthesis onto a substrate<sup>[17,50–52]</sup> results in a rough surface, while less rough than the calcination and subsequent electrochemical reduction of planar Cu foils which resulted in greater electrochemically active surface area (ESCA).<sup>[42]</sup> Using OD-Cu (anodic treated, from copper(I)oxide films or calcinated), Cu nanowire structuring<sup>[53–58]</sup> would improve selectivity toward C<sub>2+</sub> and suppress C<sub>1</sub> compounds in eCO<sub>2</sub>R.<sup>[43,56,57,59–61]</sup> Roberts *et al.*<sup>[62]</sup> worked on copper nanocubes (**Figure 1.2a**) and found that the Cu(100) surface orientation promotes methane while Cu(111) promotes ethylene, unfortunately, these structures are found to be highly unstable.<sup>[46,62,63]</sup> Eilert *et al.* used X-ray absorption spectroscopy (XAS) to study the properties of two type of electrodes; cube-shaped nanostructured prepared from redox cycling copper oxide (Cu<sub>2</sub>O) and the disordered (without cubic geometry) equivalent from CuO – both showing very similar eCO<sub>2</sub>R performance. The higher roughness factor (ECSA/geometric electrode area) of these nanostructured electrodes would lead to an elevated local pH close to the electrode surface, which has been shown to favor C<sub>2+</sub> over C<sub>1</sub> compounds.<sup>[64]</sup> pH and CO<sub>2</sub> concentration are two descriptors for local chemical environment (**Figure 1.2b**) largely influencing the selectivity and activity in eCO<sub>2</sub>R.

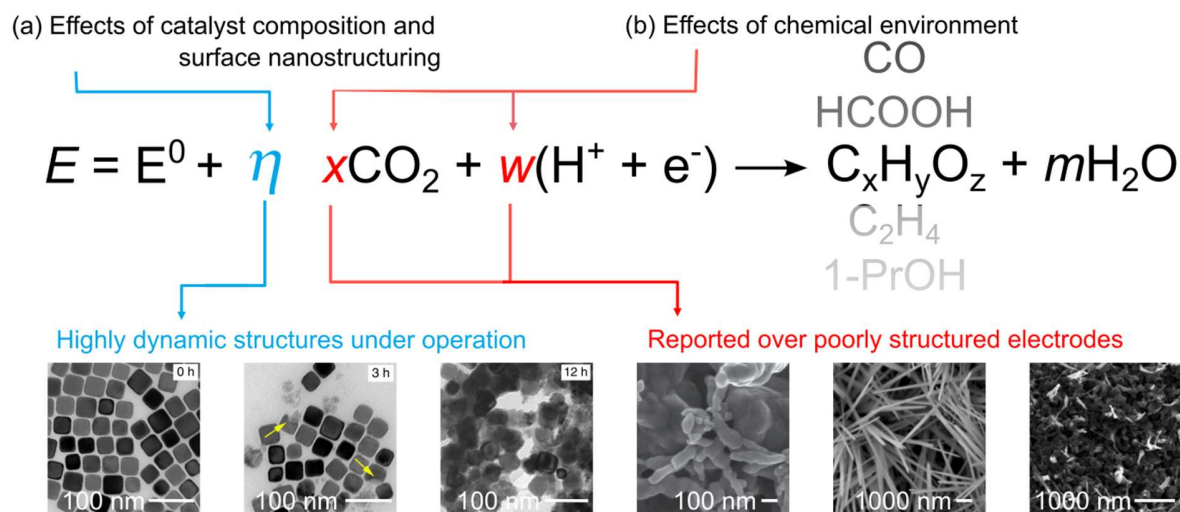


**Figure 1.2.** Main selectivity drivers on Cu catalysts. (a) Catalyst composition and nanostructuring mostly affect energetics of eCO<sub>2</sub>R as reflected in varying overpotentials.<sup>[63]</sup> (b) The local chemical environment determines availability of reacting species.<sup>[43,56,65]</sup>

Hori *et al.*<sup>[23]</sup> propose that the mechanism for C<sub>2+</sub> and C<sub>1</sub> compounds do not share rate-determining steps since the pathway toward C<sub>2+</sub> is pH independent and the pathway toward C<sub>1</sub> is pH dependent. Further evidence for this notion was provided in a series of studies on single crystal electrodes by the group of Marc Koper,<sup>[66–68]</sup> which revealed that there are two possible pathways to ethylene depending on the pH, surface structure, and overpotential. When using electrocatalytic CO reduction (eCOR) as a proxy, mechanistic insights about the pathway to further reduced products can be obtained given the key role of CO as intermediate, giving the chance to confirm the above conclusions in buffer solutions spanning a bulk pH of 6 to 12.<sup>[25]</sup> Understanding the impact of pH and CO<sub>2</sub> is a major and challenging area of study due to the dynamic reaction environment at the electrode surface and the nanometric scale at which it occurs. The local environment is actually driven by a number of factors; the composition and concentration of anions and cations can cause changes in the electrostatic interactions, buffer capacity, pH, and availability of proton donors.<sup>[21,25,69]</sup> These changes are not always straightforward to map due to intertwining effects. A local pH gradient can develop at the cathode surface due to depletion of protons/production of hydroxide ions (OH<sup>-</sup>) from the HER and eCO<sub>2</sub>R. Given that CO<sub>2</sub> forms bicarbonate (HCO<sub>3</sub><sup>-</sup>) and carbonate (CO<sub>3</sub><sup>2-</sup>) when it is purged through alkaline solutions, electrolytes for eCO<sub>2</sub>R are generally limited to neutral and acidic pH conditions. Additionally, the carbonate equilibria makes CO<sub>2</sub>

being both a reactant and a buffer, so an increased pH near the cathode surface can cause the concentration of dissolved  $\text{CO}_2$  to deviate (decrease) from that in the bulk electrolyte.<sup>[70–72]</sup> It has been shown that even modest current densities can cause the surface pH to vary significantly from that in the bulk electrolyte, perturbing the reaction thermodynamics and kinetics in several ways.<sup>[71]</sup> The precise quantification of the influence of the local chemical environment is thus of the utmost relevance and still pending, since operando tools do not allow for direct measurements of pH or  $\text{CO}_2$  concentration and poorly defined structure of electrodes do not allow for accurate modelling (**Figure 1.2b**). This thesis contributes to this end, helping the elucidation of pathways toward selective  $\text{C}_{2+}$  products.

## 1.4. Mechanistic Aspects and Model Systems

In recent years, experimental work enjoyed theoretical guidance in  $\text{eCO}_2\text{R}$  catalyst design while theoretical mechanistic investigations got support from targeted experiments.<sup>[73]</sup> This symbiotic pattern between theoreticians and experimentalists is also observed throughout this thesis. Ever since Hori's discovery in 1985,<sup>[19]</sup> theoreticians have worked with intent to elucidate the reaction mechanism of  $\text{eCO}_2\text{R}$  over Cu-based materials toward  $\text{C}_1$  and  $\text{C}_{2+}$  compounds. The  $\text{eCO}_2\text{R}$  is particularly challenging to simulate due to its complex reaction networks and the influence of ion, pH and solvent effects in their kinetics.<sup>[24,74]</sup> The field is still developing with researchers adding, removing and adjusting previously proposed pathways, with little consensus in sight. In general, the thermodynamics for electrochemical reactions are simulated by using the computational hydrogen electrode model,<sup>[75]</sup> which relies on calculations of adsorption energies and a  $\text{H}_2$  gas reference to account for the free energy of proton–electron pairs. Surface hydrogenation barriers through an adsorbed  $\text{H}^*$  are easy to determine in vacuum, but electrochemical barriers are considerably more challenging.<sup>[76]</sup>

Most mechanisms agree that the step in which  $\text{CO}_2$  is adsorbed is the rate determining step in  $\text{eCO}_2\text{R}$ . It is still debated whether the first intermediate is arrived at by concerted proton-electron transfer (CPET) or a decoupled pathway through a charged intermediate.<sup>[77]</sup> Early experimental work found that the reduction of CO on Cu leads to a similar product distribution as  $\text{CO}_2$  reduction on Cu, suggesting that CO is a key intermediate toward complex products.<sup>[21,25,69,78,79]</sup> Detailed studies of  $\text{eCOR}$  on Cu supported this claim,<sup>[25,80,81]</sup> in addition to spectroscopic observation of surface adsorbed CO under reaction conditions.<sup>[82–87]</sup> The ability to adsorb CO ( $\text{CO}^*$ ) is thus a key



descriptor for reduction activity to  $C_{2+}$  products.<sup>[88–90]</sup> Metals that bind CO too strongly will be poisoned by this intermediate, while those that bind CO too weakly will desorb it from the surface before further reaction. In agreement with the Sabatier principle,<sup>[91]</sup> the intermediate binding energy for CO on Cu is a key reason for its ability to catalyze  $CO_2$  to  $C_{2+}$  products.<sup>[92]</sup> Furthermore, studies have shown that CO adsorption on Cu suppresses the competing HER due to site blocking effects and/or changes in  $H^*$  binding energy.<sup>[21,88,92,93]</sup>

Beyond  $CO^*$ , a significant distinguishing feature between the  $C_1$  and  $C_2$  pathways is the observed sensitivity to pH, as mentioned before. Considering that ethylene formation is independent of pH on the standard hydrogen electrode (SHE) scale (whereas  $C_1$  is dependent of pH),<sup>[25,81]</sup> this would lead to the experimental observation of a lower onset potential with increased pH (*vs.* RHE) for  $C_2$  products. The limiting step in  $C_2$  formation has generally been thought to be CO dimerization.<sup>[70,94–98]</sup> While CO dimerization has been widely suggested, there are many aspects to this step that are still up for debate, such as whether CO coupling is an electrochemical step (involving a rate-limiting electron transfer)<sup>[70,94,96–98]</sup> or is purely a chemical step (not involving a rate-limiting electron transfer).<sup>[96,98]</sup> Finally, it is debated whether coupling occurs between two adsorbed CO molecules ( $CO^* + CO^*$ ),<sup>[70,94–96,98]</sup> an adsorbed and a free CO molecule ( $CO^* + CO(g)$ ),<sup>[97,99]</sup> or between species such as  $CHO^*$  and  $CO^*$ <sup>[96]</sup> or  $CO(g)$ .<sup>[95,99]</sup> This partially stems from the notion that there are two possible pathways to ethylene depending on the surface structure and overpotential, via CO dimerization or through  $CHO^*$ .<sup>[66–68]</sup> Indeed, after the C-C coupling step, the mechanism ramifies towards the different  $C_2$  products.<sup>[25,26,77,98–101]</sup>

Besides ethylene, as a major product in  $eCO_2R$ , other desired products would be  $C_{2+}$  oxygenates, such as higher alcohols. It has long been thought that aldehydes are key intermediates to alcohols after Hori and co-workers observed that acetaldehyde and propionaldehyde were easily reduced to ethanol and 1-propanol, respectively.<sup>[25]</sup> Through an operando MS connected to the GDE, it was observed that acetaldehyde and propionaldehyde are produced in 2–4 times higher abundance than ethanol or 1-propanol compared to sampling from the bulk electrolyte, where they are typically only observed as minor products.<sup>[102]</sup> Thus, the authors suggest that these aldehydes are transiently produced and relatively abundant within the local reaction environment, but are typically reduced further to the corresponding alcohols before diffusing into the bulk electrolyte.

Interestingly, it was also found that ethanol production increased at the expense of propionaldehyde at more cathodic potentials, suggesting that ethanol and propionaldehyde may share a common intermediate such as acetaldehyde.<sup>[102]</sup> As for the C<sub>3</sub> products, the number of possible elementary steps of the network increases with respect to the C<sub>2</sub> case, making their study considerably more complex, and thus, presenting more controversy among the scarcely available theoretical and experimental studies.<sup>[103-105]</sup> Adding to this complexity is that certain C<sub>3+</sub> intermediates with large dipole moments are affected by the fields induced by cations at the interface, which increases the degrees of freedom affecting both thermodynamics and kinetics.

As discussed, there is a predominant theoretical approach to mechanistic studies due to the lack of model catalysts in electrocatalysis enabling testing and quantification of products under reaction conditions. Model systems operational under reaction conditions would enable the deeper understanding from an experimental perspective. Only two studies in literature trying to address fundamental understanding using model systems could be identified. One devoted to studying tandem catalysts<sup>[106]</sup> and the other one on activity of interfacial sites.<sup>[107]</sup> The first study linked CO spillover effect with improved C<sub>2+</sub> activity. The authors of this study fabricated a series of electrodes on the microscale, designed to hold an insulating silicon-oxide (SiO<sub>2</sub>) between interdigitated silver (Ag) or gold (Au) and Cu electrodes, individually driven. They attributed the improved selectivity toward C<sub>2+</sub> oxygenates to CO spillover from Ag or Au substrate to Cu surface, increasing the CO density while reducing the H\* coverage. This study showcases a new design principle of tandem catalysis using in situ source of mobile CO to aid in eCO<sub>2</sub>R.<sup>[106]</sup> The second study, performed by colleagues in my group, linked active sites at metal-oxide interfaces (In<sub>2</sub>O<sub>3</sub>/Cu<sub>2</sub>O) to improved CO activity. They prepared a series of microfabricated electrodes, composed of islands of indium oxide on copper substrates. By modifying the geometric pattern, they varied the density of interfacial sites while keeping the same oxide coverage. They attributed the improved activity toward CO to the increased density of interfacial sites (between In<sub>2</sub>O<sub>3</sub> and Cu<sub>2</sub>O). This study showcases how active sites can be identified through compositional and morphological effects.<sup>[107]</sup> This thesis contributes to the development of model systems for fundamental mechanistic studies towards C<sub>2+</sub> products.

## 1.5. Aim of the Thesis

This thesis was generously supported by an ETH Research Grant (ETH-47 19-1) and by the European Union through the A-LEAF project (732840-A-LEAF). The primary goal is to deepen the understanding of pathways toward more complex products over copper-based catalysts in the electrocatalytic CO<sub>2</sub> reduction reaction. To this end, the thesis develops microfabrication tools able to assess catalyst stability and quantifying chemical environment effects. Furthermore, the pathways toward main C<sub>3</sub> compounds are investigated on practical catalysts. The scope of products and formation mechanisms of eCO<sub>2</sub>R is extended to C<sub>4</sub> oxygenates.

## 1.6. Outline of the Thesis

The results of this thesis are presented in four chapters (**Chapter 2-5**) followed by the conclusions and outlook (**Chapter 6**).

**Chapter 2** presents a study into synergistic effects and dynamic phenomena in multicomponent catalysts through the evaluation and characterization of microfabricated electrodes with controlled geometry and composition. This approach is applied to the study of the Cu-In system. Photolithographic templating enables the deposition of regular arrays of In<sub>2</sub>O<sub>3</sub> islands on Cu, Cu<sub>2</sub>O and copper nitride (Cu<sub>3</sub>N) surfaces, resulting in structured electrodes that can be evaluated under practical eCO<sub>2</sub>R conditions. The post-reaction characterization of the structured electrodes and the relationship of the CO evolution activity with their geometry and composition reveal the key role of interfaces and improved stability brought by nitride derived copper.

**Chapter 3** presents the first study to quantify chemical environment effects under eCO<sub>2</sub>R reaction conditions. It uses laser microstructured electrodes with controlled geometry and composition. The OD-Cu surface produced a range of C<sub>1</sub> to C<sub>3</sub> products with different selectivity patterns, yielding maps through simulation that would provide mechanistic insights and practical predictions such as the optimal conditions for the major products and the effect of varying electrolytes or stirring rates.

**Chapter 4** presents a practical approach to find the mechanistical pathway to main C<sub>3</sub> products through experimental work combined with graph network and DFT. The coupling of an oxygenated C<sub>1</sub> with a hydrogenated C<sub>2</sub> fragment would yield the key intermediate CH<sub>2</sub>CHCO\*,

an antecedent of propylene, 1-propanol and the other frequently reported products. Propylene is kinetically hindered, explaining its absence under reaction conditions.

**Chapter 5** presents the first study reporting C<sub>4</sub> compounds in eCO<sub>2</sub>R due to a reactor design that enables the high current densities required to quantify the yields of 1-butanol and 1-butanal. The first C<sub>4</sub> intermediate is formed through condensation in alkaline conditions as a chemical step supported by OD-Cu electrocatalyst. The efficient production of C<sub>4+</sub> compounds would require a multi-step process design with both alkaline and neutral conditions facilitating chemical and electrocatalytic steps.

**Chapter 6** summarizes the key results of the research introduced throughout this thesis, elaborating on strategies to obtain complex products. It identifies artificial leaves as a promising strategy to realize the distributed valorization of CO<sub>2</sub> where the findings of this thesis have direct application and clarifies efforts of future research in that direction.







## Chapter 2

# Nitride-Derived Copper Modified with Indium as a Selective and Highly Stable Catalyst for the Electroreduction of Carbon Dioxide

### 2.1. Introduction

The Paris agreement<sup>[108]</sup> established a roadmap to reduce the atmospheric concentration of CO<sub>2</sub> below 350 ppm within this century, including the important milestone of achieving a carbon-neutral economy by 2050. The eCO<sub>2</sub>R has the potential to abate anthropogenic emissions significantly within this pressing deadline, given its natural coupling with renewable energy sources and mild operating conditions. However, this vision faces the key challenge of developing selective, active, and stable electrocatalysts in aqueous media.<sup>[109]</sup> The emergence of synergistic effects in multicomponent systems provides unique opportunities to overcome the scaling relation<sup>[88,110]</sup> between the binding energies of intermediates inherently limiting the performance of transition metals typically used for this reaction.<sup>[26,111]</sup> However, a limited understanding of interfacial effects frequently accompanied by deep compositional and/or structural changes under reaction conditions<sup>[31,112–115]</sup> precludes the derivation of accurate structure-performance relationships that can guide the optimization toward breakthrough advances.

It was recently demonstrated that the controlled variation of the geometry and composition achieved by microfabrication tools can be used to derive correlations with catalytic performance, monitor dynamic processes, and gain insights into the nature of the active phase in multicomponent electrocatalysts.<sup>[107]</sup> In particular, for the highly selective Cu-In system<sup>[112,116]</sup> a direct relationship between the amount of a Cu-In bimetallic phase with low indium content and the CO partial current density ( $j$ ) was disclosed when Cu<sub>2</sub>O acted as the copper source, irrespective of the initial indium phase (In or In<sub>2</sub>O<sub>3</sub>). Moreover, its formation could be associated to a solid-state reaction developed under eCO<sub>2</sub>R conditions manifested in diffusion of indium through the copper matrix.



The reason for the crucial role of the oxidic copper phase remains unclear, but may be associated to any of the diverse features linked to  $\text{Cu}_2\text{O}$  reduced under  $\text{eCO}_2\text{R}$  conditions. Features such as a rougher surface,<sup>[117]</sup> larger density of grain boundaries<sup>[42,61]</sup> and the possible presence of residual oxygen<sup>[44,64]</sup> under operation conditions, which may also lead to characteristic electronic properties favoring the  $\text{eCO}_2\text{R}$ .<sup>[118]</sup> These results explained the marked reconstruction under reaction conditions observed in  $\text{In}_2\text{O}_3$  supported on  $\text{Cu}_2\text{O}$  ( $\text{In}_2\text{O}_3/\text{Cu}_2\text{O}$ ),<sup>[113]</sup> but also stress the difficulty in achieving, through rational optimization, a configuration with high performance over prolonged operation. Since this is one of the most prominent standing challenges toward practicality in the  $\text{eCO}_2\text{R}$ ,<sup>[111,119]</sup> these results pose the question of whether a highly active and stable phase can be achieved by modifying the copper source.

To investigate this,  $\text{Cu}_3\text{N}$  was explored, a copper phase with a slightly more covalent character than  $\text{Cu}_2\text{O}$ <sup>[120]</sup> which has been reported to display synergetic interactions with Cu in a core-shell ( $\text{Cu}_3\text{N-Cu}$ ) configuration, favoring the selectivity toward  $\text{C}_{2+}$  products in the  $\text{eCO}_2\text{R}$  as the result of  $\text{Cu}^+-\text{Cu}^0$  interactions.<sup>[121]</sup> Catalytic tests over  $\text{In}_2\text{O}_3/\text{Cu}_3\text{N}$  yielded improved activity and selectivity toward CO and an excellent structural and catalytic stability demonstrated for at least 50 h. This behavior was rationalized over microfabricated electrodes, whose analysis unambiguously associated  $\text{eCO}_2\text{R}$  activity and interface but did not observe diffusion of indium in the case of  $\text{In}_2\text{O}_3/\text{Cu}_3\text{N}$ , giving rise to stable interfaces. In stark contrast, typical diffusion lengths of a few micrometers were found over the system based on OD-Cu. Spectroscopic analyses disclosed temporary persistent nitrogen species upon reduction which may be associated to the stable behavior. This work thus unveils indium-modified copper nitride as a novel selective and robust catalyst and underlines the potential of reduced copper nitride (nitride-derived Cu, ND-Cu) to develop synergistic effects in the  $\text{eCO}_2\text{R}$ .

## 2.2. Experimental

### 2.2.1. Preparation of Catalysts in Powder Form

Cu<sub>3</sub>N was prepared by mixing CuO (0.15 g, Sigma-Aldrich) and NaNH<sub>2</sub> (1 g, Sigma-Aldrich) using a mortar and pestle in an argon-filled glovebox and transferred to a Teflon-lined steel autoclave,<sup>[122]</sup> followed by thermal treatment (443 K, 60 h, 5 K min<sup>-1</sup>) and natural cooling. The resulting powder was centrifuged multiple times using ethanol (Sigma-Aldrich) and water (whenever water is mentioned in the thesis it refers to 18.2 MΩ cm ultrapure Millipore water). Cu<sub>3</sub>N was obtained as a dark powder with a yield of 83%. Other reported solvothermal routes resulted in lower yields with large presence of metallic copper.<sup>[123,124]</sup> In<sub>2</sub>O<sub>3</sub>/Cu<sub>3</sub>N was prepared by mixing Cu<sub>3</sub>N (0.1 g) with NH<sub>4</sub>OH (6 cm<sup>3</sup>, VWR Chemicals, 25% in H<sub>2</sub>O) in ethanol (12 cm<sup>3</sup>) with a second solution containing InCl<sub>3</sub> (2, 4, 8 mg, abcr Inc.) in ethanol (13.5 cm<sup>3</sup>) and water (4.5 cm<sup>3</sup>). The resulting suspension was aged under continuous stirring (353 K, 10 min).<sup>[113]</sup> The obtained solid was transferred to a boat crucible and thermally treated (N<sub>2</sub>, 523 K, 3 h, 5 K min<sup>-1</sup>) to decompose the so-formed indium hydroxide. In<sub>2</sub>O<sub>3</sub>/Cu<sub>3</sub>N (nominal 0.5, 1.5, 4 wt.% In) was obtained with actual loadings of 0.1, 0.3, 1.7 wt.% In, respectively, determined by energy dispersive X-ray Spectroscopy (EDXS). Cu<sub>2</sub>O was solvothermally prepared by dissolving Cu(NO<sub>3</sub>)<sub>2</sub>·3 H<sub>2</sub>O (2 g, Sigma-Aldrich) in ethylene glycol (40 cm<sup>3</sup>, VWR Chemicals) under stirring, followed by its transfer into a 50 cm<sup>3</sup> Teflon-lined autoclave, thermal treatment (413 K, 10 h, 5 K min<sup>-1</sup>), and natural cooling.<sup>[125]</sup> The resulting powder was washed by centrifugation using water, resulting in Cu<sub>2</sub>O with a yield of 87%. In<sub>2</sub>O<sub>3</sub>/Cu<sub>2</sub>O (nominal 0.5, 1.5, 4 wt.% In) with actual loadings of 0.3, 0.9, 2.5 wt.% In, respectively, were synthesized adapting the procedure described for In<sub>2</sub>O<sub>3</sub>/Cu<sub>3</sub>N to target similar nominal loadings, requiring 0.5 g Cu<sub>2</sub>O and 10, 20, 40 mg of InCl<sub>3</sub>.

### 2.2.2. Preparation of Gas Diffusion Layer Electrodes

The electrodes were prepared by airbrushing a catalyst ink on a gas diffusion layer (GDL) carbon paper. The ink was prepared by ultrasonically dispersing the catalyst (100 mg) in a mixture of water (4 cm<sup>3</sup>), isopropanol (4 cm<sup>3</sup>) and 5 wt.% Nafion solution (0.05 cm<sup>3</sup>) for 30 min. The ink was then deposited with an airbrush (Iwata Eclipse HP - SBS) on the microporous layer of a GDL carbon paper (35BC, S110GL group, 12 cm<sup>2</sup> cross-sectional area) mounted on a hotplate at 353 K. A catalyst loading of 0.5-1.0 mg cm<sup>-2</sup> was typically achieved in this manner. The final electrodes were produced by cutting the GDL electrode in L-shaped pieces of *ca.* 1.5 cm<sup>2</sup> and attaching them

to a glassy carbon piece using Kapton tape to secure the electrical connection. The electrodes were photographed and their total geometric area determined with the Image J software (Wayne Rasband, National Institutes of Health). Current density reported in this work is referred to the geometric area of each electrode.

### 2.2.3. Electrochemical Tests

A custom gastight glass cell with two compartments separated by a Selemion AMV anion exchange membrane (AGC engineering) was employed for all electrochemical experiments. Each compartment contained electrolyte (40 cm<sup>3</sup>, 0.1 M KHCO<sub>3</sub> solution) and was saturated with CO<sub>2</sub> (Messer, purity 4.8) for at least 30 min prior to the start of the electrolysis, with a resulting pH of 6.8. CO<sub>2</sub> was continuously bubbled into the catholyte during the electrolysis at a flowrate of 20 cm<sup>3</sup> min<sup>-1</sup>. All electrochemical measurements were carried out at room temperature (rt) with an autolab PGSTAT302N potentiostat, using a platinum wire as the counter electrode and a Ag/AgCl reference electrode (3 M KCl, model RE-1B, ALS). Potentiostatic electrolyses were carried out with the ohmic voltage drop ( $iR$ ) compensation function set at 85% of the uncompensated resistance ( $R_u$ ), which was determined before the start of the electrolysis and updated every 10 min by electrochemical impedance spectroscopy (EIS) measurements during the electrolysis. Following this correction, the applied potentials were within 10 mV of the target potential.<sup>[26]</sup> Double-layer (DL) capacitances of the electrodes (normalized to the geometric area) were estimated by performing cyclic voltammeteries (CVs) at different scan rates (2–50 mV s<sup>-1</sup>) narrowly centered (30 mV) at the open-circuit potential (OCP) before and after electrolysis, following full stabilization of the CV response.

#### 2.2.4. Preparation of Microstructured Electrodes

Si wafers (100 mm diameter) were used as substrates for the microfabrication process. The pretreatment of the wafer consisted on depositing an electrically insulating layer of silicon oxide (SiO<sub>x</sub>, 500 nm) at 573 K under a pressure of 900 mTorr by using plasma-enhanced chemical vapor deposition (PECVD) on the Oxford Instruments Plasmalab 80 Plus system. Subsequently, tantalum (50 nm) was deposited by direct current (DC) magnetron sputtering of the metal target (Ta, MaTeCK GmbH 99.95%) at 400 mA under 80 cm<sup>3</sup> min<sup>-1</sup> Ar at a pressure of 8 mTorr to act as a diffusion barrier between the copper layers and SiO<sub>x</sub>/Si. The pretreatment of the wafer ended with the deposition of a Cu layer (10 nm) by radio frequency (RF) magnetron sputtering of the metal target (Cu, MaTeCK GmbH 99.99%) with a power of 200 W under 80 cm<sup>3</sup> min<sup>-1</sup> Ar at 8 mTorr. Subsequently, a Cu, Cu<sub>2</sub>O, or Cu<sub>3</sub>N layer was deposited (190 nm) by sputtering. The metallic Cu-based electrodes were prepared by DC magnetron sputtering of the metal target (Cu, MaTeCK GmbH 99.99%) at 250 mA under 80 cm<sup>3</sup> min<sup>-1</sup> Ar at 8 mTorr. Cu<sub>2</sub>O was prepared by DC magnetron sputtering of the metal target (Cu, MaTeCK GmbH 99.99%) at 250 mA under 80 cm<sup>3</sup> min<sup>-1</sup> Ar and 8.9 cm<sup>3</sup> min<sup>-1</sup> O<sub>2</sub> at 8 mTorr. Cu<sub>3</sub>N was prepared by RF magnetron sputtering of the metal target (Cu, MaTeCK GmbH 99.99%) with a power of 200 W under 25 cm<sup>3</sup> min<sup>-1</sup> Ar and 25 cm<sup>3</sup> min<sup>-1</sup> N<sub>2</sub> at 6 mTorr. These depositions were undertaken by using a Mantis HiPIMS deposition system equipped with confocal sources without substrate heating. After deposition of the copper phases, wafers were patterned by photolithography followed by deposition of In<sub>2</sub>O<sub>3</sub>. LOR 3A lift-off resist (Micro-Chem) was spin-coated on the substrate (3.5 s, 3500 rpm, 45 s) and baked at 423 K for 600 s. AZ nLOF 2020 negative photoresist (Merck Performance Materials) was spin-coated afterwards on the substrate (3 s, 3000 rpm, 45 s) and soft-baked at 383 K for 60 s. The coated substrates were exposed to UV light (55 mJ cm<sup>-2</sup>, 365 nm, 3 cycles) through a chrome/sode-lime glass photomask using a Karl Suss MA6 mask aligner. The photomask was designed as to define 12 patterned regions on the wafer, each including a dense hexagonal array of circles, which allowed the simultaneous fabrication of several electrodes with varying geometry (as described in the next section) in addition to control samples with either total or no coverage of In<sub>2</sub>O<sub>3</sub>. Post-exposure bake was performed at 383 K for 60 s. Afterwards, the resist was developed for 50 s in AZ 826 MIF developer (Merck Performance Materials). Once the wafer was patterned, the islands were created by depositing a layer of In<sub>2</sub>O<sub>3</sub> (100 nm) by electron beam evaporation (10 kV, 0.6 A electron beam gun source, 6 Hz beam size, 2·10<sup>-7</sup> mbar base pressure, 1·10<sup>-5</sup> mbar

operating pressure). The evaporation source was sintered granules ( $\text{In}_2\text{O}_3$ , Kurt J. Lesker 99.99%) in a graphite crucible. The remaining photoresist was removed by soaking the wafer in N-methyl-2-pyrrolidone (NMP) at 353 K for 60 min and the wafers rinsed with copious amounts of water and blow-dried with a nitrogen gun. As the last step, each wafer was coated with a protective layer of mr-PL 40 photoresist (Micro-Resist Technology GmbH) by spin-coating (3 s, 3000 rpm, 45 s) followed by a bake procedure at 383 K for 60 s. The individual electrodes ( $20 \times 20 \text{ mm}^2$ ) or ( $15 \times 20 \text{ mm}^2$ ) were finally obtained by dicing the wafer using a silicon blade in a Disco DAD 321 dicing saw. The protective layer was removed by individually dipping the electrodes in NMP at 323 K for a few minutes. Furthermore, each electrode was rinsed with copious amounts of water, and blow-dried with a nitrogen gun.

### 2.2.5. Geometrical Definitions

As described in the main text, the islands are distributed on the geometrical active surface of each electrode ( $A_{\text{total}} = 2.25 \text{ cm}^2$ ) in a periodic hexagonal array (**Figure 2.1**). This arrangement is defined by a two-dimensional unit cell in which islands of diameter  $d$  are separated by a pitch  $c$  (*i.e.*, the centre-to-centre separation). Consequently, the area of this unit cell  $A_{\text{uc}}$  is given by **Eq. 6**. The total perimeter of the islands within the unit cell is three times their circumference (**Eq. 7**). The interfacial density  $\rho_{\text{int}}$  is defined as the total length of the perimeter of the islands per unit area of the electrode. Therefore,  $\rho_{\text{int}}$  can be calculated as the ratio of  $L_{\text{uc}}$  to  $A_{\text{uc}}$ , as reflected in **Eq. 8**. It follows that this value can also be obtained by multiplying the total number of islands on the electrode  $n$  by their circumference, and then dividing by the electrode area. Analogously, the fraction of the electrode surface covered by the  $\text{In}_2\text{O}_3$  islands ( $S_C$ ) can be calculated either from the unit cell or from the total surface of the electrode, as described in **Eq. 9**.

$$vA_{\text{uc}} = \frac{3\sqrt{3}}{2} c^2 \quad \text{Eq. 6}$$

$$L_{\text{uc}} = 3\pi d \quad \text{Eq. 7}$$

$$\rho_{\text{int}} = \frac{L_{\text{uc}}}{A_{\text{uc}}} = \frac{2\pi\sqrt{3}}{3} \left(\frac{d}{c^2}\right) = \frac{n\pi d}{A_{\text{total}}} \quad \text{Eq. 8}$$

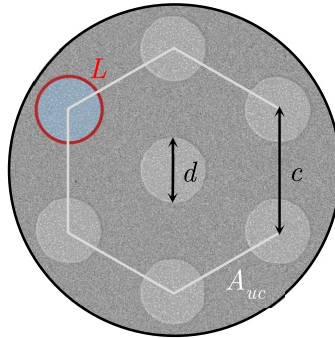


**Figure 2.1.** Representation of the unit cell defining the geometrical arrangement of the islands and main geometrical parameters considered for the design.

The fraction of the electrode surface modified by the diffusion of indium from the islands ( $S_M$ ) depends on the diameter of the islands and on the width of the concentric rings ( $x$ ), but more crucially, on the total number of islands on each electrode, which varies in the same way across different samples as the interfacial density, see **Eq. 7**. In geometric terms, the relationship between these variables is described by **Eq. 10**.

$$S_c = \frac{A_{\text{islands}}}{A_{\text{uc}}} = \frac{\pi\sqrt{3}}{6} \left(\frac{d}{c}\right)^2 = \frac{n\pi d^2}{4A_{\text{total}}} \quad \text{Eq. 9}$$

$$S_M = \frac{n\pi}{A_{\text{total}}} (x^2 + xd) = \rho_{\text{int}} \left(\frac{x^2}{d} + x\right) \quad \text{Eq. 10}$$

### 2.2.6. Electrochemical Tests of Microstructured Electrodes

The electrocatalytic tests over microstructured electrodes were conducted on a custom made gastight flow-cell consisting of two compartments separated by a Selemion AMV membrane with a continuous gas-flow under a three-electrode configuration. The cell was mounted with a GDL carbon paper acting as the counter electrode (Sigracet 39BC, SGL Carbon) and a leak-free Ag/AgCl reference electrode (3 M KCl, model LF-1, Innovative Instruments). The cathodic and anodic compartments contained 8 and 7.8 cm<sup>3</sup> of 0.1 M KHCO<sub>3</sub>, respectively. A steady flow of 20 cm<sup>3</sup> min<sup>-1</sup> CO<sub>2</sub> was bubbled through separately into each compartment, which were saturated with CO<sub>2</sub> for at least 20 min prior to the start of electrolyzes, resulting in a pH of 6.8. The electrochemical measurements were conducted by an Autolab PGSTAT302N potentiostat at rt, with all potential values reported versus the RHE scale. Prior to electrocatalytic experiments, an electrochemical pretreatment consisting of 8 consecutive CVs (−0.60 till 0.30 V *vs.* RHE) was applied to reach a stable redox response. A larger number of CVs did not show any effect on the

catalytic performance. The eCO<sub>2</sub>R experiments were carried out at  $-0.60$  V *vs.* RHE with the  $iR$  compensation function set at 85% of the uncompensated resistance  $R_u$ , determined prior to the electrolysis by EIS measurements at high frequency.  $R_u$  was calculated every 7.5 min in longer experiments and used to continuously correct the applied overpotential. Following this procedure, the applied potentials were within 10 mV of the target potential of the electrolysis.

### 2.2.7. Product Analysis

The gaseous products were analyzed by an on-line GC through a connection between the cathodic compartment and the sample loop of an SRI 8610C gas chromatograph (Multi-Gas #3 configuration). The compounds were separated using argon carrier gas under a pressure of 2.3 bar by a combination of HayeSep D column and Molecular Sieve 13X packed column. The partial current density ( $j_i$ ) for CO and H<sub>2</sub> during the electrolysis were calculated using **Eq. 11**.

$$j_i = Q_{\text{gas}} C_i nF \quad \text{Eq. 11}$$

Where  $Q_{\text{gas}}$  is the molar flow of gas through the cell,  $C_i$  is the molar concentration of the product in the outlet as determined by GC,  $n$  represents the number of electrons transferred to form the product (*i.e.*, 2 for CO and H<sub>2</sub>) and  $F$  is the Faraday's constant. The  $FE_i$  for each gas-phase product during the electrolysis was obtained by dividing the partial current density ( $j_i$ ) by the recorded current at the sampling time ( $i_t$ ), see **Eq. 12**. Formate produced during the CO<sub>2</sub> reduction electrolysis was quantified by NMR. Following the reaction, catholyte and anolyte samples (0.7 cm<sup>3</sup>) were each mixed with D<sub>2</sub>O (0.05 cm<sup>3</sup>) containing phenol (50 mM) and dimethyl sulfoxide (DMSO, 50 mM) as an internal standard. A calibration curve was obtained beforehand by analyzing samples with known amounts of formate in 0.1 M KHCO<sub>3</sub> and determining the relative integral of the formate singlet ( $\delta = 8.3$  ppm) normalized to that of the phenol triplet ( $\delta = 7.2$  ppm). 1D <sup>1</sup>H-NMR spectra with water suppression of the sample were recorded on a Bruker Avance III HD 500 MHz mounted with a Prodigy 5 mm BBO (at rt). One pulse experiment with pre-saturation on the water resonance with a  $\pi/2$  pulse of 12  $\mu$ s (at a power of 15.9 W, accounting for -12.1 dB) and a recycle delay of 5 s (with preset power of  $9.2 \cdot 10^{-5}$  W accounting for 40.38 dB) coadding 256 scans per experiment. These settings resulted in a high signal-to-noise ratio and an analysis time of *ca.* 35 min per sample. The calculation of the current efficiency for liquid-phase products is given by **Eq. 13**.

$$FE_{i,\text{gas}} = \frac{j_i}{i_t} \times 100 \quad \text{Eq. 12}$$

$$FE_{i,\text{liquid}} = \frac{V_e C_i nF}{q_{\text{total}}} \times 100 \quad \text{Eq. 13}$$

Where  $V_e$  is the volume of the electrolyte,  $C_i$  is the molar concentration of the product in the electrolyte, and  $q_{\text{total}}$  is the total charge passed during the electrolysis.

### 2.2.8. Catalyst Characterization

X-ray diffraction (XRD) patterns of the electrodes were obtained in a PANalytical X'Pert PRO MPD diffractometer with Bragg-Brentano geometry using Ni-filtered CuK $\alpha$  radiation ( $\lambda = 0.1541$  nm). The instrument was operated at 40 mA and 40 kV and the patterns were recorded in the 5-70°  $2\theta$  range with an angular step size of 0.05° and a counting time of 5 s per step. SEM-EDX spectroscopy maps from the surface of the electrodes were acquired for at least 3 h on a FEI Quanta 200F instrument equipped with an Ametek EDAX octane Super detector at 7 kV. Image treatment was performed with Image J software. Contrast enhancement (0.1% saturated pixels) with equalized histogram was applied to SEM micrographs. EDXS elemental maps underwent the same treatment and are represented in a Look-up Table comprising from (R:28; G:0; B:134) to (R:255; G:255; B:255). Samples for STEM studies were prepared by dusting respective powders onto carbon-coated nickel grids. STEM-EDXS measurements were performed on a Talos F200X instrument operated at 200 kV and equipped with an FEI SuperX detector. X-ray photoelectron spectroscopy (XPS) analysis of the microfabricated samples in **Figure 2.4d** and **Figure 2.8a** were carried out with a PHI Quantum 2000 spectrometer (Physical Electronics) equipped with a 180° spherical capacitor energy analyzer, at a base pressure of  $5 \cdot 10^{-7}$  mbar using monochromatic AlK $\alpha$  radiation (1486.68 eV). XPS results for indium-modified electrocatalysts in **Figure 2.8b** were acquired on a Thermo Scientific Sigma 2 spectrometer equipped with a hemispherical electron-energy analyzer operated at constant pass energy using polychromatic AlK $\alpha$  radiation (25 eV electron analyzer pass energy; 50° emission angle;  $2 \cdot 10^{-8}$  mbar base pressure). In both cases, the binding energy scale was calibrated with the C 1s signal at 284.8 eV.



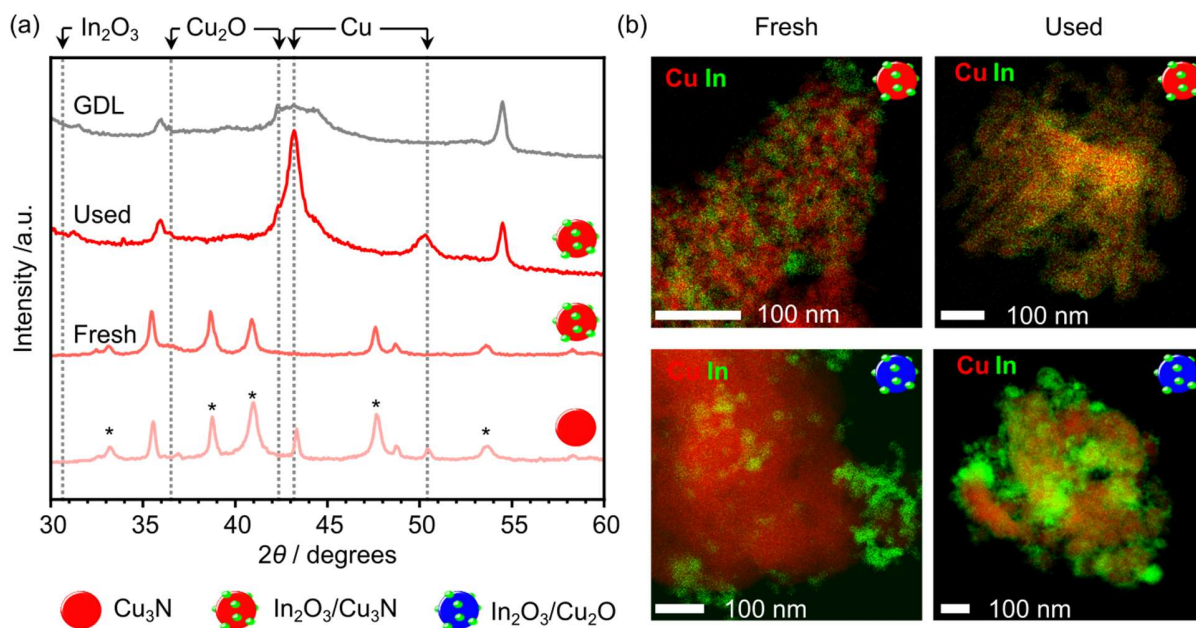


**Figure 2.2.** (a) XRD patterns of fresh and used  $\text{In}_2\text{O}_3/\text{Cu}_3\text{N}$  (1.7 wt.% In). The patterns of  $\text{Cu}_3\text{N}$  over which indium oxide was deposited and that of the underlying carbon-based GDL for the case of the used catalyst are provided for reference. The asterisks indicate reflections associated to  $\text{Cu}_3\text{N}$ . The positions of the main reflections for other relevant phases are indicated, (b) Elemental mapping obtained by STEM-EDXS showing the distribution of indium over the copper phases prior and post reaction. Separated maps for Cu and In in the case of  $\text{In}_2\text{O}_3/\text{Cu}_3\text{N}$  are presented in **Figure A.1.** to facilitate the visualization of the In distribution.

## 2.3. Results and Discussion

### 2.3.1. The High Stability and Selectivity of Indium-Modified Copper Nitride

The modest structural stability of the  $\text{In}_2\text{O}_3/\text{Cu}_2\text{O}$  system<sup>[112]</sup> was enhanced by replacing copper oxide by copper nitride without negatively affecting its high selectivity. As reference the catalyst in powder form  $\text{In}_2\text{O}_3/\text{Cu}_2\text{O}$  was taken with 7.2 wt.% indium reported previously with 65% *FE* toward CO at  $-0.60$  V *vs.* RHE.<sup>[125]</sup> A series of  $\text{In}_2\text{O}_3/\text{Cu}_2\text{O}$  and  $\text{In}_2\text{O}_3/\text{Cu}_3\text{N}$  materials were prepared with nominal loadings of 0.5, 1.5, 4 wt.% In by calcination of  $\text{In}(\text{OH})_3$  supported on  $\text{Cu}_2\text{O}$  or  $\text{Cu}_3\text{N}$  (see **Section 2.2.1**).

XRD patterns (**Figure 2.2a**) confirmed the successful formation of the nitride phase, though no reflection associated to indium phases could be identified due to the low loading (**Table A.1**) and high dispersion observable in the STEM coupled to EDXS elemental maps (**Figure 2.2b**).

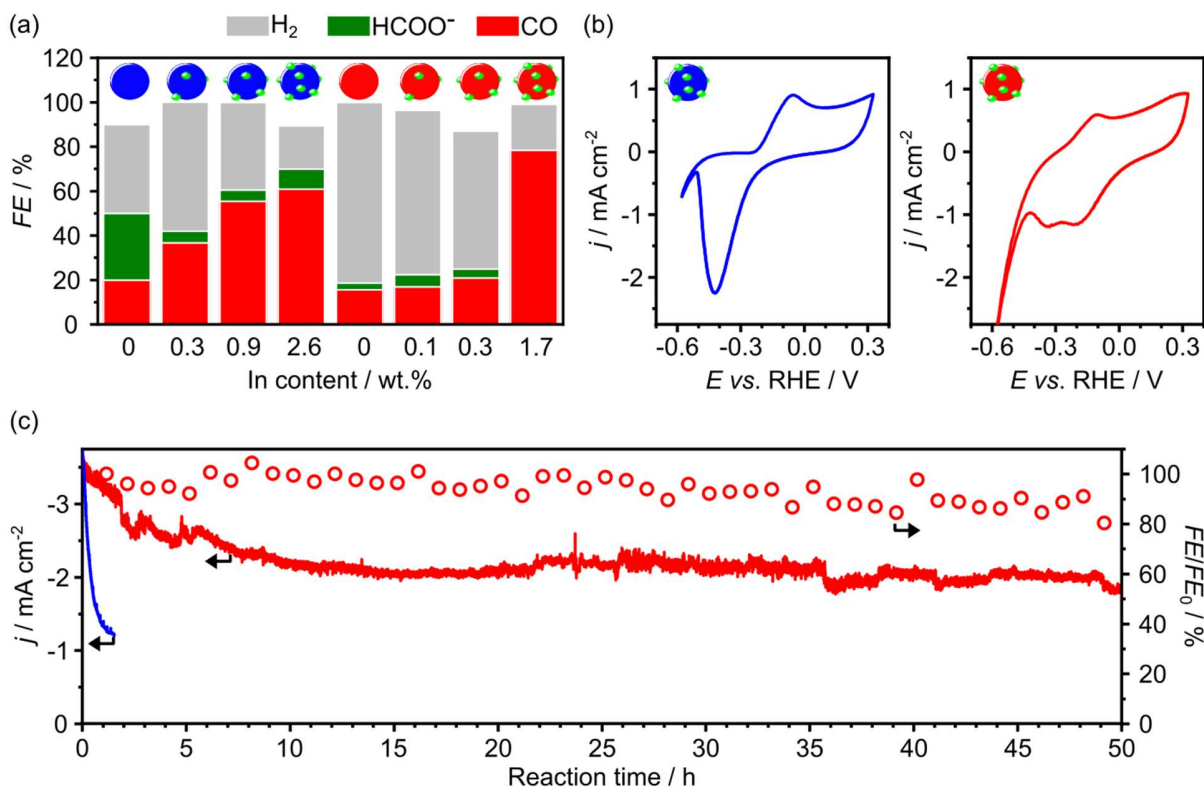


**Figure 2.3.** Catalytic evaluation and electrochemical characterization of materials in powder form. (a) Product distribution over Cu<sub>2</sub>O and Cu<sub>3</sub>N unmodified and modified with indium oxide for different indium loadings, (b) redox response after catalytic tests showing the characteristic In/In<sub>2</sub>O<sub>3</sub> redox peaks in the case of In<sub>2</sub>O<sub>3</sub>/Cu<sub>2</sub>O, (c) evolution of the current density and percentage of the initial Faradaic efficiency toward CO retained for In<sub>2</sub>O<sub>3</sub>/Cu<sub>2</sub>O (2.6 wt.% In) and In<sub>2</sub>O<sub>3</sub>/Cu<sub>3</sub>N (1.7 wt.% In) in an extended test. Operation conditions: chronoamperometry at  $-0.60$  V *vs.* RHE in 0.1 M KHCO<sub>3</sub> saturated with CO<sub>2</sub>.

Reflections associated to In<sub>2</sub>O<sub>3</sub> were nonetheless visible in oxide-based counterparts (**Figure A.1**) likely due to the slightly larger average particle size (**Figure 2.2b**). In all cases, the catalysts presented a similar surface structure composed of sub-micrometric features (**Figure A.2**). The powders were deposited on the microporous layer of a technical carbon GDL electrode prior to electrolysis by airbrushing. The catalytic properties of the copper oxide and copper nitride supports were initially investigated which yielded very modest eCO<sub>2</sub>R activity (**Figure 2.3a**).

A remarkably high *FE* toward CO of 80% as the only carbon product was achieved over In<sub>2</sub>O<sub>3</sub>/Cu<sub>3</sub>N with 1.7 wt.% In. This surpassed the best performing oxide-based system, which also promoted formation of formate, likely reflecting the catalytic nature of the oxide support and/or surface enrichment of indium,<sup>[126]</sup> as strongly suggested by the characteristic redox peaks of the

In/ $\text{In}_2\text{O}_3$  pair<sup>[126]</sup> (*ca.*  $-0.45$  V and  $-0.05$  V *vs.* RHE in **Figure 2.3b**). In turn, this result suggests metallic indium as the predominant phase under the operation potential ( $-0.60$  V *vs.* RHE). Strikingly, both materials largely diverged in terms of catalytic stability (**Figure 2.3c** and **Figure A.3**). An extended catalytic test over 50 h showed stable activity and selectivity over  $\text{In}_2\text{O}_3/\text{Cu}_3\text{N}$ , retaining approximately 90% of the initial *FE* by the end of the experiment. On the other hand, the benchmark  $\text{In}_2\text{O}_3/\text{Cu}_2\text{O}$  exhibited lower currents and an early deactivation pattern. The long-term stability studies for CO production have been primarily focused on silver-based systems so far, in view of the marked instability and/or poor scalability of the rest of highly performing materials.<sup>[119]</sup> After these observations, it can be concluded that the copper nitride phase is able to provide the Cu-In system with a remarkable conjunction of high stability and selectivity. XRD patterns after reaction did not reveal fundamental differences between the oxide- and nitride-based systems, displaying the bulk reduction of  $\text{Cu}_3\text{N}$  to metallic Cu (ND-Cu) under reaction conditions, in analogy to the OD-Cu arising from  $\text{Cu}_2\text{O}$  (**Figure 2.2a** and **Figure A.1**). The presence of reflections assigned to  $\text{In}_2\text{O}_3$  in the used  $\text{In}_2\text{O}_3/\text{Cu}_2\text{O}$  (**Figure A.1**) must be associated to the rapid oxidation that metallic indium undergoes when exposed to the atmosphere. The formation of intermetallic compounds after reaction could not be directly assessed by XRD due the small concentration of In, though small unassigned reflections between  $35$  and  $40^\circ 2\theta$  in  $\text{In}_2\text{O}_3/\text{Cu}_2\text{O}$  might be tentatively assigned to either CuIn (JCPDS 35-1150) or  $\text{Cu}_2\text{In}$  (JCPDS 42-1475). With regard to the distribution of indium over the used  $\text{In}_2\text{O}_3/\text{Cu}_3\text{N}$ , **Figure 2.2b** and **Figure A.4** show how the high initial dispersion of indium was retained after reaction, whereas over  $\text{In}_2\text{O}_3/\text{Cu}_2\text{O}$  the redistribution of indium during operation drove to homogeneous coating over extensive areas of the OD-Cu support, in line with the redox response (**Figure 2.3b**). The positive influence of the nitride copper source in the stability of the system called for further investigations, which were initiated by assessing the unmodified oxide and nitride phases under reaction conditions.

### 2.3.2. Evolution of the Unmodified Copper Nitride

The reduction of  $\text{Cu}_2\text{O}$  under  $\text{eCO}_2\text{R}$  conditions to OD-Cu has been widely reported as a prerequisite for its outstanding catalytic properties.<sup>[61,127,128]</sup> OD-Cu displays a rougher surface favoring high local pH values<sup>[117]</sup> and abundance of grain boundaries<sup>[129]</sup> and atomic defects<sup>[128,130]</sup> which may be related to the favored diffusion of indium we observed in our previous work.<sup>[107]</sup> In view of this and the foreseeable similarities between the nitride and oxide phases, prior to analyzing

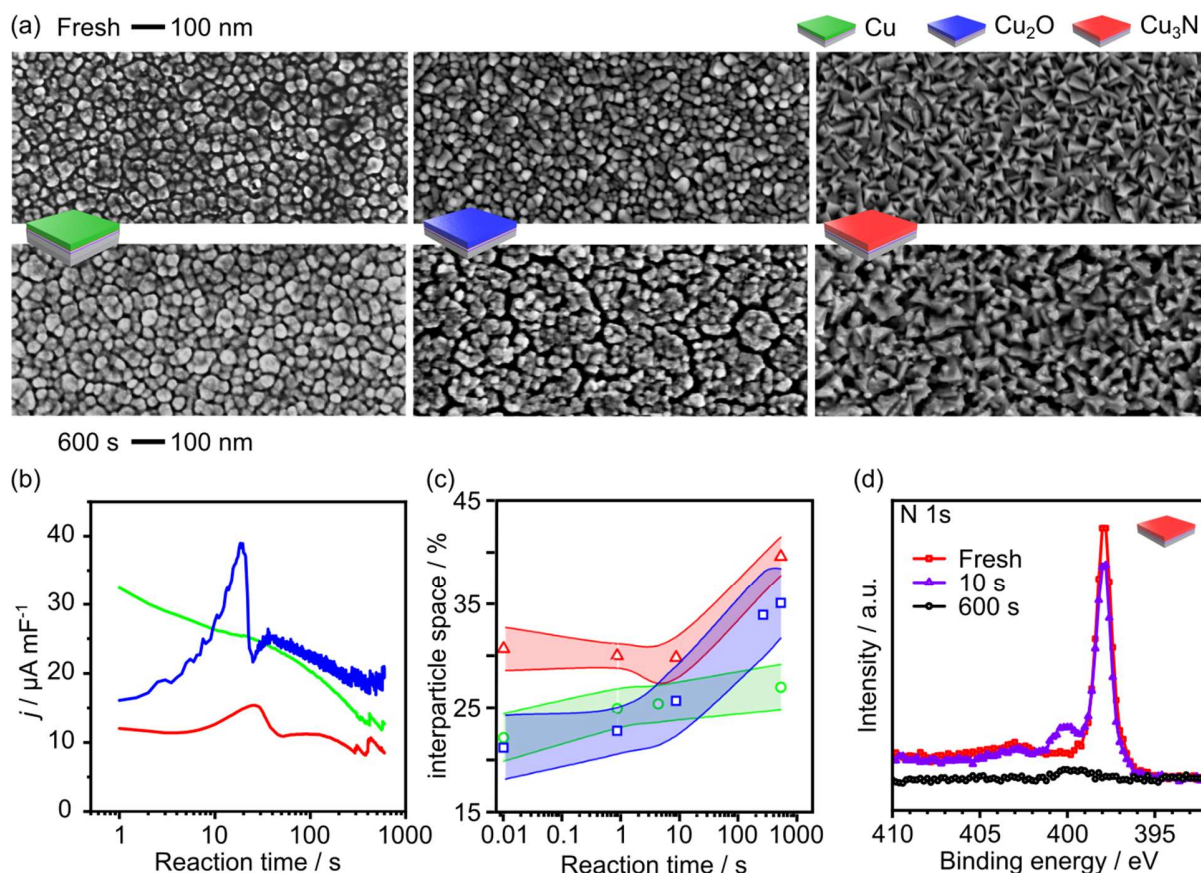


**Figure 2.4.** Evolution of unmodified copper phases films under eCO<sub>2</sub>R conditions. **(a)** Micrographs of the as-deposited substrates and after exposure to reaction conditions for 600 s, **(b)** evolution of the current normalized by double layer capacitance (see **Figure A.6.**), **(c)** evolution of the interparticle space quantified as the percentage of black areas in the micrographs. The bands indicate the standard deviation of 10 spots, **(d)** evolution of the N 1s signal obtained by XPS analysis of the copper nitride film at different reaction times.

interfacial effects we turned to analyze the evolution of copper nitride under operation conditions and compare it on the light of the oxide.

We studied sputtered films allowing fine control over the thickness and composition of metallic copper, copper oxide, and copper nitride. The surface of the as-deposited films of metallic and oxidic copper exhibited a similar aspect under SEM analysis comprising 30-50 nm particles (**Figure 2.4a**) whose expected composition was confirmed by their XRD patterns (**Figure A.5**). On the other hand, partially overlapping pyramidal particles formed the surface of the nitride film, clarifying its larger electrochemical double layer capacitance (**Figure A.6**). Upon exposure to

eCO<sub>2</sub>R conditions, XRD patterns indicated the exclusive presence of metallic Cu in all cases (**Figure A.5**), whereas micrographs displayed almost no effect of the eCO<sub>2</sub>R on the morphology of the metallic Cu, in contrast with the more open structure observed on the OD-Cu and ND-Cu (**Figure 2.4a**). Further insights followed from inspection of the current density evolution (**Figure 2.4b**).

Metallic copper yielded a monotonically decreasing current throughout the experiment, whereas Cu<sub>2</sub>O and Cu<sub>3</sub>N show a clear reduction peak at 10-20 s followed by gradual equilibration. Interestingly, the evolution of interparticle space obtained from analysis of SEM micrographs at different times could link these observations (**Figure 2.4c**). The structure of the nitride and oxide layers opens upon the reduction peak and continues until the process stabilizes after 300 s, thus providing the temporal frame where the reconstruction takes place. After 10 s, the fraction of interparticle space on ND-Cu and OC-Cu partially converged. In this respect, photoelectron emission around the N 1s provided further support to understand the reduction process of Cu<sub>3</sub>N (**Figure 2.4d**). The sharp peak at *ca.* 397.7 eV in the fresh material corresponds to the BE of nitrogen in Cu<sub>3</sub>N<sup>[131]</sup> and decreases gradually over the course of the experiment until it becomes undetectable after 600 s, supporting the complete reduction to metallic Cu on the surface. Nonetheless, the fingerprint of a different nitrogen species at *ca.* 400 eV emerges after 10 s and seems to endure to a very limited extent until the end of the experiment. A similar state has been observed during the thermal decomposition of Cu<sub>3</sub>N into Cu and N<sub>2</sub> and tentatively assigned to Cu<sub>4</sub>N, whose formation would be facilitated by the relatively easy diffusion of nitrogen in the copper lattice.<sup>[131,132]</sup> We mention the difficulty to assess *ex situ* the complete reduction of Cu<sub>2</sub>O due to the rapid reoxidation of OD-Cu upon exposure to the atmosphere.<sup>[133]</sup>

In summary, parallelisms was found between the evolution of copper oxide and nitride under eCO<sub>2</sub>R conditions toward OD-Cu and ND-Cu respectively, although the presence of a small amount of persistent nitrogen with a different chemical nature formed during the reduction was revealed. This picture made it reasonable to expect comparable synergistic mechanisms between the nitride or the oxide substrates and the indium oxide.



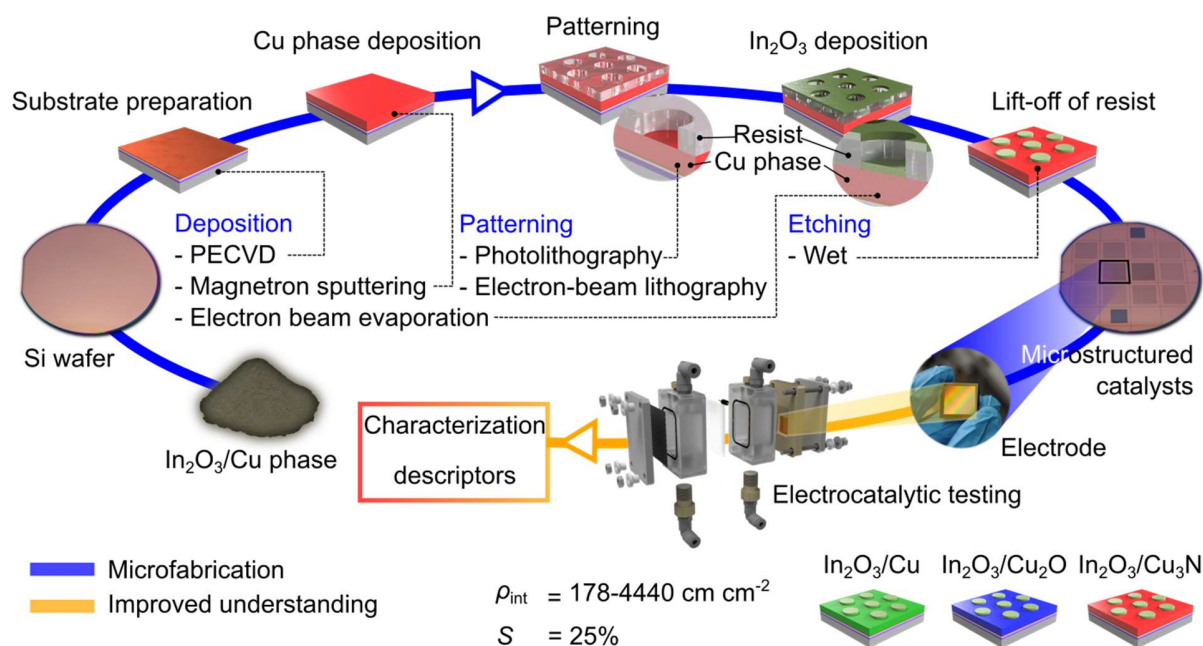


**Figure 2.5.** Microfabrication as an advanced tool to study interfacial effects in Cu-In systems. Indium oxide was patterned by microfabrication tools as a regular array of circular islands on different copper-based substrates with the aim of controlling the interfacial density  $\rho_{\text{int}}$  while keeping constant the coverage of the copper phase  $S$  constant (blue line). So-prepared electrodes were tested under reaction conditions in a standard electrochemical setup. The controlled geometry allowed identification of performance descriptors and facilitated insight into the formation of the active phase (yellow line).

### 2.3.3. Interfacial Activity and Stability in Indium-Modified Copper Nitride

Understanding the nature and the formation mechanism of the active phase in this new material would be the next step. In view of the complexity of the Cu-In system, making it poorly accessible to detailed theoretical and/or in situ studies,<sup>[17]</sup> we approached this task by applying microfabrication tools.<sup>[107]</sup> Microfabricated catalysts display a drastic reduction of the uncertainty in terms of composition and structure compared to powder forms.

Moreover, the high throughput at which can be prepared and their easier integration with characterization techniques make them a promising model platform for the understanding of multicomponent catalysts. Herein we apply this approach (**Figure 2.5**) to impose microstructure to the systems under study targeting electrodes with well-defined interfacial density (see **Section 2.2.4**). Microfabrication allowed the production of several sets of electrodes in a reduced timeframe with highly controlled composition and geometry consisting of periodic regular

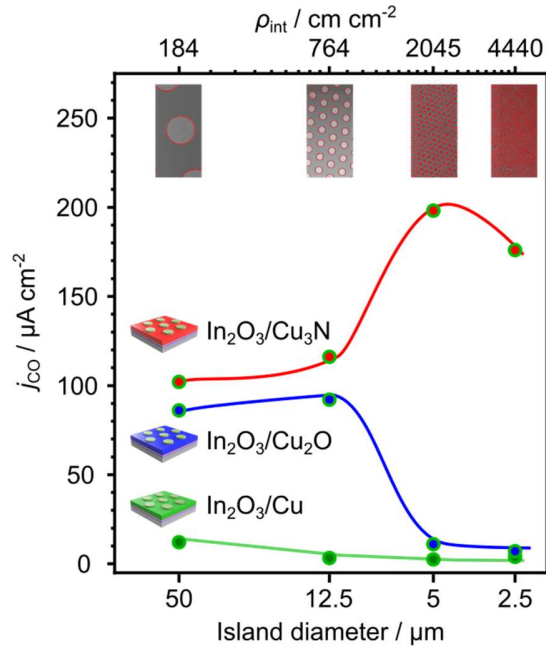


**Figure 2.6.** Electrocatalytic activity toward CO of microstructured multicomponent electrodes with different interfacial density  $\rho_{\text{int}}$  controlled by preparing regular arrays of islands with different diameter and pitch. SEM micrographs where interfacial sites are highlighted in red are added for clarity. Operating conditions:  $-0.60$  V *vs.* RHE for 600 s in 0.1 M  $\text{KHCO}_3$  saturated with  $\text{CO}_2$ .

hexagonal arrays of circular islands (100 nm height, comprising the indium oxide) deposited on a homogeneous thin film (200 nm height, the copper-based component). The main geometrical design variable was the interfacial density  $\rho_{\text{int}}$  as the total length of the perimeter of the islands per unit area of the electrode, which can be controlled by patterning a layer of photoresist via UV photolithography. With this geometry, the surface of the electrodes exposes three different possible active sites: the copper phase substrate, the indium oxide islands, and the interfacial ones, located at the perimeters.

In order to differentiate interfacial contributions within the total measured activity, we designed electrodes spanning  $\rho_{\text{int}}$  over several orders of magnitude (178-4440  $\text{cm cm}^{-2}$ ) while keeping the same coverage of the copper substrate (*ca.* 25%, see **Section 2.2.5** and **Figure A.7**). Low interfacial densities correspond to large islands and vice versa. In this manner, sets of electrodes ( $A_{\text{total}} = 2.25 \text{ cm}^2$ ) with three different compositions (denoted as island/surface) were prepared: (1)  $\text{In}_2\text{O}_3/\text{Cu}$ , (2)  $\text{In}_2\text{O}_3/\text{Cu}_2\text{O}$ , and (3)  $\text{In}_2\text{O}_3/\text{Cu}_3\text{N}$ . A more detailed information on the microfabrication process is available elsewhere<sup>[107]</sup> and in **Section 2.2.4**. The large geometrical

active area of the structured electrodes allowed their direct electrochemical testing and the quantification of the gas-phase products with a standard electrochemical cell for eCO<sub>2</sub>R studies. The catalytic activity of In<sub>2</sub>O<sub>3</sub>/Cu electrodes (**Figure 2.6**) displayed low values comparable to the pure phases (see **Figure A.8**) irrespective of the interfacial density. Nonetheless, a different picture emerged from the In<sub>2</sub>O<sub>3</sub>/Cu<sub>2</sub>O electrodes. The synergistic interaction at the interface between In<sub>2</sub>O<sub>3</sub> and Cu<sub>2</sub>O was clearly manifested by the larger activity and its positive correlation with the interfacial density,<sup>[107]</sup> which ceased at larger  $\rho_{\text{int}}$ , resulting in very low activity over electrodes with small islands (**Figure 2.6**). In stark contrast, the partial current density toward CO showed a consistent positive correlation with the interfacial density over In<sub>2</sub>O<sub>3</sub>/Cu<sub>3</sub>N. These results confirmed the role of interfacial sites in the eCO<sub>2</sub>R activity in In<sub>2</sub>O<sub>3</sub>/Cu<sub>3</sub>N and revealed the sensitivity of In<sub>2</sub>O<sub>3</sub>/Cu<sub>2</sub>O to the spatial distribution of the phases. On a methodological note, we highlight the importance of achieving a homogenous current density, achieved by adding a thin Cu layer (10 nm) under the semiconducting Cu<sub>3</sub>N and Cu<sub>2</sub>O films (see **Figure A.9** and **Section 2.2.4**). In a previous study, an appreciable diffusion of indium was observed over In<sub>2</sub>O<sub>3</sub>/Cu<sub>2</sub>O after 5 min under reaction conditions, giving rise to the Cu-In active phase.<sup>[107]</sup> In this study, we varied reaction times aiming to monitor its formation and facilitate the comparison with In<sub>2</sub>O<sub>3</sub>/Cu<sub>3</sub>N. With this idea in mind, we carefully mapped the indium distribution by SEM-EDXS over the three fresh compositions and after reaction times of 300 and 600 s (**Figure 2.7**) for electrodes populated with 5  $\mu\text{m}$  islands, on which catalytic performances differed more noticeably (**Figure 2.6**). The In<sub>2</sub>O<sub>3</sub>/Cu system showed no visible evolution of the interface, staying the deposited indium within the perimeter of the islands at all reaction times. In the case of In<sub>2</sub>O<sub>3</sub>/Cu<sub>2</sub>O, the diffusion of indium was clearly observable after 300 s, forming indium-containing halos around the individual islands associated to eCO<sub>2</sub>R activity.<sup>[107]</sup> However, after 600 s the halos merged, as reflected by the rather homogeneous and relatively rich distribution of indium among the islands.

These observations at different times explained the direct relation between activity and interfacial density over electrodes with a larger pitch among islands. As the diffusion length of indium becomes closer to the pitch over electrodes with smaller islands more quickly, the more active Cu-In phase (reasonably associated to the perimeter of the halos) might disappear upon merging of the halos, and the activity starts to resemble that of pure indium oxide (**Figure A.8**). Notably, there was



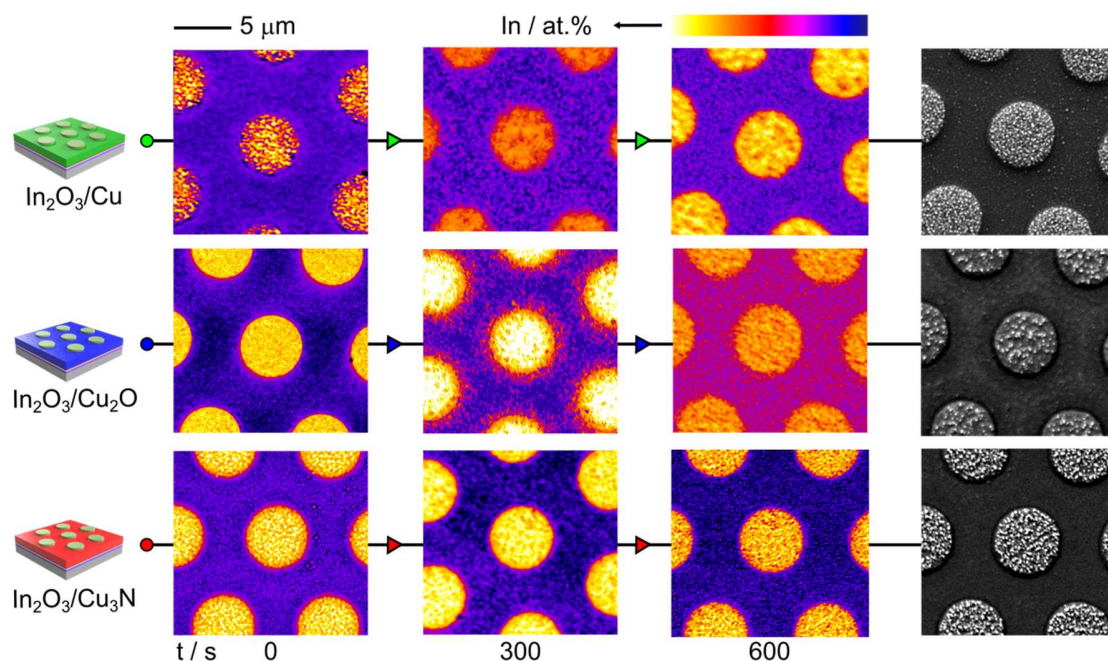


**Figure 2.7.** Evolution of the elemental distribution of indium obtained by SEM-EDXS at different reaction times in microfabricated electrodes. The corresponding SEM micrographs after 600 s are added to confirm the structural stability of the islands in all cases.

no evidence of this complex evolution process in the case of  $\text{In}_2\text{O}_3/\text{Cu}_3\text{N}$ . The diffusion of indium was not observable in this case, suggesting its restriction to the nanometre scale in case it exists. This result is in line with the retained dispersion after reaction observed over the powder form in **Figure 2.2b** and the consistent activity-interfacial density trend found in **Figure 2.6**, since overlapping of indium-rich areas do not occur. In addition, SEM micrographs discarded deterioration of the electrode surface as the reason behind differences in performance (**Figure 2.7**).

At this point, evidences collected over the nature of the active sites in microfabricated electrodes and the catalytic results obtained over the powder counterparts (**Figure 2.3**) could be directly correlated. As the next step, further insights were gained into the reason behind the interfacial stability on the  $\text{In}_2\text{O}_3/\text{Cu}_3\text{N}$  material.

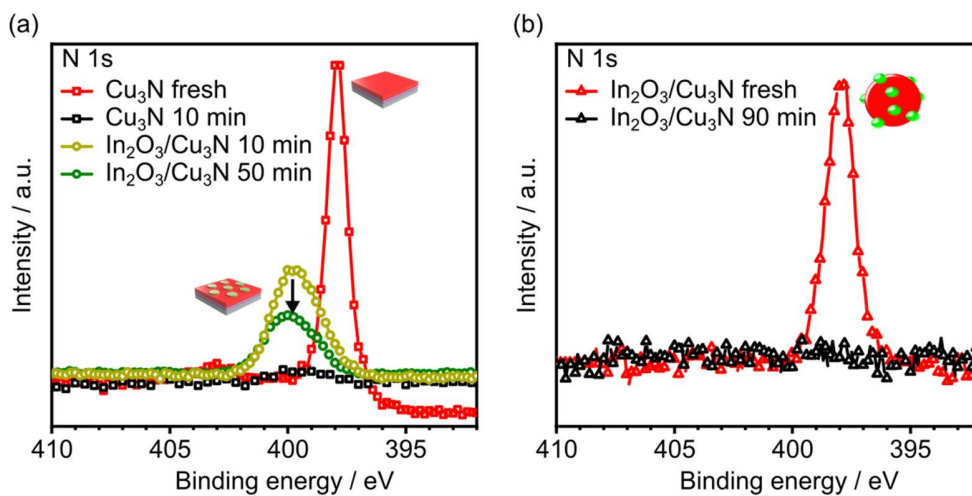


**Figure 2.8.** High resolution XPS survey around the N 1s signal for In<sub>2</sub>O<sub>3</sub>/Cu<sub>3</sub>N before and after reaction at different times. (a) for the microfabricated form (5 μm islands). The corresponding signals for the pure nitride phase are added as reference. (b) for the powder form (1.7 wt.% In). The peak at *ca.* 398 eV corresponds to the bulk Cu<sub>3</sub>N phase.

### 2.3.4. Metastable Nitrogen Species During the Reduction of Indium-Modified Copper Nitride

Even though the debate elucidating if OD-Cu contains remaining oxygen under operation conditions is still open, there is a consensus on that it would be limited to trace levels and that the reduction process occurs rapidly.<sup>[44,117]</sup> In this context, the suggested presence of nitrogen species with a different chemical environment even after exposure to reaction conditions for 600 s in Cu<sub>3</sub>N (**Figure 2.4d**) advised some differences between the two copper phases. To investigate this, we tracked the N 1s signal over the microfabricated In<sub>2</sub>O<sub>3</sub>/Cu<sub>3</sub>N after different reaction times (**Figure 2.8a**). Similarly to the case of Cu<sub>3</sub>N, the peak at 397.7 eV disappeared after 600 s, confirming the complete transformation of the surface. However, the binding energy at *ca.* 400 eV was associated to a metastable state was clearly detectable. Notably, post-reaction analysis after a more prolonged test for 3000 s (50 min) showed a gradual decrease of this signal, suggesting that the depletion of nitrogen in the indium-modified copper nitride is markedly delayed with respect to the pure phase. The existence of an appreciable amount of nitrogen in the copper matrix during the reduction and reconstruction process can then be hypothesized to hamper the fast diffusion of indium observed during the reduction and reconstruction process over OD-Cu,<sup>[107]</sup> restricting the copper-indium interaction to the close vicinity of the perimeter of the islands. After stabilization

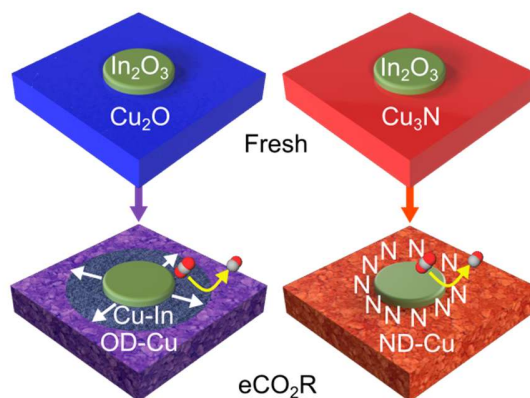


**Figure 2.9.** Configuration of the active phases under reaction conditions for  $\text{In}_2\text{O}_3/\text{Cu}_2\text{O}$  and  $\text{In}_2\text{O}_3/\text{Cu}_3\text{N}$ .

of the surface and complete elimination of metastable nitrogen at sufficiently long reaction times, the diffusion of indium on metallic copper is expected to proceed at a very low rate at rt, according to our results over  $\text{In}_2\text{O}_3/\text{Cu}$  (**Figure 2.7**) and available reports.<sup>[134]</sup> However, the participation of electronic effects associated to Cu-In-N interactions cannot be discarded at this point.

The existence of an appreciable amount of nitrogen in the copper matrix during the reduction and reconstruction process can then be hypothesized to hamper the fast diffusion of indium observed during the reduction and reconstruction process over OD-Cu,<sup>[107]</sup> restricting the copper-indium interaction to the close vicinity of the perimeter of the islands. After stabilization of the surface and complete elimination of metastable nitrogen at sufficiently long reaction times, the diffusion of indium on metallic copper is expected to proceed at a very low rate at rt, according to our results over  $\text{In}_2\text{O}_3/\text{Cu}$  (**Figure 2.7**) and available reports.<sup>[134]</sup> However, the participation of electronic effects associated to Cu-In-N interactions cannot be discarded at this point.

Similar analyses (**Figure 2.8b**) over the powder form in  $\text{In}_2\text{O}_3/\text{Cu}_3\text{N}$  with 1.7 wt.% In evidenced the complete depletion of nitrogen in the electrode after exposure to eCO<sub>2</sub>R conditions for 90 min. In conjunction with the stable performance for 50 h exhibited in **Figure 2.3c**, this observation reveals that the presence of metastable nitrogen is not required for a stable extended operation, in line with the initial stabilizing effect of nitrogen proposed for the microfabricated system.

However, we notice that the high stability displayed by the powder form can also be modulated by unaccounted phenomena not easily detectable over the microfabricated counterparts, which calls for further investigations on this matter. In summary, the set of presented results indicates that In<sub>2</sub>O<sub>3</sub>/Cu<sub>3</sub>N develops highly stable, active, and selective interfaces allowing for a stable operation, in contrast to the rapidly evolving oxide counterpart driven by the fast diffusion of indium (**Figure 2.9**). Even though the nitride phase is rapidly reduced and undergoes fast surface reconstruction, a considerable amount of nitrogen remains temporarily trapped in the lattice of the ND-Cu, likely stabilizing the copper-indium interface.

## 2.4. Conclusions

In<sub>2</sub>O<sub>3</sub>/Cu<sub>3</sub>N emerged as a selective and highly stable electrocatalyst in the reduction of CO<sub>2</sub> to CO, overperforming the humbly stable oxide-based benchmark. The use of copper nitride eliminated the uncontrolled structural and compositional changes associated to the latter. The regular composition and structure of microstructured electrodes facilitated establishing a direct relation between the Cu-In interface in In<sub>2</sub>O<sub>3</sub>/Cu<sub>3</sub>N and eCO<sub>2</sub>R activity, which was not accompanied by detectable indium diffusion into the copper matrix, as in the case of the oxide-based material. Spectroscopic evidence revealed the presence of metastable nitrogen under reaction conditions, which was associated to the improved interfacial stability. The findings reveal the potential of nitride-derived copper to engineer multicomponent systems with high efficiency for the eCO<sub>2</sub>R. In parallel, they underline microfabrication as a tool to establish synthesis-property-function relations in multicomponent systems for the range of electrocatalytic applications.







## Chapter 3

# Selectivity Patterns in the Electrocatalytic Reduction of CO<sub>2</sub> Revealed by Laser- Microstructured Copper

### 3.1. Introduction

The eCO<sub>2</sub>R toward fuels and chemicals in aqueous media must still overcome technological challenges to contribute towards a sustainable, circular economy. The lack of selectivity control on copper-based systems stands out among them, since copper is the only material known to promote at appreciable rates value-added products such as hydrocarbons, alcohols, and aldehydes.<sup>[26,27,135]</sup> The insufficient understanding of the variables to be optimized hinders precise strategies for catalyst design, operation conditions, and electrode engineering.<sup>[111,136]</sup>

Historically, research in this field has been focused on materials development<sup>[137,138]</sup> but the recent recognition of the local (electro)chemical environment as a key directing agent for selectivity has opened new avenues. The applied potential and the surface coverage of H and CO<sub>2</sub> are central parameters influencing the eCO<sub>2</sub>R and the competing HER. However, their separated analysis is unattainable, as they are intertwined in the double layer region by the carbonate chemical equilibria, diffusion processes, and the interaction of charged species in the intense electric field.<sup>[136]</sup> Despite the complexity involved, literature shows how activity and/or selectivity can be successfully enhanced via locally tuned electric fields,<sup>[139]</sup> highly alkaline environments,<sup>[140,141]</sup> mixed chemical-electrocatalytic reduction routes,<sup>[142]</sup> or free cationic/anionic species present.<sup>[35,143]</sup> In this context, rationalization efforts have become necessary to translate these observations into quantitative guidelines for the optimization of the local environment. These efforts are currently focused on C<sub>1</sub> and C<sub>2</sub> products,<sup>[21,136,144–146]</sup> while there are virtually no indications for more complex ones.



Ethylene formation is a prominent example. The fact that its selectivity can be improved in a practical GDE from 30% to 70% upon optimization of mass transport and electrolyte pH clearly reflects the sensitivity of this reaction to the environment.<sup>[141]</sup> In this regard, theoretical works predict the pH sensitivity of the rate-determining step in C-C coupling due to a non-simultaneous proton-electron transfer.<sup>[97]</sup> This idea has led to diverse proposed mechanisms toward ethylene at different overpotentials with varying pH sensitivity<sup>[97,147]</sup> and its promotion by high local CO<sub>2</sub> concentration through enhanced CO coverage.<sup>[100]</sup> Neither the precise route(s) nor a quantitative description of the local environments under which they are promoted have been firmly established. Remarkably, ethanol is thought to share a significant portion of its reaction pathway with ethylene and therefore some of its features.<sup>[47,145,148]</sup> In parallel, local conditions may also affect the parasitic HER, for which high activity has been associated to enhanced mass transport properties.<sup>[149]</sup> Unfortunately, the relevance of quantifying the local electrochemical environment is in stark contrast with the ability to measure or model the concentrations of species in the vicinity of the electrode. This fact originates from technical limitations of operando techniques<sup>[150]</sup> and the usually complex morphology of the catalysts in the relevant micrometer scale, which provides results from forcibly simplistic models mostly with a qualitative value.<sup>[151,152]</sup> The lack of well-structured systems has not allowed a systematic study of mass transport, chemical equilibria, and local cationic buffer effects.<sup>[153]</sup> With this in mind, copper-based surfaces with a variable degree of control have been reported as in the case of foams<sup>[57,154]</sup> or mesostructured layers with variable thickness.<sup>[155]</sup> They have confirmed with limited quantification, for example, the improved selectivity toward C<sub>2</sub> products under severe mass transport limitations. A clever templating strategy allowed to experimentally link cylindrical nanoporosity and larger rates of C<sub>2</sub> products rationalized through local concentration gradients and confinement effects.<sup>[156]</sup> Nonetheless, selectivity could not be linked to intrinsic physiochemical parameters but rather to the length of nanocavities.

Microfabrication can contribute to this need of describing selectivity patterns in terms of chemical environment descriptors by providing catalysts with controlled geometries. This set of techniques has been demonstrated through lithographic approaches to gather insights into the formation and nature of active sites in multicomponent systems<sup>[107,157]</sup> and into the operation of bifunctional catalysts.<sup>[106]</sup> In this study ultra-short pulsed (USP, pulse duration from fs to ps) laser

Selectivity Patterns in the Electrocatalytic Reduction of CO<sub>2</sub> Revealed by Laser-Microstructured Copper ablation<sup>[158,159]</sup> was identified as the technique of choice for the development of model copper electrodes. Whereas nanosecond pulsed laser ablation is a well-established technique for nanoparticle synthesis,<sup>[160]</sup> USP laser ablation has only found application in the field of catalysis to enhance electrode roughness.<sup>[161]</sup> Its sub-micrometer resolution (mostly limited by diffraction) displays a large potential for precise structuring, arising from the small energy input per pulse that creates negligible heat affected zones.<sup>[162]</sup> This feature adds to rapid-processing<sup>[163]</sup> (up to 1 m<sup>2</sup> min<sup>-1</sup>) and the ability to alter the chemical nature of the ablated surface when applied under reactive atmospheres.<sup>[164,165]</sup> Copper foils were ablated using this platform to develop microstructured CuO electrodes amenable to product quantification. A dense regular distribution of conical cavities (denoted as micro-probes) were designed spanning a wide range of lengths.

The combination of applied potentials and micro-probe lengths imposed distinct local electrochemical environments due to concentration gradients arising from the electrochemical reactions, CO<sub>2</sub> and cation hydrolysis equilibria, and geometry. These environments could be quantitatively described after 3D simulations, which enabled the emergence of selectivity patterns in the form of maps for a variety of C<sub>1</sub>-C<sub>3</sub> products expressed in terms of local CO<sub>2</sub> concentration and pH. Selectivity maps emerge as valuable resources for theoretical studies and as guiding tools toward optimized operation parameters.

## 3.2. Experimental

### 3.2.1. Microstructuring

Copper foils (oxygen-free 2.0040 - Cu OF > 3N, 0.3 mm, 20×20 mm<sup>2</sup>) were processed using USP laser ablation<sup>[158]</sup> to generate a regular distribution of cavities (denoted as micro-probes) with controlled geometry over 2.25 cm<sup>2</sup>. These micro-probes showed a slight conical shape with the following dimensions; 70 μm pitch, 35 μm diameter, and 0-130 μm length (**Figure 3.1**). Throughout this study, an USP Amphos laser served as source, where the fundamental beam is frequency doubled to 515 nm reaching 800 fs pulse duration and increasing the ablation efficiency of copper. The focal laser beam diameter was set to 16 μm diameter by adjusting the Galilean telescope and using a 160 mm telecentric f-theta objective lens. The laser beam was moved with the galvo scanner orthogonally over the specimen surface layer-by-layer to reach a certain depth.

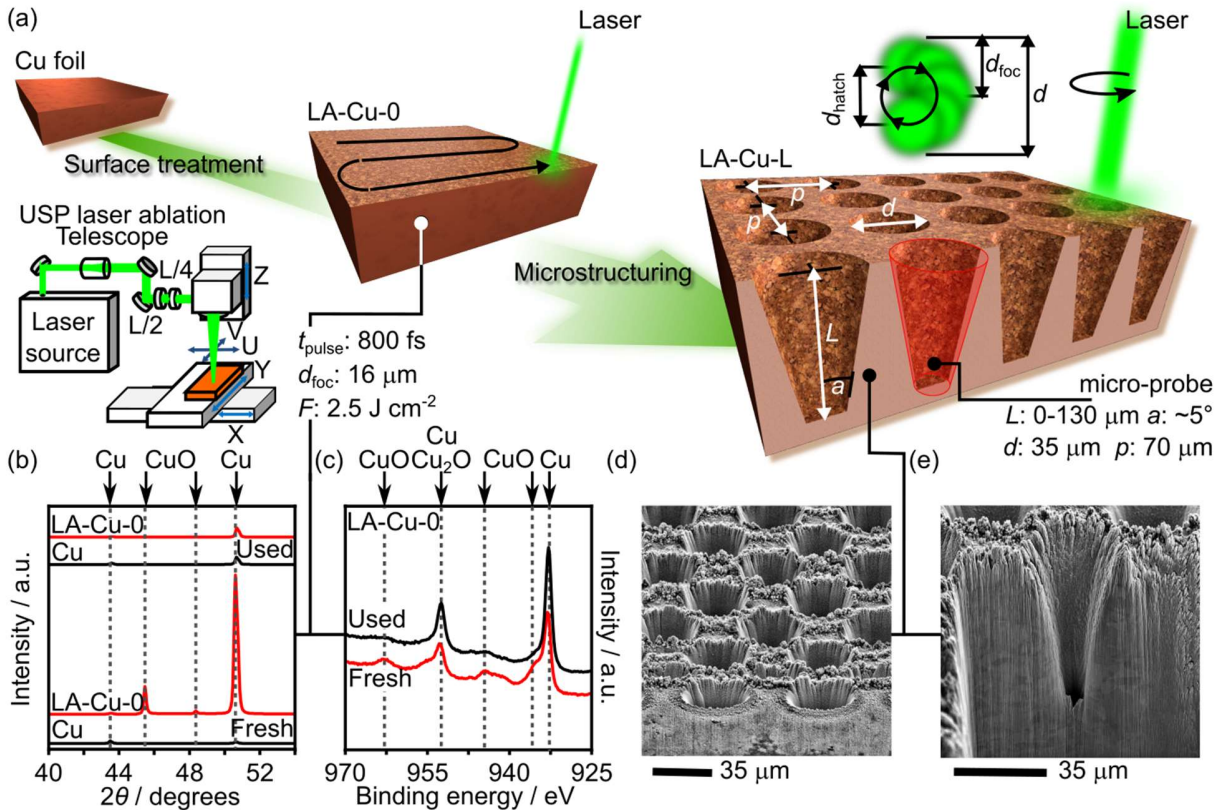


**Figure 3.1.** Microfabrication and basic characterization of microstructured electrodes. (a) The ultra-short pulsed (USP) laser beam was guided from the source in open space to a galvo scanner through modifying optics resulting in a focal diameter  $d_{foc}$ . Kinematic (XYZ) and optical (UV) axes allowed precise alignment of laser and the copper substrate, whereas galvo mirrors enabled fast circular hatching ( $d_{hatch}$ ) and distribution of the laser pulses for material removal. Cu foils were initially pretreated by ablation of a 2  $\mu\text{m}$  layer (LA-Cu-0) and subsequently patterned to create regular arrays of micro-probes with different length (LA-Cu-L). (b) X-ray diffraction (XRD) patterns before (Cu) and after laser ablation (LA-Cu-0), (c) X-ray photoelectron spectroscopy (XPS) spectra of LA-Cu-0 before and after electrolysis. (d) Micrograph showing the periodically aligned micro-probes and a partially removed surface layer. (e) Representative Plasma Focused Ion Beam-Scanning Electron Microscopy (PFIB-SEM) cross-sectional micrograph of one micro-probe. Case shown: LA-Cu-100, after exposure to reaction conditions.

Prior to the micro-probe manufacturing, two layers of the copper foil were removed, resulting in a rougher surface (LA-Cu-0) composed of copper oxide ( $15 \times 15 \text{ mm}^2$ ), see **Figure 3.1** and **Figure A.10**. The laser beam was steered with 5  $\mu\text{m}$  distance leading to overlap at 500  $\text{mm s}^{-1}$  speed, 400 kHz repetition rate, and 2 W average power over the specimen.<sup>[159]</sup> The second layer was rotated by 90° to mitigate overlapping laser lines while removing about 2  $\mu\text{m}$  of material

within 8 min. Subsequently, the micro-probes were laser-machined by a circular movement of the beam with the introduced strategy in **Figure 3.1**.

This circle hatch was repeated for a certain time between 1 ms and 10 ms at an energy density of 2.5 J cm<sup>-2</sup>, well above the threshold of ablation for copper, with a surface speed of 500 μm s<sup>-1</sup>. All relative movements of the laser beam to the substrates were carried out with the galvo scanner, allowing a positioning speed between the probes of 2 m s<sup>-1</sup>. The micro-probes with length of 20 μm were produced from 4 layers and by increasing the time (and thus the amount of layers), the length was controlled. The micro-probes are aligned with a pitch of 70 μm and a second arrangement of micro-probes shifted half a pitch to generate a denser pattern. This led to *ca.* 92 000 micro-probes with a controlled volume generated in less than 2 h depending on desired length. The laser machining time per micro-probe was set to [1, 2, 3, 5, 10] ms to fabricate lengths of [20, 40, 60, 100, 130] μm on top of the initially removed 2 μm of material.

### 3.2.2. Electrochemical Measurements

The electrocatalytic tests over microstructured electrodes were conducted on a custom-made gastight flow-cell consisting of two compartments separated by a Selemion AMV membrane with a continuous gas-flow under a three-electrode configuration. The cell was mounted with a GDL carbon paper acting as the counter electrode (Sigracet 39BC, SGL Carbon) and 2.25 cm<sup>2</sup> exposed microfabricated electrode which were both replaced after every measurement, and a leak-free Ag/AgCl reference electrode (3 M KCl, model LF-1, Innovative Instruments). The cathodic and anodic compartments contained 8 and 7.8 cm<sup>3</sup> of 0.1 M KHCO<sub>3</sub>, respectively. A steady CO<sub>2</sub> flow of 20 cm<sup>3</sup> min<sup>-1</sup> was bubbled through separately into each compartment, which were saturated with CO<sub>2</sub> for at least 20 min prior to the start of electrolyzes, resulting in pH of 6.8. The electrochemical measurements were conducted by an Autolab PGSTAT302N potentiostat at rt, with all potential values reported versus the RHE scale. The 50 min eCO<sub>2</sub>R experiments were carried out with the *i*R compensation function set at 85% of the uncompensated resistance  $R_{\text{u}}$ , determined prior to the electrolysis by EIS measurements at high frequency.  $R_{\text{u}}$  was calculated every 7.5 min during each experiment and used to continuously correct the applied overpotential. Following this procedure, the applied potentials were within 10 mV of the target potential of the electrolysis.

### 3.2.3. Product Analysis

The gaseous products and the liquid products were detected and quantified as described in **Section 2.2.7**.

### 3.2.4. Catalyst Characterization

XRD patterns of the electrodes were obtained in a PANalytical X'Pert PRO MPD diffractometer with Bragg-Brentano geometry using Ni-filtered CuK $\alpha$  radiation ( $\lambda = 0.1541$  nm). The instrument was operated at 30 mA and 10 kV and the patterns were recorded in the 5-70°  $2\theta$  range with an angular step size of 0.05° and an integration time of 5 s per step. XPS analysis was carried out with a PHI Quantum 2000 spectrometer (Physical Electronics) equipped with a 180° spherical capacitor energy analyzer, at a base pressure of  $5 \cdot 10^{-7}$  mbar using monochromatic AlK $\alpha$  radiation (1486.68 eV). The binding energy scale was calibrated with the C 1s signal at 284.8 eV. The 3D geometry of the laser generated micro-probes was assessed by an X-ray microcomputed tomography ( $\mu$ CT) study. A RX EasyTom XL Ultra 160 device equipped with an open nano-focus tube was used at 60 kV acceleration voltage and 152  $\mu$ A current. The distance between the source and detector was 400.204  $\mu$ m with the specimen situated at 3.141  $\mu$ m after the X-ray source. In total 1440 projections were gathered and the reconstruction done with the VGStudioMax software packet leading to a cubic voxel size of 996 nm with a total number of 1806x1806x1284 voxels in x, y, z directions. This allows measuring the probe with a micrometer resolution and resolve the complex 3D shape, shown in **Figure A.11**. Additionally, a study on cross-sections machined with a plasma focused ion beam scanning electron microscope (PFIB-SEM) using Xenon ions was carried out. The Tescan Fera 3 device enabled to remove copper in fast manner whereas the SEM feature facilitated the alignment. Following, the geometry can be observed and analyzed which is in good agreement with the  $\mu$ CT measurements for the micro-probes assessed at different lengths, to be compared with **Figure A.11**.

### 3.2.5. Computational Modelling

The aim was to simulate the distribution of pH, CO<sub>2</sub> concentration, and fluxes of species involved in chemical equilibria within one individual micro-probe under the applied operating conditions. Dimensions are provided in **Figure 3.1** and the origin of the z-axis was established at the base of the probes, with positive coordinates towards the interior. All experimentally obtained results arising from the combination of different lengths and applied potentials were modeled. In order to

take into account both the influence of adjacent probes and the mild stirring resulting from CO<sub>2</sub> bubbling, the modeled domain comprised the electrolyte contained in the probe under study and the corresponding adjacent ones alongside a cylindrical volume of electrolyte, the height of which (50 μm) determines the distance at which bulk conditions apply. This distance was estimated by calculating the thickness of a diffusion layer in a rotating disk experiment setup<sup>[166]</sup> at a mild rotation rate (200 rpm) resulting in characteristic values of electrolyte speed in the bulk of 0.5 cm s<sup>-1</sup>, since diffusion was considered as the dominant mass transport mechanism. In the case of stirring, it was assumed a tangent speed of *ca.* 2 cm s<sup>-1</sup>, corresponding to an equivalent rotation rate of 400 rpm, resulting in a Prandtl layer thickness of 180 μm, leading to an estimated diffusion layer thickness of *ca.* 20 μm. Sensitivity analyses discarded a strong sensitivity of simulated results with this value. The reaction considered is the reduction of CO<sub>2</sub> and H<sub>2</sub>O in 0.1 M KHCO<sub>3</sub> saturated with CO<sub>2</sub> (34.2 mM, pH of 6.8) at 298 K at -0.60 V, -0.80 V, -1.05 V, and -1.30 V *vs.* RHE toward products listed in **Table A.3**, that contains those detected experimentally above trace levels. The considered bulk equilibria involving protonation/ deprotonation of carbon species in solution and their corresponding forward and backward rate constants<sup>[71]</sup> are given in **Table A.4**. The concentrations of H<sup>+</sup> and OH<sup>-</sup> were considered to be all times in equilibrium and with negligible effect of the ionic strength, *i.e.*,  $C_{\text{H}}$  and  $C_{\text{OH}} = 10^{-14}$ . The diffusion coefficients  $D_j$  of involved species are reflected in **Table A.5**. Under steady state, **Eq. 14** till **Eq. 17** govern the mass balances of involved species.

$$\nabla \cdot (-D_{\text{CO}_2} \nabla C_{\text{CO}_2}) = k_{1r} C_{\text{HCO}_3} - k_{1f} C_{\text{CO}_2} C_{\text{OH}} \quad \text{Eq. 14}$$

$$\nabla \cdot (-D_{\text{HCO}_3} \nabla C_{\text{HCO}_3}) = k_{1f} C_{\text{CO}_2} C_{\text{OH}} - k_{1r} C_{\text{HCO}_3} + k_{2r} C_{\text{CO}_3} - k_{2f} C_{\text{HCO}_3} C_{\text{OH}} \quad \text{Eq. 15}$$

$$\nabla \cdot (-D_{\text{CO}_3} \nabla C_{\text{CO}_3}) = k_{2f} C_{\text{HCO}_3} C_{\text{OH}} - k_{2r} C_{\text{CO}_3} \quad \text{Eq. 16}$$

$$\nabla \cdot (-D_{\text{OH}} \nabla C_{\text{OH}}) = k_{1r} C_{\text{HCO}_3} - k_{1f} C_{\text{CO}_2} C_{\text{OH}} + k_{2r} C_{\text{CO}_3} - k_{2f} C_{\text{HCO}_3} C_{\text{OH}} \quad \text{Eq. 17}$$

The initial concentrations were calculated from the corresponding equilibria and are provided in **Table A.5**. This group of equations must be complemented with the following set of boundary conditions. Bulk conditions were considered at the free end of the cylindrical volume separated 50 μm from the base of the micro-probes (**Table A.5**). A zero flux of species was imposed at the lateral wall of the cylindrical volume to reflect the symmetry of the array of micro-probes (**Eq. 18**).

At the boundaries with the Cu surface a zero-flux condition was imposed on non-reactive species, **Eq. 19**. For the species involved in the reduction of CO<sub>2</sub>, the boundary condition was imposed as the flux of consumed/produced CO<sub>2</sub> and OH<sup>-</sup> respectively according to the experimentally observed current densities and selectivity patterns under tested potentials. A first-order dependence of the CO<sub>2</sub> consumption rate was assumed upon the concentration (**Eq. 20**). Consequently, the boundary condition applied to the consumption of CO<sub>2</sub> on the Cu surface is given by **Eq. 21**. The rate constant  $k_{\text{CO}_2}$  is related to the total consumption of CO<sub>2</sub> on the walls of the electrode observed experimentally (**Eq. 22**), where the  $k$  index accounts for all observed carbon products,  $i$  represents the total current density measured,  $n_k$  and  $z_k$  represent the stoichiometric coefficients as reflected in **Table A.3**. Similarly, the corresponding boundary condition for hydroxide must consider its production from the eCO<sub>2</sub>R and from the HER. The contribution from the eCO<sub>2</sub>R can be represented simply by the parallel **Eq. 23**, where  $m_k$  is the corresponding stoichiometric coefficient for the hydroxyl species in **Table A.3**.

A simple inspection of **Eq. 22** and **Eq. 23**, and **Table A.3** reveals that  $k_{\text{OH,CO}_2\text{R}}$  and  $k_{\text{CO}_2}$  must be related linearly to each other. In regard to the HER contribution, the coverage of carbon species was assumed to decrease as the CO<sub>2</sub> concentration does and the local pH would not have a significant impact on the activity of Cu towards the HER at alkaline pH.<sup>[151]</sup> Based on this assumptions, the HER reaction rate was modeled with a linear dependency on the  $z$ -coordinate (**Eq. 24**), which leads to **Eq. 25** accounting for the contribution of HER to the production of OH<sup>-</sup>. In this regard, models assuming other HER dependency (*i.e.*, decreasing or constant HER along the  $z$ -coordinate) resulted either in physically meaningless results or did not converge. At  $z = 0$ , at the surface that was not laser drilled, the specific HER activity was assumed to be equal to the one observed over the LA-Cu-0 electrode at the corresponding potential (**Eq. 26**).

$$-D_j \nabla C_j = 0 \quad \text{for } j = \text{CO}_2, \text{HCO}_3^-, \text{CO}_3^{2-}, \text{ and OH}^- \quad \text{Eq. 18}$$

$$-D_j \nabla C_j = 0 \quad \text{for } j = \text{CO}_2, \text{HCO}_3^-, \text{CO}_3^{2-} \quad \text{Eq. 19}$$

$$r_{\text{CO}_2} = k_{\text{CO}_2} C_{\text{CO}_2} \quad \text{Eq. 20}$$

$$D_{\text{CO}_2} \nabla C_{\text{CO}_2} = k_{\text{CO}_2} C_{\text{CO}_2} \quad \text{Eq. 21}$$

$$\left(\frac{i}{F}\right) \sum_k \frac{FE_k n_k}{z_k} = \iiint_{\text{walls}} k_{\text{CO}_2} C_{\text{CO}_2} dx dy dz \quad \text{Eq. 22}$$

$$\left(\frac{i}{F}\right) \sum_k \frac{FE_k m_k}{z_k} = \iiint_{\text{walls}} k_{\text{OH,CO}_2\text{R}} C_{\text{CO}_2} dx dy dz \quad \text{Eq. 23}$$

$$r_{\text{OH,HER}} = k_{\text{OH,HER}} z \quad \text{Eq. 24}$$

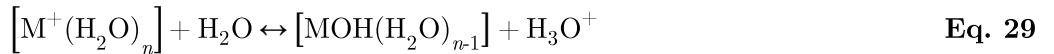
$$\left(\frac{i}{F}\right) \frac{FE_{\text{H}_2} m_{\text{H}_2}}{z_{\text{H}_2}} = \iiint_{\text{walls}} k_{\text{OH,HER}} z dx dy dz \quad \text{Eq. 25}$$

$$\left(\frac{i}{F}\right) \frac{FE_{\text{H}_2} m_{\text{H}_2}}{z_{\text{H}_2}} \Big|_{\text{LA-Cu-0}} = \iint_{z=0} k_{\text{OH,HER},0} dx dy \quad \text{Eq. 26}$$

**Eq. 24**, **Eq. 25** and **Eq. 26** lead to the boundary condition for the production of OH on the walls of the micro-probe (**Eq. 27**). At  $z = 0$ , the boundary condition is thus reflected by **Eq. 28**. The model included the local buffer effect of enhanced hydrolysis of cations (**Eq. 29**) next to the surface due to the electric potential following the description provided by Singh *et al.*<sup>[143]</sup> The fast kinetics of these ionic reactions compared to the rate of formation of hydroxide ions due to the electrochemical processes allowed to consider them in equilibrium at the interface between the micro-probes and the electrolyte. Singh *et al.*<sup>[143]</sup> propose the pKa of the hydrolysis depends on the nature of the cation and comprise two terms accounting for the interaction of the cation with (i) the water molecules in the hydration sphere and (ii) the negative charge on the surface of the electrode, giving rise to **Eq. 30**.

$$-D_{\text{OH}} \nabla C_{\text{OH}} = k_{\text{OH,CO}_2\text{R}} C_{\text{CO}_2} + k_{\text{OH,HER}} z \quad \text{Eq. 27}$$

$$-D_{\text{OH}} \nabla C_{\text{OH}} = k_{\text{OH,CO}_2\text{R}} C_{\text{CO}_2} + k_{\text{OH,HER},0} \quad \text{Eq. 28}$$



$$\text{pKa} = -A \left[ \frac{z^2}{r_w} + \frac{2\pi C N_A}{F} z V r_{\text{surf}} \left( \sqrt{1 + \frac{r_w^2}{r_{\text{surf}}^2}} - 1 \right) \right] + B \quad \text{Eq. 30}$$



A (620 pm<sup>-1</sup>) and B (17.154) correspond to fitted values,  $z$  is the effective charge of the hydrated cations (0.919 for K<sup>+</sup> and 0.930 for Cs<sup>+</sup>),  $r_w$  is the sum of the radius of the cation and the oxygen atom (132 pm for K<sup>+</sup> and 148 pm for Cs<sup>+</sup>),  $r_{\text{surf}}$  is the distance between the solvation sphere and the electrode surface and is assumed to correspond to a CO molecule (250 pm),  $C$  is the specific capacity of the surface (51 μF cm<sup>-2</sup> for Cu), and  $V$  denotes the cell voltage (**Table A.6**). The reader is referred to ref<sup>[143]</sup> for a full description. The local buffer effect was introduced in the model by imposing the equilibrium reflected in **Eq. 29** driven by **Eq. 30** and the condition of zero flux for both hydrolyzed and partially dehydrolyzed cations at the boundaries with the Cu surface, as reflected in **Eq. 31**. Similarly, **Eq. 29** was considered in equilibrium in the bulk of the solution disregarding the effect of applied potential (pKa = 14.5 for K<sup>+</sup> and pKa = 14.8 for Cs<sup>+</sup>). The considered diffusion coefficients for K<sup>+</sup> and Cs<sup>+</sup> were 2.056·10<sup>-9</sup> m<sup>2</sup> s<sup>-1</sup> and 1.957·10<sup>-9</sup> m<sup>2</sup> s<sup>-1</sup>, respectively.

$$-D_j \nabla C_j = 0 \quad \text{for } j = \text{M}^+(\text{H}_2\text{O})_n, \text{MOH}(\text{H}_2\text{O})_{n-1} \quad \text{Eq. 31}$$

The set of **Eq. 14** till **Eq. 19** with boundary conditions established by **Eq. 18**, **Eq. 19**, **Eq. 21**, **Eq. 27** till **Eq. 31** alongside **Eq. 22**, **Eq. 23**, **Eq. 25** and **Eq. 26** form a closed system, that was solved using a 3D finite element method incorporating a multi-frontal massively parallel sparse direct solver (MUMPS) with a tolerance of 0.001 in the COMSOL® platform. The size of the unit element did not affect the values of the calculated variables significantly, confirming the mathematical robustness of the model.

### 3.3. Results and Discussion

This section describes initially the preparation and characterization of microstructured copper electrodes and the associated selectivity patterns at different potentials. This set of results is subsequently used as input for 3D models enabling the quantification of the local chemical environment under eCO<sub>2</sub>R conditions. As a result, selectivity patterns for C<sub>1</sub>-C<sub>3</sub> products emerge using the simulated local pH and CO<sub>2</sub> concentration as descriptors. Finally, a mechanistic discussion and an analysis of the influence of operation parameters based on obtained maps close the section.

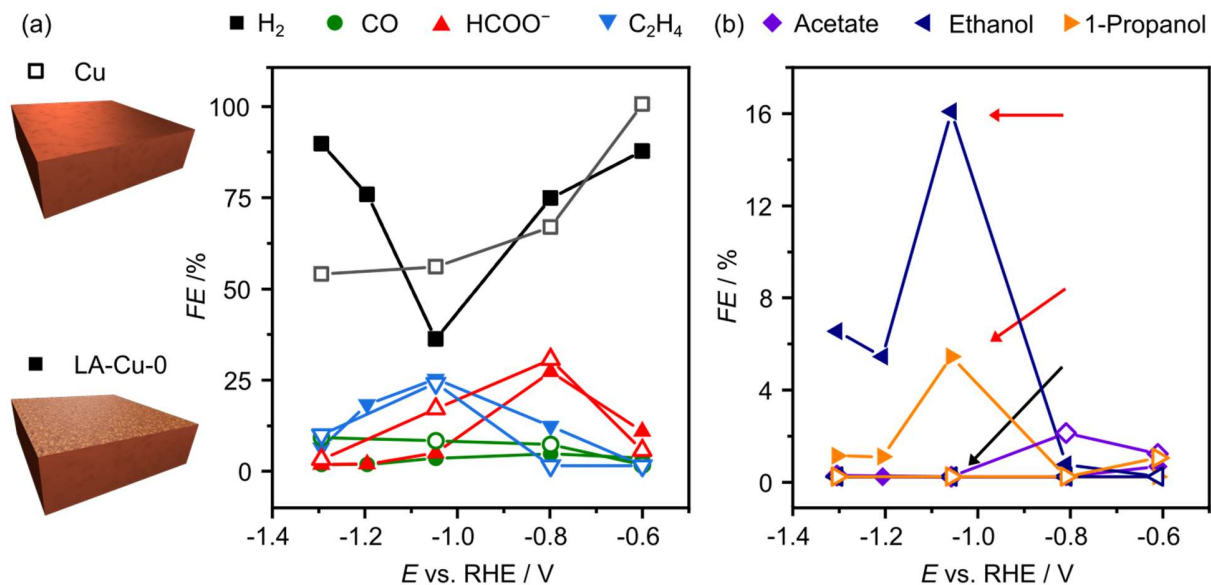


**Figure 3.2.** *FE vs. potential* for a copper foil before (Cu, void symbols) and after (LA-Cu-0, filled symbols) laser ablation. **(a)** products where Cu and LA-Cu-0 show qualitatively similar trends, **(b)** products where LA-Cu-0 outperforms Cu, highlighted for the case of propanol and ethanol (black arrow: Cu, red arrows: LA-Cu-0). Products detected at trace levels are not included (see **Table A.7**).

### 3.3.1. Fabrication and Characterization of Microstructured Electrodes

The driving idea of this study is to enable the imposition of different local chemical environments under operation conditions keeping unaltered both the potential and the catalyst. To this end, model electrodes were designed with a geometry that could influence mass transport properties and thus the local concentrations of H<sup>+</sup> and CO<sub>2</sub> species. Inspired by monoliths widely applied in thermocatalytic processes,<sup>[167]</sup> the mean diffusion pathway was anticipated to be between the active walls and the external environment which would be controlled in cylindrical or conical micro-reactors by its length ( $L$ ). The fabrication of their analogues in a copper foil demanded the ability to create regular cavities at the micrometer scale, GDE.<sup>[119]</sup> USP laser ablation has the ability to transform copper foils into model electrodes, as shown in **Figure 3.1**. The ablation was performed in air, given the enhanced production of complex products generally observed over oxidic Cu surfaces.<sup>[27]</sup> In more detail, a first ablation step pretreated the foils by removing *ca.* 2  $\mu\text{m}$  of material to produce a submicrometrically roughened surface called LA-Cu-0 (where ‘0’ denotes zero, **Figure 3.1a** and **Figure A.10**) whose composition was identified as CuO after XRD and XPS analyses (**Figure 3.1b, c** and **Figure A.12**, respectively). Importantly, to understand the

effect on the catalytic performance introduced by the USP laser ablation treatment, we first compared selectivity patterns under CO<sub>2</sub> saturated 0.1 M KHCO<sub>3</sub> for the unprocessed Cu foils and LA-Cu-0 surface (**Figure 3.2**).

The results show that the application of laser ablation brings a modest influence for CO, HCOO<sup>-</sup> and C<sub>2</sub>H<sub>4</sub> (**Figure 3.2a**) but enhances the formation of alcohols and suppresses the formation of acetate (**Figure 3.2b**). The post reaction characterization of LA-Cu-0 confirmed the expected reduction of CuO into metallic Cu (**Figure 3.1b, c** and **Figure A.12**). In this regard, improved rates toward ethylene and/or alcohols on OD-Cu have been repeatedly reported (though not in all cases<sup>[53,55]</sup>) but their origin is subject to a vivid debate.<sup>[27]</sup> Modified selectivity has been linked to the formation upon reduction of the oxide of particular active sites such as grain boundaries,<sup>[128,168]</sup> remaining interstitial oxygen,<sup>[44]</sup> or low-coordinated Cu sites.<sup>[61]</sup> Nonetheless, the idea of the chemical environment primarily directing the selectivity over these materials due to their unusually large roughness (provoking strong local pH and CO<sub>2</sub> concentration gradients) has been gaining relevance and is now openly claimed.<sup>[27,156,169]</sup> In accordance, the catalytic performances differ mainly at high potentials (*i.e.*, larger currents) and the ablation increased the roughness by a factor of 3 (**Table A.8**) due to redeposition of copper as debris (**Figure A.10**). The laser ablated LA-Cu-0 surface was subsequently microstructured to obtain the set of model electrodes. A dense regular distribution of conical micro-probes (**Figure A.13**) was prepared by a circular hatch of the laser beam (see **Figure 3.1a** and **Section 3.2.1** for a full description). Their diameter and pitch was kept constant (**Figure 3.1d** and **e**), whereas their length was controlled by the number of incident laser pulses.

The resulting electrodes (2.25 cm<sup>2</sup>) contained *ca.* 92 000 micro-probes and are denoted after their length (LA-Cu-L, with  $L = 0, 20, 40, 60, 100, 130$  μm). This strategy achieved a quasi-linear dependency of the exposed surface area with L, in spite of some deviations from the conical shape due to reflections of the laser beam, as disclosed by microcomputed tomography (**Figure A.11**). With regard to their chemical nature, all LA-Cu-L electrodes showed similar composition (**Figure A.14**), confirming the feasibility of this approach toward a set of chemically identical microstructured electrodes with favorable catalytic performance enabling the study of a variety of products.

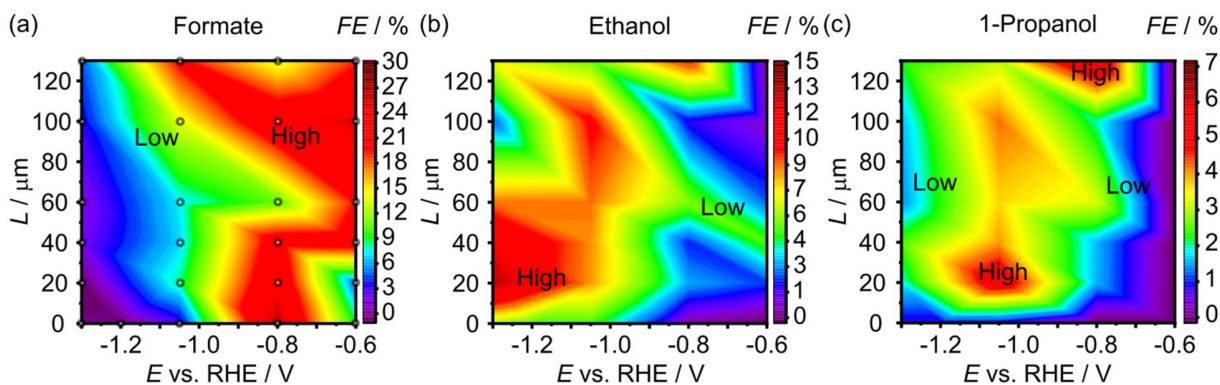


**Figure 3.3.** Selectivity maps *vs.* applied potential and geometry on microstructured electrodes. Contour maps showing *FE* for representative C<sub>1</sub> (formate), C<sub>2</sub> (ethanol), C<sub>3</sub> (propanol) products *vs.* micro-probe length (*L*) and potential. They were built upon integration of results obtained for *L* = 0-20-40-60-80-100-130  $\mu\text{m}$  measured at  $-0.60$ ,  $-0.80$ ,  $-1.05$ , and  $-1.30$  V *vs.* RHE, as indicated by grey dots in the formate map. All other products are depicted in **Figure A.15**. The performance of non-structured laser ablated regions among micro-probes was assimilated to that of Cu-LA-0. See **Section 3.2.2** for the reaction conditions.

### 3.3.2. Revealing Selectivity Patterns by Varying Applied Potential and Electrode Geometry

Qualitatively, larger *L* and more negative potentials were expected to increase the average local pH and reduce the concentration of CO<sub>2</sub>. Following this reasoning, the performance of the microstructured electrodes was evaluated at different potentials ( $-0.60$  V,  $-0.80$  V,  $-1.05$  V,  $-1.30$  V *vs.* RHE) as described in **Section 3.2.2**. Exposure to reaction conditions did not alter the structure of these electrodes as revealed by SEM (**Figure A.16**). Cyclic voltammeteries did not show unexpected redox signals or degradation either (**Figure A.17**). The products with modest *FE* were carefully quantified in view of their value to discuss potential mechanistic routes (see **Figure A.18** and **Table A.7**). The set of major products was common across all conditions (**Figure 3.2** and **Table A.9**). Selectivity patterns are presented as maps in **Figure 3.3** for representative C<sub>1</sub> (formate), C<sub>2</sub> (ethanol), and C<sub>3</sub> (1-propanol) products and for the rest in **Figure A.15**. Variations in selectivity at a fixed potential must be ascribed to the different geometry of the electrodes. A quick inspection reveals the predominance of C<sub>1</sub> products at low potentials and of C<sub>2</sub> at larger ones (**Figure A.15**), as early reported over non-structured Cu,<sup>[19]</sup> with minor impact of *L*. Turning into particular products, formate (**Figure 3.3a**) was produced

with relatively high selectivity (30-40%) over a wide zone at all  $L$  values with no clearly discernible pattern. In contrast, CO was formed with no exception at low quantities (**Figure A.15**, **Table A.9**), as it is the case for oxide-derived Cu catalysts with mild roughness promoting complex products.<sup>[169]</sup> More interestingly, the maps for ethylene (**Figure 3.3b**) and ethanol (**Figure A.15**) resemble each other considerably, suggesting partially shared mechanistic routes as already proposed by theoretical studies.<sup>[136]</sup> **Figure A.19** provides the corresponding maps for ethanol and ethylene referred to the SHE to account for the claimed pH dependency of the proposed rate determining C-C coupling step.<sup>[170]</sup> Finally, 1-propanol (**Figure 3.3c**) is favored ( $FE = 6-7\%$ ) over two different regions partly overlapping with the C<sub>2</sub> ones, thus suggesting similarities among mechanisms.<sup>[171,172]</sup> Even though these results established the feasibility of varying the geometry of the electrodes to obtain selectivity patterns, these maps show very limited practical relevance at this stage, since they reflect the performance of this particular set of electrodes under certain operation conditions. More general applicability of selectivity maps was obtained by translating potential and  $L$  into average local pH and CO<sub>2</sub> concentration as local environment descriptors.

### 3.3.3. Modelling the Local Chemical Environment under Operation Conditions on Microstructured Electrodes

The required quantitative description of the local chemical environment was attained by computational modelling. The set of experimental results comprising current densities (**Table A.10**) and  $FE$ s (**Table A.7** and **Table A.9**) alongside the geometry of the electrodes were used as input for 3D simulations targeting the concentrations and fluxes of relevant species on the flat surface and within the interior of the micro-probes. Most of the assumptions contained in our model are comparable to those found in other works developed over more ill-defined<sup>[151]</sup> or flat<sup>[71]</sup> surfaces. The model considers the local buffer effect of hydrolysis of cations as proposed by Singh *et al.*<sup>[173]</sup> **Section 3.2.5** provides a detailed description of the model. The modeled electrolyte included three regions (**Figure 3.4a**). The first one encompasses the volume contained in the micro-probe under analysis as defined in **Figure 3.1** and **Figure A.11**. To include the potential effect of neighbor micro-probes, the 8 adjacent were added as the second region. The third region accounts for the diffusion layer, as it was considered the dominant mass transport mechanism at this scale. Its thickness accounts for the degree of convection and can be tuned to simulate enhanced (small thickness) or impeded (large thickness) mass transport in the bulk of the solution.

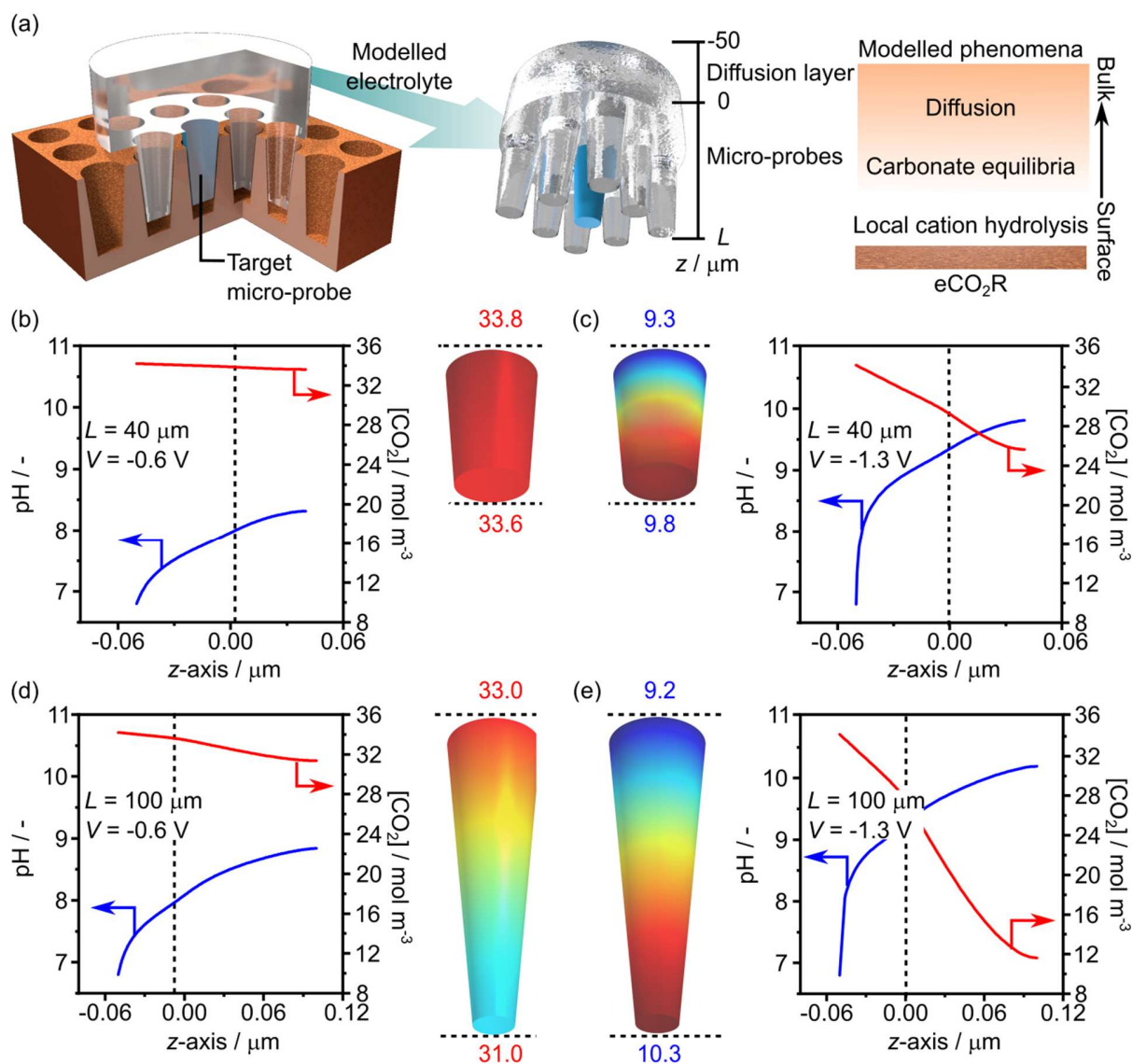


**Figure 3.4.** Computational modelling under eCO<sub>2</sub>R conditions. **(a)** The concentrations of relevant species in the interior of the micro-probe under analysis (blue) were calculated upon modelling using a finite-element approach in the COMSOL® platform. The modeled electrolyte also comprised the interior of the 8 adjacent micro-probes and the diffusion layer. Modeled phenomena are indicated. **(b)-(e)** Calculated evolution of pH and CO<sub>2</sub> concentration along the longitudinal axis (z-axis) for selected lengths and potentials. The  $z$  coordinate increases toward the interior and is zero at the base of the micro-probe. Insets show the three-dimensional representation of the simulated CO<sub>2</sub> concentration (at  $-0.60$  V vs. RHE) or pH (at  $-1.30$  V vs. RHE).

Its value (50  $\mu\text{m}$ ) reflects the mild convection imposed in the cathodic chamber by  $\text{CO}_2$  bubbling (see **Section 3.2.5** for a more extended description). The concentration and flux of  $\text{OH}^-$ ,  $\text{CO}_2$ ,  $\text{HCO}_3^-$ , and  $\text{CO}_3^{2-}$  species were calculated at steady state upon considering the interplay between the e $\text{CO}_2\text{R}$  and HER activities (**Table A.10**), the chemical equilibria of carbonate species (**Table A.4**), the local buffer effect of the hydrolysis of cations, and diffusion (**Table A.5**). Boundary conditions were imposed by bulk concentrations at the free end of the diffusion layer ( $z = -50 \mu\text{m}$  in **Figure 3.4a**), zero flux for non-reactive species on the copper surfaces, zero flux for all species on the lateral walls of the diffusion layer for symmetry reasons, and equilibrium for the hydrolysis of cations next to the copper surfaces, to account for this effect relevant at the atomic scale (see **Section 3.2.5** for calculation of the associated pKa).

Critically, experimental partial current densities enabled to impose the flux of  $\text{OH}^-$  and  $\text{CO}_2$  as the boundary condition on the copper surfaces. In more detail, the  $\text{CO}_2$  consumption rate was considered as linearly related to its concentration and the HER activity to increase linearly along the  $z$ -axis (in line with reports claiming increased HER with decreasing local  $\text{CO}$  concentration<sup>[93]</sup>), adapting the procedure developed by Raciti *et al.*<sup>[151]</sup> The reaction rate constants for both the HER and e $\text{CO}_2\text{R}$  were determined after imposing the matching of the measured current density corrected by the double layer capacitance (**Table A.8**) and the current density obtained after integrating the assumed reaction rates over the copper surfaces (see **Section 3.2.5** for an extended description). The catalytic behavior of the ablated but non-microstructured surface (*i.e.*, that between micro-probes) was considered equal to that of Cu-LA-0 (see **Figure 3.2**). Considering the fragmented mechanistic information available, the reaction rates of all products vary in the same manner along the  $z$ -coordinate, which may not accurately reflect reality. This fact constitutes an opportunity for refinement in the future. The populated set of results with 3D character and the complexity of the modeled volume demanded a strategy enabling a straightforward analysis. In view of the geometry of the micro-probes, treating the concentrations as 1D without loss of generality was considered. In fact, **Figure A.20** demonstrates that pH and  $\text{CO}_2$  concentration can be accurately described as unidimensional variables solely dependent on the  $z$ -coordinate in the interior of the micro-probes. In addition, the negligible mutual influence between adjacent probes was also unveiled. On a lateral note, a detailed analysis of the modeled flux of species revealed

that  $L$  and potential can be used as descriptors of the CO<sub>2</sub> flux, exposing the interplay among geometry, potential, and mass transport (see **Figure A.21**, **Figure A.22** and **Figure A.23**).

Finally, local concentrations of protons and CO<sub>2</sub> were quantified for each combination of potential and  $L$ . **Figure 3.4b-e** show representative cases at low ( $-0.60$  V) and high ( $-1.30$  V) potentials for shallow (LA-Cu-40) and deep (LA-Cu-100) micro-probes. The combination of low potential and shallow  $L$  (**Figure 3.4b**) led to negligible depletion of CO<sub>2</sub> along the axis but to a significant pH increase of more than one unit over the bulk at  $z = L$ . The application of low potentials to longer micro-probes (**Figure 3.4d**) did not have a strong impact on the concentration of CO<sub>2</sub> either, showing the ability of the buffered electrolyte and short diffusion paths to keep a homogeneous concentration at modest current densities (**Table A.10**). However, the effect on the pH is even more noticeable. In the case of high potentials, shallow micro-probes (**Figure 3.4c**) also exhibited relatively high concentrations of CO<sub>2</sub> with the expected variation on pH. In contrast, deep micro-probes (**Figure 3.4e**) developed large gradients of CO<sub>2</sub> concentration and pH along the axis (pH~10.2, [CO<sub>2</sub>] = 12 mol m<sup>-3</sup> at  $z = 100$  μm), suggesting a wide range of chemical environments at work. It can be concluded that at low potentials  $L$  can be used to tune the local pH while keeping a high and approximately constant CO<sub>2</sub> concentration throughout the volume, whereas at high potentials this strategy fails for large  $L$  values. After these results, the pH and CO<sub>2</sub> concentration averaged over the  $z$ -axis were taken as representative descriptors for further analyses. Maps relating these variables with  $L$  and potential are shown in **Figure A.24**. A quick inspection reveals that the average CO<sub>2</sub> concentration high approximately constant in all experiments except for the combination of large  $L$  values and high potentials, whereas the average pH is mostly dependent on the applied potential and shows a wide plateau at pH of 9.0-9.3 between  $-0.80$  V and  $-1.20$  V *vs.* RHE.

### 3.3.4. Mapping Selectivity versus Chemical Environment Descriptors

As soon as potential and micro-probe length could be correlated to average pH and CO<sub>2</sub> concentration, we mapped selectivity values versus them to expose patterns for each of the main products (**Figure 3.5**). As targeted, these maps are independent of the particular experimental setup used and thus reflect intrinsic trends of eCO<sub>2</sub>R on Cu materials. The kinetic nature of the maps was confirmed in **Figure A.25** through the current density associated to formation of carbon products. From the lack of plateau regions it can be inferred that mass transport limitations do



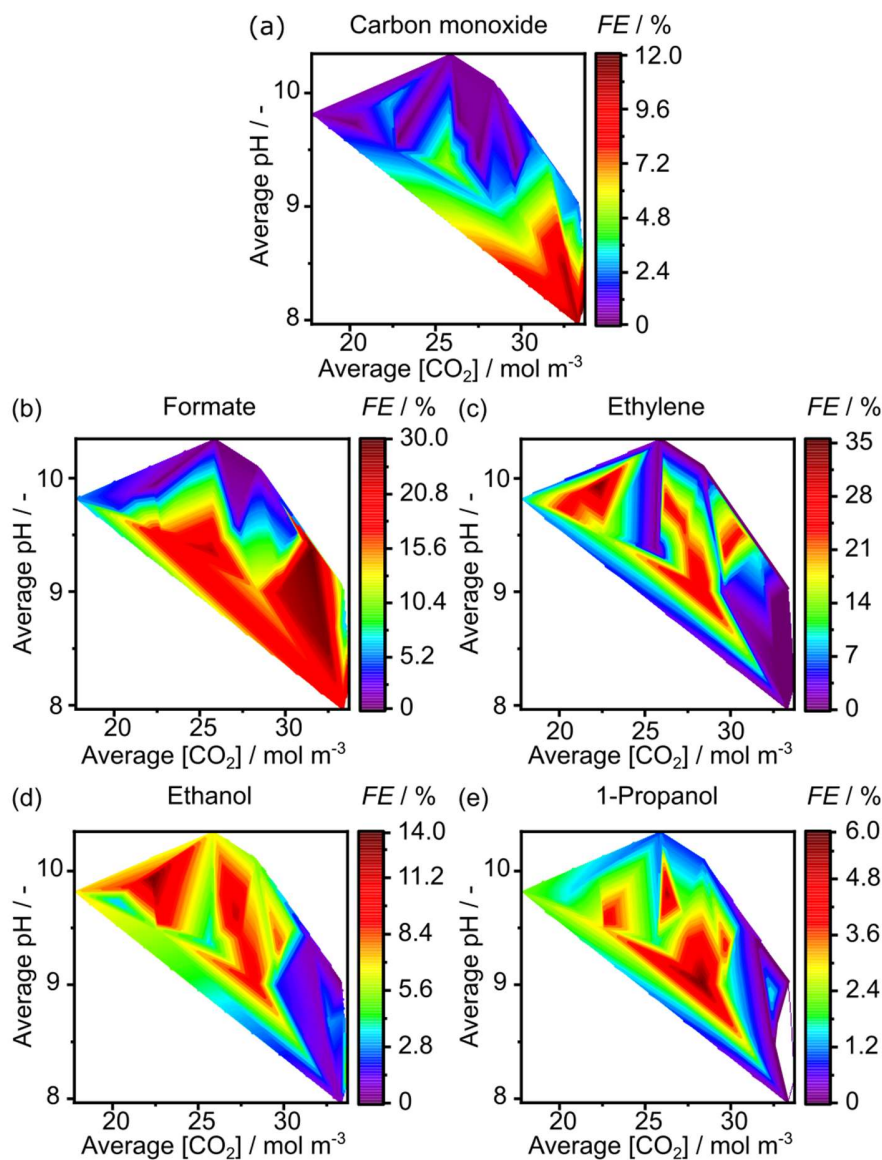


**Figure 3.5.** Selectivity maps for eCO<sub>2</sub>R products *vs.* chemical environment descriptors. Contour maps showing *FE* versus calculated average pH and CO<sub>2</sub> concentration in the interior of micro-probes for (a) carbon monoxide, (b) formate, (c) ethylene, (d) ethanol, and (e) 1-propanol. White regions correspond to pH/[CO<sub>2</sub>] pairs not allowed by equilibria under reaction conditions.

not play a relevant role and thus the observed patterns can be largely ascribed to mechanistic differences. In agreement with the lack of limiting current densities, average CO<sub>2</sub> concentrations were in all cases larger than 65% of the bulk value (34 mol m<sup>-3</sup>, **Table A.11.**). The local buffer effect of the hydrolysis of cations is relevant for an accurate assessment of the local chemical environment. The model proposed by Singh *et al.*<sup>[143]</sup> and incorporated into the calculations,

introduces a local source of H<sup>+</sup> through a fast hydrolysis equilibrium with a pKa of up to 8 under high overpotentials (see **Section 3.2.5**). **Figure A.26** compares maps shown in **Figure 3.5** with the equivalent ones where this effect is disregarded. Hydrolysis plays a modest role at mild conditions but becomes a large driver of the chemical environment at high overpotentials.

To provide a general perspective for all products regions showing high selectivity have been superimposed. The resulting map after mathematical smoothing is displayed in **Figure 3.6a** (see **Figure A.27** for the unprocessed version including experiments modeled). Some relations among products become explicit on this representation, such as the intermediate position of the C<sub>3</sub> region between C<sub>1</sub> and C<sub>2</sub> at mild pH and high concentration of CO<sub>2</sub>, where C<sub>2</sub> formations begin to rise but C<sub>1</sub> are still produced with appreciable activity. This puts forward that mild overpotentials and good mass transport conditions may favor C<sub>3</sub> formation. In this regard, a second region for 1-propanol ( $FE = 4\%$  in **Figure 3.6a**) overlapping with the corresponding region for ethylene was identified by the mathematical treatment, suggesting a second mechanism at higher pH values where ethylene may play the role of intermediate. Finally, the lack of correlation between acetate and ethanol discards an impact of chemical routes (Cannizzaro-type reactions) in the formation of the latter.<sup>[142]</sup>

### 3.3.5. Mechanistic Relevance of Selectivity Maps

The mechanistic relevance can be considered for each specific product in the map displayed in **Figure 3.6a**, the formate map (**Figure 3.5b**) points to its preferential formation under a relatively wide range of chemical environments (pH 8.0 - 9.8 and [CO<sub>2</sub>] > 20 mol m<sup>-3</sup>), suggesting a poorly sensitive mechanism. Carbon monoxide (**Figure 3.5a**) seems to share affinity for high concentrations of CO<sub>2</sub> constrained to a less alkaline pH range (< 9). This observation agrees with the promotion of formate over carbon monoxide reported as the pH increases.<sup>[152]</sup> In addition, carbon monoxide shows lower selectivity in regions where C<sub>2</sub> products develop appreciably, in line with its accepted role of key intermediate.

The ethylene map (**Figure 3.5c**) presents two regions that call for a discussion on the light of proposed mechanisms associated to high and low overpotentials.<sup>[66,95,147]</sup> The first region finds at a narrow range with high pH values and contains a maximum ( $FE = 35\%$ , [CO<sub>2</sub>] = 22 mol m<sup>-3</sup>, pH 9.9, see **Table A.9.** and **Table A.11.**) for LA-Cu-20 exposed to -1.30 V *vs.* RHE. In principle, this region could be reasonably ascribed to one of the high overpotential mechanisms with strong

pH dependence proposed either on Cu(111) or Cu(100). However, the small amount of methane produced ( $FE = 3\%$  at the maximum, **Table A.9.**) suggests additional route(s) to those proposed by the groups of Koper<sup>[66]</sup> or Goddard.<sup>[95]</sup> Similarly, the route proposed by Head-Gordon *et al.*<sup>[99]</sup> is a problematic alternative in view of the small amount of acetate detected ( $FE \sim 0.1\%$ , **Table A.7.**).

Interestingly, the other region with no distinct pH dependence at larger  $\text{CO}_2$  concentrations (maximum at  $FE \sim 30\%$ ,  $[\text{CO}_2] = 28 \text{ mol m}^{-3}$ , pH 9.1, LA-Cu-130 operated at  $-0.80 \text{ V vs. RHE}$ ) might correspond to a low overpotential route. Indeed, the relatively large amount of acetate ( $FE = 1\text{-}3\%$ ) at the upper part of this region is compatible with some contribution arising from the Head-Gordon route. The consideration of the ethanol (**Figure 3.5d**) pattern sheds additional light on this mechanistic discussion, since it largely resembles that of ethylene (also observed in **Figure 3.3b**). More specifically, the formation of ethylene glycol ( $FE \sim 1\%$ ,  $[\text{CO}_2] = 26 \text{ mM}$ , pH 9.8) in the upper part of the region in **Figure 3.6a** associated to larger  $\text{CO}_2$  concentrations further supports the Head-Gordon pathway. However, this association cannot be extended to lower pH values, where the maximum for ethanol (superimposes with the ethylene one) is located ( $FE = 9.8\%$ ,  $[\text{CO}_2] = 28 \text{ mol m}^{-3}$ , pH 9.1). Regarding the other region, at higher pH values, both maxima also overlap ( $FE_{\text{ethanol}} = 13.4\%$ ) and similarly, a tentative assignment of the predominant mechanistic route is precluded by the trace levels of minor products quantified (**Table A.7**). It can be concluded that despite the qualitative agreement, none of the proposed mechanistic routes for ethylene and/or ethanol closely match the observations, suggesting unaccounted pathways. Interestingly, the 1-propanol map (**Figure 3.5e**) also discloses a noticeable pattern. Regrettably, the mechanistic discussion based on literature is to date forcibly limited for  $\text{C}_3$  products due to their yet largely unexplored mechanistic networks. Acetaldehyde has been recently proposed as a key intermediate toward propanol through its dehydrogenative adsorption as methyl carbonyl.<sup>[153]</sup> However, the very low  $FE$  observed for acetaldehyde in the region where the 1-propanol one peaks ( $< 0.1\%$ , **Table A.7** and **Table A.9**) makes it reasonable to assign a secondary relevance to this route in the study. Ethylene has also been proposed as a key intermediate for the formation of 1-propanol.<sup>[25,172,174]</sup> Our results reveal the high sensitivity of 1-propanol formation to the chemical environment. It shows a nearly pH-independent optimal region at high  $\text{CO}_2$  concentrations that superimposes with ethylene (maximum at  $FE = 5.4\%$ ,  $[\text{CO}_2] = 28 \text{ mol m}^{-3}$ , pH 9.1) thus

supporting their mechanistic relation. Given the dependency of eCO<sub>2</sub>R equilibrium potential with the concentration of H<sup>+</sup> and CO<sub>2</sub>, the overpotentials at which 1-propanol was optimized were investigated. The overpotentials could be calculated from the Nernst equation upon correcting the standard reduction potential with the simulated concentration of species (**Figure A.15**). The selectivity map in terms of local pH and overpotential (**Figure A.28**) exhibits two favorable regions at mid (0.70 V) and high (1.10 V) overpotentials, predicting two mechanisms at work that have not been explored in the literature.

### 3.3.6. Influence of Mass Transport and Electrolyte

There may be conditions and ways to allow the selectivity maps to help defining optimal operation conditions for selectivity control. Maps contribute to rationalize the largely reported sensitivity of eCO<sub>2</sub>R to the reactor configuration and operation conditions. Cathodic catalysts in artificial leaves<sup>[135,175]</sup> usually operate in contact with liquid electrolyte and display current densities below  $-10 \text{ mA cm}^{-2}$  comparable to those reported in **Table A.10** due to the limited energy density of sunlight (*ca.*  $1 \text{ kW m}^{-2}$ ). CO<sub>2</sub> electrolyzers fed by grid electricity, on the other hand, are typically designed based on GDE whose geometric current densities may reach hundreds of  $\text{mA cm}_{\text{geo}}^{-2}$ .<sup>[119]</sup> Nevertheless, the large electrochemical surface area typically reported over porous catalytic layers<sup>[176]</sup> of more than  $30 \text{ m}^2 \text{ g}_{\text{metal}}^{-1}$  leads to current densities of tens of  $\text{mA cm}_{\text{metal}}^{-2}$  for typical catalyst loadings of  $1 \text{ mg}_{\text{metal}} \text{ cm}_{\text{geo}}^{-2}$ . Selectivity maps in **Figure 3.5** are thus directly applicable to devices such as artificial leaves and may reasonably describe the main features of CO<sub>2</sub> electrolyzers operated below extreme current densities.

The transport of CO<sub>2</sub> to the active sites is typically enhanced either by the use of stirring in liquid medium or the use of a GDE configuration. To understand the changes in the local chemical environment associated to enhanced mass transport, selected Cu-LA-L electrodes were exposed with very different geometry ( $L = 40 \text{ }\mu\text{m}$  or  $100 \text{ }\mu\text{m}$ ) to potentials where mass transport expectedly plays a role ( $E = -1.05 \text{ V}$  or  $-1.30 \text{ V vs. RHE}$ ) under mild stirring conditions in  $0.1 \text{ M KHCO}_3$ . These experiments were computationally treated by considering  $20 \text{ }\mu\text{m}$  as the thickness of the diffusion layer instead of  $50 \text{ }\mu\text{m}$  (**Figure 3.4a**) after its estimation using the Levich equation.<sup>[166]</sup> Local pH and CO<sub>2</sub> concentrations showed remarkable differences when compared with the equivalent experiment without stirring (see **Figure A.29**). **Figure 3.6a** displays the positions of representative examples (LA-Cu-100,  $-1.05 \text{ V}$  with and without stirring denoted as  $\text{K}_s^+$  and  $\text{K}^+$ ,

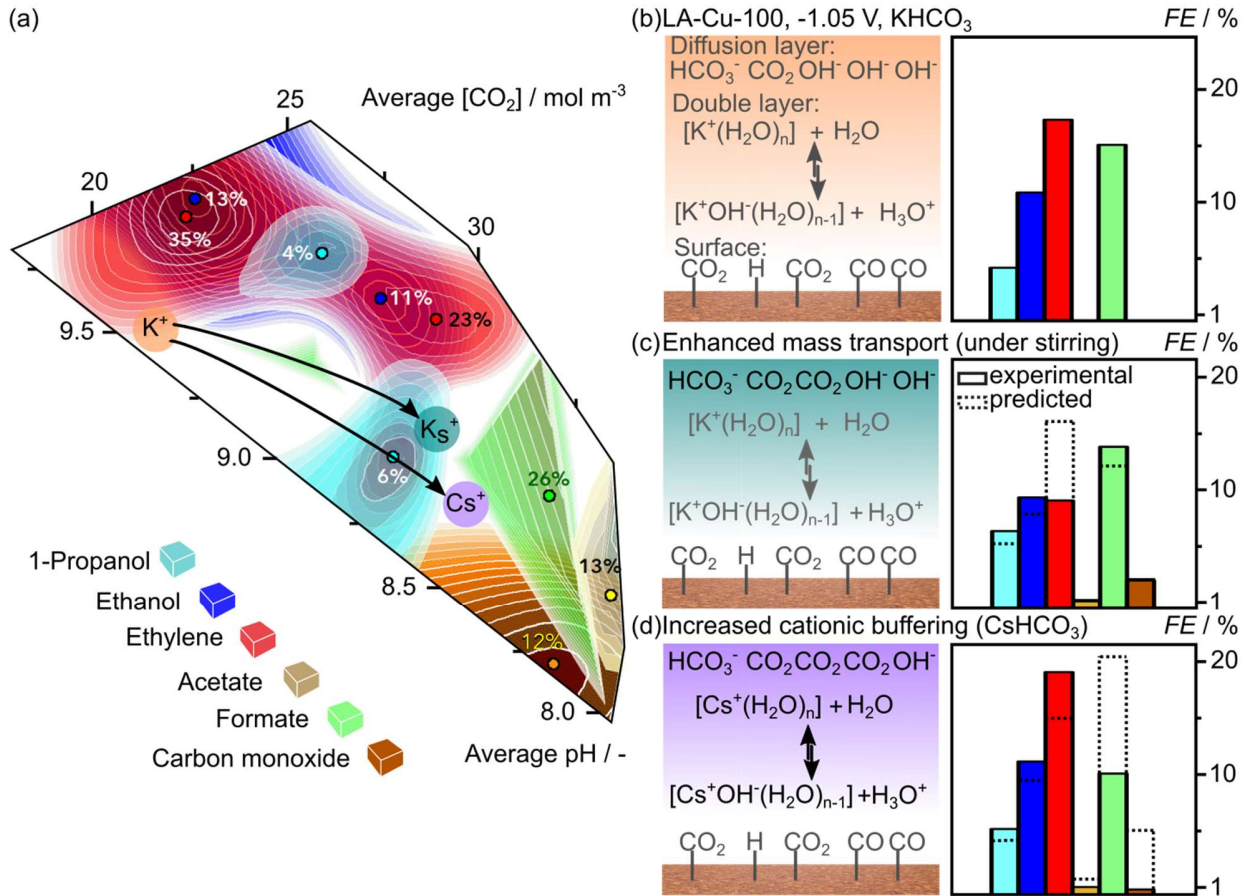


**Figure 3.6.** Effect of enhanced mass transport and electrolyte composition on selectivity. (a) Contour map showing high  $FE$  zones with respect to calculated average pH and  $CO_2$  concentration in the interior of micro-probes upon overlaying and smoothing of maps presented in **Figure 3.5**. The dots represent local  $FE$  maxima. The equivalent map built upon direct overlapping of maps and including the experiments modeled can be found in **Figure A.22**. Three circles have been overlaid, showing the calculated chemical environment for LA-Cu-100 exposed to  $-1.05$  V in  $0.1$  M  $KHCO_3$  ( $K^+$ ),  $0.1$  M  $KHCO_3$  under stirring ( $K_s^+$ ), and  $0.1$  M  $CsHCO_3$  ( $Cs^+$ ). (b) Representation of the local chemical environment next to the surface and product distribution for the case  $K^+$ . (c), (d) similar to (b) for the cases of  $K_s^+$  and  $Cs^+$ , respectively, with predicted selectivities obtained from maps in **Figure 3.5** (dashed lines).

respectively) in the global selectivity map. Stirring increases the average local  $CO_2$  concentration from  $22$  to  $29$  mol  $cm^{-3}$  and concomitantly decrease the average pH from  $9.6$  to  $9.2$  (see **Figure 3.6a**, **b**, and **Table A.11**). Remarkably, the selectivity pattern predicted for the stirring experiment by the position of  $K_s^+$  in the map (dashed bars in **Figure 3.6c**) closely predicted the experimental (solid bars). The large discrepancy found for ethylene may be related to the large

gradients in its  $FE$  associated to that region (see **Figure 3.5**), making the predicted value very sensitive to small uncertainties in simulated results.

The electrolyte of choice in the eCO<sub>2</sub>R plays a critical role in both activity and selectivity, which has been linked to the local effect of the free cationic species in the vicinity of the catalyst surface.<sup>[177]</sup> Larger cations are expected to show a lower pKa for their hydrolysis and a concomitant enlarged buffer capability (see **Section 3.2.5** for details on the calculations). Cu-LA-L electrodes ( $L = 0 \mu\text{m}$ ,  $40 \mu\text{m}$ ,  $100 \mu\text{m}$ ) were exposed to  $-1.05 \text{ V}$  in  $0.1 \text{ M CsHCO}_3$  (no additional stirring applied) and simulated the local environment upon introducing Cs<sup>+</sup> hydrolysis equilibrium parameters in the model. **Figure A.29** illustrates how local pH and CO<sub>2</sub> concentrations varied notably along the axis of the micro-probes with respect to the equivalent experiments in  $0.1 \text{ M KHCO}_3$ , facilitating a larger concentration of CO<sub>2</sub> and decreased pH. **Figure 3.6a** displays the position of the representative LA-Cu-100 exposed to  $-1.05 \text{ V}$  (denoted as Cs<sup>+</sup>, **Table A.11**). The use of CsHCO<sub>3</sub> allowed an increased CO<sub>2</sub> concentration ( $30 \text{ mol cm}^{-3}$  vs.  $22 \text{ mol cm}^{-3}$ ) and reduced pH ( $8.8$  vs.  $9.6$ ). Similarly to the case of K<sub>s</sub><sup>+</sup>, the position of Cs<sup>+</sup> predicted with notable accuracy the experimental distribution of products (**Figure 3.6c**) with the exception of formate, for the same reasons explained for ethylene in the case of stirring. It is apparent from the comparison between K<sub>s</sub><sup>+</sup> and Cs<sup>+</sup> that enhanced mass transport and electrolyte buffering effect play a somewhat similar role in varying the local chemical environment, though the latter is dependent on catalyst surface charge and thus on the potential.

From a more general perspective, these results reflect the ability of selectivity maps to account for the effect of operation conditions on the selectivity pattern. Given a target product, this feature can be used to orient basic design parameters. For example, the use of an electrolyte with mild cationic buffer effect such as KHCO<sub>3</sub> in combination with a mild stirring seems an advisable combination toward the selective production of propanol.

### 3.4. Conclusions

The application of microstructuring and advanced modelling enabled to quantify the relation between selectivity and a broad range of chemical environments in the eCO<sub>2</sub>R on Cu. Selectivity maps for the main C<sub>1</sub>-C<sub>3</sub> products were unveiled in terms of local CO<sub>2</sub> concentration and pH. This was achieved by testing microstructured Cu foils processed by laser ablation followed by simulations facilitated by the regular geometry of the electrodes. Selectivity maps disclosed clear patterns shedding light on open mechanistic queries. Ethylene and ethanol patterns could not be entirely accounted for by proposed mechanisms, whereas the role of ethylene as intermediate toward propanol is compatible with our results that suggest the presence of two mechanisms at mid- and high overpotentials. From an operational perspective, selectivity maps successfully predicted the influence of operation conditions such as stirring or the use of different electrolyte on the product distribution, suggesting their potential to guide process design.

## Chapter 4

# Mechanistic Routes toward C<sub>3</sub> Products in Copper-Catalyzed CO<sub>2</sub> Electroreduction

### 4.1. Introduction

Developing functional catalysts for the eCO<sub>2</sub>R to complex products lies at the core of new efforts to develop sustainable technologies.<sup>[27]</sup> Among available materials, copper-based electrocatalysts occupy a pivotal role due to their ability to form the C<sub>2+</sub> backbone for high-value fuels and commodity chemicals.<sup>[26,27]</sup> The type and amount of products formed are sensitive to the applied potential, electrolyte, and the preparation protocol of Cu.<sup>[47,136,178,179]</sup> The established mechanism to the C<sub>2</sub> fraction advocates that CO<sub>2</sub> first reduces to CO, which dimerises to OCCO<sup>-</sup> and subsequently reduces to hydrocarbons and alcohols. Typically, the main C<sub>2</sub> product is ethylene (up to *ca.* 74% *FE*),<sup>[180]</sup> although an exceptional ethanol selectivity (*FE* = 91%)<sup>[181]</sup> has been reported on Cu clusters. For C<sub>4</sub> products, the aldol condensation of acetaldehyde gives crotonaldehyde, which in turn reduces to 1-butanol, albeit with low yields.<sup>[182]</sup> Among C<sub>3</sub> compounds, 1-propanol can be produced with appreciable yields (*FE* ~ 23%),<sup>[103,117]</sup> whereas propylene, the corresponding C<sub>3</sub> olefin (0.36 eV less stable than 1-propanol, **Table A.12**), has only been detected as a trace product (*FE* < 0.1%).<sup>[182]</sup> This puzzling outcome contrasts with the vast formation of ethylene, which is less stable than ethanol by 0.47 eV, **Table A.12**. Furthermore, 2-propanol, which is the most thermodynamically stable C<sub>3</sub> alcohol (0.17 eV lower than 1-propanol, **Table A.12**), has never been observed in eCO<sub>2</sub>R.<sup>[104]</sup> This prompted the curiosity into the formation mechanism of C<sub>3</sub> backbone. Reports have indicated that the formation of the C<sub>3</sub> backbone at high CO concentrations and relatively mild applied potentials (-0.36 V to -0.56 V *vs.* RHE)<sup>[103,105]</sup> requires asymmetric sites on OD-Cu catalysts. Nonetheless, the reasons behind the low selectivity to C<sub>3</sub> products in eCO<sub>2</sub>R at a molecular level is very limited. This is due to the large number of elementary steps (> 10<sup>3</sup>) that prevents the use of standard reaction sampling tools based on explicit DFT and reaction profile analysis.



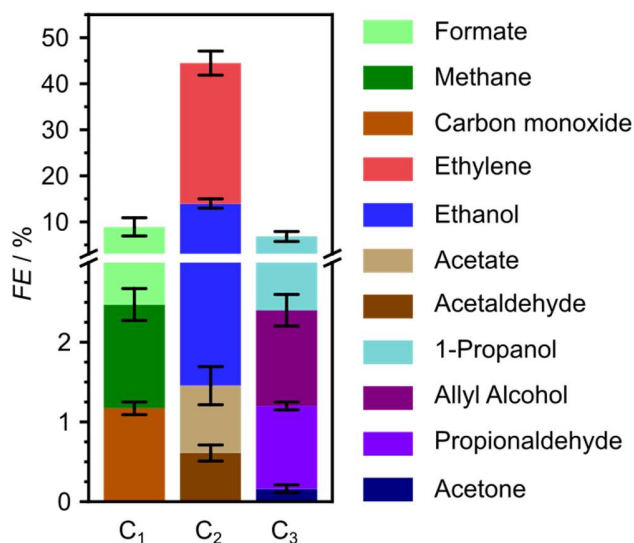


**Figure 4.1.** C<sub>1</sub>–C<sub>3</sub> products formed from the eCO<sub>2</sub>R on OD-Cu in 0.1 M KHCO<sub>3</sub> at –0.95 V *vs.* RHE. The balance is closed with hydrogen FE of 37.4%. Error bars represent the standard deviations as presented in **Table A.13**.

Herein, electrocatalytic routes were analyzed towards C<sub>3</sub> products through a divide and conquer strategy based on the generation of the network graph and computational reaction profiles combined with key electrochemical experiments involving C<sub>1</sub>, C<sub>2</sub>, and C<sub>3</sub> reagents. This new methodological approach enables us to identify the most likely C<sub>1</sub>–C<sub>2</sub> coupling steps towards C<sub>3</sub> intermediates, elucidate the bifurcation points to different C<sub>3</sub> products; and pinpoint kinetic bottlenecks hindering propylene production.

## 4.2. Experimental

The electrocatalytic reactor used for the experiments is a home-made gastight cell consisting of two compartments separated by a Nafion 211 membrane with gas-flow inlet and outlet ports. The cell has an OD-Cu working electrode, a GDL carbon paper counter electrode, and a leak-free Ag/AgCl reference electrode (further details provided in **Sections 4.2.3, 4.2.4 and 4.2.5**). Triplicate measurements were done, with the average values and standard deviations presented in **Table A.13** till **Table A.25**. The physicochemical and catalytic properties of the OD-Cu catalyst have been discussed elsewhere<sup>[169,182]</sup> while the preparation can be found in **Section 4.2.2**. eCO<sub>2</sub>R was initially performed in 0.1 M KHCO<sub>3</sub> at –0.95 V *vs.* RHE to maximise the production of multi-carbon products,<sup>[169]</sup> as shown in **Figure 4.1** (see **Figure A.30** for polarization curves). C<sub>1</sub> and

C<sub>2</sub> products account for 53% of the *FE*, whereas 7% corresponds to C<sub>3</sub> products. The observed product distribution agrees with selectivity trends presented in literature (summarized in **Figure A.31**), and paths to C<sub>2</sub> products shown in **Figure A.32** and **Figure A.33**. To unravel the selectivity patterns observed from both the literature and results in this chapter, the following workflow was constructed:

- 1) Building the reaction network by encoding the corresponding structural graphs.
- 2) Sampling the intermediates by DFT.
- 3) computing all C<sub>1</sub>–C<sub>2</sub> backbone couplings by DFT.
- 4) Pruning the network of non-viable backbone formation routes by probing the products from CO, formaldehyde, and methanol co-reduction with C<sub>2</sub> reactants (**Figure 4.2**), with particular attention to missing products.
- 5) Computing all routes from the C<sub>3</sub> backbone to the final products using DFT and linear-scaling relationships (**Table A.26**) to identify the best routes towards 1-propanol and propylene.
- 6) Experimental benchmarking of the main predicted routes via electrocatalytic tests with key intermediates.

While the routes to C<sub>1</sub> and C<sub>2</sub> products can be probed manually, as shown in the literature,<sup>[95,96,99,183–185]</sup> the analysis of routes to C<sub>3</sub> products demands automation. The full network containing all C<sub>1</sub>, C<sub>2</sub>, and C<sub>3</sub> intermediates has 463 elements, represented here as nodes in a graph (see **Section 4.2.10**). The energies of intermediates (referenced to CO<sub>2</sub>, H<sub>2</sub>O, and H<sub>2</sub>) were evaluated with the CHE<sup>[75,88]</sup> containing the DFT energy obtained with a PBE-D2 formulation<sup>[186–188]</sup> (corrected for metal overbinding), our in-house developed implicit solvation model,<sup>[189,190]</sup> and the polarization term<sup>[182,191]</sup> (see **Eq. 32** till **Eq. 35**). The D2 contribution on H\* and CO\* adsorption is small: 0.04 eV and 0.14 eV, respectively. Intermediates are linked by 2266 steps (edges linking the nodes in the graph): 55 C<sub>1</sub>–C<sub>1</sub> and 636 C<sub>1</sub>–C<sub>2</sub> couplings, 683 C–H and 305 O–H hydrogenations, and 587 C–O(H) cleavages. To ensure the desired accuracy, 586 out of all C<sub>1</sub>–C<sub>2</sub> couplings (**Table A.27** till **Table A.30**, 92% of total), 10 C–O(H) breakings (**Table A.31**), and 8 hydrogenations (**Table A.32**) were explicitly obtained via nudged elastic band (NEB)<sup>[192]</sup>

$C_2 \setminus C_1$	Carbon monoxide	Formaldehyde	Methanol	Carbon dioxide
No $C_2$	1-Propanol (0.02) <sup>A</sup> 1-Propanol (2.2) <sup>B</sup> Allyl alcohol (2.1) <sup>B</sup> Propionaldehyde (0.4) <sup>B</sup>	No $C_3^{A,B}$	No $C_3^A$	1-propanol (75.8) <sup>C</sup> Allyl alcohol (25.2) <sup>C</sup> Propionaldehyde (20.3) <sup>C</sup> Acetone (3.2) <sup>C</sup>
Oxalate	1-Propanol (0.4) <sup>A</sup>	No $C_3^A$	1-propanol (0.1) <sup>A</sup>	X
Glyoxal	1-Propanol (0.3) <sup>A</sup>	No $C_3^A$	1-Propanol (0.1) <sup>A</sup>	X
Acetate	1-Propanol (0.2) <sup>A</sup>	No $C_3^A$	No $C_3^A$	X
Ethylene glycol	1-Propanol (0.5) <sup>A</sup>	No $C_3^A$	No $C_3^A$	X
Ethanol	1-Propanol (0.2) <sup>A</sup>	No $C_3^A$	No $C_3^A$	X
Acetaldehyde	1-Propanol (12.1) <sup>B</sup> Propylene (trace) <sup>B</sup>	Propylene (1.4) <sup>B</sup> Allyl alcohol (2.0) <sup>B</sup>	X	X


<sup>A</sup> 0.1 M KOH at -0.40 V vs. RHE

<sup>B</sup> 0.1 M PPM at -1.00 V vs. RHE

<sup>C</sup> 0.1 M KHCO<sub>3</sub> at -0.95 V vs. RHE

X not performed

lower rate /  $\mu\text{mol cm}^{-2}\text{h}^{-1}$  higher



**Figure 4.2.** Summary of  $C_3$  products and their corresponding formation rates observed experimentally from the electrolysis of  $C_1$  or a mixture of  $C_1$  and  $C_2$  compounds on OD-Cu. The  $C_1$  and  $C_2$  compounds used are listed in the topmost row and leftmost column respectively, while the experimental conditions are indicated in the footnotes. The full set of experiments and product distributions are shown in **Table A.13** till **Table A.25**.

and confirmed by vibrational analysis. Initial guesses for NEB were generated automatically (see **Sections 4.2.8** and **Note A.1** till **Note A.4**). Linear scaling relationships (LSR) were employed in the initial fast-sampling of C–H and O–H hydrogenations as they are reliable for these cases (**Table A.26**).<sup>[185,193,194]</sup> The transition states for key hydrogenation steps in the main path were further refined with DFT-NEB. Heyrovsky-type reactions for C–OH breakings and C–H formations were considered (see **Note A.4**). Tests on density functionals, LSR, and charge analysis have been described in **Note A.5** and **Figure A.34** till **Figure A.37**, and demonstrate that our strategy provides an excellent cost-efficiency balance.

Benchmark electrochemical experiments (**Figure 4.2**) involving the reduction of selected  $C_1$  and  $C_2$  compounds and their mixtures were conducted at mild overpotentials ( $-0.40$  V *vs.* RHE) in alkaline pH, where the production of multi-carbon products is expected to be boosted.<sup>[141,195]</sup> In the case of aldehydes, which undergo side reactions in alkaline media,<sup>[182]</sup> electrolysis was performed in neutral potassium phosphate buffer (PPB) at  $-1.00$  V *vs.* RHE as the optimum condition for the

production of propylene (**Table A.14**). Comparing production rates (in this chapter instead of *FE*) of the carbon products formed under different conditions would avoid interference of the HER in assessing reactivity. Additional information on the experimental conditions have been reported in **Note A.6**.

#### 4.2.1. Reagents

All reagents used are commercially available: acetaldehyde (33.7  $\mu$ L, 50 mM,  $\geq$  99.5%, Sigma-Aldrich), formaldehyde (113  $\mu$ L, 50 mM, 16% w/v in ultrapure water, methanol-free, Thermo Scientific Pierce), glyoxal (60.8  $\mu$ L, 50 mM, 40 wt.% in H<sub>2</sub>O, Alfa Aesar), sodium oxalate (54 mg, 50 mM, 99.5%, Fluka BioChemika), ethanol (23.4  $\mu$ L, 50 mM, 99.8%, Fischer Chemicals), ethylene glycol (22.4  $\mu$ L, 50 mM, 98+%, Merck), sodium acetate (32.8 mg, 50 mM, 99+%, VWR Chemicals), methanol (16.2  $\mu$ L, 50 mM, Fluka Analytical), carbon monoxide (99.997%, Air Liquide), propionaldehyde (44.6  $\mu$ L, 50 mM, 97 %, Sigma-Aldrich) and allyl alcohol (41.2  $\mu$ L, 50 mM,  $\geq$  99%, Sigma-Aldrich).

#### 4.2.2. Catalyst Preparation and Characterization

Cu foils (99.9%, 15 $\times$ 22 $\times$ 0.3 mm<sup>3</sup>) were individually polished using a sequence of SiC paper (1200  $\mu$ m grit) and alumina suspensions (0.3  $\mu$ m and 0.05  $\mu$ m), after which they were sonicated in water and then in ethanol and finally dried. The foils were submerged in a one-compartment cell containing a freshly prepared electrodeposition bath under a two-electrode configuration. A constant current of 8 mA cm<sup>-2</sup> was applied for 10 min to electrodeposit CuO. A platinum (Pt) wire was used as the counter electrode. The electrodeposition bath was prepared by mixing L-tartaric acid (1.5 g, 99%, Sigma-Aldrich) and copper sulfate pentahydrate (2.5 g,  $\geq$  99%, Sigma-Aldrich) combined in 50 cm<sup>3</sup> deionized water for 10 min, then adding sodium hydroxide (4.0 g, 99.99%, Sigma-Aldrich) to adjust the pH from 1.0 to 13.4. Catalyst characterization was done using XRD, performed with a Siemens 5005 (CuK $\alpha$  radiation with graphite monochromator), in locked  $\theta$ - $2\theta$  scan mode from 20 to 100°  $2\theta$  with 0.1° resolution step and 1 s acquisition per step.

### 4.2.3. Electrochemical Measurements in 0.1 M KOH

The electrocatalytic tests using various reagents were conducted using a three-electrode configuration in a custom-made gas-tight cell consisting of two compartments separated by a Nafion 211 membrane with gas-flow inlet and outlet ports. The cell was mounted with a GDL carbon paper acting as the counter electrode (Sigracet 39BC, SGL Carbon) and a CuO-modified Cu foil electrode (0.49 cm<sup>2</sup>) as the working electrode. Before electrolysis, the working electrode was pre-reduced to OD-Cu for 5 min in pure N<sub>2</sub>-purged electrolyte at -0.60 V *vs.* RHE. A leak-free Ag/AgCl electrode (3 M KCl, model LF-1, Innovative Instruments) served as the reference. The cathodic and anodic compartments contained 8 and 7.8 cm<sup>3</sup> of 0.1 M KOH (pH 13.0), respectively. The catholyte was stirred at 400 rpm. A N<sub>2</sub> flow at a low rate of 2 cm<sup>3</sup> min<sup>-1</sup> was bubbled separately into each compartment to maximize the concentration of the gaseous products, which resulted in a quasi-batch configuration during electrolysis. Both chambers were connected to syringes allowing for a slight expansion of the headspace to minimize pressure variations. The electrochemical measurements were conducted by an Autolab PGSTAT302N potentiostat at rt, with all potential values reported versus the RHE scale. The experiments were carried out with the *i*R compensation function set at 85% of the uncompensated resistance ( $R_u$ ), determined by EIS measurements at high frequency (10 000 Hz).  $R_u$  was calculated every 10 min and used to continuously correct the applied overpotential during the entire 90 min electrolysis. Following this procedure, the applied potentials were within 10 mV of the target potential.

### 4.2.4. Electrochemical Measurements in 0.1 M (K<sub>2</sub>HPO<sub>4</sub> + KH<sub>2</sub>PO<sub>4</sub>)

The electrolysis experiments were performed in an H-type cell separated by an anion-exchange membrane (Selemion AMVN, AGC Asahi Glass). The cell was mounted with the CuO-modified Cu foil electrode (exposed geometric area of 0.785 cm<sup>2</sup>) as the working electrode, Ag/AgCl reference electrode (saturated KCl, Pine), and graphite rod as the counter electrode. Before electrolysis, the working electrode was pre-reduced to OD-Cu for 5 min in pure N<sub>2</sub> purged electrolyte at -0.60 V *vs.* RHE. The cathodic and anodic compartments contained 12 and 8 cm<sup>3</sup> of 0.1 M potassium phosphate buffer (PPB, pH 7.0; 0.062 M K<sub>2</sub>HPO<sub>4</sub> + 0.038 M KH<sub>2</sub>PO<sub>4</sub>), respectively. A N<sub>2</sub> flow of 5 cm<sup>3</sup> min<sup>-1</sup> was separately bubbled into each compartment, with a continuous flow from the cathode chamber into an online GC (Agilent 7890A) for detection of gaseous products. The electrochemical measurement was performed using a Gamry Reference 600

potentiostat/galvanostat at rt and the current interrupt method was used to compensate for the  $iR$  drop throughout the 60 min electrolysis.

#### 4.2.5. Electrochemical Measurements in 0.1 M KHCO<sub>3</sub>

Electrolysis of CO<sub>2</sub> was performed in an H-type cell separated by an anion-exchange membrane (Selemion AMVN, AGC Asahi Glass). The cell was mounted with the CuO-modified Cu foil electrode (exposed geometric area of 0.785 cm<sup>2</sup>) as the working electrode, Ag/AgCl as the reference electrode (saturated KCl, Pine) and graphite rod as the counter electrode. Before electrolysis, the working electrode was pre-reduced to OD-Cu for 5 min in N<sub>2</sub>-purged electrolyte at  $-0.60$  V *vs.* RHE. The cathodic and anodic compartments contained 12 and 8 cm<sup>3</sup> of 0.1 M KHCO<sub>3</sub> (99.99%, Meryer), respectively. CO<sub>2</sub> was bubbled into each compartment at 20 cm<sup>3</sup> min<sup>-1</sup>. The gases in the headspace of the cathode chamber were continuously flowed into an online GC (Agilent 7890A) for the detection of gaseous products. The electrochemical measurement was performed using a Gamry Reference 600 potentiostat/galvanostat at rt and the current interrupt method was used to compensate for the  $iR$  drop throughout the 60 min electrolysis. Linear sweep voltammetry (LSV) was performed in N<sub>2</sub>- and CO<sub>2</sub>- purged 0.1 M KHCO<sub>3</sub> using the same cell setup as CO<sub>2</sub> electrolysis. Before the measurement, the CuO-modified Cu foil was pre-reduced to OD-Cu for 5 min in N<sub>2</sub>-purged electrolyte at  $-0.60$  V *vs.* RHE. The OD-Cu was then used as the working electrode for the LSV measurement. Ag/AgCl (saturated KCl, Pine) was used as the reference electrode and a graphite rod was used as the counter electrode. The electrolyte was purged with N<sub>2</sub> or CO<sub>2</sub> for at least 30 min before being used for experiments. During the measurement, the cell was continuously purged with N<sub>2</sub> or CO<sub>2</sub> at a rate of 20 cm<sup>3</sup> min<sup>-1</sup>. The scan rate used was 5 mV s<sup>-1</sup>. The conditions of  $-0.95$  V *vs.* RHE and 0.1 M KHCO<sub>3</sub> were chosen to maximize the *FE* of C<sub>2+</sub> products using OD-Cu from eCO<sub>2</sub>R.<sup>[169]</sup> As for the co-reduction experiments, a mild potential of  $-0.40$  V *vs.* RHE was applied in an alkaline pH (0.1 M KOH). Such conditions have been linked to increased C–C coupling rates.<sup>[27]</sup> Aldehydes undergo side reactions at alkaline pH, as demonstrated in literature.<sup>[182]</sup> For example, acetaldehyde is not stable in alkaline pH, as it deprotonates to the ethenyloxy anion (CH<sub>2</sub>CHO<sup>-</sup>) which in turn is reactive to competing pathways leading away from C<sub>3</sub> products. Ethenyloxy undergoes aldol condensation with the remaining acetaldehyde to produce crotonaldehyde and 1-butanol. The aldehydes can also be hydrated to form diols, which are electrochemically inactive. Thus, for experiments where aldehydes were used,

a neutral pH buffer (PPB) was used as the supporting electrolyte. Additionally,  $-1.00\text{ V vs. RHE}$  has also been identified as the optimal potential for propylene production from the co-reduction of formaldehyde and acetaldehyde, see **Table A.14**.

#### 4.2.6. Product Analysis

Liquid products formed during electrolysis in 0.1 M KOH were quantified by  $^1\text{H-NMR}$ . Following the reaction, catholyte and anolyte samples ( $0.7\text{ cm}^3$ ) were each mixed with  $\text{D}_2\text{O}$  ( $0.05\text{ cm}^3$ ) containing phenol (50 mM) and dimethyl sulfoxide (50 mM) as internal standards. 1D  $^1\text{H-NMR}$  spectra of the sample with water suppression were recorded on a Bruker Avance III HD 500 MHz mounted with a 5 mm BBO Prodigy (at rt). Pulse experiments were pre-saturated on the water resonance with a  $\pi/2$  pulse of  $12\text{ }\mu\text{s}$  (at a power of 15.9 W, accounting for -12.1 dB) and a recycle delay of 5 s (with pre-set power of  $9.2\cdot 10^{-5}\text{ W}$  accounting for 40.38 dB) was implemented while co-adding 256 scans per experiment. These settings resulted in a high signal-to-noise ratio and an analysis time of *ca.* 35 min per sample. The detection limit is 0.5  $\mu\text{M}$ . Propylene production during electrolysis in 0.1 M KOH was quantified by headspace GC-MS. All GC-MS measurements were conducted using Agilent 7890B (G3440B) GC connected to an Agilent 5977A (G7039A) MS. The 20  $\text{cm}^3$  headspace vials (Agilent 5188-2753 Hdsp cap 18 mm magnetic PTFE/Sil Agilent 5188-2759) were placed in an autosampler (PAL RSI 120 G7368-64100). All separations were carried out using helium carrier gas over an Agilent 121-5522LTM DB column. The detection limit is around 0.1 ppm. Gaseous products formed during electrolysis in 0.1 M PPB and 0.1 M  $\text{KHCO}_3$ , were quantified using on-line GC with flame ionization detector (FID) and thermal conductivity detector (TCD) sampling every 19.6 min. The detection limit is 0.5 ppm, which is equivalent to a production rate of  $0.5\text{ }\mu\text{mol cm}^{-2}\text{ h}^{-1}$ . Alcohols and carbonyl compounds were analyzed by headspace GC (Agilent, 7890B and 7697A). The detection was performed by FID, with a detection limit of 0.2  $\mu\text{M}$ , equivalent to a production rate of  $0.3\text{ mol cm}^{-2}\text{ h}^{-1}$ . HPLC analysis of formate and acetate was conducted using Agilent 1260 Infinity with a variable wavelength detector (VWD), using 0.5 mM sulfuric acid (96% Suprapur, Merck) as the mobile phase. The resulting detection limit is 2  $\mu\text{M}$ , corresponding to a production rate of  $3\text{ mol cm}^{-2}\text{ h}^{-1}$ .

#### 4.2.7. Density Functional Theory

Periodic DFT calculations were performed with the Vienna Ab-initio Simulation Package (VASP)<sup>[196]</sup> and Perdew–Burke–Ernzerhof (PBE)<sup>[186]</sup> density functional including van der Waals

D2 corrections.<sup>[187]</sup> To avoid the over-binding tendency of the D2 method, the reparametrized  $C_6$  coefficients were employed for the metals.<sup>[188]</sup> Core electrons were represented by projector augmented wave (PAW)<sup>[197]</sup> method while valence electrons were expanded in plane waves with a kinetic cut-off energy of 450 eV. The Cu surface was modeled as a four-layer Cu(100) slab, the most stable surface at working potentials.<sup>[147,198]</sup> The Brillouin zone was sampled by a  $\Gamma$ -centered k-points mesh from the Monkhorst-Pack method with a reciprocal grid size smaller than 0.03 Å<sup>-1</sup>. Transition states were identified from the climbing image version of the Nudged Elastic Band (CI-NEB) method.<sup>[192]</sup> All structures were converged by forces, using as thresholds 0.02 eV Å<sup>-1</sup> and 0.05 eV Å<sup>-1</sup> for adsorbates and transition states, respectively. Computed structures are available through the 5 ioChem-BD database.<sup>[199,200]</sup> The solvent was introduced through our in-house developed implicit model, VASP-MGCM.<sup>[189,190]</sup> The Computational Hydrogen Electrode (CHE)<sup>[75,88]</sup> was used as the electrochemical model. Accuracy tests on density functionals (comparing PBE-D2 barriers with BEEF-vdW), LSR, and charge analysis are described in **Note A.7** and **Figure A.34** till **Figure A.37**.

#### 4.2.8. Automatic Generation of Intermediates

Due to the high number of species involved, around 500, the intermediates of the reaction network were automatically generated. Initially the fully hydrogenated C<sub>1</sub>–C<sub>3</sub> species were considered: methane, methanol, formic acid, acetic acid, ethane, ethanol, ethylene glycol, 1-propanol, 2-propanol, 1,2-propanediol, and 1,3-propanediol. The molecules in the previous list were taken as energy references and converted to graphs.<sup>[185]</sup> A graph is when each node represents an atom, labelled with its element, and the edges represent the bonds between atoms, for each structure. These graphs after which they were processed in the following methodological steps:

- 1) A hydrogen node from the graph is selected.
- 2) The hydrogen atom is removed by generating a subgraph without the selected node.
- 3) An isomorphism test is performed to compare the subgraph with the rest of the generated subgraphs thus avoiding chemically equivalent geometries.
- 4) If no equivalent subgraphs are found, the subgraph is stored along with its connection to its mother graph.

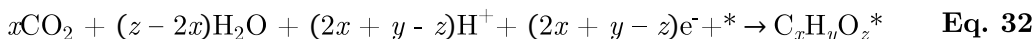


- 5) Repeat the process on the newly generated subgraphs (step 4) until no hydrogen nodes are found in the subgraph.

With the connectivity information, all graphs are then adjusted to their most likely adsorption conformations (see **Note A.6** for additional clarification) and their energies are explicitly evaluated with DFT.

#### 4.2.9. Formation Energies of Intermediates and Transition States

The energies as obtained by VASP were initially written as a function of the clean surface, CO<sub>2</sub>, H<sub>2</sub>O, and H<sup>+</sup> as energy references, **Eq. 32** and **Eq. 33**. Following the CHE formalism, the DFT energy of H<sup>+</sup> ( $E_{\text{H}^+}$ ) at the RHE scale is approximated as  $\frac{1}{2}\text{H}_2$  (as obtained from VASP, **Eq. 34**). The result inside the curly brackets of **Eq. 33** is called DFT energy. Implicit solvation<sup>[189,190]</sup> and polarization corrections ( $\Delta Q_{\text{B}} \cdot U$ )<sup>[191]</sup> were applied to get the potential energies ( $E$ ) used throughout the chapter, see **Eq. 35** (**Eq. 33**). The energy related to electron transfers equals the number of electrons transferred times the electric potential ( $U$ ). Some molecules drag electronic density from the surface; for instance, OH\* has around 8 electrons, obtained from their Bader charges (benchmarked against Mulliken or dipole derived provide similar estimates), instead of the nominal charge of the neutral fragment 7 than would be employed in the standard CHE approach.<sup>[201]</sup> Thus, the external potential contribution, written as  $-(2x+y-z)e^- U$ , requires an additional polarization term  $\Delta Q_{\text{B}} \cdot U$  that has been added as a correction to the DFT energy, **Eq. 35**. To assess the validity of the Bader polarization term, charge estimates were performed with two alternative methodologies, taking derived from the dipole correction and Mulliken population analyses respectively, **Figure A.36** and **Figure A.37**. The tests demonstrate that the choice of Bader charges is reasonable besides easier to implement.



$$E_{\text{C}_x\text{H}_y\text{O}_z^*, \text{DFT}} = E_{\text{C}_x\text{H}_y\text{O}_z^*, \text{VASP}} - E_{*, \text{VASP}} - xE_{\text{CO}_2, \text{VASP}} + (2x-z)E_{\text{H}_2\text{O}, \text{VASP}} + (-2x-y+z)E_{\text{H}^+} + (-2x-y+z)e^- U \quad \text{Eq. 33}$$

Reaction energies and barriers were obtained from **Eq. 36** and **Eq. 37**, where  $E_{\text{IS}}$ ,  $E_{\text{FS}}$ , and  $E_{\text{TS}}$  represent the energies of initial states (IS), final states (FS), and transition states (TS), respectively. As uncertainty in such quantities may affect selectivity trends,<sup>[202–205]</sup> all relevant transition states were explicitly calculated via DFT. These include all 586 C<sub>1</sub>–C<sub>2</sub> couplings and 8 C–H/O–H

hydrogenations and 10 C–O(H) bond breakings from CH<sub>2</sub>CHCHO to 1-propanol and propylene. The remaining energies for C–H and O–H hydrogenations were approximated from LSR available for Cu,<sup>[185]</sup> **Eq. 38** and **Table A.26**. These equations also hold in solvated environments.<sup>[190]</sup> We found that, for C–H and O–H hydrogenation reactions, LSR describe with sufficient accuracy of the DFT results, **Figure A.35**. Differences in Bader charges upon reaction, shown in **Table A.29**, were calculated from **Eq. 39**, and typically ranges between –0.3 to +0.7 e<sup>–</sup> (**Table A.29**). The energy profiles (**Figure A.32**, **Figure A.33**, **Figure A.40** till **Figure A.42**), we considered that all hydrogenations as Tafel-like elementary steps, except from O\* or OH\* stripping, which would involve a Heyrovsky-like step, **Note A.4**.

$$E_{\text{H}^+} = \frac{1}{2} E_{\text{H}_2, \text{VASP}} \quad \text{Eq. 34}$$

$$E = E_{\text{C}_x\text{H}_y\text{O}_z^*} = E_{\text{C}_x\text{H}_y\text{O}_z^*, \text{DFT}} + \Delta Q_{\text{B}} \cdot U + E_{\text{solv}} \quad \text{Eq. 35}$$

$$\Delta E = E_{\text{FS}} - E_{\text{IS}} \quad \text{Eq. 36}$$

$$E_{\text{a}} = \max(E_{\text{IS}}, E_{\text{FS}}, E_{\text{TS}}) - E_{\text{IS}} \quad \text{Eq. 37}$$

$$E_{\text{TS,LSR}} = (1-\alpha)E_{\text{IS}} + \alpha E_{\text{FS}} + \beta \quad \text{Eq. 38}$$

$$\Delta \Delta Q_{\text{B}} = \Delta Q_{\text{B,FS}} - \Delta Q_{\text{B,IS}} \quad \text{Eq. 39}$$

#### 4.2.10. Graph Representation of the Reaction Network

The intermediate generation procedure keeps track of all the dehydrogenation reactions. Additionally, C–C, C–O, and C–OH bond breakings and formations were considered. In a row the following aspects were considered for each intermediate graph: First, they were split into two different fragments (subgraphs) depending on the selected bond breaking. Second, each generated subgraph was compared to closely related subgraphs that showed matching elements from other families. Finally, if an equivalent structure was found, the connection between those subgraphs was stored. The information of the intermediates and their connections were stored in a directed network graph (n-graph).<sup>[206]</sup> In this n-graph, the intermediates correspond to the nodes while the edges represented the reactions.

### 4.3. Results and Discussion

#### 4.3.1. Routes to Main C<sub>1</sub> and C<sub>2</sub> Products and Precursors

The main outcome of previous computational studies on the manually-analyzed network for eCO<sub>2</sub>R to C<sub>1</sub> and C<sub>2</sub> products over Cu(111) or Cu(100) can be summarized as follows:<sup>[95,96,99,183-185]</sup> CO<sub>2</sub> adsorbs on the metal and reduces to CO, a precursor for methanol and methane. Alternatively, CO dimerises to OCCO<sup>-</sup>, which has been claimed to be the rate-determining step in the formation of the C<sub>2</sub> backbone.<sup>[95,96,99,183,184]</sup> On Cu(100), this process is endergonic by 0.84 eV at -0.40 V *vs.* RHE, (with an activation barrier of 1.42 eV), but can be promoted on defective surfaces.<sup>[207]</sup> Additionally, OCCO<sup>-</sup> can be stabilized by electrolyte cations<sup>[208,209]</sup> and the electric field at the cathode.<sup>[191,209,210]</sup> OCCO<sup>-</sup> is further protonated and then dehydrated to CCO upon a proton-coupled electron transfer step. The latter intermediate is subsequently hydrogenated to CH<sub>2</sub>CHO.<sup>[27,77]</sup> If hydrogenolysis occurs on the remaining O atom, CH<sub>2</sub>CH is formed, leading to ethylene. If hydrogenation occurs on the α-C (CαH<sub>2</sub>CHO), ethanol is formed (**Figure A.32** and **Figure A.33**).

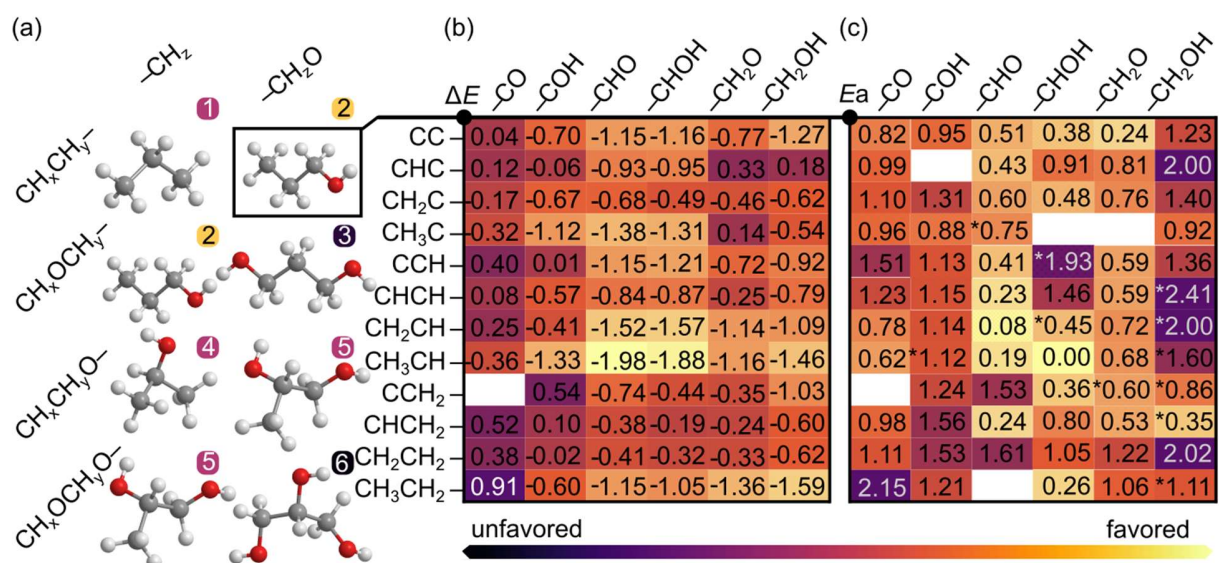


**Figure 4.3.** Screening process to narrow down the C<sub>1</sub>-C<sub>2</sub> coupling steps. (a) C<sub>x</sub>H<sub>y</sub>O<sub>z</sub> backbones that can be obtained through C<sub>1</sub>-C<sub>2</sub> couplings (only the fully hydrogenated product is shown). The numbers label six families of molecules and the color stands for their abundance reported in literature. (b) and (c) Show reaction and activation energies for CH<sub>x</sub>CH<sub>y</sub>-CH<sub>z</sub>O couplings between C<sub>2</sub> hydrocarbon and C<sub>1</sub> oxygenate, depicted in ΔE and E<sub>a</sub>.

### 4.3.2. Exploring C<sub>1</sub>–C<sub>2</sub> Coupling Reactions

To unravel the most likely reaction routes towards C<sub>3</sub> backbone formation, a sequential analysis combining available reports, experiments and theory was applied. The possible C<sub>1</sub>–C<sub>2</sub> couplings shown in **Figure 4.3a** and **Table A.27** till **Table A.29** emerge from combining 10 C<sub>1</sub> (–CH<sub>x</sub>O\* or –CH<sub>x</sub>\*) and 70 C<sub>2</sub> precursors that can be hydrocarbons (CH<sub>y</sub>CH<sub>z</sub>\*–) or oxygenates (CH<sub>y</sub>OCH<sub>z</sub>O\*–, CH<sub>y</sub>OCH<sub>z</sub>\*–, CH<sub>y</sub>CH<sub>z</sub>O\*–). This gives rise to oxygenate-to-oxygenate, hydrocarbon-to-oxygenate, and hydrocarbon-to-hydrocarbon C–C coupling reactions. Thus, six families of intermediates, namely C<sub>3</sub>H<sub>x</sub>, 1-C<sub>3</sub>OH<sub>x</sub>, 1,3-C<sub>3</sub>O<sub>2</sub>H<sub>x</sub>, 2-C<sub>3</sub>OH<sub>x</sub>, 1,2-C<sub>3</sub>O<sub>2</sub>H<sub>x</sub> and 1,2,3-C<sub>3</sub>O<sub>3</sub>H<sub>x</sub>,  $x = 0-8$  (families **1–6** in **Figure 4.3a**) are formed, where the prefix numbers show the position of the oxygenated functional group, irrespective of it having alcohol, alkoxy, aldehyde, or ketone character. Molecular fragments with carboxylate, carboxylic acid, ethers, or cyclic backbones were not considered, as these functionalities have not been found experimentally in the pool of C<sub>3</sub> products. The C<sub>3</sub> products formed from the electrolysis of mixtures of CO with different C<sub>2</sub> molecules (glyoxal, ethylene glycol, oxalate, acetate, ethanol, acetaldehyde) were compared at OCP and –0.40 V and –1.00 V *vs.* RHE (**Figure 4.2**, **Table A.17**, **Table A.19** and **Table A.20**). At –0.40 V *vs.* RHE, all these mixtures generate 1-propanol at rates much larger than the reduction of CO alone (**Table A.16**). Mixtures with ethylene glycol gave the highest yield, while those with ethanol and acetate gave the lowest. Propylene was not detected (detection limits of gaseous products are equivalent to 0.5 μmol cm<sup>–2</sup> h<sup>–1</sup>, see **Section 4.2.6**). Overall, if a set of products with a given C<sub>x</sub>O<sub>y</sub> backbone is not observed experimentally, then such couplings can be considered unlikely, and the routes pruned from the network. To further verify the nature of the active C<sub>1</sub> fragment leading to 1-propanol, electrocatalytic tests of the C<sub>2</sub> compounds with either methanol or formaldehyde (**Figure 4.2**) were conducted. 1-propanol was not detected in some of these experiments, though allyl alcohol and propylene were observed from the electrolysis of a formaldehyde and acetaldehyde mixture. Moreover, the reduction of CH<sub>2</sub>O itself produced only CH<sub>3</sub>OH and CH<sub>4</sub> (**Figure 4.2** and **Table A.16**), but it does not produce C<sub>2</sub> and C<sub>3</sub> compounds as it is hardly broken into the more reactive CH<sub>2</sub>\* and CHO\* species (**Table A.33**). CH<sub>3</sub>OH, on the other hand, was electrochemically inert (**Table A.23** and **Table A.24**). The unique predominance of 1-propanol in experiments using CO indicates that CO\* (or a derivative like CHO\*) is instrumental in promoting 1-propanol formation. This is further confirmed by the

absence of 1-propanol in experiments starting with  $\text{CH}_2\text{O}$  or  $\text{CH}_3\text{OH}$  (**Figure 4.2**). After considering the experimental input, there was a switch to theory to explore the  $\text{C}_1$ - $\text{C}_2$  coupling reactions based on the reaction energies ( $\Delta E$ , **Table A.27**), activation energies obtained by DFT-NEB ( $E_a$ , **Table A.28**), and complemented by the electrochemical driving force computed as the polarization variation upon reaction ( $\Delta\Delta Q_B$  in **Eq. 39**, **Table A.29**). The most likely coupling candidates were then selected among all couplings, which reduced the set to  $\text{CH}_2\text{CH-CHO}$  and  $\text{CH}_3\text{CH-CHO}$ . In the following paragraphs, we describe how the different coupling families are retained or discarded during the analysis of the network based on abovementioned literature, experimental, and theoretical analyses:

### 4.3.3. 1,2,3- $\text{C}_3\text{O}_3\text{H}_x$ Backbone

Early computational studies proposed that the  $\text{C}_3$  backbone was formed via trimerization of  $\text{CO}^*$ <sup>[211,212]</sup> (**6** in **Figure 4.3a**, 1,2,3- $\text{C}_3\text{O}_3\text{H}_x$ ). When computing this potential reaction, relatively high activation barrier of  $E_a = 0.96$  eV was found. Furthermore, the  $\text{CO}$ -trimer reverts  $0.14 e^-$  to the surface, so the net reaction is therefore expected to be hindered under reductive potentials (**Table A.30**). Alternatively, a sequential process can be envisaged where  $\text{CO}$  dimerises to  $\text{OCCO}^-$ , which further reacts with  $\text{CHO}$  ( $E_a = 0.73$  eV,  $\Delta\Delta Q_B = -0.81 e^-$ ), or  $\text{COCHO}$  with  $\text{CO}$  ( $E_a = 0.78$  eV,  $\Delta\Delta Q_B = -0.39 e^-$ ) to form  $\text{COCOCO}$  as the base of the 1,2,3- $\text{C}_3\text{O}_3\text{H}_x$  backbone. Only the latter reaction would be promoted at more reducing potentials. However, should this reaction occur, glycerol would likely appear as a product of  $\text{CO}_2$  reduction, but this has not been reported in the literature. Thus, the absence of glycerol as a product combined with the medium to high computed barriers and electrochemical penalties suggest that 1,2,3- $\text{C}_3\text{O}_3\text{H}_x$  (**6** in **Figure 4.3a**) intermediates are unlikely to participate in the main mechanistic route.

### 4.3.4. 1,2- $\text{C}_3\text{O}_2\text{H}_x$ and 1,3- $\text{C}_3\text{O}_2\text{H}_x$ Backbones

There are two families of  $\text{C}_3\text{O}_2\text{H}_x$  intermediates, with O atoms in different positions: 1,2- $\text{C}_3\text{O}_2\text{H}_x$  (**5**, in **Figure 4.3a**) and 1,3- $\text{C}_3\text{O}_2\text{H}_x$  (**3**, **Figure 4.3a**). Among the products derived from 1,2- $\text{C}_3\text{O}_2\text{H}_x$ , only 1-hydroxyacetone has been reported in the literature, albeit in trace quantities.<sup>[26]</sup> Indeed, some  $\text{CH}_x\text{CH}_y\text{O}^*-\text{CH}_2\text{O}^*$  pairs have low coupling barriers, such as the coupling of  $\text{CH}_2\text{CO}$ ,  $\text{CH}_3\text{CO}$ , and  $\text{CH}_3\text{COH}$  with  $\text{CHO}$  (up to 0.32 eV, **Table A.28**). Remarkably, the  $\text{CHO}$  coupling is expected to be strongly promoted under reductive potentials ( $\Delta\Delta Q_B = -0.52 e^-$ , **Table A.29**). However, these  $\text{C}_2$  intermediates have higher potential energies than other structural isomers

(**Figure A.33**). As such, their concentration is expected to be too low at  $-0.40$  V *vs.* RHE to form any significant amount of 1,2-C<sub>3</sub>O<sub>2</sub>H<sub>*x*</sub> products, as confirmed by the range of products observed in our experiments (**Table A.19** till **Table A.24**). The formation of 1,3-C<sub>3</sub>O<sub>2</sub>H<sub>*x*</sub> products is expected to proceed from CH<sub>2</sub>OCH–CHO(H) ( $E_a \leq 0.34$  eV) or CH<sub>2</sub>OHCH–CHO ( $E_a < 0.16$  eV). These reactions would occur as chemical steps and are not favored under eCO<sub>2</sub>R conditions (according to computational charge considerations, **Table A.29**). Our simulation results may also explain why 1,3-C<sub>3</sub>O<sub>2</sub>H<sub>*x*</sub> products (3-propanediol and 3-hydroxypropanal) have not been experimentally observed for Cu-based catalysts.

#### 4.3.5. 2-C<sub>3</sub>OH<sub>*x*</sub> Backbone via H<sub>*x*</sub>C<sub>1</sub>–C<sub>2</sub>H<sub>*y*</sub>O Coupling

The paths generating mono-oxygenated C<sub>3</sub> intermediates are next to consider. 2-C<sub>3</sub>OH<sub>*x*</sub> products can be produced from the coupling of a CH<sub>*x*</sub>CH<sub>*y*</sub>O\*– fragment, such as CH<sub>3</sub>CHO\*– and CH<sub>2</sub>CHO\*–, with a C<sub>1</sub> hydrocarbon, –CH<sub>*x*</sub>\* (**4** in **Figure 4.3a**). This pathway may expectedly yield 2-propanol, which is 0.17 eV more stable than 1-propanol (as mentioned in the introduction), whereas intermediates leading to these two species show similar stabilities (**Figure A.38**). However, 2-propanol was not experimentally detected (**Figure 4.2**). Previous experiments on Cu-based catalysts have only detected small amounts of acetone,<sup>[26]</sup> in line with our present results ( $FE = 0.2\%$ , **Figure 4.1**). Acetone is likely produced by coupling CH<sub>3</sub>CO with CH<sub>2</sub>, ( $\Delta E = -1.57$  eV;  $E_a = 0.28$  eV) and the further hydrogenation of the unsaturated aliphatic carbon atom.

#### 4.3.6. 1-C<sub>3</sub>OH<sub>*x*</sub> Backbone

Most of the C<sub>3</sub> products detected in our experiments belong to the 1-C<sub>3</sub>OH<sub>*x*</sub> family (**2** in **Figure 4.3a**), namely 1-propanol (CH<sub>3</sub>CH<sub>2</sub>CH<sub>2</sub>OH, 1-C<sub>3</sub>OH<sub>8</sub>), with propionaldehyde (CH<sub>3</sub>CH<sub>2</sub>CHO, 1-C<sub>3</sub>OH<sub>6</sub>) and allyl alcohol (CH<sub>2</sub>CHCH<sub>2</sub>OH, 1-C<sub>3</sub>OH<sub>6</sub>) produced at smaller rates (**Figure 4.2**).<sup>[21,26]</sup> Considering the experimentally observed scarcity of C<sub>3</sub>O<sub>2</sub>H<sub>*x*</sub> and C<sub>3</sub>O<sub>3</sub>H<sub>*x*</sub> products, it was concluded that there is only one oxygen atom present during the coupling, either on the C<sub>1</sub> or the C<sub>2</sub> moiety. Reported experiments<sup>[23,172,213,214]</sup> show that during eCO<sub>2</sub>R, the maximum production of 1-propanol occurs when high amounts of CO and C<sub>2</sub>H<sub>4</sub> are formed simultaneously. Indeed, the lowest activation barriers are found for the highly exothermic CH<sub>2</sub>CH–CHO and CH<sub>3</sub>CH–CHO(H) couplings ( $\Delta E < -1.50$  eV,  $E_a \leq 0.19$  eV, **Figure 4.3b and c**).

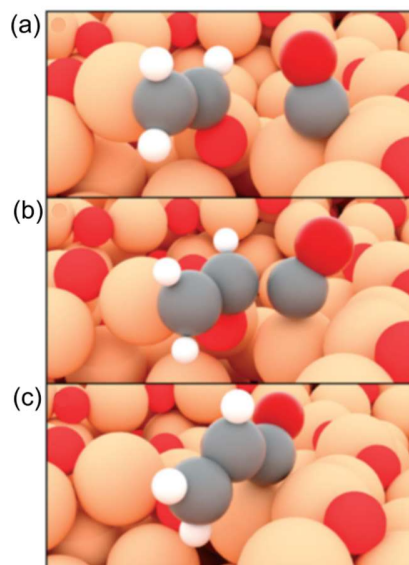


**Figure 4.4.** CH<sub>2</sub>CHO–CO coupling on OD-Cu models.<sup>[207]</sup> (a) The Initial state, (b) the transition state, (c) the final state of key bonding step between C<sub>1</sub> oxygenate and C<sub>2</sub> oxygenate. Additionally, a surface cavity with high oxygen affinity assists the C–O bond breaking of the CH<sub>2</sub>CHO\* precursor prior to bonding weakly adsorbs the CO through a neighbouring Cu<sup>δ+</sup>, polarized site.

As CH<sub>2</sub>CH\* is a precursor of C<sub>2</sub>H<sub>4</sub>, and CHO(H)\* is directly formed from CO, it can be concluded that all such paths are highly likely to occur. Couplings involving C<sub>2</sub> moieties less hydrogenated than CH<sub>2</sub>CH or CH<sub>2</sub>-CHO (another C<sub>2</sub>H<sub>4</sub> precursor) are therefore less likely. In the remaining region, most C<sub>1</sub>–C<sub>2</sub> couplings are highly activated (**Figure 4.3c**). Thus, CH<sub>2</sub>CHCHO\* and CH<sub>3</sub>CHCHO\* intermediates are common precursors for C<sub>3</sub> products. To a lesser degree, CH<sub>2</sub>CHCO\* can also be formed if the coupling starts with –CO instead of –CHO, **Figure 4.4**. Finally, reactions involving C<sub>2</sub> oxygenated precursors (**Table A.27** till **Table A.29**) have higher barriers, such as the CH<sub>2</sub>–CCH<sub>2</sub>O coupling (while the process is exothermic,  $\Delta E = -1.61$  eV, the activation barrier,  $E_a = 0.39$  eV cannot be neglected). Upon reaction, part of the electronic density of CH<sub>2</sub>CHCHO\* is returned to the surface ( $-0.30 e^-$ ). The reaction is therefore not favored at strongly reductive potentials, which explains the decrease in 1-propanol production as the potential becomes more negative.<sup>[26,27]</sup> The activation barriers of the transition states associated with the formation of key C<sub>3</sub> intermediates are sensitive to surface geometry and ensembles. Since defective Cu surfaces have been reported as selective to 1-propanol formation,<sup>[211,214]</sup> the role of defects on OD-Cu models<sup>[207]</sup> was assessed for the concerted coupling of CH<sub>2</sub>CH(O)\*–CO\* to yield the simplest C<sub>3</sub> precursor, CH<sub>2</sub>CHCO, **Figure 4.4**. The Cu and CuO<sub>x</sub> structures were optimized for

10 ps through ab initio molecular dynamics and recurrent morphological motifs occurred upon surface reconstruction.<sup>[207]</sup> Out of twelve surface motifs assessed (**Figure A.39**),<sup>[207]</sup> an active site consisting of a surface cavity (**Figure 4.4a, center**) and a neighboring Cu<sup>δ+</sup> atom (**Figure 4.4a, right**) is the most suitable for promoting the coupling. While CH<sub>2</sub>CHO\* is trapped at the surface cavity, the high oxygen affinity of this site leads to the breaking of its C–O bond to give CH<sub>2</sub>CH\* (**Figure 4.4b**). On the other hand, CO adsorption is almost thermoneutral on the polarized copper site. Thus, the CH<sub>2</sub>CH\* fragment can easily couple to the weakly bound CO\* to form the C<sub>3</sub> backbone (exergonic by 0.13 eV; **Figure 4.4c**). In absence of polarized Cu sites (**Figure A.39**), this step is endergonic by at least 0.6 eV, thus confirming the instrumental role of surface polarization. This coupling mechanism may explain the high selectivity toward 1-propanol (*FE* = 23% at –0.44 V *vs.* RHE) achieved on highly defective Cu surfaces containing a large number of surface cavities.<sup>[103,211,214]</sup> This concept can be extended to other key C<sub>1</sub>–C<sub>2</sub> coupling reactions from moieties directly derived from CH<sub>2</sub>CHO and CO, such as CH<sub>2</sub>CH–CHO and CH<sub>3</sub>CH–CHO. Going beyond pure copper catalysts, it was proposed that intermetallic alloys containing high oxygen affinity elements coupled with weak CO binding sites could be highly selective to C<sub>3</sub> as well. For instance, Cu–Ag alloys exhibited enhanced propanol selectivity depending on the silver atomic ratio,<sup>[105,215]</sup> suggesting a CO spillover mechanism from Ag domains to facilitate the formation of CH<sub>2</sub>CH–CO.

#### 4.3.7. Routes to C<sub>3</sub> Products: 1-Propanol and Propylene

Once the C<sub>3</sub> backbone is formed, the C<sub>3</sub> subnetwork (**Figure 4.5**) starting from CH<sub>2</sub>CHCHO\* (orange) and CH<sub>2</sub>CHCO\* (black) can be employed to analyze selectivity trends. The color code of the boxes in **Figure 4.5** represents the computed relative stability of the intermediates (thermodynamics), while the thickness of the lines linking the intermediates accounts for the barriers (thicker lines stand for faster steps). The hydrogenation of CH<sub>2</sub>CHCO\* gives CH<sub>2</sub>CHCHO\*, which then evolves via CH<sub>3</sub>CHCHO\* → propionaldehyde (CH<sub>3</sub>CH<sub>2</sub>CHO\*) → propanoxy (CH<sub>3</sub>CH<sub>2</sub>CH<sub>2</sub>O\*) → 1-propanol. The existence of this path is confirmed experimentally, since the electrochemical reduction of propionaldehyde on OD-Cu yielded predominantly 1-propanol (**Figure 4.6c, Table A.34**). Alternatively, the 1-propanol formation can proceed through CH<sub>2</sub>CH<sub>2</sub>CO\* → CH<sub>2</sub>CH<sub>2</sub>CO\*H → CH<sub>3</sub>CH<sub>2</sub>COH\* → CH<sub>3</sub>CH<sub>2</sub>CHOH\* → 1-propanol (bottom path in **Figure 4.5**, and **Figure 4.6a**).



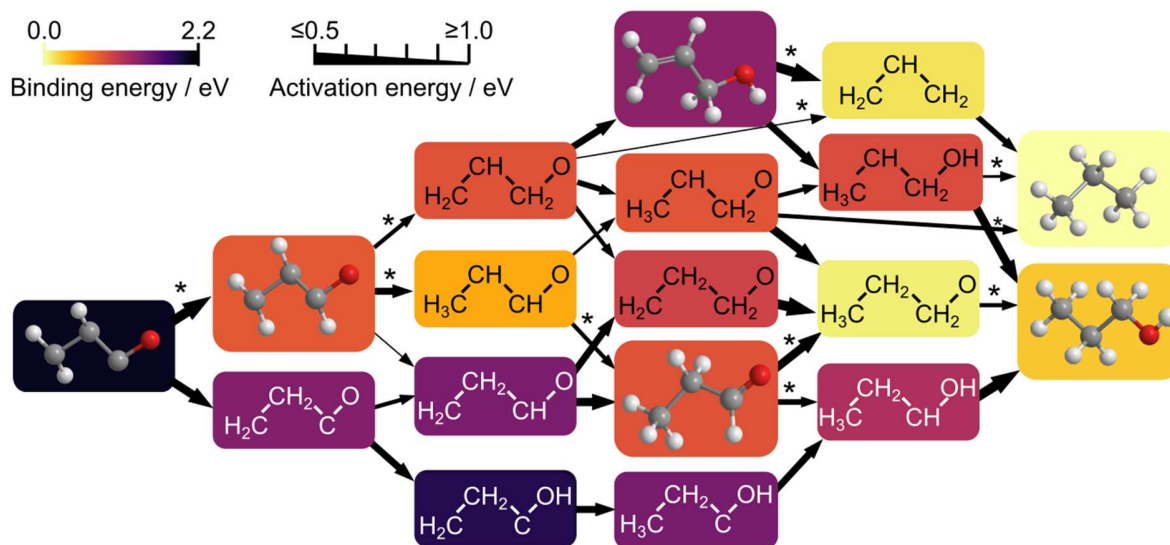


**Figure 4.5.** Computed subnetwork for  $\text{CH}_2\text{CHCO}$  and  $\text{CH}_2\text{CHCHO}$  conversion to propylene ( $\text{C}_3\text{H}_6$ ) and 1-propanol ( $\text{C}_3\text{H}_7\text{OH}$ ) at  $-0.40\text{ V vs. RHE}$  (full network in **Figure A.40** till **Figure A.42**). The colors of the boxes scale with the relative DFT energy of their intermediates and relevant intermediates are drawn in 3D. The thickness of the arrows connecting the intermediates account for the  $E_a$ , obtained by LSR (those obtained explicitly by DFT are denoted by \*).

Mono-oxygenates can be converted to propylene via dehydration reactions starting from  $\text{CH}_2\text{CHCO}(\text{H})^*$ ,  $\text{CH}_2\text{CHCHO}(\text{H})^*$ ,  $\text{CH}_3\text{CHCHO}(\text{H})^*$ ,  $\text{CH}_2\text{CHCH}_2\text{O}(\text{H})^*$ , and  $\text{CH}_3\text{CHCH}_2\text{O}(\text{H})^*$ , where (H) represents an optional hydrogen. The corresponding barriers of these ten reactions were computed (**Table A.31**). Most C–O(H) bonds are relatively difficult to activate ( $E_a > 1.00\text{ eV}$ ), thus, the ones showing relatively lower barriers ( $\text{CH}_2\text{CHCH}_2\text{–OH}^*$  and  $\text{CH}_3\text{CHCH}_2\text{–OH}^*$ ,  $E_a = 0.17\text{ eV}$  and  $0.94\text{ eV}$ , respectively) are depicted in **Figure 4.6a** and **b**. A selectivity switch to propylene occurs when the aldehyde carbon on  $\text{CH}_2\text{CHCHO}^*$  is hydrogenated to form  $\text{CH}_2\text{CHCH}_2\text{O}^*$ , which in turn produces allyl alcohol ( $\text{CH}_2\text{CHCH}_2\text{OH}$ ). To generate propylene, OH is eliminated from the allyl alcohol intermediate, which is then hydrogenated (**Figure 4.6b**). However, this path is not fully selective, as allyl alcohol can also undergo hydrogenation to  $\text{CH}_3\text{CHCH}_2\text{OH}^*$  to form 1-propanol. The C–OH bond breaking in allyl alcohol ( $\text{CH}_2\text{CHCH}_2\text{OH}$ ) has a low barrier of  $0.17\text{ eV}$  and it is strongly promoted by reducing potentials, with a net charge gain of  $0.87\text{ e}^-$  (**Table A.31** and **Figure 4.6b**). Therefore, the production of propylene could be

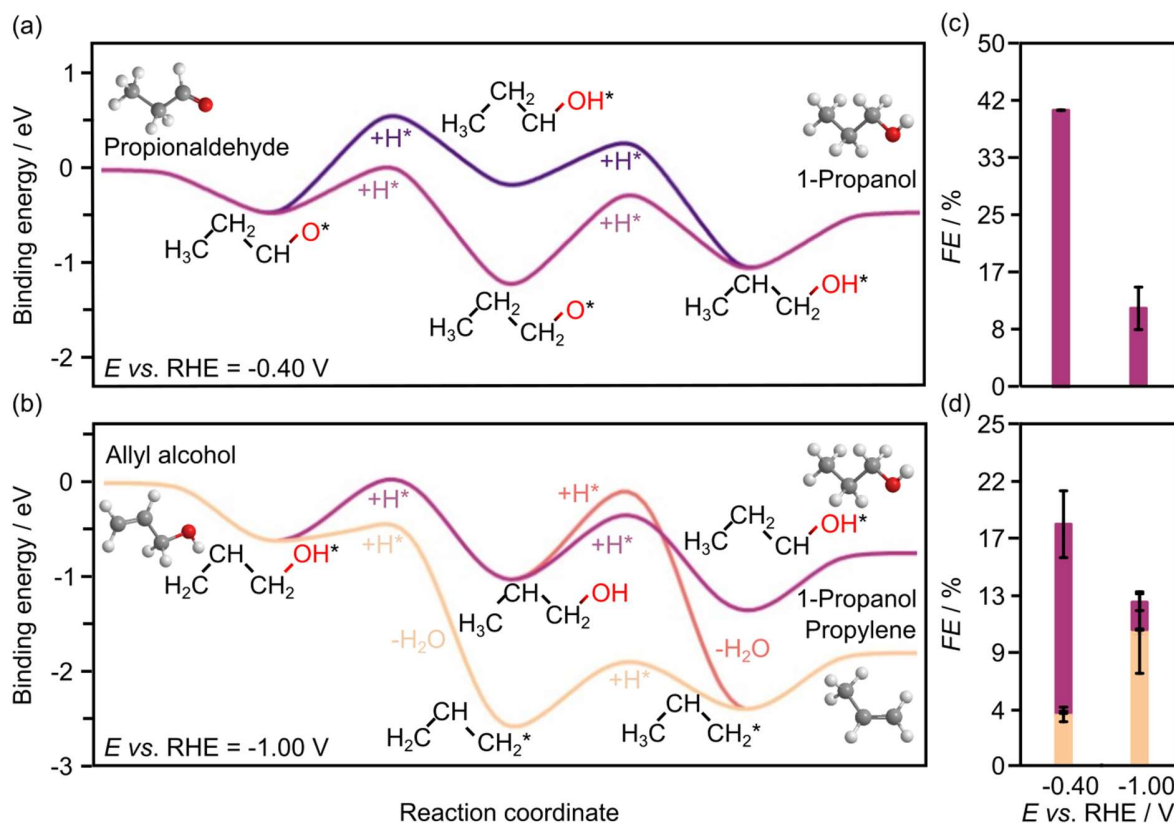


**Figure 4.6.** Energy profiles for electrocatalytic reduction of (a) propionaldehyde and (b) allyl alcohol in most relevant conditions are shown while all the other energy profiles can be found in **Figure A.43** till **Figure A.45** (energy reference shifted to zero, based on Cu(100) using H<sub>2</sub>, CO<sub>2</sub>, and H<sub>2</sub>O as thermodynamic sinks) Detailed DFT values can be found in **Table A.31** and **Table A.32**. Corresponding experimental results of electrocatalytic reduction of (c) propionaldehyde and (d) allyl alcohol are shown here with full product distributions shown in **Table A.34** and **Table A.35**. Showing the formation of 1-propanol (purple) and propylene (orange) while the (\*) symbol refers to species adsorbed on the surface.

traced to the allyl alkoxy (CH<sub>2</sub>CHCH<sub>2</sub>O) intermediate, which is also a direct precursor of allyl alcohol. This proposition was verified experimentally by reducing allyl alcohol on OD-Cu (**Figure 4.6d**), which gave noticeable amounts of propylene as theoretically predicted. Moreover, allyl alcohol (1.97 μmol cm<sup>-2</sup> h<sup>-1</sup>) was detected alongside propylene (1.44 μmol cm<sup>-2</sup> h<sup>-1</sup>) from the reduction of a mixture of acetaldehyde and formaldehyde (**Figure 4.2**). In this combination, the most likely path occurs when acetaldehyde loses an acidic α-hydrogen (H<sub>α</sub>-CH<sub>2</sub>CHO)<sup>[182]</sup> to form CH<sub>2</sub>CHO, which dehydrates to form CH<sub>2</sub>CH. The latter compound reacts with CH<sub>2</sub>O to form CH<sub>2</sub>CHCH<sub>2</sub>O\* (**Figure 4.5** and **Figure A.40** till **Figure A.42**) which is mainly selective towards allyl alcohol and propylene, but not 1-propanol (**Figure 4.2**). Interestingly, it can be

noted that CO<sub>2</sub> reduction produced 1-propanol ( $FE = 4.4\%$ ) and allyl alcohol ( $FE = 1.2\%$ ) (**Figure 4.1**), while propylene was absent. This can be rationalized by a mild eCO<sub>2</sub>R interface alkalization, which occurs under reaction conditions, favoring the desorption of allyl alkoxy (protonated in solution into allyl alcohol) and thus preventing propylene synthesis.

## 4.4. Conclusions

In conclusion, an integrated mechanistic analysis of the eCO<sub>2</sub>R to C<sub>3</sub> products was performed with all the individual steps available in the open database. Methodological implementations including structural graph network generation, fast energy screenings, and network pruning of irrelevant paths through experimental input allow the effective sampling of the complex C<sub>3</sub> network pointing out the difficulties found when only a part of the reaction network is sampled.<sup>[216]</sup> C<sub>2</sub> and C<sub>3</sub> products were found to share a common precursor, CH<sub>2</sub>CHO\*. Our findings rationalize the generally observed low selectivity of eCO<sub>2</sub>R toward C<sub>3</sub> products, as well as their enhancement on nanostructured Cu catalysts: (i) C<sub>3</sub> backbones are formed via the sluggish coupling of CO or CHO with CH<sub>2</sub>CH\*, preferentially at defects. (ii) All C<sub>3</sub> precursors end up containing at least one O atom, *i.e.*, CH<sub>*x*</sub> + C<sub>2</sub>H<sub>*y*</sub> couplings are highly unlikely. The most stable mono-oxygenated intermediate CH<sub>2</sub>CHCHO\* gives access to propylene, propionaldehyde, and 1-propanol. The inaccessible allyl alkoxy intermediate is identified as the most likely kinetic trap preventing propylene production as indicated by simulations and further reinforced with the electrolysis of allyl alcohol leading to propylene. Our mechanistic understanding paves the way towards the development of advanced electrocatalysts that promote C<sub>3</sub> products, particularly alkenes.

## Chapter 5

# Electrochemical Reduction of Carbon Dioxide to 1-Butanol on Oxide-Derived Copper

### 5.1. Introduction

The eCO<sub>2</sub>R to fuels and chemicals, when powered by renewable electricity, is a potentially sustainable way to alleviate our pressing global energy demands and to avert climate change.<sup>[217]</sup> Copper-based materials are the only family of catalysts that can reduce CO<sub>2</sub> to C<sub>2+</sub> molecules with significant *FE* and *j*.<sup>[51,141]</sup> Among the multi-carbon products, C<sub>2</sub> molecules such as ethylene and ethanol can be facilely formed (*FE* = 30–50%).<sup>[26,51]</sup> The main C<sub>3</sub> product reported is 1-propanol (*FE* = 20–23%),<sup>[39]</sup> alongside small quantities of propionaldehyde, allyl alcohol, acetone, propylene and propane.<sup>[26,57]</sup> Reports on the formation of C<sub>4</sub> molecules, many of which with much higher commercial value, are scarce and have been limited to hydrocarbons showing a *FE* of < 1%.<sup>[41]</sup> The drastic decrease in the selectivity upon increase of the number of carbon atoms suggests that the coupling mechanism to form C<sub>2+</sub> products follows a ‘polymerization’ scheme of CO\* that obeys the Flory-Schulz distribution.

Interestingly, the direct production of 1-butanol (C<sub>4</sub>H<sub>9</sub>OH) from eCO<sub>2</sub>R has not been reported. This oxygenate, which has a high volumetric energy density and is less hygroscopic and corrosive than ethanol, has been suggested for direct use as a fuel or in diesel-blends.<sup>[218]</sup> Schmid *et al.*<sup>[219]</sup> have utilized bacteria to convert CO (generated from CO<sub>2</sub> electrolysis) to 1-butanol. More recently, a mechanistic study of CO<sub>2</sub> reduction to 1-propanol revealed that minor and yet-to-be-quantified amounts of 1-butanol can be co-produced from the electrochemical reduction of acetaldehyde and CO in 0.1 M KOH on OD-Cu electrodes.<sup>[153]</sup> Still, no strategy to successfully electro-synthesize 1-butanol or any C<sub>4</sub> oxygenate from CO<sub>2</sub> has been conceived. To tackle this challenge, it is crucial to understand and map out the mechanism and kinetics for its formation.

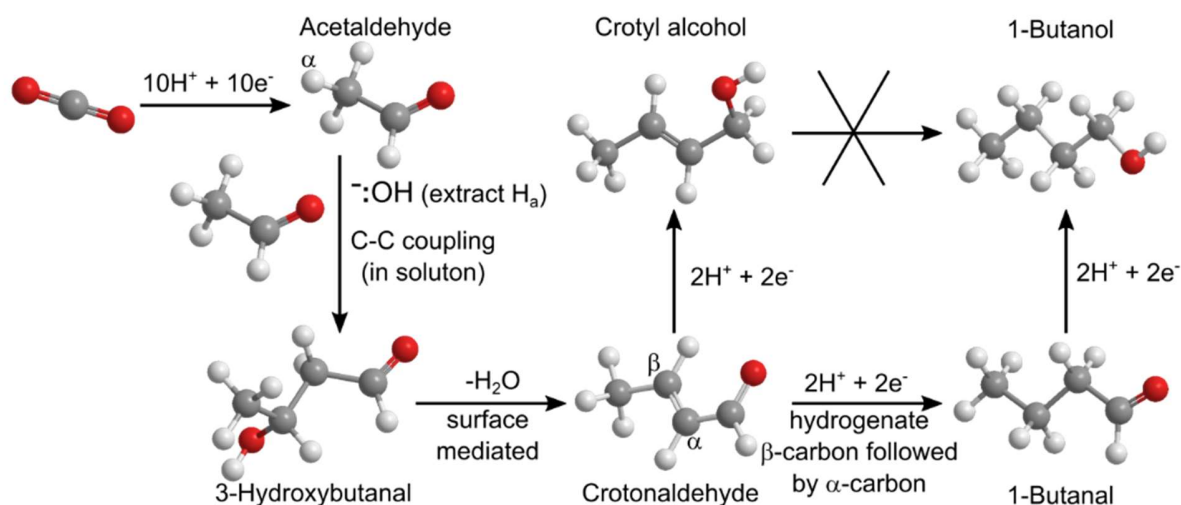


**Figure 5.1.** Simplified reaction scheme for CO<sub>2</sub> reduction to 1-butanol. Further details are provided in Note A.8.

Herein, for the first time the formation of C<sub>4</sub> oxygenates is reported from alkaline electrolysis of CO<sub>2</sub> using OD-Cu GDE in a flow cell. The predominant C<sub>4</sub> product was 1-butanol ( $FE = 0.056\%$ ,  $j = -0.080 \text{ mA cm}^{-2}$ ) at  $-0.48 \text{ V vs. RHE}$ . The reaction mechanism was elucidated by combining analyses of reaction products from electrolysis of possible intermediates combined to DFT investigations. The formation of the critical C<sub>4</sub> intermediate, crotonaldehyde (C<sub>2</sub>H<sub>4</sub>=C<sub>2</sub>H<sub>2</sub>O), was traced to the aldol condensation (C-C bond formation) of two acetaldehyde (CH<sub>3</sub>CHO) molecules generated from eCO<sub>2</sub>R (**Figure 5.1**). The aldol reaction is promoted by both OH<sup>-</sup> ions in the electrolyte and the electrocatalyst surface, creating crotonaldehyde which then undergoes a two-step electroreduction to 1-butanol. In this process the critical role of pH at different stages of the reaction mechanism is pointing towards new strategies for increasing the performance of electro-assisted conversion of CO<sub>2</sub> into 1-butanol.

## 5.2. Experimental

### 5.2.1. Catalysts and Anode Preparation

A homogeneous Cu layer was deposited on GDLs, (Sigracet 38 BC) by magnetron sputtering using a Denton Vacuum Discovery 18 system. RF sputtering at 100 W was performed while operating under 10 mTorr pressure and 13 cm<sup>3</sup> min<sup>-1</sup> argon. The distance between the Cu target (> 99.99%, Latech Scientific Supply) and the substrate was 10.16 cm. The deposited Cu layer aided in the subsequent electrodeposition process by ensuring uniform conductivity and decreased the

hydrophobicity of the GDL. The electrodeposited CuO was prepared according to a previously published method.<sup>[169]</sup> The electrodeposition bath, which had a pH of 13.0, consisted of 30 g L<sup>-1</sup> L-tartaric acid (> 99%, Sigma-Aldrich), 50 g L<sup>-1</sup> CuSO<sub>4</sub>·5 H<sub>2</sub>O (99%, GCE) and 70 g L<sup>-1</sup> NaOH (99.0%, GCE). A constant current of at +8 mA cm<sup>-2</sup> was applied to electrodeposit CuO onto the Cu-sputtered GDLs (10 min). Prior to electrolysis, the electrodeposited CuO films were pre-reduced to OD-Cu for 5 min in pure N<sub>2</sub>-purged electrolyte at -0.60 V *vs.* RHE.

Cu discs (99.99%, 15 mm diameter, Goodfellow) were sequentially polished with SiC paper (1200 μm, Struers), followed by 15 μm and 3 μm Diapro slurries (Struers). The discs were then sonicated in ultrapure deionized water and dried with nitrogen gas. CuO was electrodeposited onto the polished Cu discs with the above-mentioned procedure for 30 min. The pre-reduction treatment was applied as described above.

IrO<sub>2</sub> GDEs were used as anodes in the flow cells. IrO<sub>2</sub> nanoparticles were synthesized following a previously published procedure.<sup>[220]</sup> The synthesized colloidal suspension of IrO<sub>2</sub> was centrifuged at 5000 rpm for 20 min, washed twice with ultrapure water by centrifugation, dried overnight at 373 K in air and ground into a fine powder. IrO<sub>2</sub> nanoparticles (30 mg) were dispersed by sonication in a solution containing 400 μL ultrapure deionized water, 400 μL 2-propanol (≥ 99.5%, Avantor) and 13.4 μL Nafion perfluorinated resin solution (5 wt.% in lower aliphatic alcohols and water, Sigma-Aldrich) to obtain a homogenized ink. This ink was hand-painted onto a GDL (9 cm<sup>2</sup> geometric area) and dried using a heat lamp.

### 5.2.2. Catalyst Characterization

Scanning electron microscopy (SEM) was performed using a JEOL JSM-6701F instrument. XRD patterns were acquired by a Siemens 5005 instrument (CuKα radiation with graphite monochromator), in a locked  $\theta$ - $2\theta$  scan mode from 15° to 100°  $2\theta$  with 0.1° resolution step and 1 s acquisition time per step. XPS signals were acquired using a Physical Electronics Quantum 2000 instrument. The applied monochromatic Al Kα radiation (1486.6 eV) was generated from an electron beam operating at 15 kV and 32.3 W with residual pressure during measurements at 5·10<sup>-8</sup> Pa. For high-resolution spectra, pass energies of 46.95 eV were used (full width at half maximum for Ag 4f<sub>7/2</sub> = 1.00 eV at these conditions) with a neutralizer operating during analysis. The

acquired spectra were analyzed without adjustment of the energy scale since no charging was observed due to their electrical conductivity.

The as-deposited CuO electrodes and CuO-derived Cu (OD-Cu) electrodes after CO<sub>2</sub> electrolysis were characterized by SEM, XRD and XPS. SEM revealed that the as-deposited CuO films were composed of agglomerated 0.2-0.5 μm sized particles (**Figure A.48a**). After CO<sub>2</sub> reduction, the catalyst retained the roughened morphology of (pre-reduced) OD-Cu (**Figure A.48b**). As shown in **Figure A.48c**, XRD analysis of the electrodes confirmed their chemical identities as CuO (as-deposited) and metallic Cu (after electrolysis). The latter finding is consistent with predictions from the Pourbaix-diagram of the copper-water system,<sup>[221]</sup> and previous works that show the reduction of Cu oxides to metallic Cu upon the application of negative potentials necessary for CO<sub>2</sub> electrolysis.<sup>[51]</sup> A weak peak corresponding to Cu<sub>2</sub>O (111) was also detected. This is likely formed from surface oxidation of the OD-Cu which occurred when it was exposed to air<sup>[222]</sup> during its transfer to the XRD instrument for analysis. XPS analysis, which probes the top few nanometers of the sample, reveals that the surface of the as deposited film is composed of CuO, as seen from the Cu 2p<sub>3/2</sub> and 2p<sub>1/2</sub> signals at 934.1 eV and 954.0 eV respectively, and the strong satellite peaks (**Figure A.48d**). After electrolysis, the Cu 2p<sub>3/2</sub> and 2p<sub>1/2</sub> signals were shifted to 932.8 eV and 952.7 eV, respectively. These values coincide with binding energy shifts of metallic Cu, and are consistent with the observation of metallic Cu in the XRD data. However, we note that Cu 2p signals of Cu<sub>2</sub>O have similar binding energy shifts as metallic Cu, making it difficult to distinguish the two oxidation states using XPS.<sup>[222]</sup> Nonetheless, the presence of some Cu<sub>2</sub>O on the catalyst surface would also be in agreement with Cu<sub>2</sub>O signals in the XRD analysis. A weaker set of Cu 2p XPS signals at 934.8 eV and 954.7 eV, along with some weak satellite peaks, were also detected. These signals can be assigned to a mixture of CuO and Cu(OH)<sub>2</sub>, which were also formed from the surface oxidation of OD-Cu, though at a slower rate than Cu<sub>2</sub>O.<sup>[222]</sup> The lower concentration of Cu(OH)<sub>2</sub> and CuO formed could explain why their signals were not detected in the XRD analysis. Collectively, our characterization data point to metallic Cu as the predominant component of OD-Cu, after considering the influences from surface oxide formation. Elucidating the oxidation state of copper during eCO<sub>2</sub>R remains a challenge in the field. While many works have shown that copper oxides are unstable under CO<sub>2</sub> reduction conditions and metallic Cu is the active catalytic surface,<sup>[51,99,104]</sup> small amounts of subsurface residual oxides have also been detected.<sup>[64]</sup> The use of

highly sensitive in-situ or even operando techniques to accurately detect and study these subsurface residual oxides in order to assess their impact on CO<sub>2</sub> reduction activity is still a very active area of investigation.

CuO-derived Cu deposited on Cu discs was characterized as described in the following paragraph. Similar to the OD-Cu GDE, SEM analysis of the as-deposited samples reveals a film composed of agglomerated particles (**Figure A.52a**). After the pre-reduction, the OD-Cu film showed a roughened appearance with cracks and particles of 0.1  $\mu\text{m}$  size (**Figure A.52b**). This morphology is retained after 1 h electrolysis of acetaldehyde in 0.1 M KOH (**Figure A.52c**). After performing 1 h electrolysis of acetaldehyde in 0.1 M KOH, we observed that the anion exchange membrane had turned brown. To investigate this, we immersed one piece of membrane in solution A, which contained 0.1 M KOH and another piece in solution B, which contained 50 mM acetaldehyde in 0.1 M KOH. After immersion for 3 h, the membrane in solution A remained colorless, while the membrane in solution B turned brown (**Figure A.53**). The liquid remained colorless in both cases. This suggests that under alkaline conditions, the acetaldehyde might have affected the membrane. We further neutralized and analyzed solution B using HSGC. The analysis reveals that, despite the membrane turning brown, there was no difference in products detected by HSGC between solution B (after membrane immersion for 3 h) and a membrane-free solution of 50 mM acetaldehyde in 0.1 M KOH aged for the same duration (**Figure A.54**). There were also no acetaldehyde reduction products detected. This rules out the influence of the membrane on the product distribution of acetaldehyde electroreduction.

### 5.2.3. Electrolysis Experiments

CO<sub>2</sub> electrolyses were performed in a flow cell using the OD-Cu GDE as the cathode (exposed geometric area: 0.72 cm<sup>2</sup>), Ag/AgCl saturated KCl (Pine) as the reference electrode, and the IrO<sub>2</sub> GDE as the anode. The duration of each electrolysis was 45 min. The cathodic (2.5 cm<sup>3</sup>) and anodic compartments were separated by an anion-exchange membrane (Selemin AMVN, AGC Asahi Glass). CO<sub>2</sub> gas (99.999%, Linde Gas) was flowed through the back of the cathodic half-cell at a rate of 5 cm<sup>3</sup> min<sup>-1</sup>. 1.0 M KOH (99.97% Alfa Aesar) was pumped through the cell at 0.1 cm<sup>3</sup> min<sup>-1</sup> using a syringe pump. All electrochemical measurements were performed using a Gamry Reference 600 potentiostat/galvanostat and the current interrupt method was always used to compensate for the  $iR$  drop.



H-type cell electrolyses (60 min) of acetaldehyde (> 99.5%, Sigma-Aldrich), crotonaldehyde (98%, TCI), 1-butanal (> 99.5%, Sigma-Aldrich) and crotyl alcohol (> 97.0%, Sigma-Aldrich) were performed in 0.1 M KOH (99.97%, Alfa Aesar) or 0.1 M PPB (pH 7.0), which was composed of 0.062 M K<sub>2</sub>HPO<sub>4</sub> (≥ 99.0%, Sigma-Aldrich) and 0.038 M KH<sub>2</sub>PO<sub>4</sub> (≥ 99.0%, Sigma-Aldrich). As a two-phase (liquid-electrode) interface is more suitable for the mass transport of liquid reactants to the electrode than the tri-phase (gas-liquid-electrode) interface in the flow cell, a two-compartment Teflon H-type cell separated by an anion-exchange membrane (Selemin AMVN, AGC Asahi Glass) was used for the electrolyses. The cathodic compartment (20 cm<sup>3</sup>) was filled with 12 cm<sup>3</sup> of electrolyte and housed the working electrode (exposed geometric surface area: 0.785 cm<sup>2</sup>) and the reference electrode (Ag/AgCl saturated KCl, Pine). A graphite rod (Ted Pella) was used as counter electrode. The electrolyte was purged with N<sub>2</sub> gas at 10 cm<sup>3</sup> min<sup>-1</sup> for 5 min prior to electrolysis and this was maintained until the end of the experiment.

#### 5.2.4. Product Analysis

The gaseous products (H<sub>2</sub>, CO, CH<sub>4</sub>, C<sub>2</sub>H<sub>4</sub>, C<sub>2</sub>H<sub>6</sub>, C<sub>3</sub>H<sub>6</sub>) were continuously detected from the cathodic compartment by an on-line GC, (Agilent 7890A) with FID and TCD. Gas products were sampled every 13.5 min. After electrolysis, alkaline catholytes were neutralized by 4 M H<sub>2</sub>SO<sub>4</sub> and the liquid products were quantified with a headspace GC (HSGC, Agilent, 7890B and 7697A) and HPLC, (Agilent 1260 Infinity). Aldehydes, ketones and alcohols were detected using HSGC with FID while formate and acetate were detected using HPLC with a VWD, and 0.5 mM H<sub>2</sub>SO<sub>4</sub> mobile phase. The HSGC chromatogram of the calibration standards is shown in **Figure A.46**.

1D <sup>1</sup>H NMR spectra with water suppression and 2-D heteronuclear single quantum coherence (HSQC) <sup>1</sup>H - <sup>13</sup>C NMR spectra were recorded on a Bruker Avance III HD 500 MHz mounted with a 5 mm BBO Prodigy (at rt). Phenol (7.2 ppm) and DMSO (2.6 ppm) were dissolved in D<sub>2</sub>O (4.8 ppm) and added to the samples as internal standards. For the 1D <sup>1</sup>H NMR analysis, one pulse experiment was pre-saturated on the water resonance with a  $\pi/2$  pulse of 12  $\mu$ s, and a recycle delay of 5 s was implemented while coadding 256 scans per experiment. These settings resulted in a high signal-to-noise ratio and high resolution per measurement. Solutions of 10 mM acetaldehyde (> 99.5%, puriss, p.a., anhydrous, Sigma-Aldrich) and crotonaldehyde (> 99.5%, puriss, Fluka) in ultrapure deionized water and in 0.1 M KOH were measured within a few minutes after individual preparation, unless mentioned otherwise. For the 2D HSQC NMR analysis, an experimental pulse

program for the reference compounds was set with TD 1024 and 256 fid size, with 2 scans per experiment. Solutions of the reference compounds 10 mM 1-propanol (> 99%, reagent grade, VWR Chemicals), 1-butanol (> 99%, anhydrous, VWR Chemicals) and 1-butanal (> 99.0%, puriss, Fluka) in 0.1 M KOH were individually measured to provide a standard for signal assignment. The assignment of the unknown peak at 0.8 ppm needed 8 scans per experiment in the 2D experiments to obtain a sufficient signal-to-noise ratio and resolution.

### 5.2.5. Computational Details

The periodic DFT package VASP<sup>[223]</sup> was used to model the catalytic process, choosing the PBE<sup>[186]</sup> density functional. We included van der Waals contributions with a reparametrized DFT-D2 method.<sup>[187,188]</sup> Inner electrons were represented by PAW pseudopotentials while the basis set for valence electrons was expanded as plane waves with a kinetic energy cut-off of 450 eV.<sup>[224]</sup> The catalyst was modeled as Cu(100), taking four metal layers, which is the most stable surface for the working potentials. The Brillouin zone was sampled by a  $\Gamma$ -centered k-points mesh from the Monkhorst-Pack method with a reciprocal grid size smaller than 0.03  $\text{\AA}^{-1}$ .<sup>[225]</sup> All relevant data are available from the authors. All structures are available through the ioChem-BD repository.<sup>[199]</sup>

The interaction of the solvent with the electrode is complex and would require longtime first-principles simulations to account for the fluctuations of the solvent on the surface. As these are computationally expensive approaches, simpler techniques have been put forward to study chemical processes in solution. The most successful technique, in terms of balancing cost and accuracy, requires the inclusion of few explicit water molecules that can interact with the solute or the adsorbates, while the rest are represented in a mean-field approach and characterized by the relative permittivity of the solvent. For periodic systems, continuum solvation models have been introduced only recently.<sup>[189]</sup> In this case, a mixed implicit-explicit scheme was always investigated. The implicit (mean-field) solvation part was included within the VASP-MGCM model,<sup>[189,190]</sup> as it is essential to accurately describe the stability of electrochemical species.<sup>[201]</sup> In particular, anionic species in solution were computed as an ionic pair (with K<sup>+</sup> as the counter-cation) and an explicit water molecule, while the OH<sup>-</sup> anion required two explicit water molecules to ensure the right basicity (**Figure A.47a**). This method captured most of the effects from the aqueous environment. For the adsorbed species, solvation energies can be estimated only with implicit solvation within typical accuracies of 0.1 eV (**Figure A.47b**) when compared to fully

explicit water models.<sup>[190]</sup> In **Figure A.47c**, we compare the results with implicit water and the mixed scheme for 2 explicit water molecules. While we observe that the accuracy was improved to 0.05 eV, it is important to note that the large number of conformations associated with these extra degrees of freedom limit our possibilities for sampling all conformations for all 30 intermediates.

Several high-level methodologies can describe the perturbations of electric field and potential on the bonding of adsorbates.<sup>[76,95,99]</sup> In particular, Ref.<sup>[99]</sup> analyzed the key reactions controlling the selectivity to C<sub>2</sub> products, such CH<sub>3</sub>CHO, from CO<sub>2</sub> reduction. However, in our case, the large number of intermediates and conformations prevents us from using these methodologies. Thus the electric potential and pH effects were introduced via the CHE.<sup>[75]</sup> The CHE may have large deviations for elementary steps, such as CO dimerization, which involve adsorbates with very high dipole moments.<sup>[191]</sup> Error bars in such cases are typically in the order of 0.1 eV – 0.3 eV, and require corrections related to the work function<sup>[76]</sup> or the number of electrons.<sup>[99]</sup> These corrections can be confidently disregarded in our study as the relevant molecules treated are aldehydes or alcohols with small electric dipoles rather parallel to the surface. As an extreme case in the 1-butanol route, we consider atomic oxygen on Cu, (dipole of 0.52 Debye or 0.108 eÅ).<sup>[226]</sup> The potential of zero charge of Cu electrodes lies between +0.03 V to -0.22 V *vs.* RHE at pH of 13.0,<sup>[227]</sup> thus our optimal working potential (-0.44 V *vs.* RHE) would deviate between 0.20 V and 0.50 V with respect to the potential of zero charge. Assuming the electric DL thickness to be 3 Å,<sup>[75]</sup> the dipole contribution would be smaller than 0.02 eV (0.108 eÅ \* 0.50 V / 3 Å), which is a much smaller correction than intrinsic DFT accuracy. Finally, transition state energies were estimated from LSR available for Cu.<sup>[185,190]</sup> This approach can be employed as LSR holds when any combination of implicit-explicit solvation models is used.<sup>[185]</sup>

### 5.3. Results and Discussion

CO<sub>2</sub> was electroreduced at various potentials using OD-Cu GDE cathodes in a flow cell (**Figure 5.2** and **Section 5.2.1**, **5.2.2** and **Table A.36** and **Table A.37**). The catalyst was electrodeposited onto the GDE using a previously-published procedure.<sup>[169]</sup> Aqueous 1.0 M KOH was used as the electrolyte. The high eCO<sub>2</sub>R current densities from the flow cell electrolysis (**Figure 5.2d**), which circumvents mass transport limitations, combined with the use of highly sensitive headspace gas chromatography (**Figure 5.2e**) improves the detection and quantification of liquid products with low *FEs* and current densities. This allows us to detect CO<sub>2</sub> reduction

products that have, to date, never been observed. The total *FEs* of carbonaceous products were 68-69% at -0.48 V and -0.58 V *vs.* RHE (**Figure 5.3, Table A.36**). The major multicarbon products are ethylene and ethanol, which are typically formed on OD-Cu catalysts.<sup>[51,145]</sup> The highest *FE*<sub>C<sub>2</sub></sub> of 48% was observed at -0.58 V *vs.* RHE, with a corresponding *j*<sub>C<sub>2</sub></sub> of -210 mA cm<sup>-2</sup>. Minor C<sub>2</sub> products, acetaldehyde and ethane, were also detected. In the case of acetaldehyde, the low *FE* is a result of the chemical and/or electrochemical transformations it readily undergoes, as discussed below. C<sub>3</sub> species, mainly 1-propanol, were detected with a maximum *FE*<sub>C<sub>3</sub></sub> of 6.5% obtained at -0.48 V and -0.58 V *vs.* RHE. Overall, the catalytic activities toward C<sub>2</sub> and C<sub>3</sub> molecules from CO<sub>2</sub> reduction are comparable or higher than previously reported values for OD-Cu catalysts loaded onto carbon GDEs (**Table A.38**).

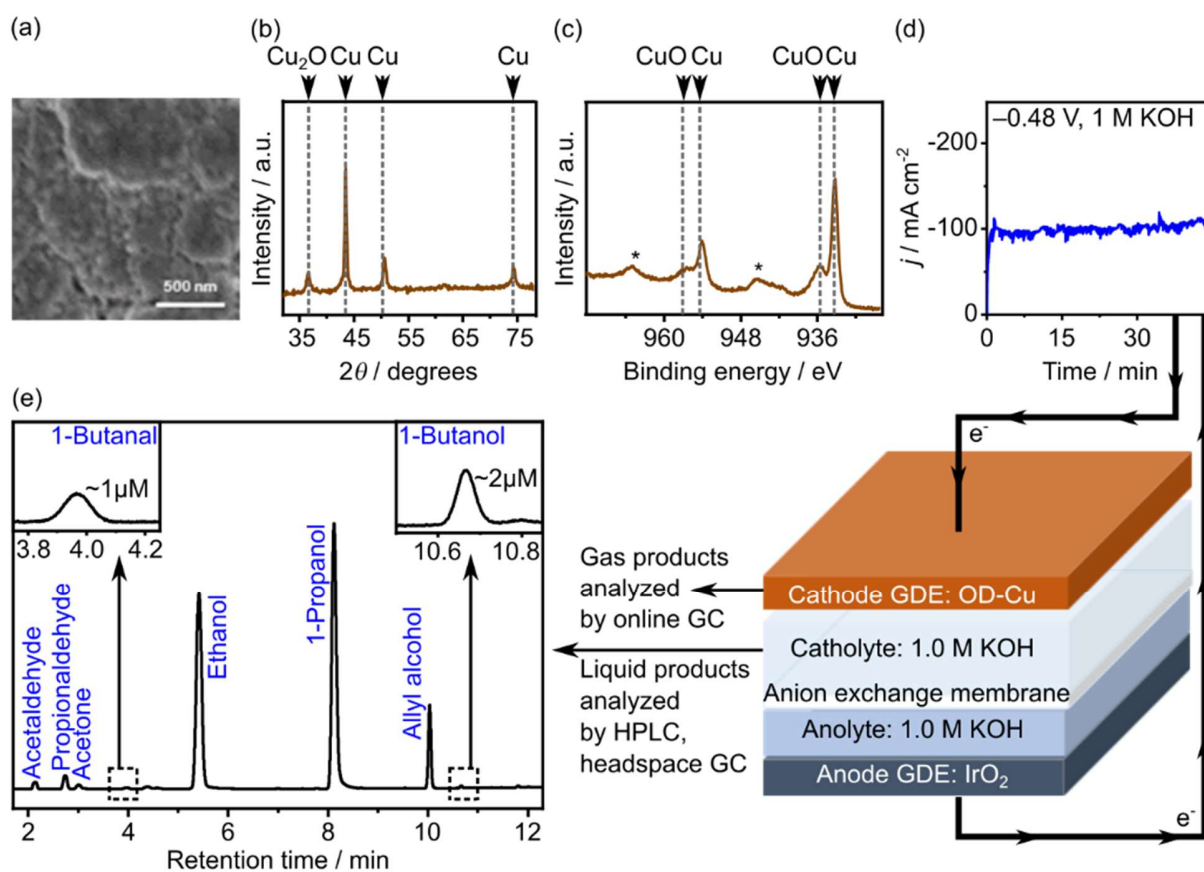


**Figure 5.2.** Diagram of CO<sub>2</sub> flow cell electrolysis set up: characterization of OD-Cu cathodes by (a) SEM, (b) XRD and (c) XPS (CuO and Cu(OH)<sub>2</sub> signals overlap, Cu and Cu<sub>2</sub>O signals overlap). (d) Large CO<sub>2</sub> reduction current densities (in the order of -100 mA cm<sup>-2</sup>) gave a sufficient rate of product formation to allow detection of minor products. (e) Sensitive analytical techniques like headspace GC can quantify minor products down to the μM-scale.

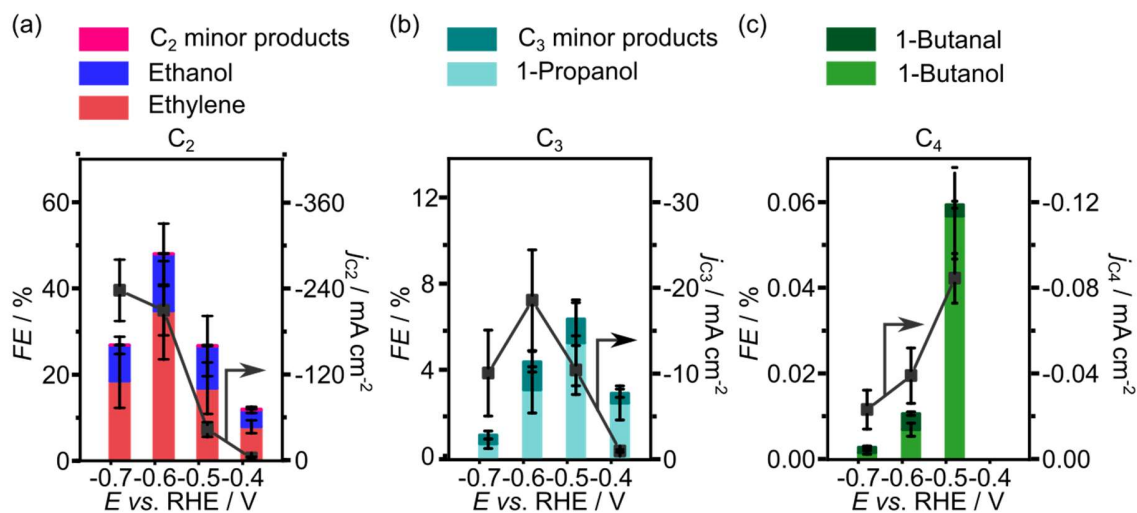


**Figure 5.3.** FE and partial current densities of (a)  $C_2$ , (b)  $C_3$  and (c)  $C_4$  products from electrolysis of  $CO_2$  on OD-Cu GDE in 1.0 M KOH. The major  $C_2$ ,  $C_3$  and  $C_4$  products are ethylene, 1-propanol and 1-butanol, respectively. Other detected products are shown in **Table A.36**.

Interestingly,  $C_4$  oxygenates such as 1-butanol and 1-butanal (maximum total  $FE_{C_4}$  of 0.060%, **Figure 5.3c**) were detected. In contrast to previous studies which only identified  $C_4$  hydrocarbons,<sup>[188,190]</sup> The dominant product was 1-butanol, which is in line with the fact that aldehydes can be easily electroreduced to their corresponding alcohols, as demonstrated in the cases of formaldehyde and acetaldehyde.<sup>[94]</sup> No carbon containing products were found in control experiments performed without applied potentials. As 1-butanol is the sole  $C_4$  alcohol product, it could not come from C-C coupling of four individual  $C_1$  adsorbates such as  $CO^*$  in a Flory-Schulz distribution, since 2-butanol was not observed. This led to the postulation that the formation of 1-butanol could occur through a combination of electrochemical and chemical steps.

Specifically, the aldol condensation of two acetaldehydes, which would give rise to the  $C_4$  backbone of crotonaldehyde. This in turn is further reduced to  $C_4$  terminal oxygenates like butanal and 1-butanol (**Figure 5.1**). While mechanisms for the formation of major  $C_2$  and  $C_3$  products, including acetaldehyde, have been widely discussed in the literature,<sup>[27,59,99,103,153,172]</sup> pathways for producing  $C_4$  products are rarely mentioned. Herein, focus lies on acetaldehyde reactivity as it is much less explored mechanistically. Nonetheless, the two steps preceding acetaldehyde formation were also presented, which involve the key ethenyloxy intermediate,  $CH_2CHO^*$ , and discuss the lateral pathways for  $CO_2$  reduction to  $C_1$ - $C_3$  products in **Note A.8**.

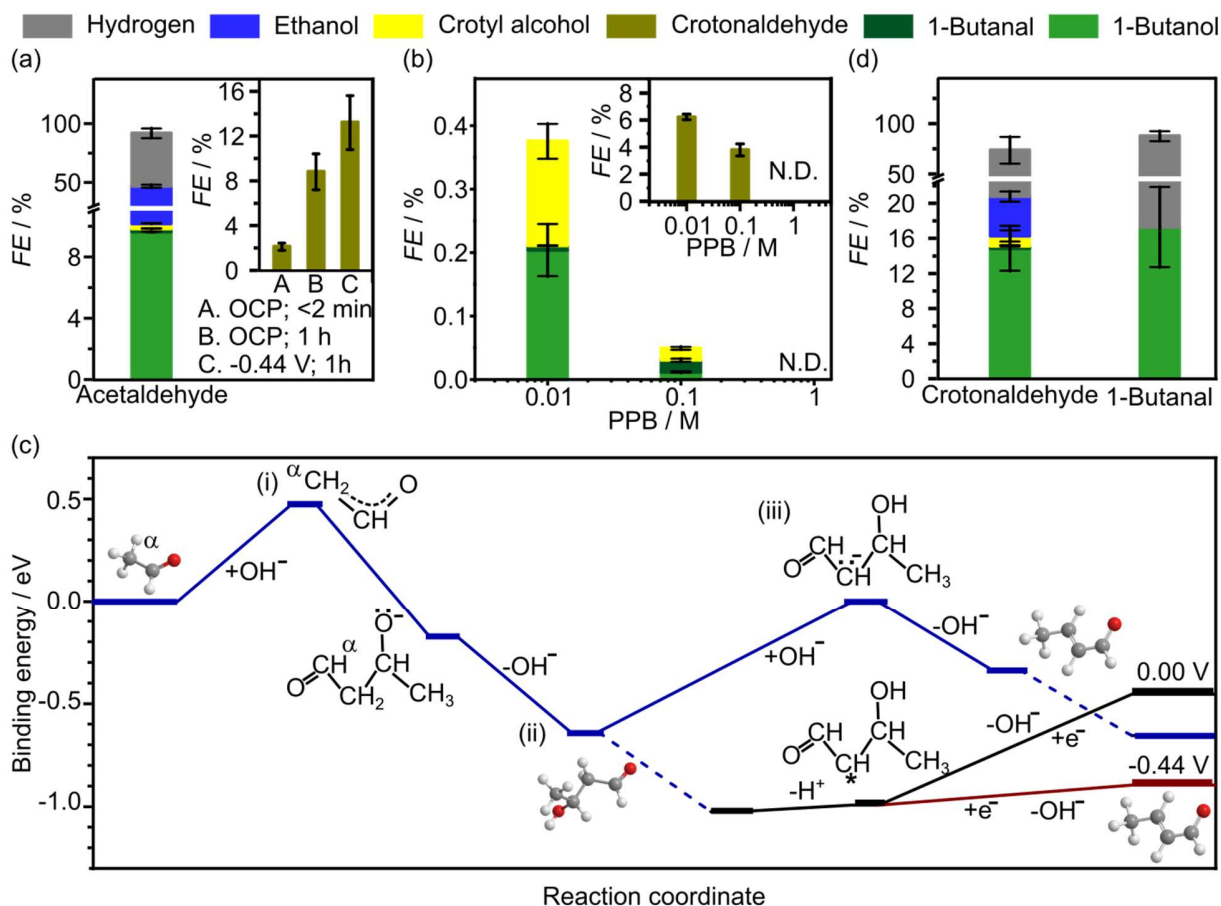


**Figure 5.4.** Faradaic efficiencies of products from 1 h electrolysis of 50 mM acetaldehyde on CuO-derived Cu (a) in alkaline (Table A.39) and (b) neutral (PPB) electrolyte (Table A.40 and Table A.41). The insets of (a) and (b) show the percentage of acetaldehyde that was converted to crotonaldehyde in the electrolyte in each case. (c) Potential energy diagram of acetaldehyde condensation to crotonaldehyde in solution (dark blue) and mediated by the surface (black). The final OH<sup>-</sup> removal, which can be assisted by one electron donated from the surface, is promoted by reductive potentials (dark red). Water molecules were omitted for clarity. (d) FEs of products from alkaline electrolyzes of 50 mM crotonaldehyde and 50 mM 1-butanol on OD-Cu.

To test this hypothesis for 1-butanol formation via acetaldehyde, 50 mM acetaldehyde was electroreduced in 0.1 M KOH on OD-Cu electrodes (Table A.39 and Section 5.2.2). The product distribution at an optimized potential of -0.44 V vs. RHE is summarized in Figure 5.4a (see also Table A.39 for product distributions at other applied potentials). The product with the highest selectivity was 1-butanol (FE of 9.6%,  $j = -1.06 \text{ mA cm}^{-2}$ ), consistent with expectations from a base catalyzed aldol condensation C-C coupling step. The remaining electrolysis products

were other  $C_4$  oxygenates, 1-butanol ( $C_4H_8O$ ) and crotyl alcohol ( $C_2H_4=C_2H_3OH$ ), as well as ethanol ( $C_2H_5OH$ ). During the electrolysis, some coloration of the anion-exchange membrane was observed due to the alkaline exposure of acetaldehyde containing electrolyte. Fortunately, control experiments excluded the interference with electrolysis results (**Figure A.53** and **Figure A.54**). Detection of crotonaldehyde (3.3 mM, equivalent to 13.2% acetaldehyde conversion) after electrolysis suggests that the  $C_4$  backbone of 1-butanol could be formed via a base-catalyzed aldol condensation (**Figure 5.4a**, inset). The increase in local pH close to the electrode under electroreduction conditions was utilized to test this hypothesis and performed fixed-current electrolyses of 50 mM acetaldehyde in 0.01, 0.1 and 1.0 M PPB (pH 7.0, **Figure 5.4b**, **Note A.9**). Higher buffer concentrations mitigate the local pH increase during electroreduction, thus lowering the overall local pH. These results reveal that electrolysis in 0.01 M PPB gave the highest selectivity toward  $C_4$  products (*FE* of 0.4%, with 1-butanol as the main product) and percentage of acetaldehyde converted to crotonaldehyde (1.5 mM, equivalent to 6.2% acetaldehyde conversion). In contrast, neither 1-butanol nor crotonaldehyde were detected from experiments performed in 1.0 M PPB (**Figure 5.4b** inset). These observations of an alkaline local pH promoting the production of 1-butanol on Cu directly support its formation via the aldol condensation of two acetaldehyde molecules and suggest an enhanced reaction rate close to the catalytic surface under electrolysis conditions. The base-catalyzed aldol condensation mechanism, forming the  $C_4$  backbone, was investigated by using DFT. High-level methods including solvent and potential effects have been employed to study electrochemical networks up to  $C_2$  species, including the formation of acetaldehyde from  $CO_2$ .<sup>[99]</sup> However, the multiple conformations of  $C_4$  molecules and the complexity of the reaction network with chemical (bulk solvent and interface) and electrochemical steps limits us to the use of DFT coupled to the CHE. The formation of the  $C_4$  backbone comprises two steps: the C-C coupling between two acetaldehyde molecules to form 3-hydroxybutanal ( $C_2H_4(OH)C_2H_3O$ ), and the subsequent dehydration of the latter to crotonaldehyde (**Figure 5.4c**). In solution, the aldol condensation starts with the stripping of an  $\alpha$ -hydrogen from acetaldehyde by  $OH^-$  to form an ethenyloxy anion ( $C_2H_3O^-$ , (i) in **Figure 5.4c**). The  $\alpha$ -carbon of  $C_2H_3O^-$  then attacks the carbonyl group of a second acetaldehyde molecule, which is subsequently protonated to 3-hydroxybutanal ((ii) in **Figure 5.4c**). Then, 3-hydroxybutanal loses an  $\alpha$ -hydrogen as a proton, to generate a carbene species ((iii) in **Figure 5.4c**), which forms

crotonaldehyde by hydroxyl elimination. Consistent with findings from the literature,<sup>[75]</sup> the latter is the rate-determining step in solution. For the case of eCO<sub>2</sub>R, adsorbed ethenyloxy species is formed as a precursor of acetaldehyde and ethanol,<sup>[77,99]</sup> and thus can also readily react with an acetaldehyde molecule in solution and be subsequently hydrogenated to form 3-hydroxybutanal (**Note A.8**). The amount of acetaldehyde converted to crotonaldehyde during electrolysis (13.2%) is larger than the 8.8% conversion (or 2.2 mM crotonaldehyde) when 50 mM acetaldehyde was aged in 0.1 M KOH for 1 h without applied potential (inset in **Figure 5.4a**). This observation suggests that the Cu surface can promote the aldol condensation at cathodic potentials. DFT analysis reveals that this alternative pathway starts with 3-hydroxybutanal adsorbing exothermically on Cu and losing an  $\alpha$ -hydrogen as an adsorbed H (dark red in **Figure 5.4c**). The hydroxyl group is then eliminated, in parallel with an electron transfer, to give crotonaldehyde. On the Cu surface, this step is promoted by negative applied potentials. Overall, the DFT investigation reveals that the alkaline electrolyte promotes the initial C-C coupling step between two acetaldehyde molecules, while the Cu surface promotes the subsequent dehydration step to crotonaldehyde. To elucidate the fate of C<sub>4</sub> species after the aldol condensation step, 50 mM crotonaldehyde was electrolyzed on OD-Cu in 0.1 M KOH at  $-0.44$  V *vs.* RHE (**Figure 5.4d** and **Table A.42** till **Table A.44**). The major carbonaceous product was 1-butanol (*FE* of 14.8%), while small amounts of 1-butanal (*FE* of 0.3%) and crotyl alcohol (*FE* of 1.1%) were also detected. The selectivity of 1-butanol (normalized by the *FE* of all the C<sub>4</sub> products) from crotonaldehyde electrolysis was 91.4%, which is similar to the case of acetaldehyde (94.7%, **Table A.44**). This reinforces the role of crotonaldehyde as the main intermediate in the electrosynthesis of acetaldehyde to C<sub>4</sub> oxygenates. The presence of ethanol (*FE* of 4.5%) was attributed to the reduction of acetaldehyde present due to the hydroxide-catalyzed retro-aldol reaction of crotonaldehyde, which is known to occur at rt.<sup>[228]</sup> This observation highlights the complexity of crotonaldehyde chemistry under aqueous alkaline conditions, and leads us to infer that the low total *FE* of 72.2% is a consequence of undetected products from other side reactions of crotonaldehyde in the alkaline electrolyte (**Figure A.55**). 1-Butanal and crotyl alcohol are known intermediates in the gas-phase hydrogenation of crotonaldehyde to 1-butanol,<sup>[229]</sup> and their presence during crotonaldehyde electrolysis suggests that they are potential



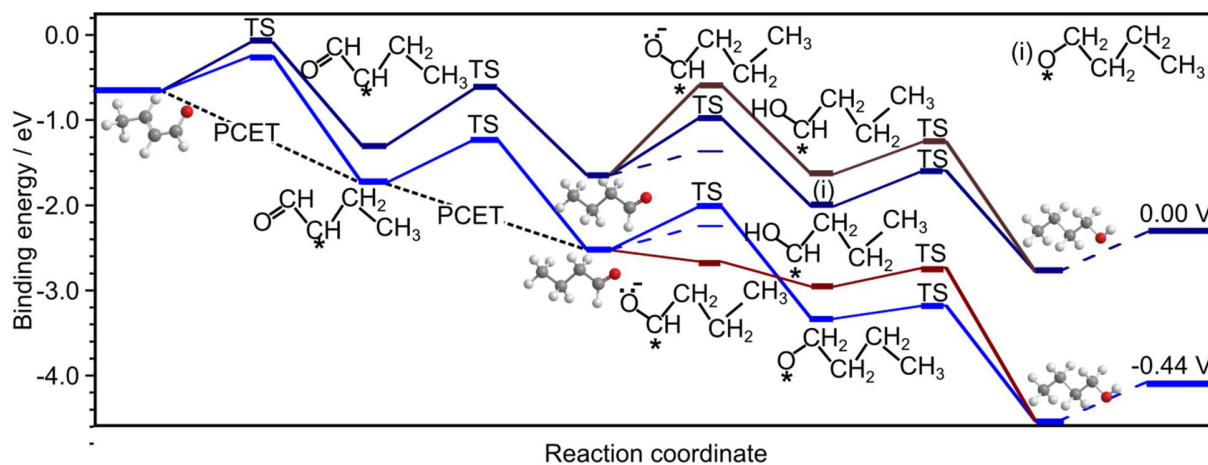


**Figure 5.5.** Potential energy diagram of crotonaldehyde reduction to 1-butanol via butanal (blue). Under negative potentials, butanal can be adsorbed via a one-electron transfer (dark red), which promotes its further reaction instead of desorption. Dashed lines represent adsorptions/desorptions. Dotted lines represent proton-coupled electron transfers (PCET). Adsorbed species denoted with \*. Additional (electro)chemical routes are shown in **Note A.8**.

electrochemically-active intermediates to 1-butanol. Therefore, 1-butanal and crotyl alcohol were electrolyzed under the same conditions (**Figure 5.4d**, **Table A.43**). 1-Butanol was the sole product from the electroreduction of 1-butanal (*FE* of 17.3%; the balance product is  $H_2$ ). Only hydrogen was detected during the electrolysis of crotyl alcohol, which indicates that the latter is electrochemically inert, in good agreement with theoretical calculations in **Figure A.56**. Theoretical analysis of crotonaldehyde reduction reveals that 1-butanal is formed by sequential hydrogenation of the band  $\alpha$ -carbons of crotonaldehyde (**Figure 5.5**). Once formed, butanal tends to desorb rather than further react. However, at potentials more reductive than  $-1.02$  V *vs.* SHE, 1-butanal receives an electron from the cathode surface to form the  $C_3H_7C^*HO^-$  anion (**Figure 5.5**). As this adsorption does not involve proton transfers, it is independent of the electrolyte pH in the SHE scale.  $C_3H_7C^*HO^-$  is subsequently protonated to yield 1-hydroxybutyl (**Figure 5.5**), which is further hydrogenated in a chemical step ( $E_a = 0.39$  eV) to produce 1-butanol. These theoretical findings are corroborated by our results from crotonaldehyde electrolysis performed at pH = 7.0 and pH = 13.0 (**Table A.43**). At  $-1.20$  V *vs.* SHE, 1-butanol was the most selective product in both electrolytes, consistent with the pH-independent adsorption

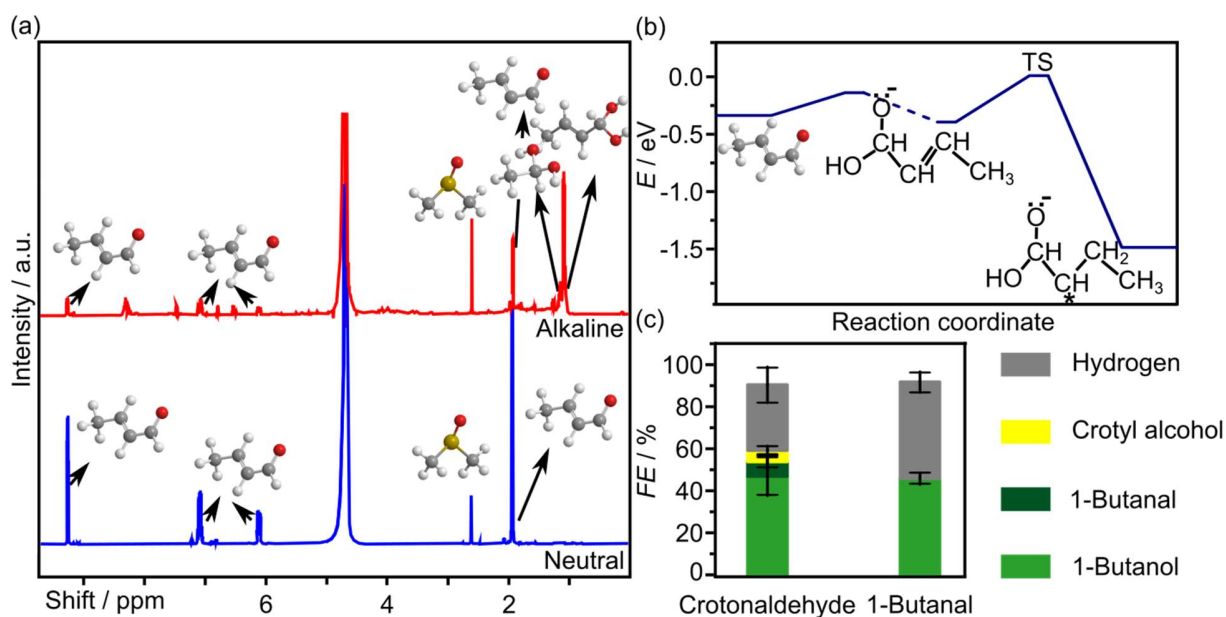


**Figure 5.6.** (a) <sup>1</sup>H NMR spectra of 50 mM crotonaldehyde in alkaline environment (0.1 M KOH, red line) and neutral (ultrapure deionized water, blue line). Phenol (7.2 ppm) and DMSO (2.6 ppm) were dissolved in D<sub>2</sub>O (residual H<sub>2</sub>O peak at 4.8 ppm) and added as internal standards. (b) Potential energy diagram of crotonaldehyde hydration and subsequent hydrogenation. Dashed lines represent adsorption/desorption. (c) FEs of crotonaldehyde and 1-butanol electrolysis products on OD-Cu in PPB electrolyte.

of 1-butanol. However, at  $-0.90$  V *vs.* SHE, 1-butanol was the most selective product, indicating that this potential was insufficient for its further reduction to 1-butanol. Alternative chemical routes from 1-butanol to 1-butanol are shown in **Figure A.57**. Aldehydes can be hydrated to geminal diols in aqueous alkaline solution. Signals belonging to hydrated crotonaldehyde ( $C_2H_4=C_2H_2(OH)_2$ ) were observed in NMR spectroscopic analyses of 50 mM crotonaldehyde or acetaldehyde dissolved in 0.1 M KOH (**Figure 5.6a**, **Figure A.58**). Hydrated crotonaldehyde can be considered as a possible intermediate to 1-butanol. DFT suggests that hydrated crotonaldehyde cannot be further electrochemically reduced due to a larger activation barrier (+0.41 eV) compared to its desorption energy (+0.26 eV), as shown in **Figure 5.6b**. This result was corroborated by the  $FE_{1-Butanol}$  of 46-47% observed from the crotonaldehyde and butanal electrolyses in 0.1 M PPB at  $-0.79$  V *vs.* RHE (**Figure 5.6c**, **Table A.43** and **Table A.44**), which was almost three times more than the values from electrolyses in 0.1 M KOH. **Figure 5.6a** shows that in a neutral medium, only peaks corresponding to crotonaldehyde were observed. The neutral buffer electrolyte

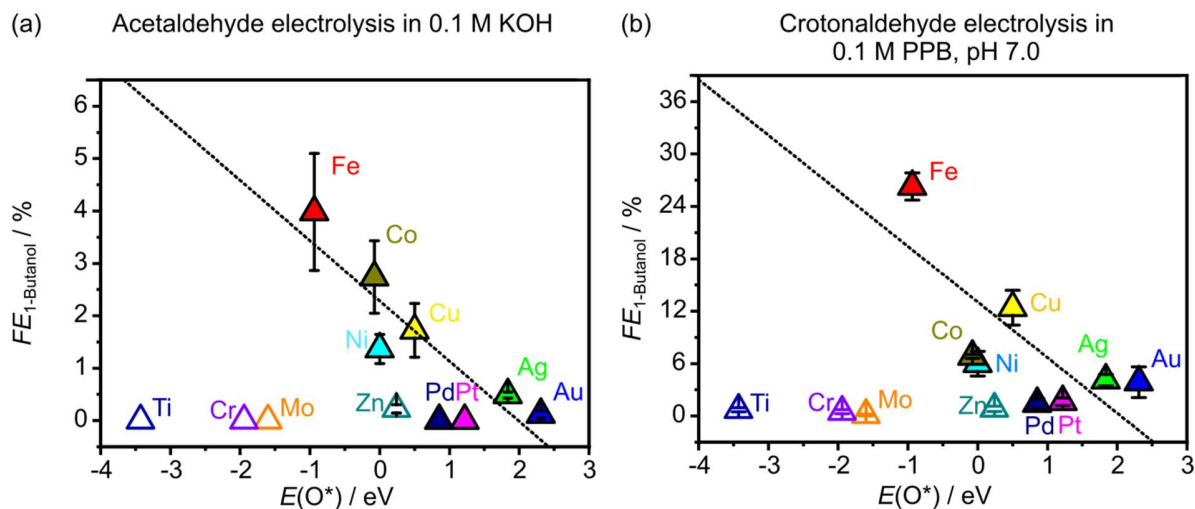


**Figure 5.7.** *FEs* of 1-butanol from  $-10 \text{ mA cm}^{-2}$  constant-current electrolysis of (a) acetaldehyde and (b) crotonaldehyde on selected metals as a function of the DFT-computed adsorbed oxygen stability on these metals with respect to water and hydrogen. Metals that are typically oxides at 0.00 V *vs.* RHE at the pH of the supporting electrolyte are shown as hollow symbols.

Therefore, likely suppressed the hydration process and increased the availability of unhydrated crotonaldehyde for reduction.

To find a better electrocatalyst to enhance the selectivity toward 1-butanol from acetaldehyde and crotonaldehyde reduction, an activity descriptor should be identified. To this end, acetaldehyde was electrolyzed in 0.1 M KOH and crotonaldehyde in 0.1 M PPB on different metal discs (**Note A.10**). Both the formation of 1-butanol and 1-butanal and the reactivity of crotonaldehyde are affected by the (local) pH. Therefore, a constant-current electrolysis was employed at  $-10 \text{ mA cm}^{-2}$  to identify the different reactivities of the metals. For acetaldehyde electrolysis, a selectivity was found of Cu, Fe, Co, Ni, Ag, and Au towards 1-butanol (**Figure 5.7a**) and all  $C_4$  products (**Figure A.59a**) can be correlated to the cathode metal-oxygen bond strength, with Fe showing the highest selectivity towards 1-butanol ( $FE = 4.0\%$ ). A similar trend was observed for the six abovementioned metals and also Pd and Pt for crotonaldehyde reduction to 1-butanol (**Figure 5.7b**), with Fe also showing the highest *FE* of 26.3%. The LSR end sharply in a selectivity cliff.<sup>[230]</sup> The origin of the discontinuity is likely due to a phase transformation. According to their Pourbaix-diagrams,<sup>[231]</sup> Zn, Ti, Cr, and Mo may have surface oxide layers under the working cathodic potentials and thus have poor yields towards 1-butanol and the other  $C_4$  products. Incidentally, these metals were more selective for reducing acetaldehyde

to crotyl alcohol (**Table A.45**), and crotonaldehyde to 1-butanol (**Table A.46**), probably because the dominating LSR differ from those of the pure metals. Based on these results, it was put forward that the C<sub>4</sub> product selectivity is influenced by the affinity of the catalyst to oxygen. Collectively, our results gave the reasons for the low selectivity to 1-butanol during the eCO<sub>2</sub>R on OD-Cu. The first factor is the low activity for acetaldehyde production on copper materials ( $FE_{C_2H_4O} = 0.1\%$  in **Table A.36**,  $FE_{C_2H_4O} < 2.1\%$  in the literature<sup>[26,232]</sup>). The second factor is that the conversion of acetaldehyde to ethanol on copper is kinetically facile and strongly competing ( $FE_{ethanol} = 36.5\%$ , while  $FE_{1-Butanol} = 9.6\%$  at  $-0.44$  V *vs.* RHE, **Figure 5.7a**).<sup>[25,59]</sup> The third factor is that the formation of the C<sub>4</sub> backbone and its subsequent reduction to 1-butanol are promoted by conflicting experimental conditions. While an alkaline environment facilitates aldol condensation between acetaldehyde molecules to crotonaldehyde, its hydration to an unreactive form is also promoted.

## 5.4. Conclusions

In summary, for the first time C<sub>4</sub> oxygenates were detected from CO<sub>2</sub> electroreduction on OD-Cu, with 1-butanol being the most favored product amongst them ( $FE = 0.056\%$ ,  $j = -0.080$  mA cm<sup>-2</sup> at  $-0.48$  V *vs.* RHE). The quantification was made possible by a combination of the high-rate electrolysis, achieved by using a GDE in a flow cell, and sensitive analytical techniques. The formation of 1-butanol did not originate from the C-C coupling of four individual C<sub>1</sub> adsorbates, such as CO\*. Instead, the combination of experimental and theoretical studies established a rich reaction mechanism that combines chemical and electrochemical steps, where the electrocatalytically generated acetaldehyde plays a prominent role. Its base-catalyzed aldol condensation, promoted by high local pH and the catalyst surface, produces crotonaldehyde, which is subsequently electroreduced to 1-butanol.

This work further highlights the challenges associated with the one-pot approach to converting a low molecular weight feedstock like CO<sub>2</sub> into complex functionalized molecules. It was confirmed that contrasting catalysts and conditions are required to maximize the yield of each step. In addition to operating under highly alkaline conditions, a single electrocatalytic surface can hardly optimize all the required steps. For example, among the metal discs tested, Fe was identified as the most selective catalyst for acetaldehyde reduction to 1-butanol, but it is not active per se for CO<sub>2</sub> reduction.

Therefore, designing a one-pot reactor for the electrosynthesis of large molecules would inevitably be associated with low performance. Instead, it would be proposed that a more viable synthetic strategy would be to deconvolute the multi-step process into sequential operation units. Therein, chemical or electrochemical reactions with different process conditions could be independently optimized. The separate stepwise-optimized reactors could then be placed in tandem for the efficient conversion of each intermediate, leading to increased yield of the desired product.

## Chapter 6

### Conclusions and Outlook

This thesis designs understanding tools that allow for strengthened understanding of compositional effects and chemical environment and explores the mechanisms in eCO<sub>2</sub>R toward C<sub>3</sub> and C<sub>4</sub> compounds.

#### 6.1. Conclusions

In<sub>2</sub>O<sub>3</sub>/Cu<sub>3</sub>N emerged as a selective and highly stable electrocatalyst in the reduction of CO<sub>2</sub> to CO, overperforming the humbly stable oxide-based benchmark. The use of copper nitride eliminated the uncontrolled structural and compositional changes associated to the latter. The regular composition and structure of microstructured electrodes facilitated establishing a direct relation between the Cu-In interface in In<sub>2</sub>O<sub>3</sub>/Cu<sub>3</sub>N and eCO<sub>2</sub>R activity. This relation was not accompanied by detectable indium diffusion into the copper matrix, as in the case of the oxide-based material. Spectroscopic evidence revealed the presence of metastable nitrogen under reaction conditions, which was associated to the improved interfacial stability. The findings reveal the potential of ND-Cu to engineer multicomponent systems with high efficiency for the eCO<sub>2</sub>R. In parallel, they underline microfabrication as a tool to establish synthesis-property-function relations in multicomponent systems for the range of electrocatalytic applications.

The application of microfabrication and advanced modelling enabled to quantify the relation between selectivity and a broad range of chemical environments in the eCO<sub>2</sub>R on OD-Cu, unveiling selectivity maps for the main C<sub>1</sub>-C<sub>3</sub> products in terms of local CO<sub>2</sub> concentration and pH. This was achieved by testing microstructured Cu foils processed by laser ablation followed by simulations facilitated by the regular geometry of the electrodes. Selectivity maps disclosed clear patterns shedding light on open mechanistic queries. Ethylene and ethanol patterns could not be entirely accounted for by proposed mechanisms, whereas the role of ethylene as intermediate toward 1-propanol is compatible with the results that suggest the presence of two mechanisms at mid- and high overpotentials. From an operational perspective, selectivity maps successfully predicted the influence of operation conditions such as stirring or the use of different electrolyte on the product distribution, suggesting their potential to guide process design.

The mechanistical pathway was established toward main C<sub>3</sub> products within the eCO<sub>2</sub>R framework and a key shared intermediate was identified. Through methodological approach, graph network and DFT simulations were supported by performing a wide range of experiments coupling C<sub>1</sub> and C<sub>2</sub> compounds. This approach revealed how the C<sub>3</sub> backbone was likely formed through a coupling of CO\* (or CHO\*) with CH<sub>2</sub>CH\* giving the key intermediate, CH<sub>2</sub>CHCHO\*. The network connects the key intermediate to 1-propanol through propionaldehyde. The pathway from propionaldehyde to 1-propanol was confirmed experimentally. Secondly, the network revealed pathways to propylene and 1-propanol through allyl alcohol, which was again confirmed experimentally. The allyl alkoxy intermediate is the precursor for propylene, but a large kinetic barrier prevents its formation. This mechanistic understanding paves the way towards the development of advanced electrocatalysts that promote C<sub>3</sub> products.

For the first time C<sub>4</sub> oxygenates were detected from eCO<sub>2</sub>R, with 1-butanol being the most favored product amongst them showing a  $FE = 0.056\%$  on OD-Cu. The quantification was made possible by a combination of the high-rate electrolysis, achieved by using a GDE in a flow cell, and highly sensitive analytical techniques. The formation of 1-butanol was ruled out to originate from the C-C coupling of four individual C<sub>1</sub> adsorbates, such as CO\*. Instead, the combination of experimental and theoretical studies established a rich reaction mechanism that combines chemical and electrochemical steps, where the electrocatalytically generated acetaldehyde plays a prominent role. Its base-catalyzed aldol condensation, promoted by high local pH and the catalyst surface, produces crotonaldehyde, which is subsequently electroreduced to 1-butanol. It naturally follows that a multi-step approach would need to be designed for C<sub>4+</sub> product formation rather than attempting a one-pot approach.

## 6.2. Outlook

Different strategies can be highlighted as recommended work based on knowledge gathered in this thesis. This work did not tackle compositional effects in the OD-Cu system due to a lack of time, while being one of the most debated aspects of eCO<sub>2</sub>R. Herein, a strategy is proposed based on using halogen-modified copper catalysts. Since its first mention as a catalyst, OD-Cu has been characterized ex-situ and its level of reminiscent oxygen during reaction conditions elucidated from theoretical studies and frequently contradicting operando measurements. Ex-situ characterization is of limited help, since once the catalyst is taken out of the reactor, its surface would immediately oxidize in the open-air leaving any relevant catalytic characterization wanting. To bypass this conundrum, oxygen in copper oxide could be substituted with an element not naturally present in air in anionic form, ideally easily detectable in post reaction studies, enabling the study of how copper polarization affects catalytic performance. Halides could prove helpful such as Cl<sup>-</sup> or Br<sup>-</sup> to act as Cu foil modifiers. A first work illustrating this concept is under preparation.

Regarding the further development of tools towards model systems, further efforts may be directed to achieving nanometric structural control to access molecular understanding. Techniques that would allow for patterning on the nanoscale are; electron beam lithography, focused ion beam lithography, molecular self-assembly, rapid prototyping and laser machining, just to name a few. While the techniques mentioned here are reported to operate at the nanoscale, it can be argued that they should be more appropriately be labelled as sub-micro scale, since the range of control is in the 50 to 100 nm range. There is thus a technological gap before model systems at the nanometric scale can be effectively designed. Another research line arises after considering that model systems in thermocatalysis are as scarcely used as in electrocatalysis mainly due to their typically low specific surface area hindering their catalytic evaluation. Nevertheless, the transfer of microfabrication tools developed in this thesis to study electrocatalysis could bring equally valuable insights in its sister discipline. The demonstration of this idea resulted in a parallel collaboration during the latest stages of the experimental work of this thesis that successfully related the density of interfacial sites between Cu and ZnO with activity in methanol synthesis.<sup>[233]</sup>



The ultimate goal of research into complex product formation from eCO<sub>2</sub>R is to produce value added compounds on an industrial scale powered by green energy (*e.g.* solar energy). While some products (*e.g.* building blocks like ethylene) have a natural fit in a centralized system, others (*e.g.* energy carriers like alcohols) would benefit from a distributed scheme. This is where an artificial leaf (a-leaf) can provide an advantage producing the latter from green energy for on site consumption. A-leaves are intended to mimic plants in nature which already make use of sunlight as an energy source when they convert atmospheric CO<sub>2</sub> and water into fuel (glucose) with a solar-to-fuel (STF) efficiency of 1%.<sup>[234]</sup> A-leaves are at an incipient stage of development but have already achieved higher efficiencies, specifically for solar-to-formate of up to 10%.<sup>[235–237]</sup> and solar-to-hydrogen (efficiencies of 10%<sup>[124,238,239]</sup>) if the concept is extended to non-carbon compounds. The investigations realized in this thesis were partly funded by the European Union through the A-LEAF project, aiming to demonstrate this technology, and resulting in a prototype a-leaf with 7% STF efficiency toward formate (HCOO<sup>-</sup>) using CuS<sub>x</sub> as electrocatalyst in eCO<sub>2</sub>R. This project required an integral design approach among different disciplines. The knowledge collected in this thesis could be of interest to strengthen the potential of a-leaves. One example is the control of the chemical environment to tune product distribution, which could be achieved by tuning the flow of the electrolyte, for example. A current collaboration is working on exemplifying this concept for the production of syngas with variable composition. The desirable aim would be, nevertheless, its application for the production of multicarbon energy carriers. Only two examples can be cited, thus far, that successfully produced solar-to-C<sub>2</sub> hydrocarbons (energy efficiency 2.3%).<sup>[240,241]</sup> However, these studies have not yielded absolute selectivity of their products as reported for C<sub>1</sub> counterparts. This is where the mechanistic understanding from Chapter 4 and 5 could be of high value. While industrial implementation is still far from reality, it remains promising to see more efforts into cross-disciplinary a-leaf projects.

Finally, and aiming at the long term, herein lies also the possibility of expanding the concept of a leaf to other small molecules like nitrogen, as in an artificial ammonia leaf. The access to fertilizers would very much benefit from an electrocatalytic approach where water would serve as the hydrogen source and production is executed in a decentralized manner. This world is run as an ammonia-based economy and without investment in innovation, we risk a shortage of food resulting in the fall of our society, as we know it. This field, however, remains young and underdeveloped and catalyst discovery would require a solid foundation of ammonia product quantification. As a lateral project during this thesis, Martín and Veenstra *et al.*<sup>[242]</sup> contributed to this by designing a simplified product quantification method making accurate ammonia quantification with low-grade nuclear magnetic resonance spectrometers possible. Further work on catalyst discovery in eN<sub>2</sub>R would require an investment of time that was not available for this thesis and thus is part of this outlook.



## Bibliography

- [1] Mitigation and Adaptation Solutions – Climate Change, *Vital Signs of the Planet* (Report) **2022**, available online at <https://climate.nasa.gov/> (Accessed on August 26, 2022).
- [2] United Nations, *Paris Agreement* (Report) **2015**, available online at [https://unfccc.int/files/meetings/paris\\_nov\\_2015/application/pdf/paris\\_agreement\\_english\\_.pdf](https://unfccc.int/files/meetings/paris_nov_2015/application/pdf/paris_agreement_english_.pdf) (Accessed on August 26, 2022).
- [3] B. Obama, *Science (1979)* **2017**, *355*, 126–129.
- [4] Worldbank data, *GDP per unit of energy use (PPP \$ per kg of oil equivalent)* (Online Database) **2022**, available online at [https://data.worldbank.org/indicator/EG.GDP.PUSE.KO.PP?name\\_desc=true](https://data.worldbank.org/indicator/EG.GDP.PUSE.KO.PP?name_desc=true) (Accessed on August 26, 2022).
- [5] I. Gyuk, *Progress in Grid Energy Storage* (Report) **2012**, available online at <https://www.energy.gov/sites/default/files/Presentation%20to%20the%20EAC%20-%20Progress%20in%20Grid%20Energy%20Storage%20-%20Imre%20Gyuk.pdf> (Accessed on August 26, 2022).
- [6] Z. Yang, J. Zhang, M. C. W. Kintner-Meyer, X. Lu, D. Choi, J. P. Lemmon, J. Liu, *Chem. Rev.* **2011**, *111*, 3577–3613.
- [7] IPCC Special Reports UNFCCC, *Global Warming of 1.5 °C* (Report) **2022**, available online at <https://www.ipcc.ch/sr15/> (Accessed on August 26, 2022).
- [8] A. Majumdar, J. Deutch, *Joule* **2018**, *2*, 801–809.
- [9] Global CCS Institute, *The global status of CCS* (Report) **2013**, available online at <https://www.globalccsinstitute.com/resources/publications-reports-research/the-global-status-of-ccs-2013/> (Accessed on August 26, 2022).
- [10] M. Eckert, G. Fleischmann, R. Jira, H. M. Bolt, *Ullmann's Encyclopedia of Industrial Chemistry*, Wiley-VCH Verlag GmbH & Co. KGaA, **2000**.
- [11] M. R. Dubois, D. L. Dubois, *Acc. Chem. Res.* **2009**, *42*, 1974–1982.
- [12] A. M. Appel, J. E. Bercaw, A. B. Bocarsly, H. Dobbek, D. L. Dubois, M. Dupuis, J. G. Ferry, E. Fujita, R. Hille, P. J. A. Kenis, C. A. Kerfeld, R. H. Morris, C. H. F. Peden, A. R. Portis, S. W. Ragsdale, T. B. Rauchfuss, J. N. H. Reek, L. C. Seefeldt, R. K. Thauer, G. L. Waldrop, *Chem. Rev.* **2013**, *113*, 6621–6658.
- [13] S. G. Jadhav, P. D. Vaidya, B. M. Bhanage, J. B. Joshi, *Chem. Eng. Res. Design* **2014**, *92*, 2557–2567.
- [14] G. A. Olah, A. Goepfert, G. K. S. Prakash, *Beyond Oil and Gas: The Methanol Economy*, John Wiley & Sons, Inc., **2006**.
- [15] F. Studt, M. Behrens, E. L. Kunkes, N. Thomas, S. Zander, A. Tarasov, J. Schumann, E. Frei, J. B. Varley, F. Abild-Pedersen, J. K. Nørskov, R. Schlögl, *ChemCatChem* **2015**, *7*, 1105–1111.

- [16] S. J. Davis, N. S. Lewis, M. Shaner, S. Aggarwal, D. Arent, I. L. Azevedo, S. M. Benson, T. Bradley, J. Brouwer, Y. M. Chiang, C. T. M. Clack, A. Cohen, S. Doig, J. Edmonds, P. Fennell, C. B. Field, B. Hannegan, B. M. Hodge, M. I. Hoffert, E. Ingersoll, P. Jaramillo, K. S. Lackner, K. J. Mach, M. Mastrandrea, J. Ogden, P. F. Peterson, D. L. Sanchez, D. Sperling, J. Stagner, J. E. Trancik, C. J. Yang, K. Caldeira, *Science* **2018**, *360*.
- [17] A. D. Handoko, F. Wei, Jenndy, B. S. Yeo, Z. W. Seh, *Nat Catal* **2018**, *1*, 922–934.
- [18] M. Carmo, D. L. Fritz, J. Mergel, D. Stolten, *Int. J. Hydrogen Energy* **2013**, *38*, 4901–4934.
- [19] Y. Hori, K. Kikuchi, S. Suzuki, *Chem. Lett.* **1985**, 1695–1698.
- [20] Y. Hori, K. Kikuchi, A. Murata, S. Suzuki, *Chem. Lett.* **1986**, 897–898.
- [21] Y. Hori, A. Murata, R. Takahashi, *J. Chem. Soc Faraday Trans. I* **1989**, *85*, 2309–2326.
- [22] Y. Hori, H. Wakebe, T. Tsukamoto, O. Koga, *Electrochim Acta* **1994**, *39*, 1833–1839.
- [23] Y. Hori, I. Takahashi, O. Koga, N. Hoshi, *J. Phys. Chem. B* **2002**, *106*, 15–17.
- [24] X. Liu, J. Xiao, H. Peng, X. Hong, K. Chan, J. K. Nørskov, *Nat. Commun.* **2017**, *8*, 15438.
- [25] Y. Hori, R. Takahashi, Y. Yoshinami, A. Murata, *J. Phys. Chem. B* **1997**, *101*, 7075–7081.
- [26] K. P. Kuhl, E. R. Cave, D. N. Abram, T. F. Jaramillo, *Energy and Environ. Sci.* **2012**, *5*, 7050–7059.
- [27] S. Nitopi, E. Bertheussen, S. B. Scott, X. Liu, A. K. Engstfeld, S. Horch, B. Seger, I. E. L. Stephens, K. Chan, C. Hahn, J. K. Nørskov, T. F. Jaramillo, I. Chorkendorff, *Chem. Rev.* **2019**, *119*, 7610–7672.
- [28] X. Sun, X. Kang, Q. Zhu, J. Ma, G. Yang, Z. Liu, B. Han, *Chem. Sci.* **2016**, *7*, 2883–2887.
- [29] H. Xiang, S. Rasul, B. Hou, J. Portoles, P. Cumpson, E. H. Yu, *ACS Appl. Mater. Interf.* **2020**, *12*, 601–608.
- [30] K. Nakata, T. Ozaki, C. Terashima, A. Fujishima, Y. Einaga, *Angew. Chem. Int. Ed.* **2014**, *53*, 871–874.
- [31] T. Shinagawa, G. O. Larrazábal, A. J. Martín, F. Krumeich, J. Pérez-Ramírez, *ACS Catal.* **2018**, *8*, 837–844.
- [32] D. Yang, Q. Zhu, C. Chen, H. Liu, Z. Liu, Z. Zhao, X. Zhang, S. Liu, B. Han, *Nat. Commun.* **2019**, *10*, 677.
- [33] Y. Liu, S. Chen, X. Quan, H. Yu, *J. Am. Chem. Soc.* **2015**, *137*, 11631–11636.
- [34] E. Andreoli, *Nat. Catal.* **2021**, *4*, 8–9.
- [35] C. S. Chen, J. H. Wan, B. S. Yeo, *J. Phys. Chem. C* **2015**, *119*, 26875–26882.
- [36] J. Tamura, A. Ono, Y. Sugano, C. Huang, H. Nishizawa, S. Mikoshiba, *Phys. Chem. Chem. Phys.* **2015**, *17*, 26072–26078.

- [37] L. Wang, D. C. Higgins, Y. Ji, C. G. Morales-Guio, K. Chan, C. Hahn, T. F. Jaramillo, *PNAS* **2020**, *117*, 12572–12575.
- [38] K. Zhao, X. Nie, H. Wang, S. Chen, X. Quan, H. Yu, W. Choi, G. Zhang, B. Kim, J. G. Chen, *Nat. Commun.* **2020**, *11*, 2455.
- [39] T. Jaster, A. Gawel, D. Siegmund, J. Holzmann, H. Lohmann, E. Klemm, U. P. Apfel, *iScience* **2022**, *25*, 1–30.
- [40] T. Kim, G. T. R. Palmore, *Nat. Commun.* **2020**, *11*, 3622.
- [41] S. Lee, D. Kim, J. Lee, *Angew. Chem. Int. Ed.* **2015**, *127*, 14914–14918.
- [42] C. W. Li, M. W. Kanan, *J. Am. Chem. Soc.* **2012**, *134*, 7231–7234.
- [43] C. W. Li, J. Ciston, M. W. Kanan, *Nature* **2014**, *508*, 504–507.
- [44] H. Mistry, A. S. Varela, C. S. Bonifacio, I. Zegkinoglou, I. Sinev, Y. W. Choi, K. Kisslinger, E. A. Stach, J. C. Yang, P. Strasser, B. R. Cuenya, *Nat. Commun.* **2016**, *7*, 12123.
- [45] Q. Lu, J. Rosen, F. Jiao, *ChemCatChem* **2015**, *7*, 38–47.
- [46] F. S. Roberts, K. P. Kuhl, A. Nilsson, *Angew. Chem. Int. Ed.* **2015**, *127*, 5268–5271.
- [47] Y. Kwon, Y. Lum, E. L. Clark, J. W. Ager, A. T. Bell, *ChemElectroChem* **2016**, *3*, 1012–1019.
- [48] C. S. Chen, A. D. Handoko, J. H. Wan, L. Ma, D. Ren, B. S. Yeo, *Catal. Sci. Technol.* **2015**, *5*, 161–168.
- [49] W. Tang, A. A. Peterson, A. S. Varela, Z. P. Jovanov, L. Bech, W. J. Durand, S. Dahl, J. K. Nørskov, I. Chorkendorff, *Phys. Chem. Chem. Phys.* **2012**, *14*, 76–81.
- [50] R. Kas, R. Kortlever, A. Milbrat, M. T. M. Koper, G. Mul, J. Baltrusaitis, *Phys. Chem. Chem. Phys.* **2014**, *16*, 12194–12201.
- [51] D. Ren, Y. Deng, A. D. Handoko, C. S. Chen, S. Malkhandi, B. S. Yeo, *ACS Catal.* **2015**, *5*, 2814–2821.
- [52] D. Kim, S. Lee, J. D. Ocon, B. Jeong, J. K. Lee, J. Lee, *Phys. Chem. Chem. Phys.* **2015**, *17*, 824–830.
- [53] D. Raciti, K. J. Livi, C. Wang, *Nano Lett.* **2015**, *15*, 6829–6835.
- [54] M. Ma, K. Djanashvili, W. A. Smith, *Phys. Chem. Chem. Phys.* **2015**, *17*, 20861–20867.
- [55] S. Min, X. Yang, A. Y. Lu, C. C. Tseng, M. N. Hedhili, L. J. Li, K. W. Huang, *Nano Energy* **2016**, *27*, 121–129.
- [56] M. Ma, K. Djanashvili, W. A. Smith, *Angew. Chem. Int. Ed.* **2016**, *128*, 6792–6796.
- [57] M. Rahaman, A. Dutta, A. Zanetti, P. Broekmann, *ACS Catal.* **2017**, *7*, 7946–7956.
- [58] D. Raciti, L. Cao, K. J. T. Livi, P. F. Rottmann, X. Tang, C. Li, Z. Hicks, K. H. Bowen, K. J. Hemker, T. Mueller, C. Wang, *ACS Catal.* **2017**, *7*, 4467–4472.
- [59] E. Bertheussen, A. Verdaguer-Casadevall, D. Ravasio, J. H. Montoya, D. B. Trimarco, C. Roy, S. Meier, J. Wendland, J. K. Nørskov, I. E. L. Stephens, I. Chorkendorff, *Angew. Chem. Int. Ed.* **2016**, *128*, 1472–1476.
- [60] X. Feng, K. Jiang, S. Fan, M. W. Kanan, *ACS Centr. Sci.* **2016**, *2*, 169–174.

- [61] A. Verdaguer-Casadevall, C. W. Li, T. P. Johansson, S. B. Scott, J. T. McKeown, M. Kumar, I. E. L. Stephens, M. W. Kanan, I. Chorkendorff, *J. Am. Chem. Soc.* **2015**, *137*, 9808–9811.
- [62] F. S. Roberts, K. P. Kuhl, A. Nilsson, *ChemCatChem* **2016**, *8*, 1119–1124.
- [63] J. Huang, N. Hörmann, E. Oveisi, A. Loiudice, G. L. de Gregorio, O. Andreussi, N. Marzari, R. Buonsanti, *Nat. Commun.* **2018**, *9*, 3117.
- [64] A. Eilert, F. Cavalca, F. S. Roberts, J. Osterwalder, C. Liu, M. Favaro, E. J. Crumlin, H. Ogasawara, D. Friebel, L. G. M. Pettersson, A. Nilsson, *J. Phys. Chem. Lett.* **2017**, *8*, 285–290.
- [65] Y. Lum, B. Yue, P. Lobaccaro, A. T. Bell, J. W. Ager, *J. Phys. Chem. C* **2017**, *121*, 14191–14203.
- [66] K. J. P. Schouten, Z. Qin, E. P. Gallent, M. T. M. Koper, *J. Am. Chem. Soc.* **2012**, *134*, 9864–9867.
- [67] K. J. P. Schouten, E. Pérez Gallent, M. T. M. Koper, *J. Electroanal. Chem.* **2014**, *716*, 53–57.
- [68] K. J. P. Schouten, E. Pérez Gallent, M. T. M. Koper, *ACS Catal.* **2013**, *3*, 1292–1295.
- [69] Y. Hori, A. Murata, R. Takahashi, S. Suzuki, *J. Am. Chem. Soc.* **1987**, *109*, 5022–5023.
- [70] M. Gattrell, N. Gupta, A. Co, *J. Electroanal. Chem.* **2006**, *594*, 1–19.
- [71] N. Gupta, M. Gattrell, B. MacDougall, *J. Appl. Electrochem.* **2006**, *36*, 161–172.
- [72] B. R. W. Pinsent, L. Pearson, F. J. W. Roughton, *Colloid Sci.* **1956**, 1512–1520.
- [73] Z. W. She, J. Kibsgaard, C. F. Dickens, I. Chorkendorff, J. K. Nørskov, T. F. Jaramillo, *Science (1979)* **2017**, *355*.
- [74] L. D. Chen, M. Urushihara, K. Chan, J. K. Nørskov, *ACS Catal.* **2016**, *6*, 7133–7139.
- [75] J. K. Nørskov, J. Rossmeisl, A. Logadottir, L. Lindqvist, J. R. Kitchin, T. Bligaard, H. Jónsson, *J. Phys. Chem. B* **2004**, *108*, 17886–17892.
- [76] K. Chan, J. K. Nørskov, *J. Phys. Chem. Lett.* **2015**, *6*, 2663–2668.
- [77] R. Kortlever, J. Shen, K. J. P. Schouten, F. Calle-Vallejo, M. T. M. Koper, *J. Phys. Chem. Lett.* **2015**, *6*, 4073–4082.
- [78] K. Hara, A. Tsuneta, A. Kudo, T. Sakata, *J. Electrochem. Soc.*, **1994**, *141*, 2097–2103.
- [79] J. J. Kim, D. P. Summers, K. W. Frese, *Reduction of CO, and CO to Methane on Cu Foil Electrodes*, Elsevier Sequoia S.A, **1988**.
- [80] E. Bertheussen, T. V. Hogg, Y. Abghoui, A. K. Engstfeld, I. Chorkendorff, I. E. L. Stephens, *ACS Energy Lett.* **2018**, *3*, 634–640.
- [81] L. Wang, S. A. Nitopi, E. Bertheussen, M. Orazov, C. G. Morales-Guio, X. Liu, D. C. Higgins, K. Chan, J. K. Nørskov, C. Hahn, T. F. Jaramillo, *ACS Catal.* **2018**, *8*, 7445–7454.
- [82] M. B. Ross, C. T. Dinh, Y. Li, D. Kim, P. de Luna, E. H. Sargent, P. Yang, *J. Am. Chem. Soc.* **2017**, *139*, 9359–9363.

- [83] C. M. Gunathunge, V. J. Ovalle, Y. Li, M. J. Janik, M. M. Waegele, *ACS Catal.* **2018**, *8*, 7507–7516.
- [84] I. V. Chernyshova, P. Somasundaran, S. Ponnurangam, *PNAS* **2018**, *115*, E9261–E9270.
- [85] Y. Hori, A. Murata, T. Tsukamoto, H. Wakebe, O. Koga, H. Yamazaki, *Electrochim Acta* **1994**, *39*, 2495–250.
- [86] Y. Hori, O. Koga, H. Yamazaki, T. Matsuo, *Electrochim Acta* **1995**, *40*, 2617–2622.
- [87] A. Wuttig, C. Liu, Q. Peng, M. Yaguchi, C. H. Hendon, K. Motobayashi, S. Ye, M. Osawa, Y. Surendranath, *ACS Centr. Sci.* **2016**, *2*, 522–528.
- [88] A. A. Peterson, F. Abild-Pedersen, F. Studt, J. Rossmeisl, J. K. Nørskov, *Energy Environ. Sci.* **2010**, *3*, 1311–1315.
- [89] A. A. Peterson, J. K. Nørskov, *J. Phys. Chem. Lett.* **2012**, *3*, 251–258.
- [90] K. P. Kuhl, T. Hatsukade, E. R. Cave, D. N. Abram, J. Kibsgaard, T. F. Jaramillo, *J. Am. Chem. Soc.* **2014**, *136*, 14107–14113.
- [91] P. Sabatier, *Deutschen Chem. Gesellschaft* **1911**, *258*, 1984–2001.
- [92] Y. Hori, A. Murata, Y. Yoshinami, *J. Chem. Soc. Faraday Trans.* **1991**, *87*, 125–128.
- [93] H. Ooka, M. C. Figueiredo, M. T. M. Koper, *Langmuir* **2017**, *33*, 9307–9313.
- [94] K. J. P. Schouten, Y. Kwon, C. J. M. van der Ham, Z. Qin, M. T. M. Koper, *Chem. Sci.* **2011**, *2*, 1902–1909.
- [95] T. Cheng, H. Xiao, W. A. Goddard III, *PNAS* **2017**, *114*, 1795–1800.
- [96] J. D. Goodpaster, A. T. Bell, M. Head-Gordon, *J. Phys. Chem. Lett.* **2016**, *7*, 1471–1477.
- [97] F. Calle-Vallejo, M. T. M. Koper, *Angew. Chem. Int. Ed.* **2013**, *52*, 7282–7285.
- [98] J. H. Montoya, C. Shi, K. Chan, J. K. Nørskov, *J. Phys. Chem. Lett.* **2015**, *6*, 2032–2037.
- [99] A. J. Garza, A. T. Bell, M. Head-Gordon, *ACS Catal.* **2018**, *8*, 1490–1499.
- [100] X. Liu, P. Schlexer, J. Xiao, Y. Ji, L. Wang, R. B. Sandberg, M. Tang, K. S. Brown, H. Peng, S. Ringe, C. Hahn, T. F. Jaramillo, J. K. Nørskov, K. Chan, *Nat. Commun.* **2019**, *10*, 32.
- [101] Y. Lum, T. Cheng, W. A. Goddard III, J. W. Ager, *J. Am. Chem. Soc.* **2018**, *140*, 9337–9340.
- [102] E. L. Clark, A. T. Bell, *J. Am. Chem. Soc.* **2018**, *140*, 7012–7020.
- [103] J. Li, F. Che, Y. Pang, C. Zou, J. Y. Howe, T. Burdyny, J. P. Edwards, Y. Wang, F. Li, Z. Wang, P. de Luna, C. T. Dinh, T. T. Zhuang, M. I. Saidaminov, S. Cheng, T. Wu, Y. Z. Finprock, L. Ma, S. H. Hsieh, Y. S. Liu, G. A. Botton, W. F. Pong, X. Du, J. Guo, T. K. Sham, E. H. Sargent, D. Sinton, *Nat. Commun.* **2018**, *9*, 4614.
- [104] L. Mandal, K. R. Yang, M. R. Motapothula, D. Ren, P. Lobaccaro, A. Patra, M. Sherburne, V. S. Batista, B. S. Yeo, J. W. Ager, J. Martin, T. Venkatesan, *ACS Appl. Mater. Interf.* **2018**, *10*, 8574–8584.
- [105] X. Wang, Z. Wang, T. T. Zhuang, C. T. Dinh, J. Li, D. H. Nam, F. Li, C. W. Huang, C. S. Tan, Z. Chen, M. Chi, C. M. Gabardo, A. Seifitokaldani, P. Todorović, A. Proppe, Y.



- Pang, A. R. Kirmani, Y. Wang, A. H. Ip, L. J. Richter, B. Scheffel, A. Xu, S. C. Lo, S. O. Kelley, D. Sinton, E. H. Sargent, *Nat. Commun.* **2019**, *10*, 5186.
- [106] Y. Lum, J. W. Ager, *Energy Environ. Sci.* **2018**, *11*, 2935–2944.
- [107] G. O. Larrazábal, T. Shinagawa, A. J. Martín, J. Pérez-Ramírez, *Nat. Commun.* **2018**, *9*, 1477.
- [108] W. Steffen, K. Richardson, J. Rockström, S. E. Cornell, I. Fetzer, E. M. Bennett, R. Biggs, S. R. Carpenter, W. de Vries, C. A. de Wit, C. Folke, D. Gerten, J. Heinke, G. M. Mace, L. M. Persson, V. Ramanathan, B. Reyers, S. Sörlin, *Science* **2015**, *347*, 736–746.
- [109] A. J. Martín, G. O. Larrazábal, J. Pérez-Ramírez, *Green Chem.* **2015**, *17*, 5114–5130.
- [110] H. A. Hansen, J. B. Varley, A. A. Peterson, J. K. Nørskov, *J. Phys. Chem. Lett.* **2013**, *4*, 388–392.
- [111] G. O. Larrazábal, A. J. Martín, J. Pérez-Ramírez, *J. Phys. Chem. Lett.* **2017**, *8*, 3933–3944.
- [112] S. Rasul, D. H. Anjum, A. Jedidi, Y. Minenkov, L. Cavallo, K. Takanebe, *Angew. Chem. Int. Ed.* **2015**, *54*, 2146–2150.
- [113] G. O. Larrazábal, A. J. Martín, S. Mitchell, R. Hauert, J. Pérez-Ramírez, *ACS Catal* **2016**, *6*, 6265–6274.
- [114] Y. Huang, Y. Deng, A. D. Handoko, G. K. L. Goh, B. S. Yeo, *ChemSusChem* **2018**, *11*, 320–326.
- [115] J. He, K. E. Dettelbach, D. A. Salvatore, T. Li, C. P. Berlinguette, *Angew. Chem. Int. Ed.* **2017**, *129*, 6164–6168.
- [116] Z. B. Hoffman, T. S. Gray, K. B. Moraveck, T. B. Gunnoe, G. Zangari, *ACS Catal* **2017**, *7*, 5381–5390.
- [117] D. Gao, R. M. Arán-Ais, H. S. Jeon, B. Roldan Cuenya, *Nat. Catal.* **2019**, *2*, 198–210.
- [118] M. Favaro, H. Xiao, T. Cheng, W. A. Goddard III, E. J. Crumlin, *PNAS* **2017**, *114*, 6706–6711.
- [119] O. G. Sánchez, Y. Y. Birdja, M. Bulut, J. Vaes, T. Breugelmans, D. Pant, *Current Opinion Green Sus. Chem.* **2019**, *16*, 47–56.
- [120] A. Zakutayev, *J. Mater. Chem. A* **2016**, *4*, 6742–6754.
- [121] Z. Q. Liang, T. T. Zhuang, A. Seifitokaldani, J. Li, C. W. Huang, C. S. Tan, Y. Li, P. de Luna, C. T. Dinh, Y. Hu, Q. Xiao, P. L. Hsieh, Y. Wang, F. Li, R. Quintero-Bermudez, Y. Zhou, P. Chen, Y. Pang, S. C. Lo, L. J. Chen, H. Tan, Z. Xu, S. Zhao, D. Sinton, E. H. Sargent, *Nat. Commun.* **2018**, *9*, 3828.
- [122] A. Miura, T. Takei, N. Kumada, *J. Asian Ceramic Soc.* **2014**, *2*, 326–328.
- [123] R. K. Sithole, L. F. E. MacHogo, M. A. Airo, S. S. Gqoba, M. J. Moloto, P. Shumbula, J. van Wyk, N. Moloto, *New J. Chem.* **2018**, *42*, 3042–3049.
- [124] T. Nakamura, N. Hiyoshi, H. Hayashi, T. Ebina, *Mater. Lett.* **2015**, *139*, 271–274.
- [125] G. O. Larrazábal, A. J. Martín, F. Krumeich, R. Hauert, J. Pérez-Ramírez, *ChemSusChem* **2017**, *10*, 1255–1265.

- [126] J. L. White, A. B. Bocarsly, *J. Electrochem. Soc.* **2016**, *163*, H410–H416.
- [127] Y. Lum, J. W. Ager, *Nat Catal* **2019**, *2*, 86–93.
- [128] R. G. Mariano, K. Mckelvey, H. S. White, M. W. Kanan, *Science* **2017**, *358*, 1187–1192.
- [129] D. Gao, I. Zegkinoglou, N. J. Divins, F. Scholten, I. Sinev, P. Grosse, B. Roldan Cuenya, *ACS Nano* **2017**, *11*, 4825–4831.
- [130] R. Gonzalez-Arrabal, N. Gordillo, M. S. Martin-Gonzalez, R. Ruiz-Bustos, F. Agulló-López, *J Appl Phys* **2010**, *107*, 103513.
- [131] S. J. Patil, D. S. Bodas, A. B. Mandale, S. A. Gangal, *Thin Solid Films* **2003**, *444*, 52–57.
- [132] D. Depla, J. Haemers, R. de Gryse, *Plasma Sources Sci. Technol* **2002**, *11*, 91–96.
- [133] Y. Lum, J. W. Ager, *Angew. Chem. Int. Ed.* **2018**, *130*, 560–563.
- [134] C. L. Yu, S. S. Wang, T. H. Chuang, *J. Electronic Mater.* **2002**, *31*, 488–493.
- [135] A. J. Martín, J. Pérez-Ramírez, *Joule* **2019**, *3*, 2602–2621.
- [136] Y. Y. Birdja, E. Pérez-Gallent, M. C. Figueiredo, A. J. Göttle, F. Calle-Vallejo, M. T. M. Koper, *Nat. Energy* **2019**, *4*, 732–745.
- [137] A. Vasileff, C. Xu, Y. Jiao, Y. Zheng, S. Z. Qiao, *Chem* **2018**, *4*, 1809–1831.
- [138] L. Zhang, Z. J. Zhao, J. Gong, *Angew. Chem. Int. Ed.* **2017**, *129*, 11482–11511.
- [139] M. Liu, Y. Pang, B. Zhang, P. de Luna, O. Voznyy, J. Xu, X. Zheng, C. T. Dinh, F. Fan, C. Cao, F. P. G. de Arquer, T. S. Safaei, A. Mepham, A. Klinkova, E. Kumacheva, T. Filleter, D. Sinton, S. O. Kelley, E. H. Sargent, *Nature* **2016**, *537*, 382–386.
- [140] A. S. Varela, M. Kroschel, T. Reier, P. Strasser, *Catal. Today* **2016**, *260*, 8–13.
- [141] C. T. Dinh, T. Burdyny, M. G. Kibria, A. Seifitokaldani, C. M. Gabardo, F. P. G. D. Arquer, A. Kiani, J. P. Edwards, P. de Luna, O. S. Bushuyev, C. Zou, R. Quintero-Bermudez, Y. Pang, D. Sinton, E. H. Sargent, *Science (1979)* **2018**, *360*, 783–787.
- [142] Y. Y. Birdja, M. T. M. Koper, *J. Am. Chem. Soc.* **2017**, *139*, 2030–2034.
- [143] M. R. Singh, Y. Kwon, Y. Lum, J. W. Ager, A. T. Bell, *J. Am. Chem. Soc.* **2016**, *138*, 13006–13012.
- [144] Y. Y. Birdja, E. Pérez-Gallent, M. C. Figueiredo, A. J. Göttle, F. Calle-Vallejo, M. T. M. Koper, *Nat Energy* **2019**, *4*, 732–745.
- [145] R. Kas, R. Kortlever, H. Yilmaz, M. T. M. Koper, G. Mul, *ChemElectroChem* **2015**, *2*, 354–358.
- [146] D. Raciti, M. Mao, J. H. Park, C. Wang, *J. Electrochem. Soc.* **2018**, *165*, F799–F804.
- [147] W. Luo, X. Nie, M. J. Janik, A. Asthagiri, *ACS Catal.* **2016**, *6*, 219–229.
- [148] C. Hahn, T. Hatsukade, Y. G. Kim, A. Vailionis, J. H. Baricuatro, D. C. Higgins, S. A. Nitopi, M. P. Soriaga, T. F. Jaramillo, *PNAS* **2017**, *114*, 5918–5923.
- [149] C. F. C. Lim, D. A. Harrington, A. T. Marshall, *Electrochim Acta* **2017**, *238*, 56–63.
- [150] B. Fuladpanjeh-Hojaghan, M. M. Elautohy, V. Kabanov, B. Heyne, M. Trifkovic, E. P. L. Roberts, *Angew. Chem. Int. Ed.* **2019**, *131*, 16971–16975.
- [151] D. Raciti, M. Mao, C. Wang, *Nanotechnology* **2018**, *29*.
- [152] P. Bumroongsakulsawat, G. H. Kelsall, *Electrochim Acta* **2014**, *141*, 216–225.

- [153] X. Chang, A. Malkani, X. Yang, B. Xu, *J. Am. Chem. Soc.* **2020**, *142*, 2975–2983.
- [154] A. Dutta, M. Rahaman, M. Mohos, A. Zanetti, P. Broekmann, *ACS Catal.* **2017**, *7*, 5431–5437.
- [155] H. Song, M. Im, J. T. Song, J. A. Lim, B. S. Kim, Y. Kwon, S. Ryu, J. Oh, *Appl. Catal. B: Environ.* **2018**, *232*, 391–396.
- [156] K. D. Yang, W. R. Ko, J. H. Lee, S. J. Kim, H. Lee, M. H. Lee, K. T. Nam, *Angew. Chem. Int. Ed.* **2017**, *129*, 814–818.
- [157] F. L. P. Veenstra, A. J. Martín, J. Pérez-Ramírez, *ChemSusChem* **2019**, *12*, 3501–3508.
- [158] N. Ackerl, P. Boerner, K. Wegener, *J. Laser Appl.* **2019**, *31*, 022501.
- [159] N. Ackerl, M. Warhanek, J. Gysel, K. Wegener, *J. European Ceramic Soc.* **2019**, *39*, 1635–1641.
- [160] H. Fang, J. Yang, M. Wen, Q. Wu, *Adv. Mater.* **2018**, *30*, 1–10.
- [161] K. Lange, M. Schulz-Ruhtenberg, J. Caro, *ChemElectroChem* **2017**, *4*, 570–576.
- [162] R. Weber, T. Graf, C. Freitag, A. Feuer, T. Kononenko, V. I. Konov, *Opt Express* **2017**, *25*, 3966.
- [163] V. Lang, T. Roch, A. F. Lasagni, *Adv. Eng. Mater.* **2016**, *18*, 1342–1348.
- [164] T. C. Chong, M. H. Hong, L. P. Shi, *Laser Photon. Rev.* **2010**, *4*, 123–143.
- [165] A. Gillner, J. Finger, P. Gretzki, M. Niessen, T. Bartels, M. Reininghaus, *J. Laser Micro Nanoeng.* **2019**, *14*, 129–137.
- [166] A. J. Bard, L. R. Faulkner, *Electrochemical Methods: Fundamentals and Applications*, John Wiley & Sons, Inc., **2001**.
- [167] T. A. Nijhuis, M. T. Kreutzer, A. C. J. Romijn, F. Kapteijn, J. A. Moulijn, *Chem. Eng. Sci.* **2001**, *56*, 823–829.
- [168] X. Feng, K. Jiang, S. Fan, M. W. Kanan, *J. Am. Chem. Soc.* **2015**, *137*, 4606–4609.
- [169] D. Ren, J. Fong, B. S. Yeo, *Nat. Commun.* **2018**, *9*, 925.
- [170] F. Calle-Vallejo, M. T. M. Koper, *Angew. Chem. Int. Ed.* **2013**, *52*, 7282–7285.
- [171] R. Kortlever, I. Peters, C. Balemans, R. Kas, Y. Kwon, G. Mul, M. T. M. Koper, *Chem. Commun.* **2016**, *52*, 10229–10232.
- [172] D. Ren, N. T. Wong, A. D. Handoko, Y. Huang, B. S. Yeo, *J. Phys. Chem. Lett.* **2016**, *7*, 20–24.
- [173] M. R. Singh, Y. Kwon, Y. Lum, J. W. Ager III, A. T. Bell, *J. Am. Chem. Soc.* **2016**, *138*, 13006–13012.
- [174] T. T. Zhuang, Z. Q. Liang, A. Seifitokaldani, Y. Li, P. de Luna, T. Burdyny, F. Che, F. Meng, Y. Min, R. Quintero-Bermudez, C. T. Dinh, Y. Pang, M. Zhong, B. Zhang, J. Li, P. N. Chen, X. L. Zheng, H. Liang, W. N. Ge, B. J. Ye, D. Sinton, S. H. Yu, E. H. Sargent, *Nat. Catal.* **2018**, *1*, 421–428.
- [175] J. R. Galan-Mascaros, *Catal. Sci. Technol.* **2020**, *10*, 1967–1974.
- [176] E. Brightman, G. Hinds, R. O'Malley, *J. Power Sources* **2013**, *242*, 244–254.
- [177] M. R. Thorson, K. I. Siil, P. J. A. Kenis, *J. Electrochem. Soc.* **2013**, *160*, F69–F74.

- [178] B. Schmid, C. Reller, S. S. Neubauer, M. Fleischer, R. Dorta, G. Schmid, *Catalysts* **2017**, *7*.
- [179] X. Wang, A. Xu, F. Li, S. F. Hung, D. H. Nam, C. M. Gabardo, Z. Wang, Y. Xu, A. Ozden, A. S. Rasouli, A. H. Ip, D. Sinton, E. H. Sargent, *J. Am. Chem. Soc.* **2020**, *142*, 3525–3531.
- [180] J. Li, Z. Wang, C. McCallum, Y. Xu, F. Li, Y. Wang, C. M. Gabardo, C. T. Dinh, T. T. Zhuang, L. Wang, J. Y. Howe, Y. Ren, E. H. Sargent, D. Sinton, *Nat. Catal.* **2019**, *2*, 1124–1131.
- [181] H. Xu, D. Rebollar, H. He, L. Chong, Y. Liu, C. Liu, C. J. Sun, T. Li, J. V. Muntean, R. E. Winans, D. J. Liu, T. Xu, *Nat. Energy* **2020**, *5*, 623–632.
- [182] L. R. L. Ting, R. García-Muelas, A. J. Martín, F. L. P. Veenstra, S. T. J. Chen, Y. Peng, E. Y. X. Per, S. Pablo-García, N. López, J. Pérez-Ramírez, B. S. Yeo, *Angew. Chem. Int. Ed.* **2020**, *59*, 21072–21079.
- [183] Y. Huang, Y. Chen, T. Cheng, L. W. Wang, W. A. Goddard III, *ACS Energy Lett.* **2018**, *3*, 2983–2988.
- [184] Y. Zheng, A. Vasileff, X. Zhou, Y. Jiao, M. Jaroniec, S. Z. Qiao, *J. Am. Chem. Soc.* **2019**, *141*, 7646–7659.
- [185] Q. Li, R. García-Muelas, N. López, *Nat. Commun.* **2018**, *9*, 526.
- [186] J. P. Perdew, K. Burke, M. Ernzerhof, *Phys. Rev. Lett.* **1996**, *77*, 3865–3868.
- [187] S. Grimme, *J. Comput. Chem.* **2006**, *27*, 1787–1799.
- [188] N. Almora-Barrios, G. Carchini, P. Błoński, N. López, *J. Chem. Theory Comput.* **2014**, *10*, 5002–5009.
- [189] M. Garcia-Ratés, N. López, *J. Chem. Theory Comp.* **2016**, *12*, 1331–1341.
- [190] M. Garcia-Ratés, R. García-Muelas, N. López, *J. Phys. Chem. C* **2017**, *121*, 13803–13809.
- [191] R. B. Sandberg, J. H. Montoya, K. Chan, J. K. Nørskov, *Surf. Sci.* **2016**, *654*, 56–62.
- [192] G. Henkelman, H. Jónsson, *J. Chem. Phys.* **2000**, *113*, 9978–9985.
- [193] M. García-Mota, B. Bridier, J. Pérez-Ramírez, N. López, *J. Catal.* **2010**, *273*, 92–102.
- [194] S. Pablo-García, M. Álvarez-Moreno, N. López, *Int. J. Quantum Chem.* **2021**, *121*, 1–8.
- [195] J. J. Lv, M. Jouny, W. Luc, W. Zhu, J. J. Zhu, F. Jiao, *Adv. Mater.* **2018**, *30*, 1–8.
- [196] G. Kresse, J. Hafner, *Phys. Rev. B* **1993**, *47*, 558–561.
- [197] G. Kresse, D. Joubert, *Phys. Rev. B* **1999**, *59*, 1758–1775.
- [198] Y. G. Kim, J. H. Baricuatro, A. Javier, J. M. Gregoire, M. P. Soriaga, *Langmuir* **2014**, *30*, 15053–15056.
- [199] M. Álvarez-Moreno, C. de Graaf, N. López, F. Maseras, J. M. Poblet, C. Bo, *J. Chem. Inf. Model.* **2015**, *55*, 95–103.
- [200] G. García-Muelas, S. Pablo-García, N. Lopez, *database iochem-bd* (Online Dataset) 2020, available online at <https://doi.org/10.19061/iochem-bd-1-159>.
- [201] R. García-Muelas, F. Dattila, T. Shinagawa, A. J. Martín, J. Pérez-Ramírez, N. López, *J. Phys. Chem. Lett.* **2018**, *9*, 7153–7159.

- [202] N. Yang, A. J. Medford, X. Liu, F. Studt, T. Bligaard, S. F. Bent, J. K. Nørskov, *J. Am. Chem. Soc.* **2016**, *138*, 3705–3714.
- [203] E. Walker, S. C. Ammal, G. A. Terejanu, A. Heyden, *J. Phys. Chem. C* **2016**, *120*, 10328–10339.
- [204] J. E. Sutton, D. G. Vlachos, *J. Catal.* **2016**, *338*, 273–283.
- [205] A. J. Medford, J. Wellendorff, A. Vojvodic, F. Studt, F. Abild-Pedersen, K. W. Jacobsen, T. Bligaard, J. K. Nørskov, *Science (1979)* **2014**, *345*, 193–197.
- [206] D. B. West, *Introduction to Graph Theory*, Prentice Hall, **2001**.
- [207] F. Dattila, R. Garclá-Muelas, N. López, *ACS Energy Lett.* **2020**, *5*, 3176–3184.
- [208] E. Pérez-Gallent, G. Marcandalli, M. C. Figueiredo, F. Calle-Vallejo, M. T. M. Koper, *J. Am. Chem. Soc.* **2017**, *139*, 16412–16419.
- [209] J. Resasco, L. D. Chen, E. Clark, C. Tsai, C. Hahn, T. F. Jaramillo, K. Chan, A. T. Bell, *J. Am. Chem. Soc.* **2017**, *139*, 11277–11287.
- [210] K. Jiang, R. B. Sandberg, A. J. Akey, X. Liu, D. C. Bell, J. K. Nørskov, K. Chan, H. Wang, *Nat. Catal.* **2018**, *1*, 111–119.
- [211] Y. Pang, J. Li, Z. Wang, C. S. Tan, P. L. Hsieh, T. T. Zhuang, Z. Q. Liang, C. Zou, X. Wang, P. de Luna, J. P. Edwards, Y. Xu, F. Li, C. T. Dinh, M. Zhong, Y. Lou, D. Wu, L. J. Chen, E. H. Sargent, D. Sinton, *Nat. Catal.* **2019**, *2*, 251–258.
- [212] H. Xiao, T. Cheng, W. A. Goddard III, *J. Am. Chem. Soc.* **2017**, *139*, 130–136.
- [213] F. L. P. Veenstra, N. Ackerl, A. J. Martín, J. Pérez-Ramírez, *Chem* **2020**, *6*, 1707–1722.
- [214] T. T. Zhuang, Y. Pang, Z. Q. Liang, Z. Wang, Y. Li, C. S. Tan, J. Li, C. T. Dinh, P. de Luna, P. L. Hsieh, T. Burdyny, H. H. Li, M. Liu, Y. Wang, F. Li, A. Proppe, A. Johnston, D. H. Nam, Z. Y. Wu, Y. R. Zheng, A. H. Ip, H. Tan, L. J. Chen, S. H. Yu, S. O. Kelley, D. Sinton, E. H. Sargent, *Nat. Catal.* **2018**, *1*, 946–951.
- [215] A. Herzog, A. Bergmann, H. S. Jeon, J. Timoshenko, S. Köhl, C. Rettenmaier, M. Lopez Luna, F. T. Haase, B. Roldan Cuenya, *Angew. Chem. Int. Ed.* **2021**, *60*, 7426–7435.
- [216] M. T. Tang, H. J. Peng, J. H. Stenlid, F. Abild-Pedersen, *J. Phys. Chem. C* **2021**, *125*, 26437–26447.
- [217] O. S. Bushuyev, P. de Luna, C. T. Dinh, L. Tao, G. Saur, J. van de Lagemaat, S. O. Kelley, E. H. Sargent, *Joule* **2018**, *2*, 825–832.
- [218] W. R. D. S. Trindade, R. G. D. Santos, *Renew. Sustain. Energy Rev.* **2017**, *69*, 642–651.
- [219] T. Haas, R. Krause, R. Weber, M. Demler, G. Schmid, *Nat. Catal.* **2018**, *1*, 32–39.
- [220] K. Chakrapani, S. Sampath, *Chem. Commun.* **2015**, *51*, 9690–9693.
- [221] B. Beverskoga, I. Puigdomenech, *J. Electrochem. Soc.* **1997**, *144*, 3476–3483.
- [222] I. Platzman, R. Brenner, H. Haick, R. Tannenbaum, *J. Phys. Chem. C* **2008**, *112*, 1101–1108.
- [223] G. Kresse, J. Furthmüller, *Comput. Mater. Sci.* **1996**, *6*, 15–50.
- [224] P. E. Blochl, *Phys. Rev. B* **1994**, *50*, 17953–17979.
- [225] H. J. Monkhorst, J. D. Pack, *Phys. Rev. B* **1976**, *13*, 5188–5192.

- [226] X. Duan, O. Warschkow, A. Soon, B. Delley, C. Stampfl, *Phys. Rev. B* **2010**, *81*, 1–15.
- [227] A. Łukomska, J. Sobkowski, *J. Electroanal. Chem.* **2004**, *567*, 95–102.
- [228] J. P. Guthrie, *J. Am. Chem. Soc* **1991**, *113*, 7249–7255.
- [229] M. Englisch, A. Jentys, J. A. Lercher, *J. Catal.* **1997**, *166*, 25–35.
- [230] J. Pérez-Ramírez, N. López, *Nat. Catal.* **2019**, *2*, 971–976.
- [231] M. Pourbaix, *Atlas of Electrochemical Equilibria in Aqueous Solutions*, National Association of Corrosion, Houston, **1974**.
- [232] Y. Hori, I. Takahashi, O. Koga, N. Hoshi, *J. Mol. Catal. A: Chem.* **2003**, *199*, 39–47.
- [233] M. S. Frei, F. L. P. Veenstra, D. Capeder, J. A. Stewart, D. Curulla-Ferré, A. J. Martín, C. Mondelli, J. Pérez-Ramírez, *Small Methods* **2021**, *5*, 1–9.
- [234] R. E. Blankenship, D. M. Tiede, J. Barber, G. W. Brudvig, G. Fleming, M. Ghirardi, M. R. Gunner, W. Junge, D. M. Kramer, A. Melis, T. A. Moore, C. C. Moser, D. G. Nocera, A. J. Nozik, D. R. Ort, W. W. Parson, R. C. Prince, R. T. Sayre, *Science* **2011**, *332*, 805–809.
- [235] H. Yang, Y. Huang, J. Deng, Y. Wu, N. Han, C. Zha, L. Li, Y. Li, *J. Energy Chem.* **2019**, *37*, 93–96.
- [236] U. Kang, S. k. Choi, D. J. Ham, S. M. Ji, W. Choi, D. S. Han, A. Abdel-Wahab, H. Park, *Energy Environ. Sci.* **2015**, *8*, 2638–2643.
- [237] X. Zhou, R. Liu, K. Sun, Y. Chen, E. Verlage, S. A. Francis, N. S. Lewis, C. Xiang, *ACS Energy Lett.* **2016**, *1*, 764–770.
- [238] J. Jia, L. C. Seitz, J. D. Benck, Y. Huo, Y. Chen, J. W. D. Ng, T. Bilir, J. S. Harris, T. F. Jaramillo, *Nat. Commun.* **2016**, *7*, 13237.
- [239] J. D. Benck, S. C. Lee, K. D. Fong, J. Kibsgaard, R. Sinclair, T. F. Jaramillo, *Adv. Energy Mater.* **2014**, *4*, 1–8.
- [240] T. N. Huan, D. A. Dalla Corte, S. Lamaison, D. Karapinar, L. Lutz, N. Menguy, M. Foldyna, S. H. Turren-Cruz, A. Hagfeldt, F. Bella, M. Fontecave, V. Mougel, *PNAS* **2019**, *116*, 9735–9740.
- [241] J. He, C. Janáky, *ACS Energy Lett.* **2020**, *5*, 1996–2014.
- [242] A. J. Martín, F. L. P. Veenstra, J. Lüthi, R. Verel, J. Pérez-Ramírez, *Chem. Catal.* **2021**, *1*, 1505–1518.
- [243] R. García-Muelas, Q. Li, N. López, *ACS Catal.* **2015**, *5*, 1027–1036.
- [244] J. Neugebauer, M. Scheser, *Phys. Rev. B* **1992**, *46*, 16067–16080.
- [245] N. D. Lang, W. Kohn, *Phys. Rev. B* **1973**, *7*, 3541–3549.
- [246] R. García-Muelas, N. López, *J. Phys. Chem. C* **2014**, *118*, 17531–17537.
- [247] S. Ma, M. Sadakiyo, R. Luo, M. Heima, M. Yamauchi, P. J. A. Kenis, *J. Power Sources* **2016**, *301*, 219–228.
- [248] T. T. H. Hoang, S. Ma, J. I. Gold, P. J. A. Kenis, A. A. Gewirth, *ACS Catal.* **2017**, *7*, 3313–3321.

- [249] Y. Wang, H. Shen, K. J. T. Livi, D. Raciti, H. Zong, J. Gregg, M. Onadeko, Y. Wan, A. Watson, C. Wang, *Nano Lett.* **2019**, *19*, 8461–8468.
- [250] N. S. Romero Cuellar, K. Wiesner-Fleischer, M. Fleischer, A. Rucki, O. Hinrichsen, *Electrochim Acta* **2019**, *307*, 164–175.

# Appendix A

## Annexes

### Chapter 2

**Table A.1.** Target and actual loading of the modified Cu<sub>2</sub>O and Cu<sub>3</sub>N catalysts expressed as the wt.% In obtained by SEM-EDX spectroscopy and the atomic ratio of Cu to In. Related to **Figure 2.2**.

Catalyst	Target wt.% In	Actual wt.% In	Actual Cu/In
In <sub>2</sub> O <sub>3</sub> /Cu <sub>2</sub> O	0.5	0.3	30
	1.5	0.9	92
	4.0	2.6	252
In <sub>2</sub> O <sub>3</sub> /Cu <sub>3</sub> N	0.5	0.1	32
	1.5	0.3	98
	4.0	1.7	400

**Table A.2.** Overview of CO and H<sub>2</sub> partial current density obtained at various interfacial densities over microfabricated electrodes. Related to **Figure 2.6**.

$\rho_{\text{int}}$ cm cm <sup>-2</sup>	Island $d$ $\mu\text{m}$	In <sub>2</sub> O <sub>3</sub> /Cu <sub>3</sub> N		In <sub>2</sub> O <sub>3</sub> /Cu <sub>2</sub> O	
		$j_{\text{CO}}$ $\mu\text{A cm}^{-2}$	$j_{\text{H}_2}$ $\mu\text{A cm}^{-2}$	$j_{\text{CO}}$ $\mu\text{A cm}^{-2}$	$j_{\text{H}_2}$ $\mu\text{A cm}^{-2}$
0 <sup>a</sup>	0 <sup>a</sup>	36 <sup>a</sup>	1800 <sup>a</sup>	25 <sup>a</sup>	1100 <sup>a</sup>
184	50	102	1500	86	250
764	12.5	116	1200	92	148
2045	5	198	561	11	143
4440	2.5	176	532	2	148

a Pure Cu<sub>3</sub>N or Cu<sub>2</sub>O phase



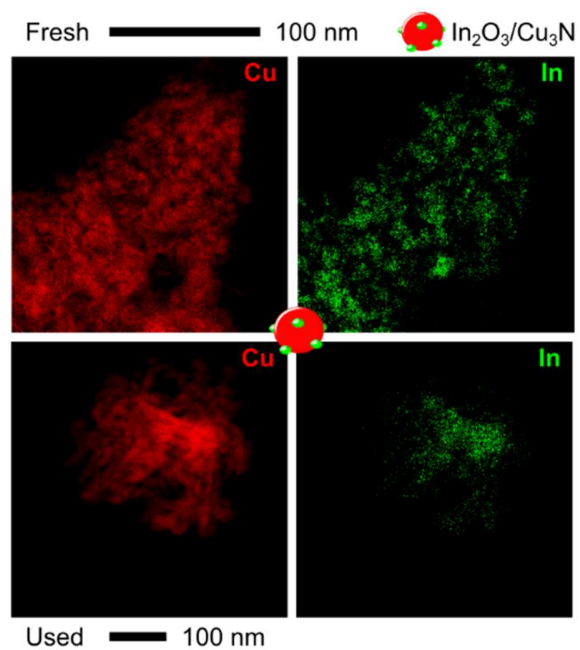


**Figure A.1.** Elemental mapping of In<sub>2</sub>O<sub>3</sub>/Cu<sub>3</sub>N (1.7 wt.% In) obtained by STEM-EDXS showing the distinct distribution of indium and the copper phase prior and post reaction. Related to **Figure 2.2**.

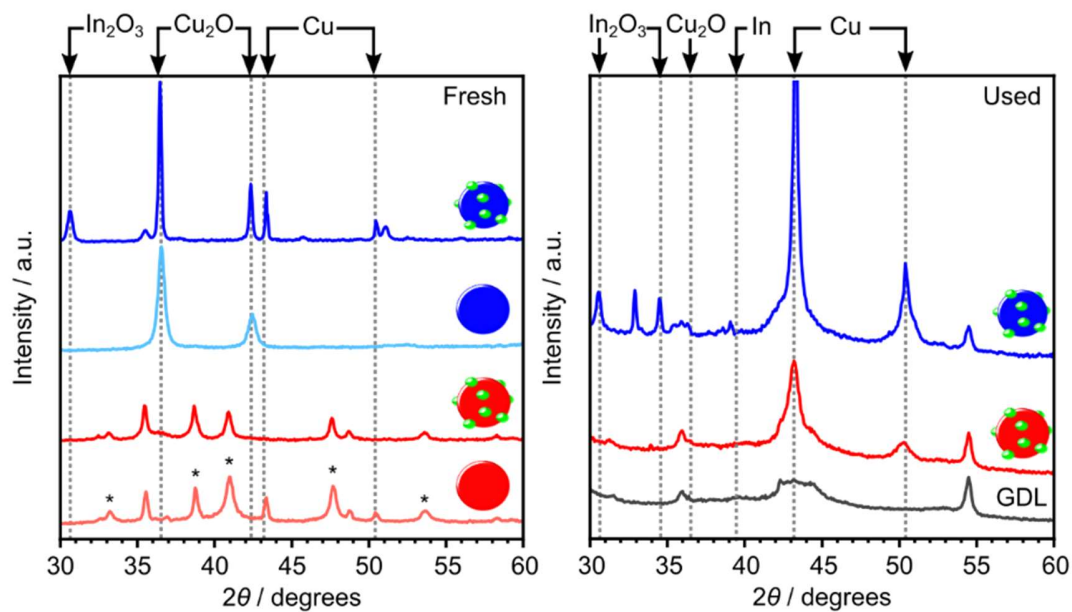


**Figure A.2.** XRD patterns of representative fresh and used powder systems (1.7 wt.% In ( $\text{In}_2\text{O}_3/\text{Cu}_2\text{O}$ ) and 2.6 wt.% In ( $\text{In}_2\text{O}_3/\text{Cu}_3\text{N}$ )). The patterns of  $\text{Cu}_3\text{N}$  and  $\text{Cu}_2\text{O}$  over which indium oxide was deposited and that of the underlying carbon-based gas diffusion layer for the case of the used catalysts are provided for reference. Indium-related reflections are absent in the case of  $\text{In}_2\text{O}_3/\text{Cu}_3\text{N}$  in accordance with the high dispersion observed by elemental mapping. The asterisks indicate reflections associated to  $\text{Cu}_3\text{N}$ . The positions of the main reflections for other relevant phases are indicated. Related to **Figure 2.2**.

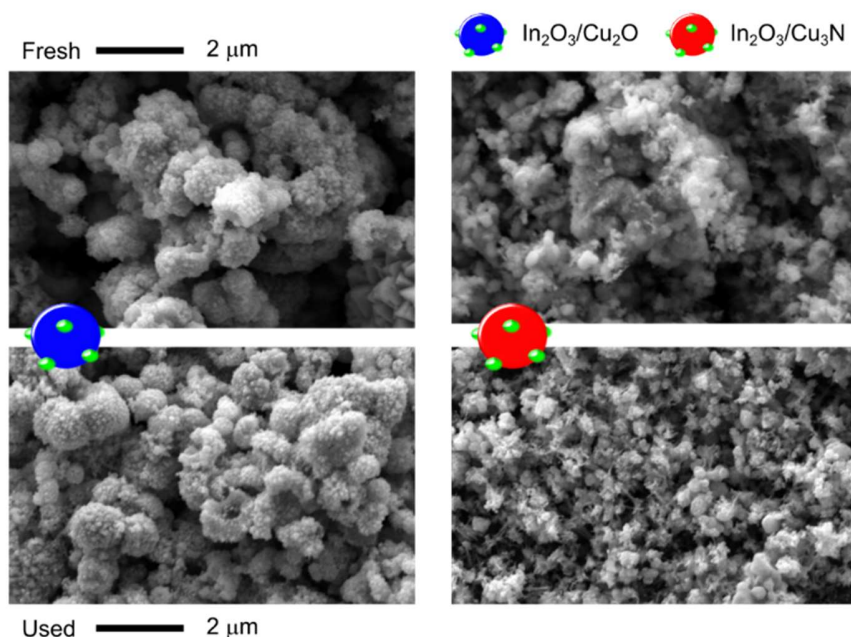


**Figure A.3.** Representative SEM micrographs of catalysts in powder form before and after reaction. Indium loadings shown: 0.9 wt.% for  $\text{In}_2\text{O}_3/\text{Cu}_2\text{O}$  and 0.3 wt.% for  $\text{In}_2\text{O}_3/\text{Cu}_3\text{N}$ . Operating conditions:  $-0.60\text{ V vs. RHE}$  in  $0.1\text{ M KHCO}_3$  saturated with  $\text{CO}_2$  (pH of 6.8) for 90 min. Related to **Figure 2.2**.

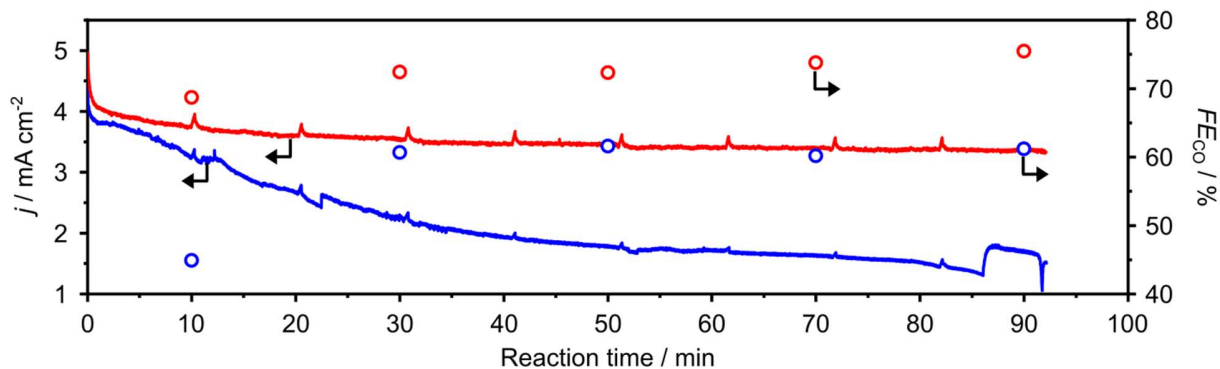


**Figure A.4.** Evolution of the current density and Faradaic efficiency toward CO for  $\text{In}_2\text{O}_3/\text{Cu}_3\text{N}$  (1.7 wt.% In, **blue**) and  $\text{In}_2\text{O}_3/\text{Cu}_2\text{O}$  (2.6 wt.% In, **red**) during 90 min electrolysis. Spikes correspond to determination of the uncompensated resistance by electrochemical impedance spectroscopy. Operation conditions:  $-0.60\text{ V vs. RHE}$  in  $0.1\text{ M KHCO}_3$  saturated with  $\text{CO}_2$  (pH of 6.8). Related to **Figure 2.3**.

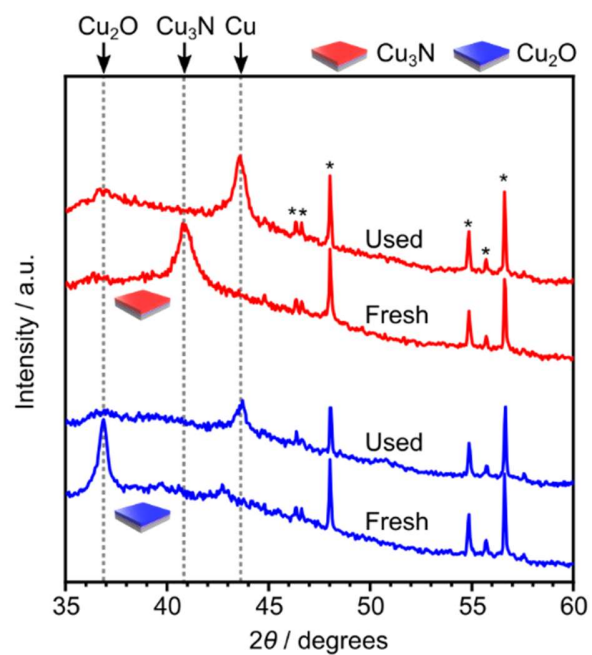


**Figure A.5.** XRD patterns of microfabricated  $\text{Cu}_2\text{O}$  and  $\text{Cu}_3\text{N}$  electrodes before and after exposure to  $\text{eCO}_2\text{R}$  conditions. The main reflections of the fresh and reduced copper phases are indicated. Used electrodes exclusively show the presence of metallic copper. Asterisks indicate reflections stemming from underlying layers, namely Ta,  $\text{SiO}_x$ , or Si. Related to **Figure 2.4**.

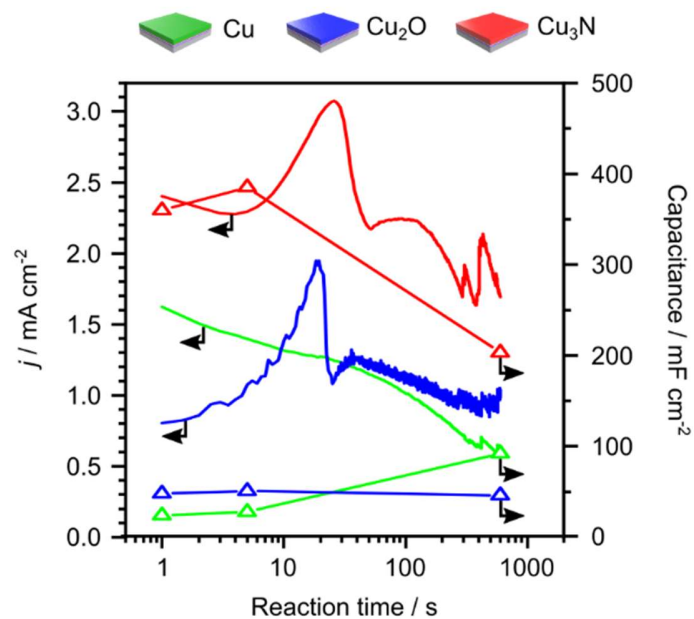


**Figure A.6.** Evolution of the current normalized by the geometric area and of the double layer capacitance with time of unmodified copper phases. Positive currents indicate reduction. Operating conditions:  $-0.60$  V *vs.* RHE in  $0.1$  M  $\text{KHCO}_3$  saturated with  $\text{CO}_2$  (pH of 6.8). Related to **Figure 2.4**.

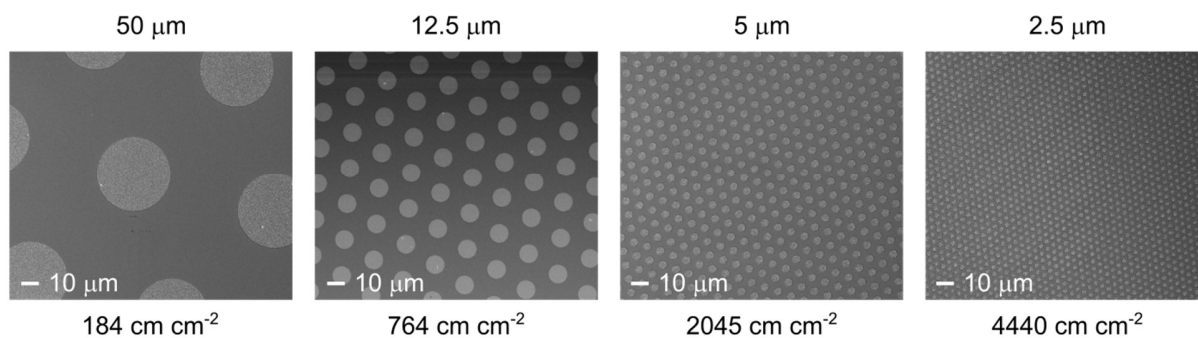


**Figure A.7.** SEM micrographs of fresh microfabricated electrodes showing the different regular hexagonal patterns of indium oxide islands aiming a controlled variation of the interfacial density. Island diameters are indicated above and interfacial density below the images. Related to **Figure 2.5**.

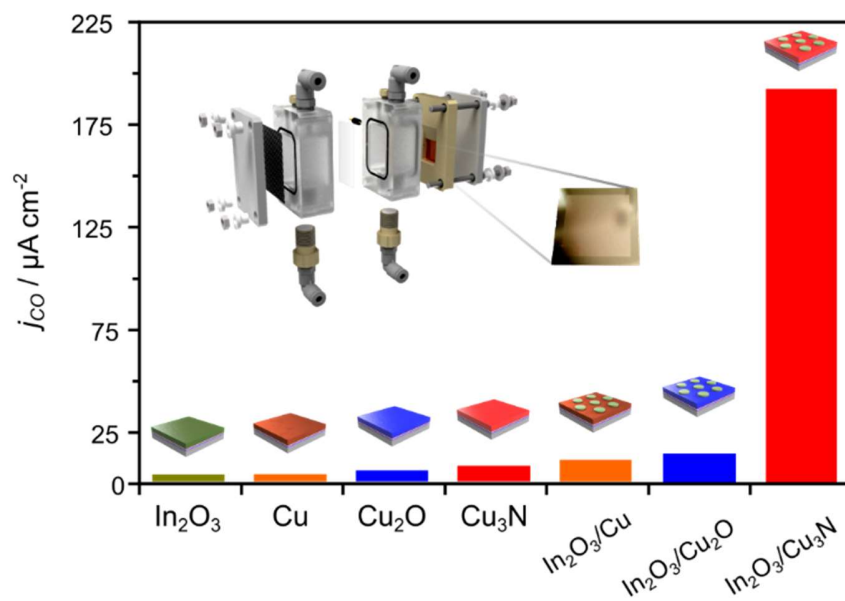


**Figure A.8.** Electrocatalytic activity toward CO over pure indium and copper phases. The activity for multicomponent systems is added for reference (values corresponding to indium oxide islands of 5  $\mu m$  in **Figure 2.5**). Operating conditions:  $-0.60 V$  vs. RHE in 0.1 M  $KHCO_3$  saturated with  $CO_2$  (pH of 6.8) for 600 s. Related to **Figure 2.6**.

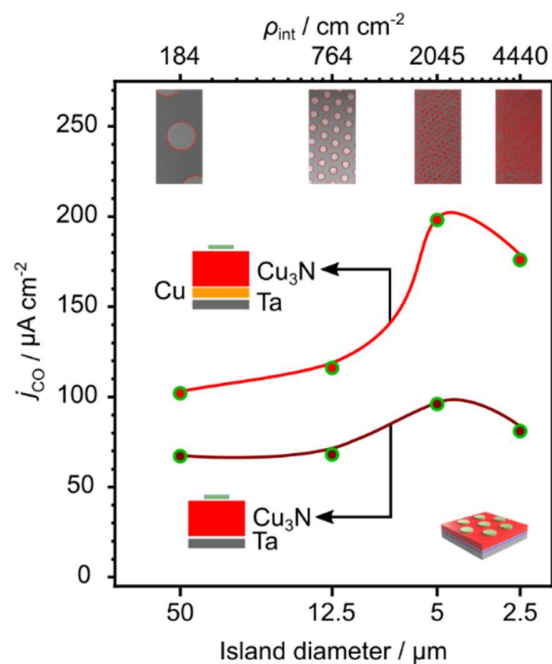


**Figure A.9.** Electrocatalytic activity of microstructured  $\text{In}_2\text{O}_3/\text{Cu}_3\text{N}$  systems with different interfacial density  $\rho_{\text{int}}$  with and without a 10 nm copper layer underneath aiming to improve the homogenization of the current density on the surface of the electrode, in view of the semiconducting nature of the nitride. Trend lines are added to guide the eye. Operating conditions:  $-0.60$  V *vs.* RHE in 0.1 M  $\text{KHCO}_3$  saturated with  $\text{CO}_2$  (pH of 6.8) for 600 s. Related to **Figure 2.6**.

## Chapter 3

**Table A.3.** Reactions considered in the model and corresponding stoichiometric parameters:  $n_k$  and  $m_k$  are the stoichiometric coefficients for  $\text{CO}_2$  and  $\text{OH}^-$ , respectively, and  $z_k$  the number of electrons transferred per molecule of product. Related to **Figure 3.4**.

Reaction	$n_k$	$m_k$	$z_k$
$2\text{H}_2\text{O} + 2\text{e}^- \rightarrow \text{H}_2 + 2\text{OH}^-$	-	2	2
$\text{CO}_2 + \text{H}_2\text{O} + 2\text{e}^- \rightarrow \text{CO} + 2\text{OH}^-$	1	2	2
$\text{CO}_2 + \text{H}_2\text{O} + 2\text{e}^- \rightarrow \text{HCOO}^- + \text{OH}^-$	1	1	2
$\text{CO}_2 + 6\text{H}_2\text{O} + 8\text{e}^- \rightarrow \text{CH}_4 + 8\text{OH}^-$	1	8	8
$2\text{CO}_2 + 9\text{H}_2\text{O} + 12\text{e}^- \rightarrow \text{C}_2\text{H}_5\text{OH} + 12\text{OH}^-$	2	12	12
$2\text{CO}_2 + 8\text{H}_2\text{O} + 12\text{e}^- \rightarrow \text{C}_2\text{H}_4 + 12\text{OH}^-$	2	12	12
$2\text{CO}_2 + 10\text{H}_2\text{O} + 14\text{e}^- \rightarrow \text{C}_2\text{H}_6 + 14\text{OH}^-$	2	14	14
$3\text{CO}_2 + 13\text{H}_2\text{O} + 18\text{e}^- \rightarrow \text{C}_3\text{H}_7\text{OH} + 18\text{OH}^-$	3	18	18

**Table A.4.** Bulk equilibria reactions at 298 K considered in the model and corresponding rate constants. Related to **Figure 3.4**.

Reaction	$k_{\text{forward}}$ $\text{M}^{-1} \text{s}^{-1}$	$k_{\text{reverse}}$ $\text{s}^{-1}$
$\text{CO}_2(\text{aq}) + \text{OH}^- \leftrightarrow \text{HCO}_3^-$	$5.93 \cdot 10^3$	$1.34 \cdot 10^{-4}$
$\text{HCO}_3^- + \text{OH}^- \leftrightarrow \text{CO}_3^{2-} + \text{H}_2\text{O}$	$1 \cdot 10^9$ (assumed)	$2.5 \cdot 10^4$

**Table A.5.** Diffusion coefficients at infinite dilution at 298 K and bulk concentrations in  $\text{CO}_2$ -saturated 0.1 M  $\text{KHCO}_3$ . Related to **Figure 3.4**.

Species	$D_0$ $\text{m}^2 \text{s}^{-1}$	$C_{\text{bulk}}$ $\text{mol m}^{-3}$
$\text{CO}_2$	$1.91 \cdot 10^{-9}$	34.2
$\text{HCO}_3^-$	$9.23 \cdot 10^{-10}$	99.7
$\text{CO}_3^{2-}$	$1.19 \cdot 10^{-9}$	29.4
$\text{OH}^-$	$5.27 \cdot 10^{-9}$	$6.3 \cdot 10^{-2}$



**Table A.6.** Cell voltages at different cathodic potentials in 0.1 M KHCO<sub>3</sub> over microstructured electrodes. Related to **Figure 3.5**.

<b>Micro-probe length</b> <b>μm</b>	<b>-0.60 V vs.</b> <b>RHE</b> <b>V</b>	<b>-0.80 V vs.</b> <b>RHE</b> <b>V</b>	<b>-1.05 V vs.</b> <b>RHE</b> <b>V</b>	<b>-1.30 V vs.</b> <b>RHE</b> <b>V</b>
LA-Cu-0 <sup>a</sup>	3.24	4.00	5.40	7.40
LA-Cu-20	3.30	4.21	5.70	8.40
LA-Cu-40	3.14	3.76	5.22	7.88
LA-Cu-60	3.35	4.37	5.60	7.80
LA-Cu-100	3.50	4.10	5.15	7.20
LA-Cu-130	3.45	4.50	5.75	8.92

<sup>a</sup> LA-Cu-0 was also tested at -1.2 V vs. RHE, 5.97 V

**Table A.7.** Faradaic efficiencies for secondary products at different potentials on microstructured electrodes. Related to **Figure 3.2**.

Micro-probe length $\mu\text{m}$	Potential $E$ vs. RHE V	$\text{CH}_4$ FE %	$\text{CH}_3\text{OH}$ FE %	$\text{C}_2\text{H}_4\text{O}$ FE %	$\text{C}_2\text{H}_6\text{O}_2$ FE %	Acetone FE %	Propionaldehyde FE %	Allyl alcohol FE %
Cu foil	-0.60	0	0	0	1	0	0	0
LA-Cu-0	-0.60	0	0	0	0	0	0	0
LA-Cu-20	-0.60	0	0.129	0.386	2.573	1.287	0	0
LA-Cu-40	-0.60	0	0.095	0.284	0	0	0.190	0
LA-Cu-60	-0.60	0	0.082	0.082	0.082	0.041	0.164	0.082
LA-Cu-100	-0.60	0	0.058	0.404	0	0	0.346	0
LA-Cu-130	-0.60	0	0	0	0	0	0	0
Cu foil	-0.80	0	0	0	1.917	0	0	0
LA-Cu-0	-0.80	0	0.014	0	0	0	0	0
LA-Cu-20	-0.80	0	0.034	0.103	0	0.855	0.274	0.308
LA-Cu-40	-0.80	0	0.056	0.111	0	0.028	0.223	0.167
LA-Cu-60	-0.80	0	0.044	0.074	0.088	0	0.118	0.324
LA-Cu-100	-0.80	0	0	0	0	0	0	0
LA-Cu-130	-0.80	0	0.047	0.095	0.111	0	0.190	0.605
Cu foil	-1.05	0	0.116	0	0	0	0.225	0.859
LA-Cu-0	-1.05	0	0.087	0	0	0	0	1.711
LA-Cu-20	-1.05	0	0.108	0.108	1.294	0	0.647	1.213
LA-Cu-40	-1.05	0	0.030	0.100	0.450	0	0.200	0.599
LA-Cu-60	-1.05	0	0.029	0.775	0.097	0	0.581	0.775
LA-Cu-100	-1.05	0	0.093	0.037	1.773	0	0.187	0.630
LA-Cu-130	-1.05	0	0	0.092	0	0	0.184	0.415
LA-Cu-0	-1.20	0	0.026	0	0	0	0	0.210
Cu foil	-1.30	0	0.051	0	0.059	0	0.041	0.314
LA-Cu-0	-1.30	0	0.051	0.051	0	0	0	0.230
LA-Cu-20	-1.30	3	0.057	0.057	0.137	0	0.106	0.456
LA-Cu-40	-1.30	1.5	0.049	0	0	0	0	0.294
LA-Cu-60	-1.30	1.4	0.049	0.063	0.102	0	0.068	0.322
LA-Cu-100	-1.30	0	0.013	0.022	0.026	0	0.087	0.167
LA-Cu-130	-1.30	1.6	0.095	0	0.190	0.009	0	0

**Table A.8.** Double layer capacitances and ratios related to Cu foil of microstructured electrodes. Related to **Figure 3.1**.

<b>Electrode</b>	<b>Capacitance <math>\mu\text{F cm}^{-2}</math></b>	<b>Ratio -</b>
Cu foil	27.63	1.00
LA-Cu-0	84.86	3.02
LA-Cu-20	173.27	6.40
LA-Cu-40	768.92	27.80
LA-Cu-60	864.11	32.12
LA-Cu-100	1309.71	43.37
LA-Cu-130	1636.76	59.21

**Table A.9.** Faradaic efficiencies for major products at different potentials in 0.1 M KHCO<sub>3</sub> on microstructured electrodes. Related to **Figure 3.2**.

Micro-probe length $\mu\text{m}$	Potential <i>E vs. RHE</i> V	H <sub>2</sub> <i>FE</i> %	CO <i>FE</i> %	HCO <sub>2</sub> <sup>-</sup> <i>FE</i> %	C <sub>2</sub> H <sub>4</sub> <i>FE</i> %	C <sub>2</sub> H <sub>3</sub> O <sub>2</sub> <sup>-</sup> <i>FE</i> %	C <sub>2</sub> H <sub>5</sub> OH <i>FE</i> %	C <sub>3</sub> H <sub>7</sub> OH <i>FE</i> %
Cu foil	-0.60	100	0.3	4.3	2.0	0.8	0.0	0.0
LA-Cu-0	-0.60	87	2.2	9.5	0.0	0.4	0.0	0.0
LA-Cu-20	-0.60	67	2.7	5.5	0.1	13.3	2.5	0.0
LA-Cu-40	-0.60	29	12.0	22.3	0.1	1.6	5.4	0.0
LA-Cu-60	-0.60	46	6.0	19.7	0.1	1.4	2.8	0.0
LA-Cu-100	-0.60	41	11.0	24.9	0.0	1.2	0.9	0.0
LA-Cu-130	-0.60	61	10.9	19.3	0.0	0.9	0.5	0.0
Cu foil	-0.80	66	6.0	29.4	1.9	0.0	0.0	0.0
LA-Cu-0	-0.80	74	3.3	26.0	11.0	0.0	0.6	0.0
LA-Cu-20	-0.80	45	5.2	23.4	0.1	0.0	3.3	1.6
LA-Cu-40	-0.80	65	3.0	21.8	0.1	0.0	2.3	1.6
LA-Cu-60	-0.80	52	2.0	11.2	7.0	0.0	5.9	3.2
LA-Cu-100	-0.80	54	4.0	23.0	2.0	0.0	2.0	2.0
LA-Cu-130	-0.80	36	3.0	14.0	30.0	0.8	9.8	5.8
Cu foil	-1.05	55	6.9	15.7	0.0	0.0	2.3	1.4
LA-Cu-0	-1.05	35	2.1	3.5	24.0	0.0	5.3	0.9
LA-Cu-0 <sup>b</sup>	-1.05 <sup>b</sup>	63 <sup>b</sup>	1.2 <sup>b</sup>	20.9 <sup>b</sup>	1.8 <sup>b</sup>	0.5 <sup>b</sup>	6.7 <sup>b</sup>	4.9 <sup>b</sup>
LA-Cu-20	-1.05	51	0.1	9.0	26.0	0.0	8.6	5.3
LA-Cu-40	-1.05	52	0.1	7.6	25.0	0.0	8.7	4.0
LA-Cu-40 <sup>a</sup>	-1.05 <sup>a</sup>	62 <sup>a</sup>	2.5 <sup>a</sup>	12.3 <sup>a</sup>	19.8 <sup>a</sup>	0.6 <sup>a</sup>	7.2 <sup>a</sup>	5.2 <sup>a</sup>
LA-Cu-40 <sup>b</sup>	-1.05 <sup>b</sup>	55 <sup>b</sup>	0.0 <sup>b</sup>	10.4 <sup>b</sup>	20.0 <sup>b</sup>	0.5 <sup>b</sup>	10.8 <sup>b</sup>	4.8 <sup>b</sup>
LA-Cu-60	-1.05	55	0.1	8.0	22.0	0.0	9.0	3.7
LA-Cu-100	-1.05	77	0.1	14.0	16.0	0.0	10.2	4.2
LA-Cu-100 <sup>a</sup>	-1.05 <sup>a</sup>	55 <sup>a</sup>	2.3 <sup>a</sup>	13.0 <sup>a</sup>	8.7 <sup>a</sup>	0.7 <sup>a</sup>	8.9 <sup>a</sup>	6.3 <sup>a</sup>
LA-Cu-100 <sup>b</sup>	-1.05 <sup>b</sup>	58 <sup>b</sup>	0.4 <sup>b</sup>	9.6 <sup>b</sup>	17.7 <sup>b</sup>	0.6 <sup>b</sup>	10.6 <sup>b</sup>	5.2 <sup>b</sup>
LA-Cu-130	-1.05	68	2.0	20.2	14.0	0.5	5.7	3.1
LA-Cu-0	-1.20	75	0.4	0.5	0.0	0.0	5.3	0.9
Cu foil	-1.30	53	7.9	1.7	0.1	0.0	6.4	0.6
LA-Cu-0	-1.30	89	0.4	0.4	0.0	0.0	6.4	0.9
LA-Cu-20	-1.30	40	3.0	0.2	35.4	0.0	13.4	1.9
LA-Cu-40	-1.30	58	0.3	2.6	6.2	0.1	7.5	1.3
LA-Cu-40 <sup>a</sup>	-1.30 <sup>a</sup>	60 <sup>a</sup>	0.8 <sup>a</sup>	3.3 <sup>a</sup>	32.9 <sup>a</sup>	0.3 <sup>a</sup>	11.1 <sup>a</sup>	3.8 <sup>a</sup>
LA-Cu-60	-1.30	75	1.4	2.2	24.5	0.0	9.0	1.4
LA-Cu-100	-1.30	55	0.1	4.1	25.4	0.0	2.7	1.6
LA-Cu-100 <sup>a</sup>	-1.30 <sup>a</sup>	49 <sup>a</sup>	0.7 <sup>a</sup>	3.4 <sup>a</sup>	21.1 <sup>a</sup>	0.3 <sup>a</sup>	14.2 <sup>a</sup>	3.9 <sup>a</sup>
LA-Cu-130	-1.30	54	0.6	5.5	7.8	0.2	7.1	2.2

a under stirring    b in 0.1 M CsHCO<sub>3</sub>

**Table A.10.** Total current densities related to the geometrical area at different cathodic potentials in 0.1 M  $\text{KHCO}_3$  over microstructured electrodes. Related to **Figure 3.2**.

Micro-probe length $\mu\text{m}$	-0.60 V vs. RHE $j$ $\text{mA cm}^{-2}$	-0.80 V vs. RHE $j$ $\text{mA cm}^{-2}$	-1.05 V vs. RHE $j$ $\text{mA cm}^{-2}$	-1.30 V vs. RHE $j$ $\text{mA cm}^{-2}$
LA-Cu-0 <sup>a</sup>	-1.17	-2.71	-7.39	-17.88
LA-Cu-20	-0.70	-2.58	-8.26	-18.77
LA-Cu-40	-0.96	-3.09	-9.64	-18.01
LA-Cu-60	-1.96	-6.80	-9.35	-19.50
LA-Cu-100	-1.51	-6.52	-9.99	-20.27
LA-Cu-130	-1.70	-6.33	-9.92	-33.41

a La-Cu-0 was also tested at -1.20 V vs. RHE, -12.37  $\text{mA cm}^{-2}$

**Table A.11.** Values obtained from simulations for the concentration of CO<sub>2</sub> and pH averaged over the z-axis, and the maximum flux of CO<sub>2</sub> and its position. Related to **Figure 3.5**.

Micro-probe length $\mu\text{m}$	Potential <i>E vs. RHE</i> V	Averaged z-axis		Maximum CO <sub>2</sub> flux	
		[CO <sub>2</sub> ] mol m <sup>-3</sup>	pH -	Value mol m <sup>-2</sup> s <sup>-1</sup>	<i>z</i> $\mu\text{m}$
LA-Cu-0	-0.60	33.362	9.0315	-	-
LA-Cu-20	-0.60	33.509	8.7357	0.0216	-1.5
LA-Cu-40	-0.60	33.725	8.1758	0.0172	5
LA-Cu-60	-0.60	32.665	8.6625	0.0541	9
LA-Cu-100	-0.60	32.537	8.4721	0.0519	19
LA-Cu-130	-0.60	33.332	7.9652	0.02495	17
LA-Cu-0	-0.80	31.552	9.3945	-	-
LA-Cu-20	-0.80	25.677	9.3632	0.296	-1.5
LA-Cu-40	-0.80	32.362	8.9124	0.0653	5
LA-Cu-60	-0.80	29.395	9.2443	0.1685	9
LA-Cu-100	-0.80	29.641	8.9924	0.142	19
LA-Cu-130	-0.80	28.332	9.0093	0.1708	26
LA-Cu-0	-1.05	30.569	9.5249	-	-
LA-Cu-0 <sup>b</sup>	-1.05 <sup>b</sup>	29.733 <sup>b</sup>	9.3226 <sup>b</sup>	-	-
LA-Cu-0 <sup>c</sup>	-1.05 <sup>c</sup>	26.081 <sup>c</sup>	9.9221 <sup>c</sup>	-	-
LA-Cu-20	-1.05	26.275	9.7995	0.261	0
LA-Cu-40	-1.05	29.719	9.3429	0.1607	6.3
LA-Cu-40 <sup>a</sup>	-1.05 <sup>a</sup>	31.841 <sup>a</sup>	9.2123 <sup>a</sup>	0.1447 <sup>a</sup>	7 <sup>a</sup>
LA-Cu-40 <sup>b</sup>	-1.05 <sup>b</sup>	32.597 <sup>b</sup>	8.3501 <sup>b</sup>	-	-
LA-Cu-40 <sup>c</sup>	-1.05 <sup>c</sup>	29.821 <sup>c</sup>	9.3276 <sup>c</sup>	0.1565 <sup>c</sup>	5.5 <sup>c</sup>
LA-Cu-60	-1.05	27.468	9.4184	0.2358	10
LA-Cu-100	-1.05	22.714	9.5703	0.354	16
LA-Cu-100 <sup>a</sup>	-1.05 <sup>a</sup>	29.062 <sup>a</sup>	9.1631 <sup>a</sup>	0.213 <sup>a</sup>	22 <sup>a</sup>
LA-Cu-100 <sup>b</sup>	-1.05 <sup>b</sup>	30.133 <sup>b</sup>	8.8079 <sup>b</sup>	-	-
LA-Cu-100 <sup>c</sup>	-1.05 <sup>c</sup>	25.293 <sup>c</sup>	9.3917 <sup>c</sup>	0.275 <sup>c</sup>	17 <sup>c</sup>
LA-Cu-130	-1.05	22.611	9.4905	0.3363	23
LA-Cu-0	-1.20	28.381	10.105	-	-
LA-Cu-0	-1.30	25.9	10.345	-	-
LA-Cu-20	-1.30	22.335	9.9382	0.39	0
LA-Cu-40	-1.30	27.219	9.6134	0.2463	6.3
LA-Cu-40 <sup>a</sup>	-1.30 <sup>a</sup>	30.469 <sup>a</sup>	9.4137 <sup>a</sup>	0.2277 <sup>a</sup>	6.5 <sup>a</sup>
LA-Cu-60	-1.30	20.983	9.8611	0.451	9.7
LA-Cu-100	-1.30	20.243	9.7271	0.424	14
LA-Cu-100 <sup>a</sup>	-1.30 <sup>a</sup>	26.696 <sup>a</sup>	9.3993 <sup>a</sup>	0.3113 <sup>a</sup>	18 <sup>a</sup>
LA-Cu-130	-1.30	17.755	9.8185	0.475	15

a under stirring    b in 0.1 M CsHCO<sub>3</sub> with Cs<sup>+</sup> hydrolysis  
c in 0.1 M CsHCO<sub>3</sub> without Cs<sup>+</sup> hydrolysis    - not analyzed

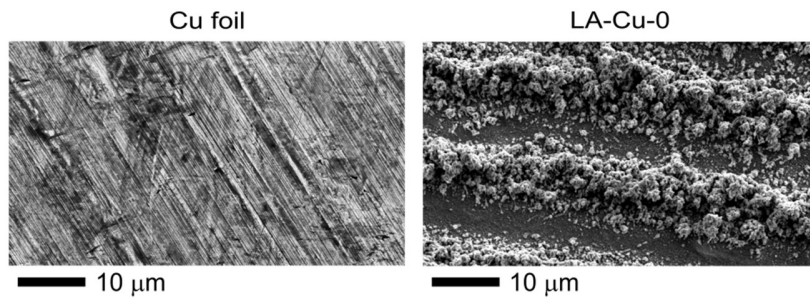


**Figure A.10.** Roughness induced by laser ablation, SEM micrographs of a pristine Cu foil and after laser ablation, showing the redeposition of ablated Cu following the beam track. Related to **Figure 3.1**.

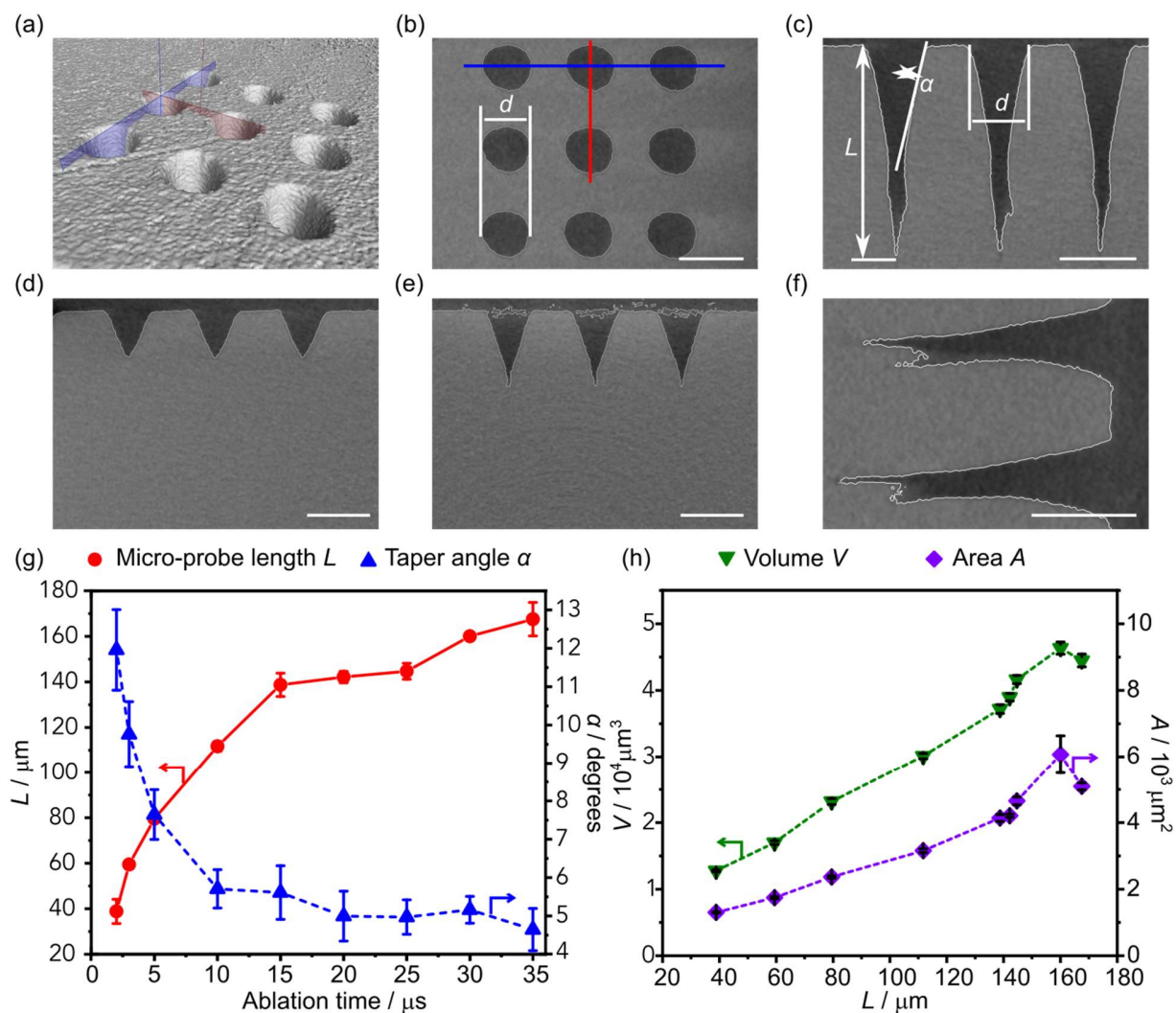


**Figure A.11.** Geometrical characterization of micro-probes, Microcomputed tomography study on a set of 9 micro-probes per laser parameter used for the manufacturing, (a) and (b) show the reconstructed volume with two perpendicular planes aligned to the center of adjacent micro-probes. This enables the determination of main geometrical parameters defining the volume, depicted in (c). By increasing the number of laser pulses per hole, the length was increased, as observed in (d) and (e). The deformation in (f) is caused by multiple reflections of the laser beam. The variations of the length and taper angle with the time exposed to the laser beam (ablation time) are shown in (g). The volume and the area linearly correlate with the length, as shown in (h). Scale bars represent 50  $\mu\text{m}$ . Related to **Figure 3.1**.



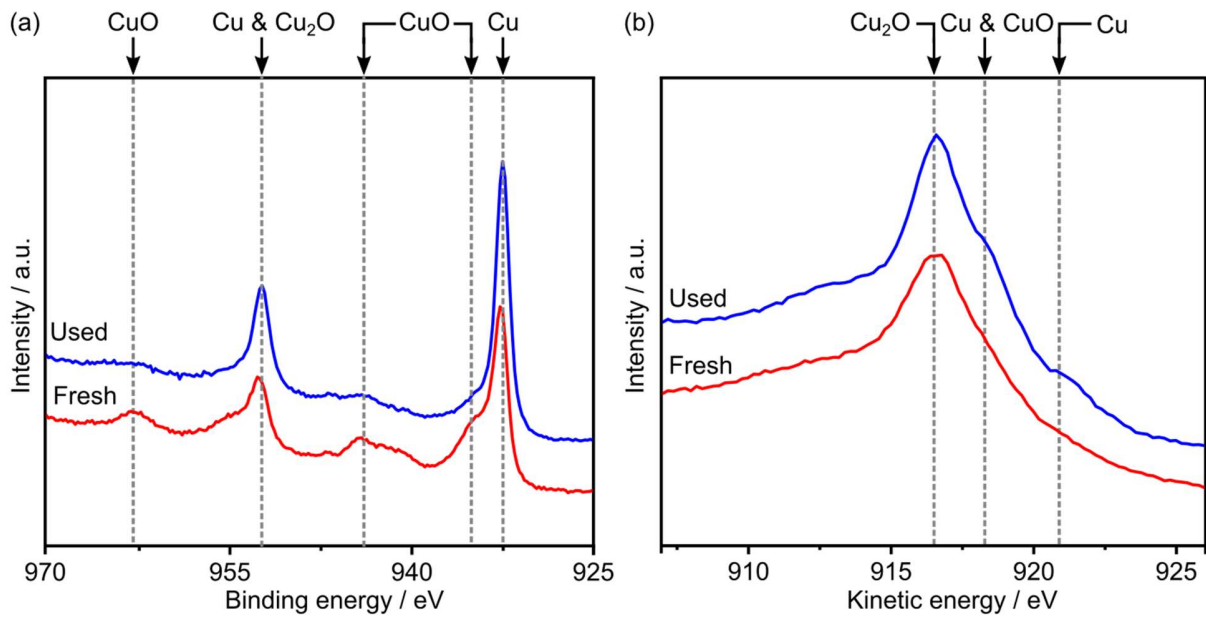


**Figure A.12.** Surface compositional analysis of laser ablated surfaces. XPS core level and Auger analyses of fresh and used laser ablated copper foils (LA-Cu-0), (a) showing the Cu 2p spectra, (b) showing the Cu  $L_{3}M_{4.5}M_{4.5}$  spectra. The presence of  $Cu_{2}O$  can be ascribed to the oxidation of Cu upon exposure to air. Related to **Figure 3.1**.

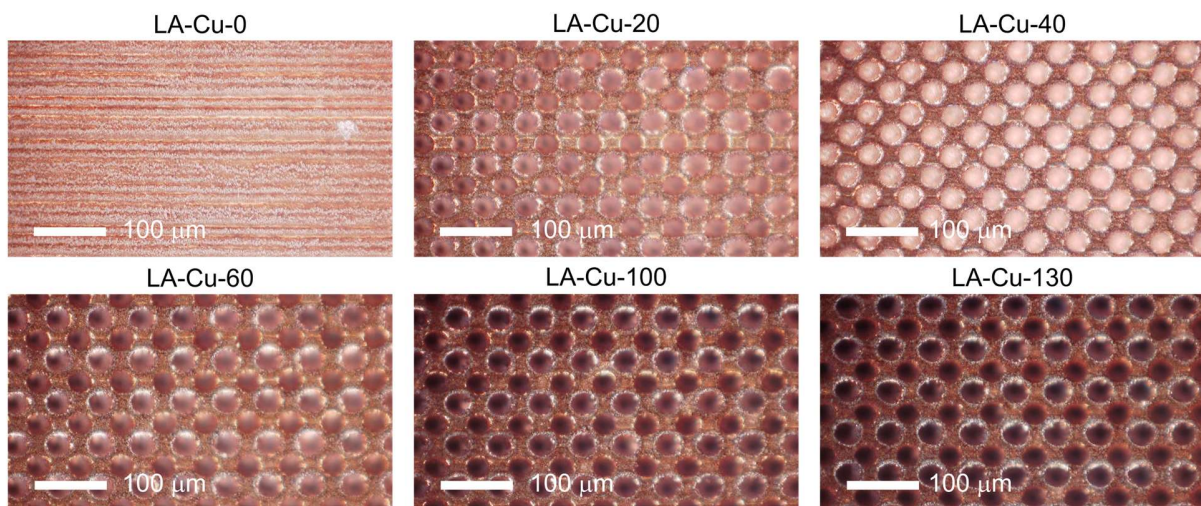


**Figure A.13.** Optical microscopy characterization of microstructured electrodes, optical microscopy images (obtained with white light) of representative electrodes for all studied micro-probe lengths. Pitch:  $70\ \mu\text{m}$ , diameter:  $35\ \mu\text{m}$ , length: 0-130  $\mu\text{m}$ . Scale bars represent  $100\ \mu\text{m}$ . Related to **Figure 3.1**.

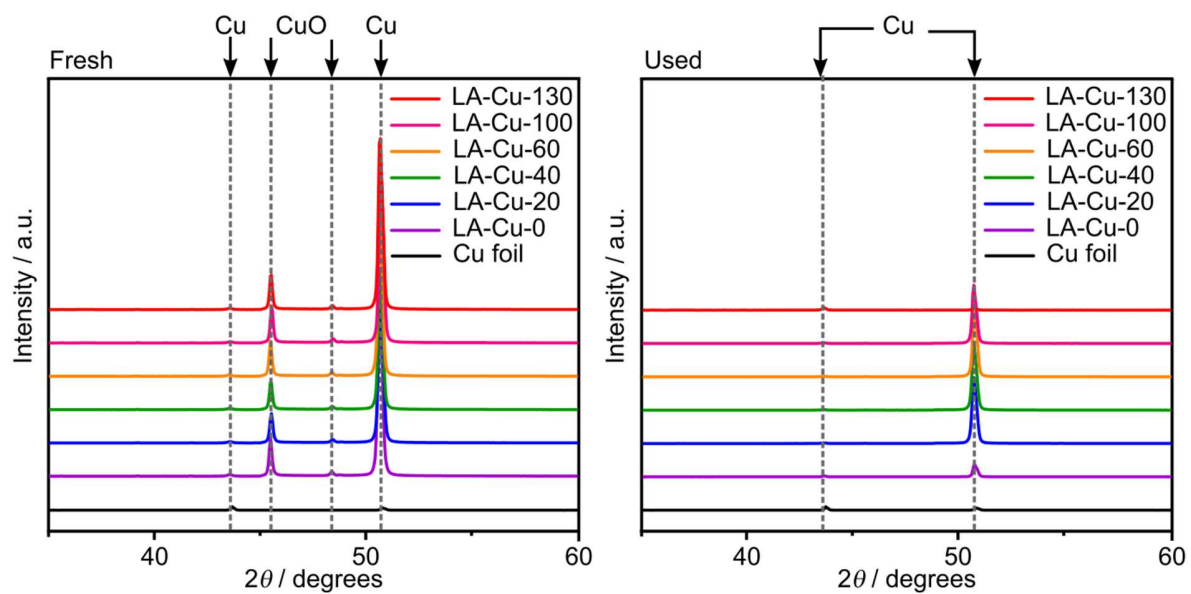


**Figure A.14.** Crystalline structure and phase identification of microstructured electrodes. XRD patterns before and after electrolysis. The position of the main reflections for relevant phases is indicated. Related to **Figure 3.1**.

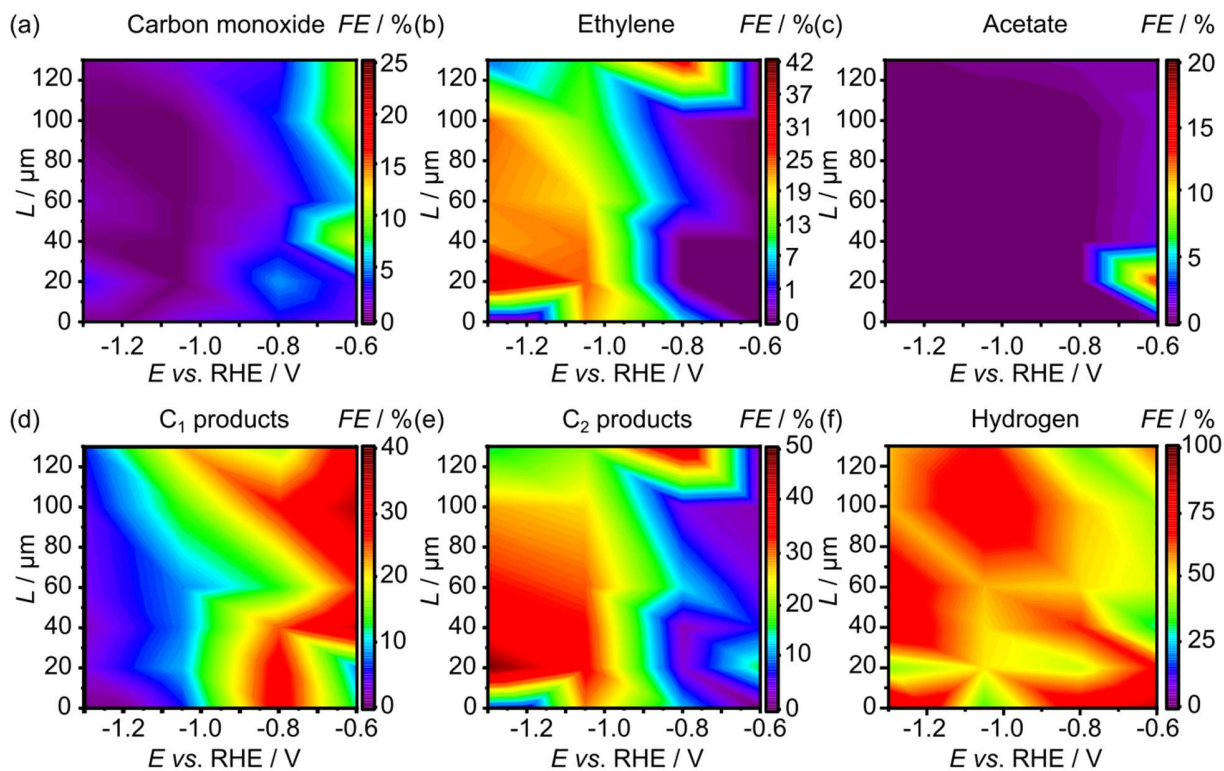


**Figure A.15.** Selectivity *vs.* potential and geometry on microstructured electrodes, Contour maps showing Faradaic efficiency ( $FE$ ) *vs.* micro-probe length ( $L$ ) and potential ( $E$  *vs.* RHE) as subsidiary results to **Figure 3.3** (top row). Aggregated maps showing the sum of  $FE$  for C<sub>1</sub> and C<sub>2</sub> products and the contour map for the parasitic H<sub>2</sub> formation are shown in the bottom row. Related to **Figure 3.2**.

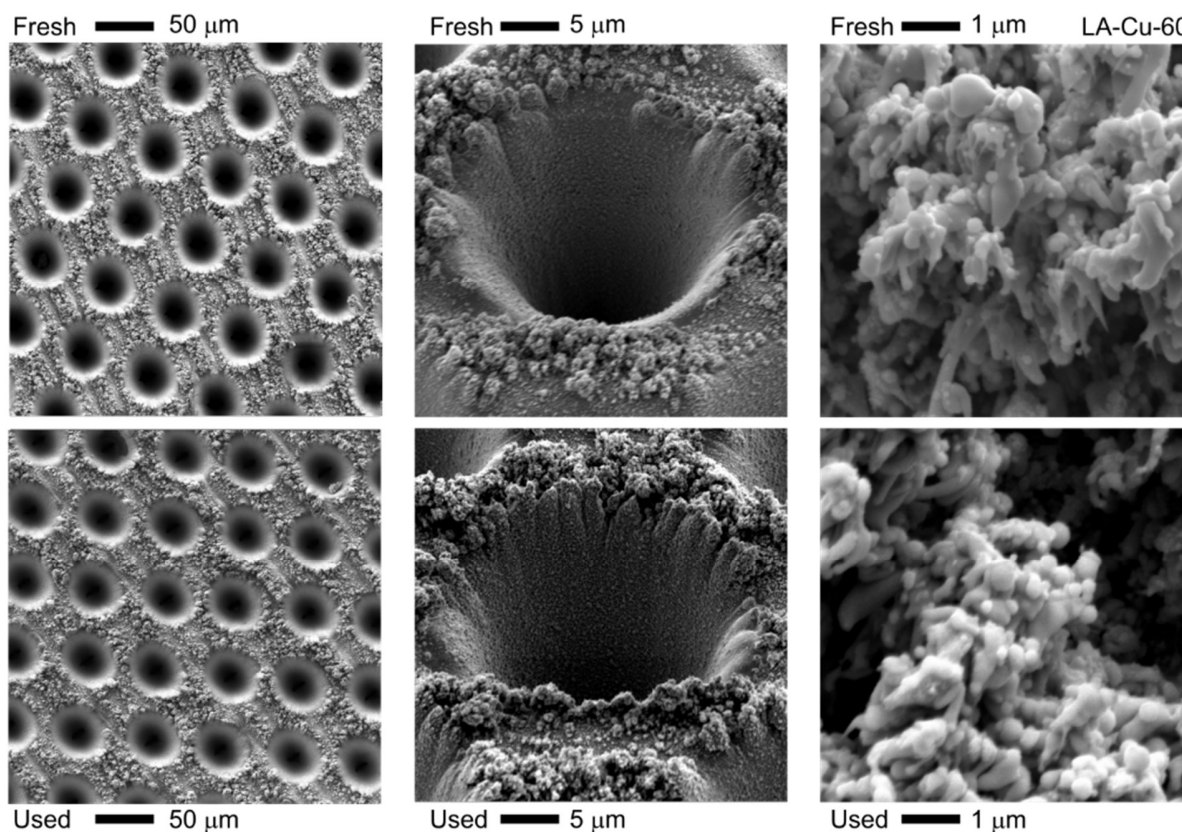


**Figure A.16.** SEM analysis of microstructured electrodes, SEM micrographs of Cu-LA-60 before and after electrocatalytic tests. Scale bar represents 50  $\mu\text{m}$  (left), 5  $\mu\text{m}$  (center), 1  $\mu\text{m}$  (right). Related to **Figure 3.2**.

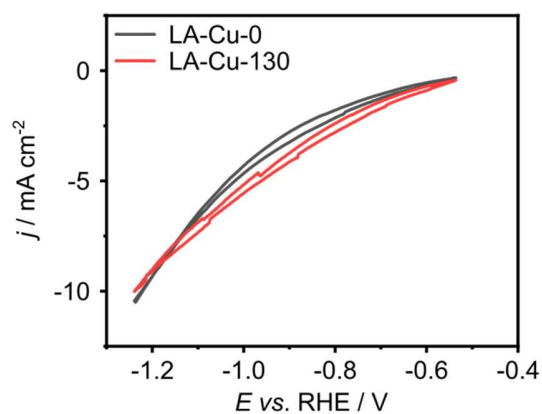


**Figure A.17.** Cyclic voltammeteries for LA-Cu-0 and LA-Cu-130 after exposure to reaction conditions, Cyclic voltammeteries in the reaction medium (0.1 M  $\text{KHCO}_3$  saturated with  $\text{CO}_2$ ) of a copper foil after laser ablation pretreatment (LA-Cu-0) and subsequent microstructuring (LA-Cu-130). Related to **Figure 3.2**.



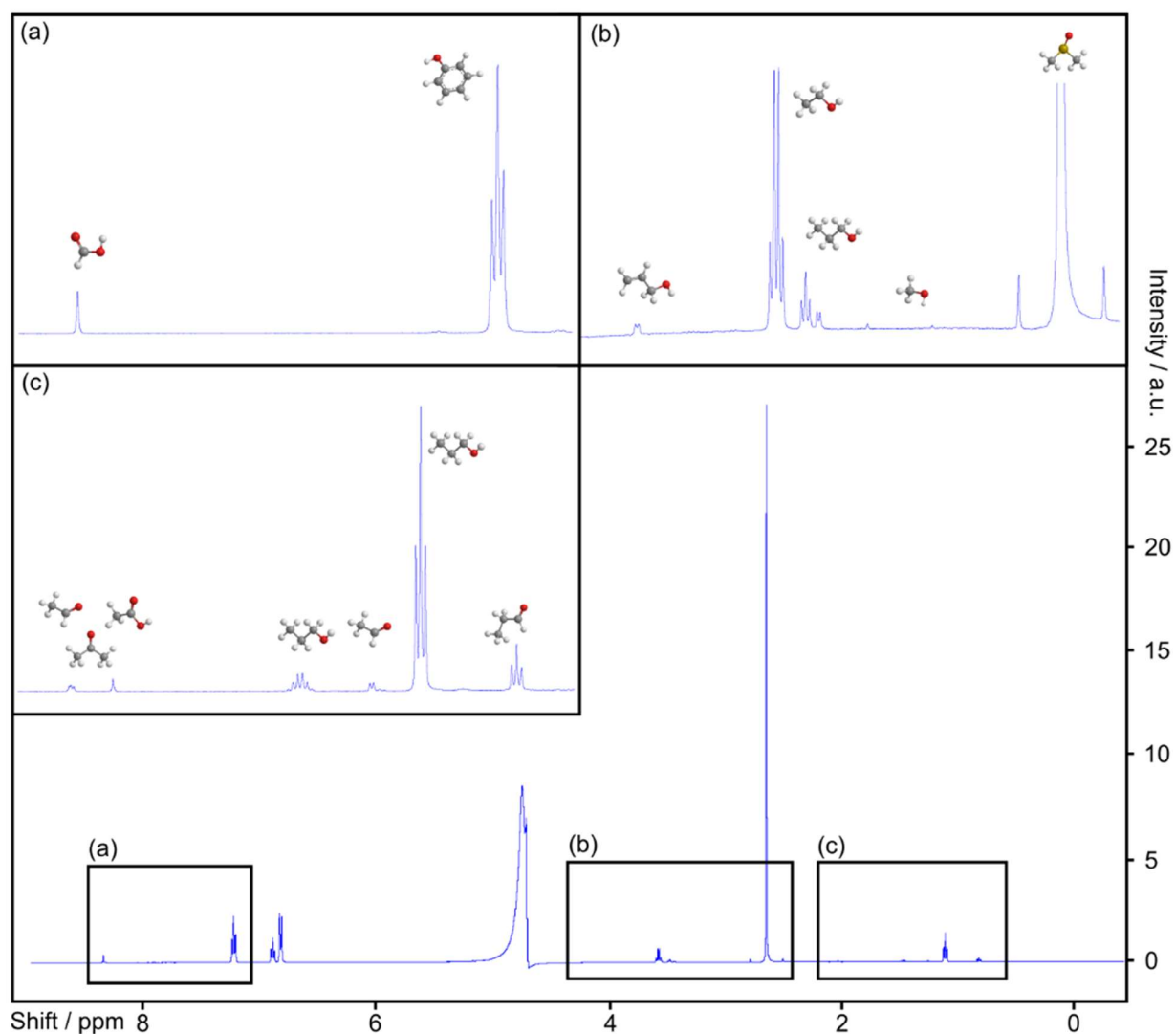


**Figure A.18.** Identification and quantification of liquid products, Representative  $^1\text{H-NMR}$  spectrum obtained from analysis of the catholyte after electrolysis. Case shown: LA-Cu-0 exposed to  $-1.05\text{ V vs. RHE}$ . (a) Formate and phenol (internal standard), (b) allyl alcohol, ethanol, propanol, methanol, dimethyl sulfoxide (internal standard), (c) acetaldehyde with acetone, acetate, propanol, acetaldehyde, ethanol, propionaldehyde, and propanol. Spectra were obtained with a Bruker III 500 MHz. Color code: oxygen (red), carbon (grey), hydrogen (white). Related to **Figure 3.2**.

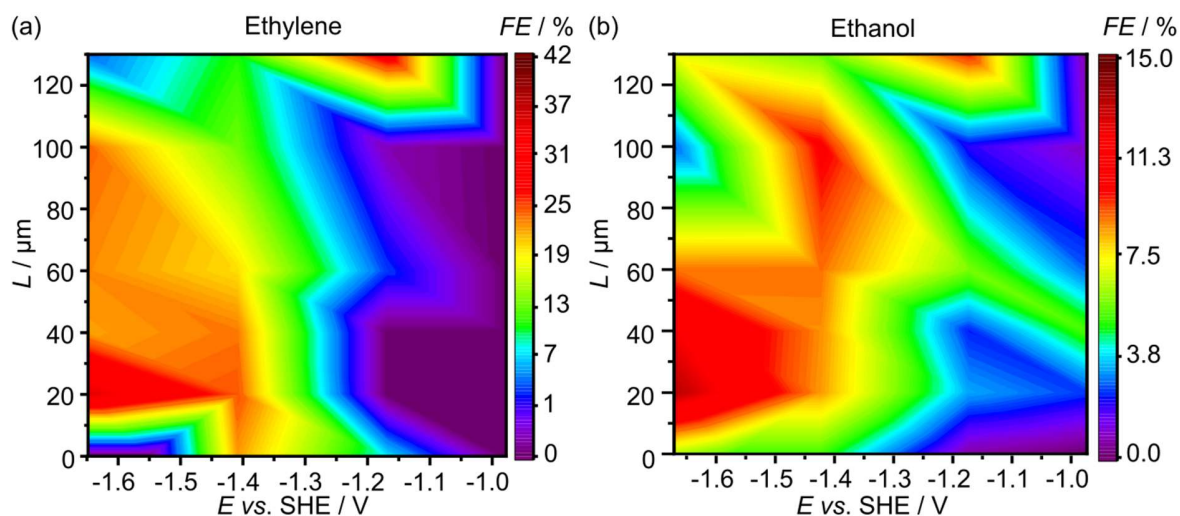


**Figure A.19.** Selectivity toward ethylene and ethanol *vs.* standard hydrogen electrode (SHE) potential and geometry on microstructured electrodes. Contour maps showing Faradaic efficiency ( $FE$ ) *vs.* micro-probe length ( $L$ ) and  $E$  *vs.* SHE as subsidiary results to (a) ethylene in **Figure A.15**. and (b) ethanol in **Figure 3.3**. Related to **Figure 3.2**.

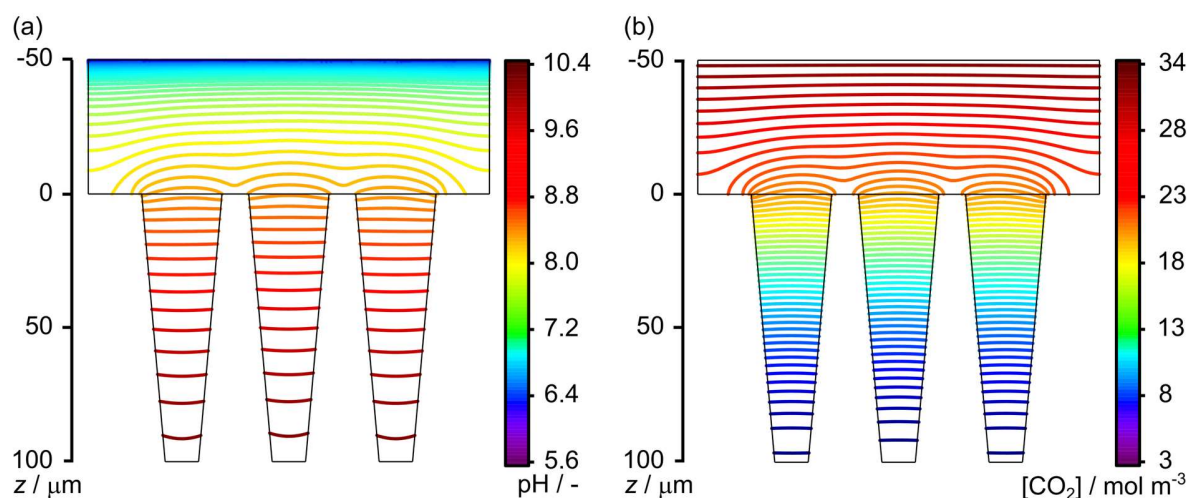


**Figure A.20.** Simulated 2D isocontours under eCO<sub>2</sub>R conditions. Representative case (LA-Cu-100 exposed to  $-1.30$  V *vs.* RHE) showing isocontour lines obtained from simulations for (a) pH and (b) CO<sub>2</sub> concentration over a cross-section comprising the axes of three adjacent probes. The almost perpendicular shape of isocontour lines in the interior of the micro-probes with respect to the longitudinal axis allows considering these two 3D variables as 1D, only dependent on the  $z$ -coordinate, without loss of generality. Related to **Figure 3.4**.

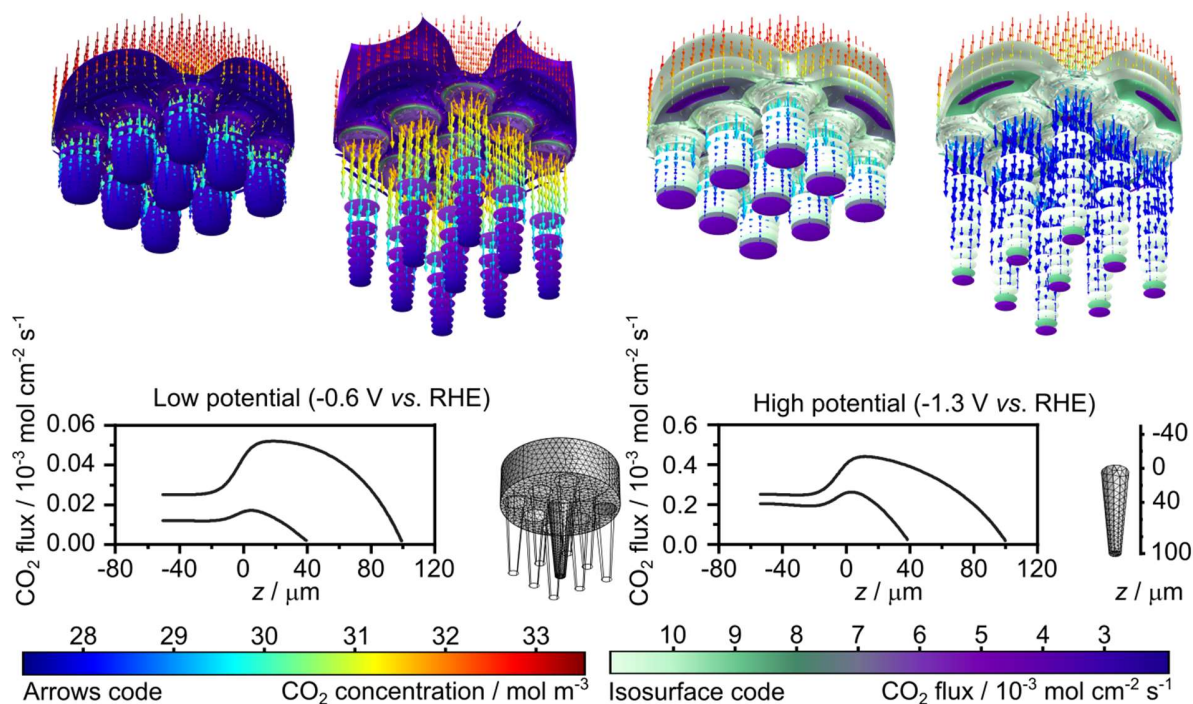


**Figure A.21.** Simulated  $\text{CO}_2$  flux under e $\text{CO}_2\text{R}$  conditions, distribution of the  $\text{CO}_2$  flux over LA-Cu-40 and LA-Cu-100 operated at low ( $-0.60\text{ V vs. RHE}$ ) and high ( $-1.30\text{ V vs. RHE}$ ) potentials (see **Figure A.22** for the corresponding  $\text{OH}^-$  simulations). The  $\text{CO}_2$  flux is described by its value (isosurfaces) and direction (arrows) and develops from the bulk toward the interior. Differences between low (left) and high (right) potentials are readily noticeable. The electrodes operated at low potentials display negligible flux of  $\text{CO}_2$  irrespective of  $L$ , since the overall  $\text{CO}_2$  concentration is close to the bulk one due to the low reaction rate (**Error! Reference source not found.**). The  $\text{OH}^-$  flux is also modest and follows the opposite direction, *i.e.*, toward the exterior of the micro-probes, as shown in **Figure A.22**. On the other hand, higher potentials present values of  $\text{CO}_2$  flux one order of magnitude larger, thus suggesting a more heterogeneous environment less prone to fine control. Nonetheless, the 2D evolutions of the  $\text{CO}_2$  flux along the  $z$ -axis show a common behavior defined by an initial increase from  $z = 0$  until a maximum and a further decline toward zero at  $z = L$  (boundary condition). Notably, the maximum flux is closely controlled by the potential and its position by  $L$  (**Figure A.23**). Related to **Figure 3.4**.

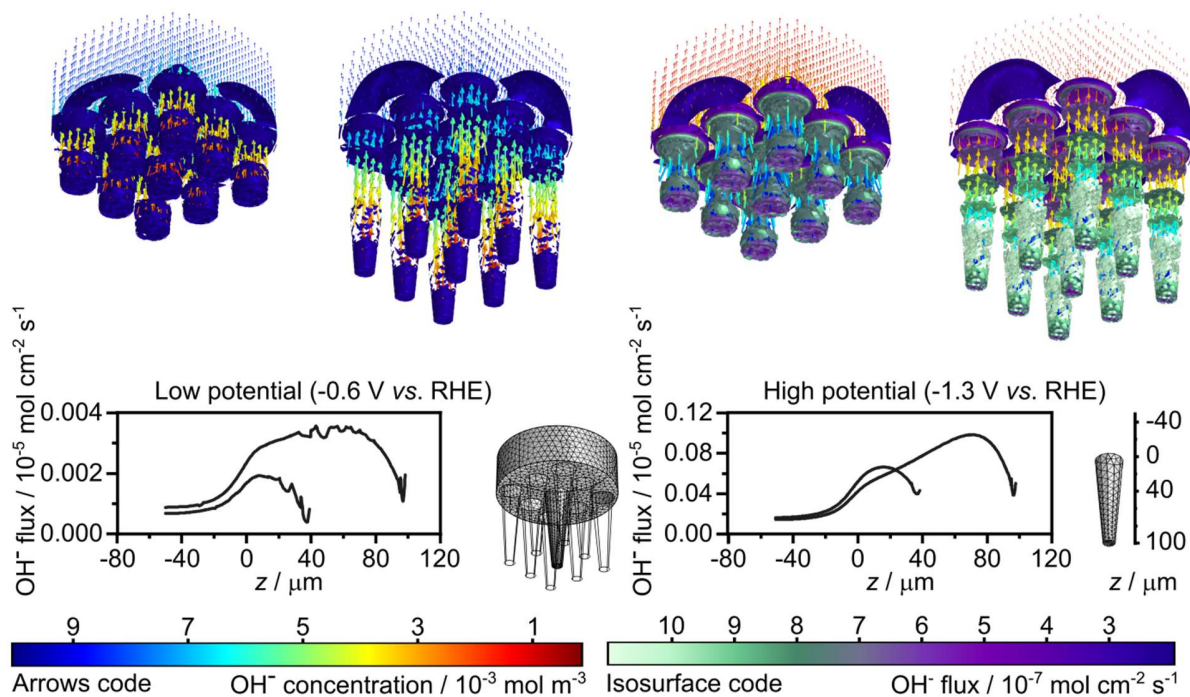


**Figure A.22.** Simulated OH<sup>-</sup> flux. Isosurfaces displaying the distribution of the OH<sup>-</sup> flux. Arrows show the flux direction and are colored according to the local concentration of OH<sup>-</sup>, whereas their length is proportional to the total flux value. Insets represent the evolution along the z-axis. Cases shown: LA-Cu-40 and LA-Cu-100 at low (-0.60 V *vs.* RHE, left) and high potentials (-1.30 V *vs.* RHE, right). Related to **Figure 3.4**.



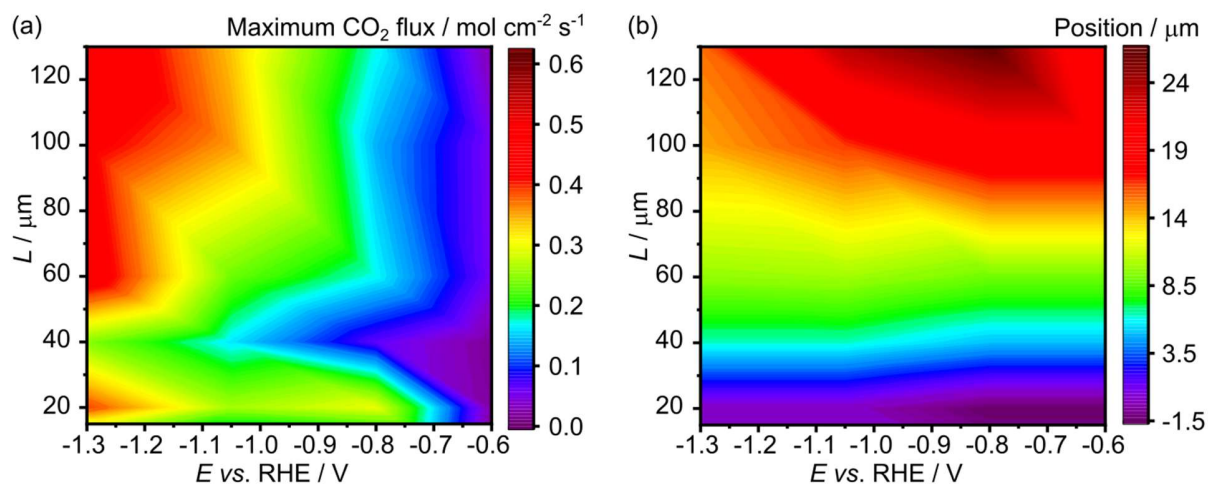


**Figure A.23.** Dependence of the maximum CO<sub>2</sub> flux inside the micro-probes with the applied potential and geometry. Contour maps showing (a) the maximum CO<sub>2</sub> flux and (b) its position in the  $z$ -axis obtained in the simulations, represented *vs.* micro-probe length and potential. Related to **Figure 3.4**.

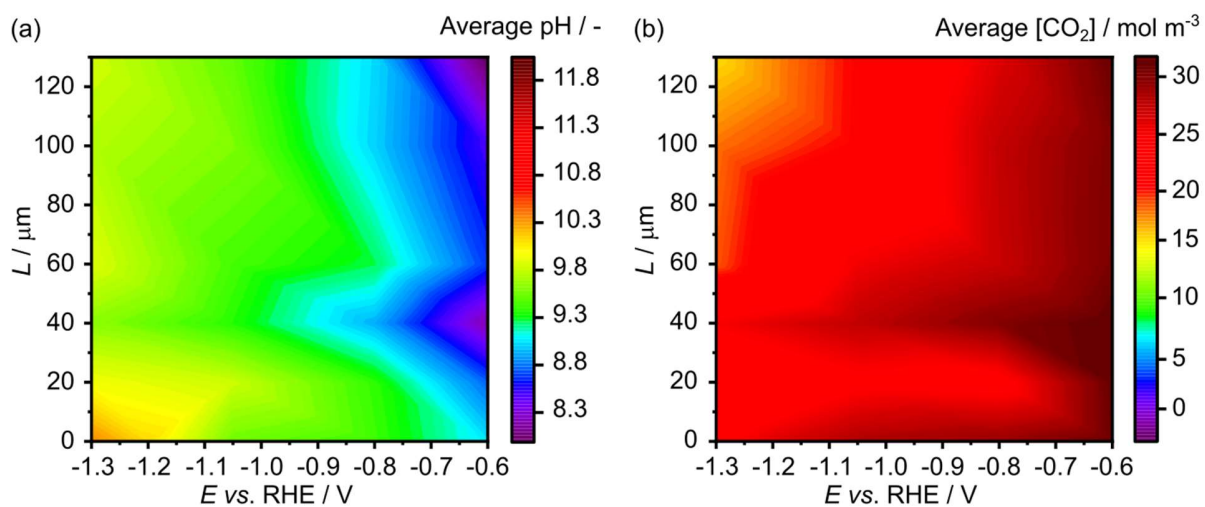


**Figure A.24.** Dependence of the chemical environment descriptors in the micro-probes with the applied potential and geometry. Contour maps displaying average (a) pH and (b) CO<sub>2</sub> concentration *vs.* micro-probe length and applied potential. Related to **Figure 3.4**.

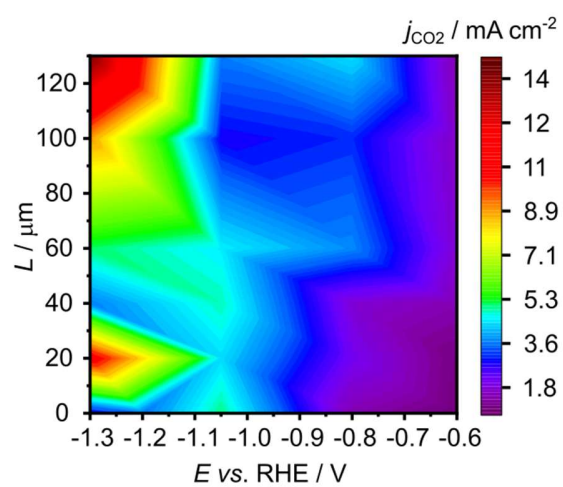


**Figure A.25.** CO<sub>2</sub> reduction current vs. potential and geometry on microstructured electrodes. Contour map showing the sum of measured partial current densities for carbon products vs. micro-probe length ( $L$ ) and potential. Related to **Figure 3.2**.

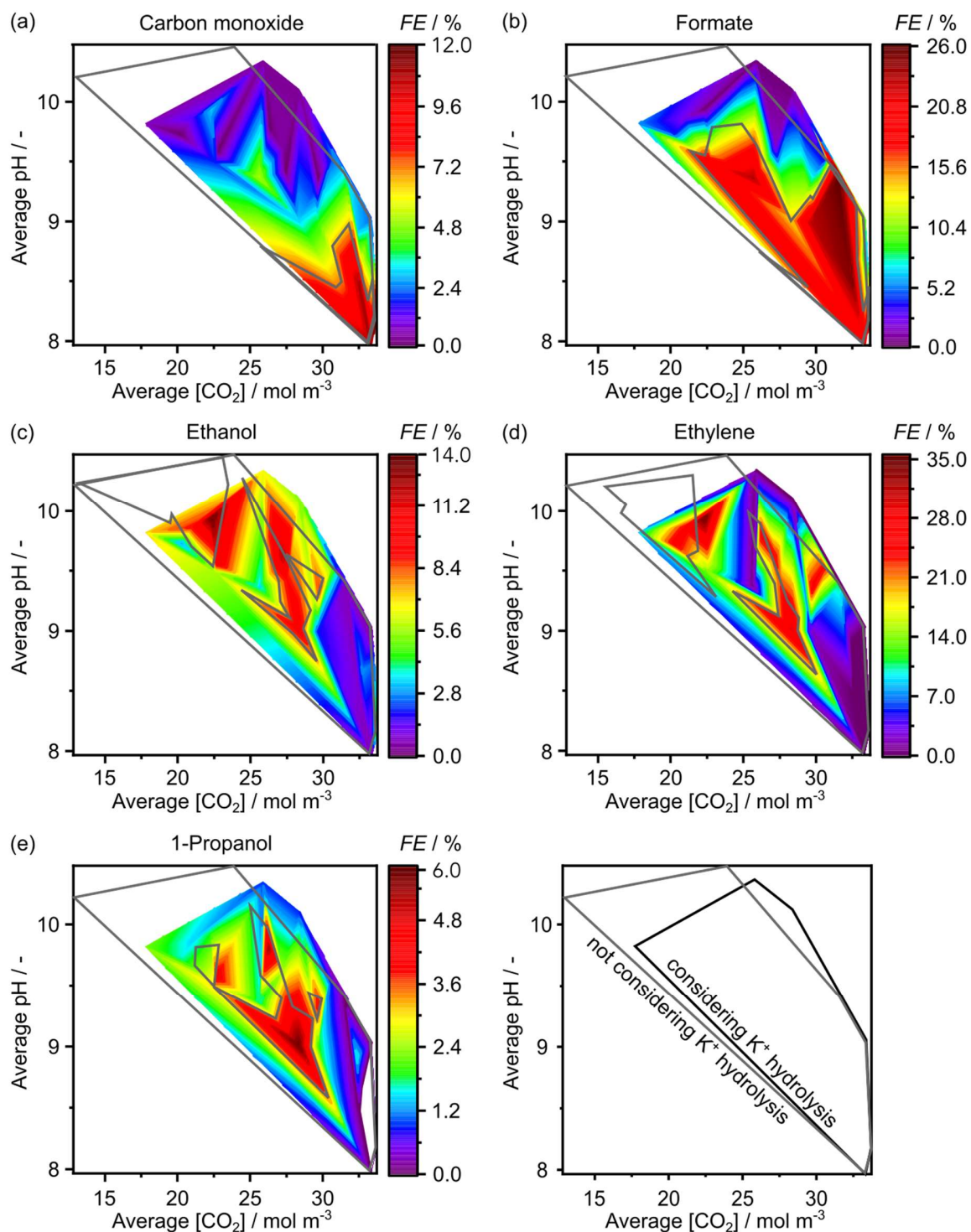


**Figure A.26.** Effect of cation hydrolysis in the local chemical environment. Comparison between selectivity maps obtained through simulations including (solid lines) and not including (dashed lines) the effect of hydrolysis of  $K^+$  in the vicinity of the catalyst surface. For the sake of simplicity, only the contour of the maps and high selectivity regions are shown for the simulations disregarding hydrolysis. Related to **Figure 3.5**.

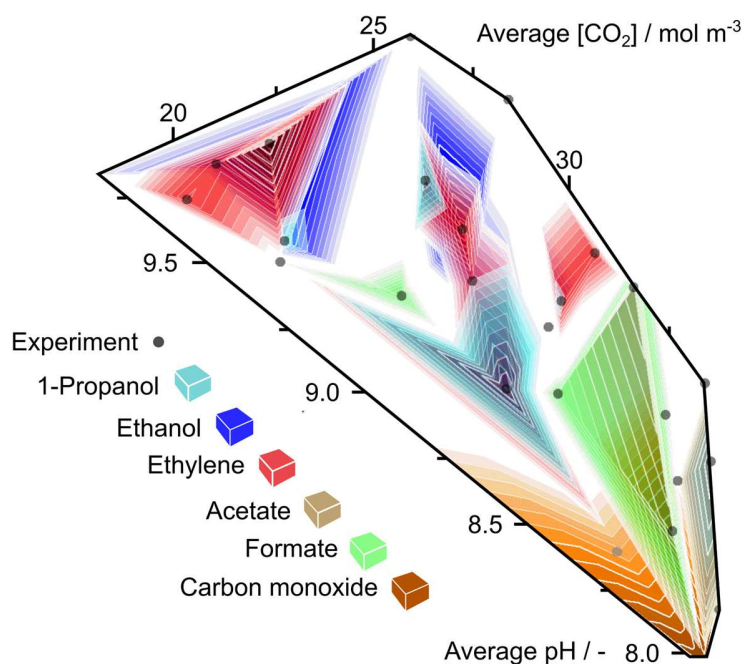


**Figure A.27.** Combined selectivity map. Contour map showing regions with high Faradaic efficiency for relevant products with respect to calculated average pH and  $\text{CO}_2$  concentration in the interior of the microprobes upon overlaying of maps presented in **Figure 3.5**. Grey dots indicate modeled experiments (see **Figure 3.2**). Related to **Figure 3.6**.

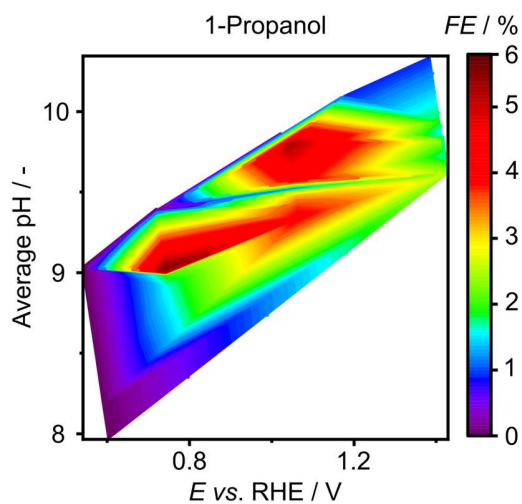


**Figure A.28.** Faradaic efficiency vs. calculated overpotential and average pH for the case of propanol, Contour map showing regions where propanol is favored. Overpotentials were calculated based on applied potentials and the Nernst equation after considering correction by the simulated local concentrations of  $\text{H}^+$  and  $\text{CO}_2$ . Related to **Figure 3.5**.

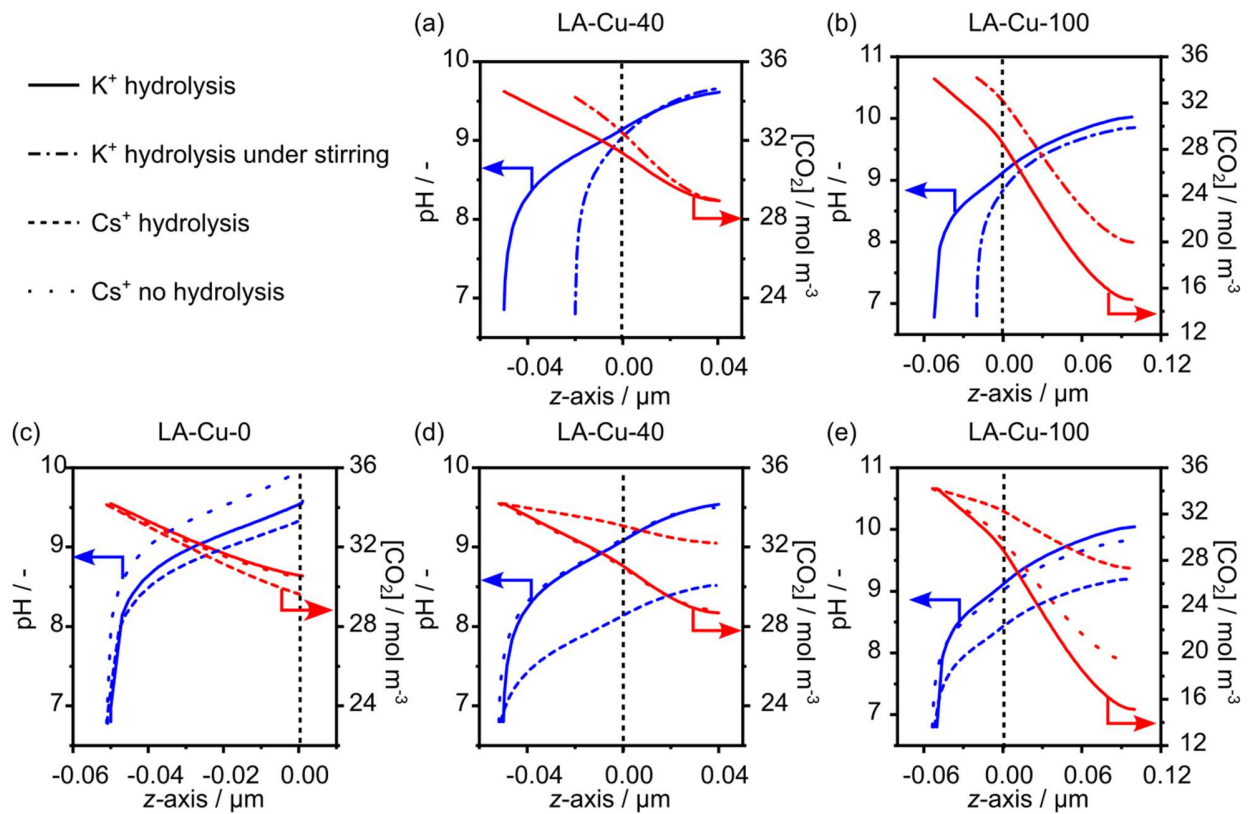


**Figure A.29.** Effect on the chemical environment in the micro-probes of enhanced mass transport and the nature of the electrolyte, Evolution along the axis of micro-probes of pH and CO<sub>2</sub> concentration for representative electrodes. (a) and (b) display the effect of stirring, whereas (c)-(e) display the effect of using CsHCO<sub>3</sub> instead of KHCO<sub>3</sub>. Related to **Figure 3.6**.

## Chapter 4

### Note A.1. On the Analysis of the Reaction Network

The total number of intermediates and transition states were computed explicitly by DFT. Originally, 463 intermediates were considered, out of which 17 were  $C_1$ ,<sup>[201,243]</sup> 55  $C_2$ ,<sup>[185]</sup> 387  $C_3$ , and 4 that did not contain any C atom ( $H_2O$ , OH, O, H). Among the  $C_1$ , 5, 8, and 4 came from the dehydrogenation of methane, methanol, and formic acid, respectively. Among the  $C_2$ , 10, 24, and 21 came from the networks of ethane, ethanol, and ethylene glycol, respectively. Among the  $C_3$ , 30 (28), 72 (70), 40 (28), 98 (83), 63 (61), and 84 (77) came from the dehydrogenation of propane, 1-propanol, 2-propanol, 1,2-propylene glycol, 1,3-propylene glycol, and glycerol, respectively. (The numbers in parenthesis indicate the intermediates that converged to the desired structure.) Thus, 40  $C_3$  intermediates did not converge, and the elementary steps associated to them were removed from the reaction network. The 463 fully converged  $C_1$ – $C_3$  intermediates were interlinked by a network containing 2266 steps, out of which 604 (27%) were fully characterized via DFT. A total of 691 consisted of C–C couplings, and among them, 55 and 636 were  $C_1$ – $C_1$  and  $C_1$ – $C_2$  couplings, respectively. This yielded both  $C_2$  and  $C_3$  intermediates, see **Figure A.33** and **Table A.27** till **Table A.29**, respectively. Originally, 10  $C_1$  and 70  $C_2$  moieties were considered to be combined to produce a  $C_3$  species. Nevertheless, as only 347 of 387  $C_3$  intermediates converged, only 636 (instead of 700) couplings were deemed possible. From them, 586 converged to the desired transition states. The remaining 114 were represented as empty spaces in **Table A.27** till **Table A.29**. Further details about selected  $C_1$ – $C_2$  couplings were shown in **Table A.30**. 286 C–O and 301 C–OH bond-breaking reactions were considered, 10 of them (5 C–O and 5 C–OH) were calculated using DFT-NEB (**Table A.31**). Regarding hydrogenations, there were 683 C–H and 305 O–H bond formations, 8 of them (4 C–H and 4 O–H) computed via DFT-NEB (**Table A.32**). The remaining hydrogenations were approximated via LSR, which have low error bars for hydrogenation processes as extensively shown in the literature and also since the TS energy is mainly assigned to the activation of H to on-top positions (**Figure A.35**).<sup>[185,193]</sup> Heyrovsky-like variations were also considered for the 301 C–OH breakings and 305 O–H hydrogenations.

**Note A.2. Computing the Transition States for the C<sub>1</sub>-C<sub>2</sub> Bond Formation**

For each C<sub>1</sub>-C<sub>2</sub> bond formation, we took the ground state of the C<sub>3</sub> product was considered as the FS. Then the IS were approximated by separating the two moieties until the carbon atoms were at a distance of 3.5 Å. To avoid the molecules getting too close or too far from the surface, this elongation was executed parallel to the xy plane, and both moieties were shifted 0.2 Å down along the z plane. These IS were then relaxed during 30 steps to reduce tensions, but explicitly avoiding a full relaxation. Four images were generated for all reactions. Then, the 8 NEB algorithm was applied as implemented in VASP-VTST and analyzed with the script of Henkelman *et al.*<sup>[192]</sup> When the predicted transition state was at a distance  $\pm 10\%$  of a given image, switching to CI-NEB. Generating a new NEB by zooming the interval around the predicted maximum. Yet, for 117 reactions, the minimum-energy path was monotonously going down without a clear maximum. They are marked as \* in **Table A.26**.

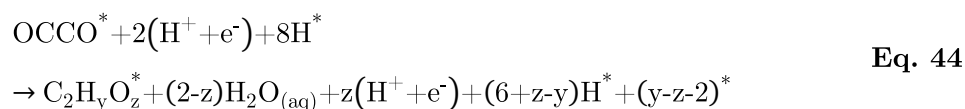
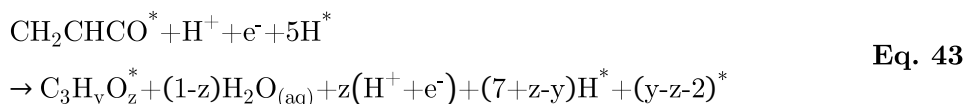
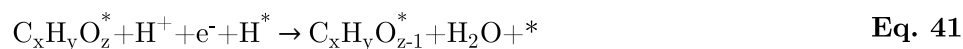
**Note A.3. Extension of the Graph Network for C<sub>3+</sub> Products**

Strategies proposed in this work can be extended for C<sub>3+</sub> networks. However, upon increase of carbon from C<sub>3</sub> to C<sub>4</sub>, there is an increase of intermediates from 463 to 700, an increase of TS from 2266 to 3900. A screening process may be needed to handle the complexity of the network due to the massive computational resources needed to compute both intermediates and transition states with DFT. This work demonstrates that only a small domain of the reactivity graph is responsible for the selectivity for desired products, and thus, only this domain needs to be strongly evaluated via DFT. Hence, a thermodynamic exploration of the reaction intermediates, discarding the reactions highly endothermic (or in a second step with high energy barriers) and only evaluating key domains of the reaction graph may be the appropriate approach to explore C<sub>3+</sub> networks.

**Note A.4. Heyrovsky and Tafel-like Steps in Energy-profiles**

The energy profiles were constructed, considering all hydrogenations occurred from adsorbed H\*, in Tafel-like elementary steps, **Eq. 40**. However, to strip O or OH groups, one hydrogenation was considered to go through a Heyrovsky-like step, **Eq. 41** and **Eq. 42**, respectively. Specifically, the energies derived from **Eq. 43** were used for all figures dealing with C<sub>3</sub> compounds (**Figure 4.3**, **Figure A.38**, **Figure A.39** and **Table A.27** till **Table A.29**), and **Eq. 44** for **Figure A.32**. H<sup>+</sup> is considered a reference value, and its DFT energy is set to 0 for the calculation of LSR.





### Note A.5. Charge Benchmarking

Charge displacement obtained from dipole moments. As an alternative to Bader analysis, a proxy of the charge taken by an adsorbate upon adsorption can be deduced by the arising net electric dipole of the adsorbate-metal system, in **Eq. 45**. Initially, such dipole were decomposed into three components. The first one is intrinsic of the asymmetric slab model used in DFT. The second one is intrinsic of the adsorbate ( $A$ ) by excluding all perturbations caused by the surface. Upon adsorption, the charge density taken by  $A$  from the surface ( $Q_{A^*} - Q_A$ ) creates a third contribution, **Eq. 46**. Thus, the net charge transfer  $\Delta Q_d$  can be approximated from **Eq. 47**. Here  $z_A$  was obtained from the average height of all atoms in the adsorbate (C, H, O), while  $z^*$  is the position of the outermost Cu layer. The dipole moments were obtained from the Neugebauer and Scheffler corrections as given by VASP, applied along  $z$ .<sup>[244]</sup> The net charge transfer obtained by this method is comparatively smaller than that obtained from Bader analysis by a factor of 0.24, **Figure A.36**. The  $\frac{1}{4}$  factor was found by Lang and Kohn when describing the interaction of a punctual charge and its induced surface charge in the metal.<sup>[245]</sup> Relation between Bader and Mulliken charges. Another proxy of the charge transferred upon adsorption is the increments in Mulliken charges,  $Q_M$ . Such quantity is calculated from the Mulliken charge around the atoms of the adsorbate, ( $A$ ), in the adsorbed structure versus the same structure put in the gas phase, **Eq. 48**. These values are prone to arbitrariness in the definition of the Wigner–Seitz radii ( $r_{ws}$ ). Here, the taken default  $r_{ws}$  values were included in the PAW files. **Figure A.37** showed the increments in Mulliken charges underestimate Bader values, which is to be expected as the integration volume is significantly lower.



$$\mu'_{\text{tot}} = \mu'_* + \mu'_A + \mu'_{\text{ads}} \quad \text{Eq. 45}$$

$$\mu'_{\text{ads}} = (Q_{A^*} - Q_A)(Z_A - Z^*)\tilde{Z} \quad \text{Eq. 46}$$

$$\Delta Q_d \equiv Q_{A^*} - Q_A = \frac{\|\mu'_{\text{tot}} - \mu'_* + \mu'_A\|}{Z_A - Z^*} \quad \text{Eq. 47}$$

$$\Delta Q_M \equiv Q_{M,A@A^*} - Q_{A,\text{gas}} \quad \text{Eq. 48}$$

### Note A.6. Conformational Search

Even simple C<sub>2</sub>-C<sub>3</sub> adsorbates could have 101-102 conformations. Herein, simplified conformational analysis was followed, based on the heuristic rules devised in ref.<sup>[243,246]</sup> and summarized in the following steps:

- 1) The unsaturated bonds were placed close to the surface.
- 2) Oxygen atoms were also placed close to the surface.
- 3) Intermediates containing at least two oxygen atoms that can form intramolecular hydrogen bonds were put maximized their number of intramolecular hydrogen bonds.
- 4) Carbon tails face the surface.
- 5) If the intermediate has cis-trans isomers, both were calculated, but only the most stable one was retained for subsequent analysis.
- 6) If the intermediate did not converge to a reasonable structure (for instance, very unsaturated C<sub>3</sub> structures generated cyclopropane analogues), the molecule was readjusted manually, trying up to 6 conformations that preserve the rules (1 till 4).

### Note A.7. LSR for C<sub>1</sub>-C<sub>2</sub> Couplings

All transition state energies were originally estimated using LSR from **Table A.26**. As derived from these values, **Eq. 49** approximates all activation energies as 0.64 eV for all C-C couplings. Due to this lack of sensitivity, all C<sub>1</sub>-C<sub>2</sub> coupling reactions were calculated explicitly using the NEB method.

$$E_{\text{TS}} = E_{\text{C}_1} + E_{\text{C}_2} + 0.64 \quad \text{Eq. 49}$$

**Table A.12.** Reaction enthalpies from CO<sub>2</sub> and H<sub>2</sub> to H<sub>2</sub>O(g) and relevant C<sub>2</sub>-C<sub>3</sub> products. A more negative enthalpy indicates a more favorable formation of the product from CO<sub>2</sub> and H<sub>2</sub>. Related to **Figure 4.3**.

Product	$\Delta H$ eV
Ethylene	-1.32
Ethanol	-1.79
Propylene	-2.59
1-Propanol	-2.95
2-Propanol	-3.12

**Table A.13.** Production rates ( $r$ ), Faradaic efficiencies ( $FE$ ) and geometric partial current densities of products detected from the electrolysis of CO<sub>2</sub> (C<sub>1</sub> reagent) on OD-Cu in 0.1 M KHCO<sub>3</sub> at -0.95 V *vs.* RHE for 60 min. The values shown are an average taken from three experiments, with their standard deviations given in the brackets. Related to **Figure 4.1**.

Products	$r$ $\mu\text{mol cm}^{-2} \text{ h}^{-1}$	Stdev -	$FE$ %	Stdev -	$j$ $\text{mA cm}^{-2}$	Stdev -
Hydrogen	5710	506	37.4	3.2	-5.3	1.3
Carbon monoxide	182	15	1.17	0.08	-0.17	0.02
Methane	47.5	8.5	1.3	0.2	-0.19	0.03
Ethylen	819	78	30.5	2.6	-4.4	0.4
Ethane	-	-	-	-	-	-
Propylene	-	-	-	-	-	-
Propane	-	-	-	-	-	-
Methanol	-	-	-	-	-	-
Formate	1000	97	6.4	2	-0.92	0.28
Ethanol	326	28	12.5	1	-1.79	0.16
Acetaldehyde	18.8	3.1	0.61	0.1	-0.09	0.02
Acetate	32.9	7.1	0.85	0.24	-0.12	0.04
1-Propanol	75.8	16.3	4.4	1.1	-0.63	0.13
Propionaldehyde	20.3	1.4	1.04	0.05	-0.15	0.1
Acetone	3.2	1	0.16	0.05	-0.03	0.01
Allyl alcohol	25.2	3.9	1.2	0.2	-0.18	0.06
1-Butanol	-	-	-	-	-	-

- Product not detected.

Low rates to CH<sub>4</sub> and CH<sub>3</sub>OH hint low coverages for their precursors: CHOH, CH<sub>2</sub>O, CH<sub>2</sub>OH, CH<sub>3</sub>O and CH<sub>x</sub>.

**Table A.14.** Faradaic efficiencies ( $FE$ ) of products from the electrolysis of 50 mM formaldehyde +50 mM acetaldehyde on OD-Cu in 0.1 M PPB at different potentials for 60 min. The values shown are an average taken from three experiments. Related to **Figure 4.2**.

Relevant Products	-0.80 V <i>vs.</i> RHE	-0.90 V <i>vs.</i> RHE	-1.00 V <i>vs.</i> RHE	-1.10 V <i>vs.</i> RHE
	$FE$ %	$FE$ %	$FE$ %	$FE$ %
Hydrogen	25.8	36.9	64.9	75.3
Methane	-	0.005	0.02	0.01
Ethylene	-	-	0.004	-
Ethane	-	0.007	0.06	0.002
Propylene	-	Trace	0.005	0.0003
Propane	-	-	Trace	-
Methanol	26.3	24.2	13	6.6
Ethanol	43.6	36.3	23.1	9.8
Allyl alcohol	-	-	0.003	-
1-Butanol	-	0.006	0.025	0.01
Total	95.7	97.5	101.1	91.8
Total $j$ mA cm <sup>-2</sup>	-25.89	-36	-61.9	-188

- Product not detected.

**Table A.15.** Production rates ( $r$ ) of products detected from the electrolysis of 50 mM acetaldehyde on OD-Cu in 0.1 M PPB at -1.00 V *vs.* RHE for 60 min. The values shown are an average taken from three experiments, with their standard deviations given in the brackets. Related to **Figure 4.2**.

Relevant products	$r$ $\mu\text{mol cm}^{-2} \text{ h}^{-1}$	Stdev -
Hydrogen	16937	-1888
Methane	-	-
Ethylene	34.3	-4.1
Ethane	195	-27
Propylene	-	-
Methanol	-	-
Ethanol	13339	-962
1-Propanol	-	-

- Product not detected or process not applicable.

**Table A.16.** Production rates ( $r$ ), in  $\mu\text{mol cm}^{-2} \text{h}^{-1}$ , of liquid products formed at open circuit potential (OCP) and at  $-0.40 \text{ V vs. RHE}$  on OD-Cu in  $0.1 \text{ M KOH}$  for 90 min. Production rates in  $\mu\text{mol cm}^{-2} \text{h}^{-1}$  of liquid and gaseous products detected from the electrolysis of CO or formaldehyde ( $50 \text{ mM}$ ) at  $-1.00 \text{ V vs. RHE}$  on OD-Cu in  $0.1 \text{ M PPB}$  for 60 min. Stdev refer to the  $FE$  values of  $-1.00 \text{ V vs. RHE}$ . Related to **Figure 4.2**.

Relevant products	Carbon Monoxide				Formaldehyde	
	OCP	$-0.40 \text{ V}$	$-1.00 \text{ V}$		$-1.00 \text{ V}$	
	$r$ $\mu\text{mol cm}^{-2} \text{h}^{-1}$	$r$ $\mu\text{mol cm}^{-2} \text{h}^{-1}$	$r$ $\mu\text{mol cm}^{-2} \text{h}^{-1}$	Stdev -	$r$ $\mu\text{mol cm}^{-2} \text{h}^{-1}$	Stdev -
Hydrogen	–	–	30468	5840	50490	1888
Formate	1.61	0.13	–	–	–	–
Methane	–	– <sup>a</sup>	34.9	5	16.2	0.5
Methanol	–	– <sup>a</sup>	4.6	0.4	8483	529
Ethylene	–	–	70.9	15.8	–	–
Ethane	–	–	0.15	0.06	–	–
Ethanol	0.01	0.22	26.5	4.8	–	–
Acetate	0.19	0.3	–	–	–	–
Acetaldehyde	3.16	trace	–	–	–	–
Propylene	–	–	–	–	–	–
Propionaldehyde	0.01	–	–	–	–	–
Allyl alcohol	–	–	2.1	0.4	–	–
1-Propanol	0.01	0.02	2.2	0.4	–	–

– Product not detected or process not applicable.

<sup>a</sup> Low rates to  $\text{CH}_4$  and  $\text{CH}_3\text{OH}$  hint low coverages for their precursors:  $\text{CHOH}$ ,  $\text{CH}_2\text{O}$ ,  $\text{CH}_2\text{OH}$ ,  $\text{CH}_3\text{O}$  and  $\text{CH}_x$ .

**Table A.17.** Production rates ( $r$ ) of products detected from the electrolysis of CO ( $C_1$  reagent) with 50 mM acetaldehyde ( $C_2$  reagent) on OD-Cu in 0.1 M PPB at  $-1.00$  V *vs.* RHE for 60 min. Standard deviations for the values shown are an average taken from three experiments. Related to **Figure 4.2**.

<b>Relevant products</b>	<b><math>r</math> <math>\mu\text{mol cm}^{-2} \text{h}^{-1}</math></b>	<b>Stdev -</b>
Hydrogen	15189	-5911
Methane	17	-4.6
Ethylene	105	-8
Ethane	0.26	-0.03
Propylene	Trace	
Methanol	-	
Ethanol	9842	-2578
1-Propanol	12.1	-3.8
1-Butanol	0.4	-0.1

- Product not detected or process not applicable.

**Table A.18.** Production rates ( $r$ ), Faradaic efficiencies ( $FE$ ) and geometric partial current densities ( $j$ ) of products detected from the electrolysis of 50 mM formaldehyde ( $C_1$  reagent) and 50 mM acetaldehyde ( $C_2$  reagent) on OD-Cu in 0.1 M PPB at  $-1.00$  V *vs.* RHE for 60 min. The values shown are an average taken from three experiments, with their standard deviations given in the brackets. We note that 1-propanol and acetone were not detected by headspace GC, while propane was qualitatively detected by GC. Results from control electrolysis experiments of formaldehyde (**Table A.16.**) or acetaldehyde (**Table A.17.**) allowed us to conclude that  $C_1$  products originated from formaldehyde,  $C_2$  and  $C_4$  products from acetaldehyde, and  $C_3$  products from the combination of both reactants. The  $FE$  and  $j$  values were calculated based on the number of electrons transferred from the respectively elucidated reactants. Related to **Figure 4.2.**

Relevant products	$r$ $\mu\text{mol cm}^{-2} \text{h}^{-1}$	Stdev -	$FE$ %	Stdev -	$j$ $\text{mA cm}^{-2}$	Stdev -
Hydrogen	39963	2732	64.9	0.6	-40.2	2.7
Methane	6.4	0.4	0.02	0.001	-0.0120	0.0001
Ethylene	2.9	-0.3	0.004	0.001	-0.003	0.001
Ethane	20.4	1.6	0.06	0.01	-0.037	0.009
Propylene	1.4	0.6	0.005	0.001	-0.003	0.001
Propane	Trace		Trace		Trace	
Methanol	8969	611	13	1.6	-8.0	0.5
Ethanol	16005	752	23.1	0.3	-14.3	0.7
Allyl alcohol	2	0.4	0.003	0.0004	-0.0020	0.0004
1-Butanol	8.8	0.5	0.025	$1.5 \times 10^{-7}$	-0.016	0.001

- Product not detected or process not applicable.

Appendix A

**Table A.19.** Production rates ( $r$ ), in  $\mu\text{mol cm}^{-2} \text{h}^{-1}$ , of products formed under open circuit in 0.1 M KOH in the presence of OD-Cu for 90 min upon bubbling carbon monoxide as  $\text{C}_1$  reagent in the presence of  $\text{C}_2$  reagents (50 mM). Oxalate cannot be detected by  $^1\text{H}$  NMR. Methanol and propanol were not detected by  $^1\text{H}$  NMR. Propylene was not detected by headspace GC-MS. Related to **Figure 4.2**.

Relevant products	Glyoxal	Ethylene glycol	Oxalate	Acetate	Ethanol
	$r$ $\mu\text{mol cm}^{-2} \text{h}^{-1}$	$r$ $\mu\text{mol cm}^{-2} \text{h}^{-1}$	$r$ $\mu\text{mol cm}^{-2} \text{h}^{-1}$	$r$ $\mu\text{mol cm}^{-2} \text{h}^{-1}$	$r$ $\mu\text{mol cm}^{-2} \text{h}^{-1}$
Glyoxal	-	0.12	0.00	0.00	2.22
Ethylene glycol	23.58	-	0.63	7.24	0.00
Acetate	0.13	0.05	32.57	-	0.05
Ethanol	0.00	1.04	0.00	0.12	-
Formate	3.06	0.67	1.09	1.35	1.36
Acetaldehyde	0.11	0.00	0.00	0.00	0.00

- Product not detected or process not applicable.

**Table A.20.** Production rates ( $r$ ), in  $\mu\text{mol cm}^{-2} \text{h}^{-1}$ , of products formed at  $-0.40 \text{ V vs. RHE}$  on OD-Cu in 0.1 M KOH for 90 min upon bubbling carbon monoxide as  $\text{C}_1$  reagent in the presence of  $\text{C}_2$  reagents (50 mM). Oxalate cannot be detected by  $^1\text{H}$  NMR. Propylene was not detected by headspace GC-MS. Related to **Figure 4.2**.

Relevant products	Glyoxal	Ethylene glycol	Oxalate	Acetate	Ethanol
	$r$ $\mu\text{mol cm}^{-2} \text{h}^{-1}$	$r$ $\mu\text{mol cm}^{-2} \text{h}^{-1}$	$r$ $\mu\text{mol cm}^{-2} \text{h}^{-1}$	$r$ $\mu\text{mol cm}^{-2} \text{h}^{-1}$	$r$ $\mu\text{mol cm}^{-2} \text{h}^{-1}$
Glyoxal	-	0.22	5.83	0.14	0.00
Ethylene glycol	27.86	-	0.49	0.09	0.00
Acetate	4.53	0.45	0.26	-	2.10
Ethanol	0.89	1.40	0.34	0.21	-
Methanol	0.05	0.07	0.00	0.03	0.03
Formate	3.16	1.44	1.08	1.04	1.97
Acetaldehyde	0.13	0.00	0.00	0.00	0.00
1-Propanol	0.15	0.25	0.22	0.12	0.12

- Product not detected or process not applicable.

**Table A.21.** Production rates ( $r$ ), in  $\mu\text{mol cm}^{-2} \text{h}^{-1}$ , of products formed under open circuit in 0.1 M KOH in the presence of OD-Cu for 90 min upon addition of formaldehyde (50 mM) as  $C_1$  reagent in the presence of  $C_2$  reagents (50 mM). Oxalate cannot be detected by  $^1\text{H}$  NMR. Propylene was not detected by headspace GC-MS. Related to **Figure 4.2**.

Relevant products	Glyoxal	Ethylene glycol	Oxalate	Acetate	Ethanol
	$r$ $\mu\text{mol cm}^{-2} \text{h}^{-1}$	$r$ $\mu\text{mol cm}^{-2} \text{h}^{-1}$	$r$ $\mu\text{mol cm}^{-2} \text{h}^{-1}$	$r$ $\mu\text{mol cm}^{-2} \text{h}^{-1}$	$r$ $\mu\text{mol cm}^{-2} \text{h}^{-1}$
Glyoxal	-	0.00	0.40	0.37	0.25
Ethylene glycol	29.17	-	0.45	0.41	0.00
Acetate	0.28	0.46	0.20	-	0.16
Ethanol	0.09	0.00	0.13	0.00	-
Methanol	90.20	171.96	74.43	139.17	104.75
Formate	13.12	89.25	7.36	79.12	37.55
Acetaldehyde	0.20	0.00	0.38	0.00	0.00
1-Propanol	0.01	0.00	0.10	0.00	0.00

- Product not detected or process not applicable.



**Table A.22.** Production rates ( $r$ ), in  $\mu\text{mol cm}^{-2} \text{h}^{-1}$ , of products formed at  $-0.40 \text{ V vs. RHE}$  on OD-Cu in  $0.1 \text{ M KOH}$  for 90 min upon addition of formaldehyde ( $50 \text{ mM}$ ) as  $\text{C}_1$  reagent in the presence of  $\text{C}_2$  reagents ( $50 \text{ mM}$ ). Oxalate cannot be detected by  $^1\text{H NMR}$ . 1-Propanol was not detected by  $^1\text{H NMR}$ . Propylene was not detected by headspace GC-MS. Related to **Figure 4.2**.

Relevant products	Glyoxal	Ethylene glycol	Oxalate	Acetate	Ethanol
	$r$ $\mu\text{mol cm}^{-2} \text{h}^{-1}$	$r$ $\mu\text{mol cm}^{-2} \text{h}^{-1}$	$r$ $\mu\text{mol cm}^{-2} \text{h}^{-1}$	$r$ $\mu\text{mol cm}^{-2} \text{h}^{-1}$	$r$ $\mu\text{mol cm}^{-2} \text{h}^{-1}$
Glyoxal	-	0.00	0.38	0.36	0.37
Ethylene glycol	20.47	-	0.33	0.62	0.00
Acetate	0.17	1.21	0.24	-	0.22
Ethanol	0.10	0.00	0.09	0.00	-
Methanol	376.78	123.83	212.24	176.96	207.21
Formate	12.20	148.57	51.46	30.49	23.05
Acetaldehyde	0.14	0.00	0.00	0.00	0.00

- Product not detected or process not applicable.

**Table A.23.** Production rates ( $r$ ), in  $\mu\text{mol cm}^{-2} \text{h}^{-1}$ , of products formed under open circuit in  $0.1 \text{ M KOH}$  in the presence of OD-Cu for 90 min upon addition of methanol ( $50 \text{ mM}$ ) as  $\text{C}_1$  reagent in the presence of  $\text{C}_2$  reagents ( $50 \text{ mM}$ ). Oxalate cannot be detected by  $^1\text{H NMR}$ . Propylene was not detected by headspace GC-MS. Related to **Figure 4.2**.

Relevant products	Glyoxal	Ethylene glycol	Oxalate	Acetate	Ethanol
	$r$ $\mu\text{mol cm}^{-2} \text{h}^{-1}$	$r$ $\mu\text{mol cm}^{-2} \text{h}^{-1}$	$r$ $\mu\text{mol cm}^{-2} \text{h}^{-1}$	$r$ $\mu\text{mol cm}^{-2} \text{h}^{-1}$	$r$ $\mu\text{mol cm}^{-2} \text{h}^{-1}$
Glyoxal	-	0.00	1.69	0.00	0.00
Ethylene glycol	39.61	-	0.10	0.00	0.00
Acetate	0.25	0.07	0.09	-	0.05
Ethanol	0.11	0.00	0.05	0.03	-
Formate	4.83	0.00	0.08	0.00	0.00
Acetaldehyde	0.22	0.00	0.39	0.00	0.00
1-Propanol	0.15	0.00	0.10	0.01	0.00

- Product not detected or process not applicable.

**Table A.24.** Production rates ( $r$ ), in  $\mu\text{mol cm}^{-2} \text{h}^{-1}$ , of products formed on OD-Cu at  $-0.40 \text{ V vs. RHE}$  in  $0.1 \text{ M KOH}$  for  $90 \text{ min}$  upon addition of methanol ( $50 \text{ mM}$ ) as  $\text{C}_1$  reagent in the presence of  $\text{C}_2$  reagents ( $50 \text{ mM}$ ). Oxalate cannot be detected by  $^1\text{H NMR}$ . Propylene was not detected by headspace GCMS. Related to **Figure 4.2**.

Relevant products	Glyoxal	Ethylene glycol	Oxalate	Acetate	Ethanol
	$r$ $\mu\text{mol cm}^{-2} \text{h}^{-1}$	$r$ $\mu\text{mol cm}^{-2} \text{h}^{-1}$	$r$ $\mu\text{mol cm}^{-2} \text{h}^{-1}$	$r$ $\mu\text{mol cm}^{-2} \text{h}^{-1}$	$r$ $\mu\text{mol cm}^{-2} \text{h}^{-1}$
Glyoxal	-	0.00	0.04	0.00	0.00
Ethylene glycol	26.44	-	0.00	0.00	0.00
Acetate	0.12	0.15	0.05	-	0.07
Ethanol	0.08	0.00	0.01	0.00	-
Formate	2.35	0.34	0.16	0.05	0.25
Acetaldehyde	0.14	0.00	0.25	0.00	0.00
1-Propanol	0.08	0.00	0.09	0.00	0.00

- Product not detected or process not applicable.

**Table A.25.** Concentrations and resulting background production rates of relevant impurities found in  $50 \text{ mM}$  solutions prepared with commercial glyoxal and sodium oxalate used for experiments reflected in **Table A.19.** till **Table A.24.**. Related to **Figure 4.2**.

Relevant products	Glyoxal	Oxalate	Glyoxal	Oxalate
	$C$ mM	$C$ mM	$r$ $\mu\text{mol cm}^{-2} \text{h}^{-1}$	$r$ $\mu\text{mol cm}^{-2} \text{h}^{-1}$
Ethylene glycol	3.83	0	41.69	0
Acetate	0.075	0.07	0.82	0.76
Ethanol	0.02	-	0.22	-
Methanol	-	-	-	-
Formate	0.33	0.075	3.59	0.82
Acetaldehyde	0.02	-	0.22	-
1-Propanol	-	-	-	-

- Product not detected or process not applicable.

**Table A.26.** Values of  $\alpha$  and  $\beta$  used to approximate the energies of transition states ( $E_{\text{TS}}$ ), for O-H and C-H hydrogenations.<sup>[243]</sup> The LSR with the lowest MAE on Cu was selected: BEP for O-H and C-H breakings. Parameters for C-C, C-O, and C-OH values that describe bond formations are shown as a reference. Related to **Figure 4.3**.

	Bond breaking	O-H	C-H	C-C	C-O	C-OH
$\alpha / -$		0.39	0.63	1.00	1.00	1.00
$\beta / \text{eV}$		0.89	0.81	0.64	1.24	1.48

**Table A.27.** (a) Panel clarification of the 6 families indicated by thicker lines cluster  $C_1$  and  $C_2$  couplings in (b). (b) Reaction energies,  $\Delta E$  (Eq. 34) in eV, exothermic values indicate larger thermodynamic driving forces to the corresponding  $C_3$  products. The (-) marks the direction in which the C-C bond is formed. Void boxes indicate unstable  $C_3$  species. Related to **Figure 4.3**.

(a) Panel instruction for the 6 families

1	2
2	3
4	5
5	6

(b)

	unfavored				favored					
	-C	-CH	-CH <sub>2</sub>	-CH <sub>3</sub>	-CO	-COH	-CHO	-CHOH	-CH <sub>2</sub> O	-CH <sub>2</sub> OH
CC-	-0.66	-0.83	-1.06	-1.08	0.04	-0.70	-1.15	-1.16	-0.77	-1.27
CHC-	-0.87	-0.38	-1.00	-0.94	0.12	-0.06	-0.93	-0.95	0.33	0.18
CH <sub>2</sub> C-	-0.82	-0.72	-1.05	-0.73	-0.17	-0.67	-0.68	-0.49	-0.46	-0.62
CH <sub>3</sub> C-	-1.14	-0.96	-1.03	-0.27	-0.32	-1.12	-1.38	-1.31	0.14	-0.54
CCH-	-0.21	-0.32	-0.87	-0.85	0.40	0.01	-1.15	-1.21	-0.72	-0.92
CHCH-	-0.53	-0.45	-1.01	-0.61	0.08	-0.57	-0.84	-0.87	-0.25	-0.79
CH <sub>2</sub> CH-	-0.93	-0.87	-1.50	-1.17	0.25	-0.41	-1.52	-1.57	-1.14	-1.09
CH <sub>3</sub> CH-	-1.56	-1.11	-1.82	-1.07	-0.36	-1.33	-1.98	-1.88	-1.16	-1.46
CCH <sub>2</sub> -	0.49		-0.51	-0.88		0.54	-0.74	-0.44	-0.35	-1.03
CHCH <sub>2</sub> -		0.38	-0.42	-0.42	0.52	0.10	-0.38	-0.19	-0.24	-0.60
CH <sub>2</sub> CH <sub>2</sub> -	-0.13	0.30	-0.48	-0.49	0.38	-0.02	-0.41	-0.32	-0.33	-0.62
CH <sub>3</sub> CH <sub>2</sub> -	-1.18	-0.38	-1.17	-1.36	0.91	-0.60	-1.15	-1.05	-1.36	-1.59
COC-	0.24	0.36	-0.21	-0.06	1.53	0.37	-0.25	0.35	0.48	0.28
COHC-	-0.77	-0.09	-0.99	-1.14	0.10	0.30	-0.50	-1.02	-0.66	-1.07
CHOC-	-0.99	-0.73	-0.77	-1.17	-0.30	-0.28	-1.67	-1.15	-0.51	-1.32
CHOHC-	-0.43	-0.19	-0.01	-0.54	0.87	-0.23	-0.59	0.50	-0.45	-0.17
CH <sub>2</sub> OC-	-1.68	-0.54	-1.61	-0.71	-0.64	-1.50	-1.58	-2.08		-1.24
CH <sub>2</sub> OHC-	-1.16	0.32	-0.75	-0.37	0.18	-0.90	-1.37	-0.78	-0.22	0.06
COCH-	-0.16	-0.27	-0.25	-0.21	0.92	1.01	0.17	-0.77	0.42	0.13
COHCH-	-0.01	-0.38	-0.38	-0.65	1.55	1.26		-0.34	0.00	-0.40
CHOCH-	-0.78	-0.26	-1.09	-0.91	1.10		-0.61	-0.68	-0.49	-0.76
CHOHCH-	-0.89	-0.34	-1.19	-0.85	0.11	0.01	-0.73	-0.89	-0.41	-0.65
CH <sub>2</sub> OCH-	-1.87	-1.18	-2.22	-1.59	-0.16	-1.12	-2.00	-1.88	-1.37	-1.56
CH <sub>2</sub> OHCH-	-1.38	-1.04	-1.49	-1.21	0.23	-0.84	-1.59	-1.44	-0.88	-1.11
COCH <sub>2</sub> -		-0.16	-1.02	0.18	0.52	0.04	-0.37	-0.49	0.79	0.33
COHCH <sub>2</sub> -	0.42	0.32	-0.52	-0.42	0.94	0.57	0.23	-0.09	0.03	-0.43
CHOCH <sub>2</sub> -	-0.14	0.55	-0.20	-0.26	1.24	0.94	0.40	0.36	-0.03	-0.18
CHOHCH <sub>2</sub> -	-0.01	0.59	-0.26	-0.31	0.97	0.47	0.21	-0.17	0.58	0.53
CH <sub>2</sub> OCH <sub>2</sub> -	-0.56	-0.11	-0.92	-1.27	1.60	-0.06	-0.83	-0.06	-1.02	-1.15
CH <sub>2</sub> OHCH <sub>2</sub> -	-1.00	-0.23	-0.97	-1.27	1.38	-0.28	-0.74	0.12	-0.91	-1.24

Continued Table A.27.

	-C	-CH	-CH <sub>2</sub>	-CH <sub>3</sub>	-CO	-COH	-CHO	-CHOH	-CH <sub>2</sub> O	-CH <sub>2</sub> OH
CCO-			0.51	0.18		1.63	0.79	0.95	0.66	0.30
CHCO-		0.67	-0.26	-0.82		1.72	-0.28	-0.16	0.08	-0.61
CH <sub>2</sub> CO-	-0.47	-0.44	-1.87	-1.46	0.04	-0.47	-1.19	-1.39	-0.82	-1.28
CH <sub>3</sub> CO-	-0.91	-1.11	-1.57	-0.82	0.32	-0.86	-1.06	-1.13	-0.57	-0.69
CCOH-			-0.79	-0.93		0.14	-0.85	-0.77	-0.59	-0.94
CHCOH-		-0.36	-0.33	-0.57	1.49	-0.16	-0.57	-0.06	0.16	-0.58
CH <sub>2</sub> COH-	-0.60	-0.15	-1.39	-0.91	0.21	-0.35	-0.95	-1.20	-1.14	-0.99
CH <sub>3</sub> COH-	-1.48	-1.13	-1.65	-0.46	0.14	-0.69	-1.38	-1.46	-0.34	-0.60
CCHO-				0.28		1.12	0.80			0.32
CHCHO-				0.55		0.97	0.46			0.11
CH <sub>2</sub> CHO-			0.08	-0.06		0.79	0.31	0.30	0.38	0.10
CH <sub>3</sub> CHO-	0.05	0.14	-0.98	-1.12	-0.01	-0.25	-0.67	-0.70	-0.64	-1.12
CCHOH-				-0.10			0.20		0.16	-0.06
CHCHOH-		1.06	0.01	-0.11	1.28	0.31	0.70	-0.19	0.21	-0.13
CH <sub>2</sub> CHOH-		0.41	-0.42	-0.45	0.67	0.23	-0.11	-0.30	-0.07	-0.56
CH <sub>3</sub> CHOH-	-0.80	-0.38	-1.11	-1.18	-0.05	-0.50	-0.69	-0.90	-0.96	-1.26
COCO-			-1.09	-0.70	0.83	-0.86	-0.69	-1.22	-0.34	-0.96
COHCO-	0.08	0.97	-1.04	-1.32	-0.30	-1.19	-0.66	-1.20	0.04	-0.62
CHOCO-	-0.43	-0.70	-1.43	-1.19	0.19	-0.33	-1.63	-1.79	-1.10	-1.62
CHOHCO-	-0.64	-0.95	-2.00	-1.63	-0.71	-1.24	-2.16	-2.03	-2.07	-1.71
CH <sub>2</sub> OCO-	-0.36	-0.13	-0.85	-0.49	0.75	0.57	-0.89	-1.50	-0.16	-0.44
CH <sub>2</sub> OHCO-	-0.78	-0.89	-1.38	-0.68	0.06	-0.15	-1.47	-1.19	-0.50	-0.94
COCO-		0.21	-1.26	-0.58	-0.48	-1.36	-0.40	-1.64	-0.16	-0.41
COHCO-	0.28	-0.02	-0.39	0.01	0.06	-0.73	-0.67	-0.47	-0.18	-0.17
CHOCO-	-0.69	-0.42	-0.98	-0.67	1.04	-0.65	-0.94	-1.03	-0.80	-1.05
CHOHCO-	-0.62	0.07	-1.25	-0.76	-0.22	-0.47	-1.05	-1.13	-1.28	-1.04
CH <sub>2</sub> OCO-	-1.10	-0.36	-1.84	-0.30	0.60	-0.83	-1.47	-1.94		
CH <sub>2</sub> OHCO-	-1.51	-1.17	-1.76	-0.63	0.29	-0.89	-1.79	-1.76		-0.75
COCHO-				-0.95	0.35			-0.77	-0.61	-1.26
COHCHO-	1.06	0.73	0.05	-0.08		0.59	0.31	-0.16		-0.67
CHOCHO-	1.10	0.59	-0.07	-0.13		0.68	0.08	-0.14	-0.06	-0.57
CHOHCHO-			-0.18	-0.26	0.60	0.11	-0.24	-0.02	-0.39	
CH <sub>2</sub> OCHO-			-0.47	-0.57	0.40		-0.53	-0.75	-0.17	-0.74
CH <sub>2</sub> OHCHO-	0.06	-0.32	-0.83	-1.14	-0.34	-0.86	-1.13		-0.83	-1.63
COCHO-		-0.40	-1.40	-1.46	-0.41	-0.81		-1.49	-1.41	-1.72
COHCHO-		0.10	-0.37	-0.44	0.65	-0.02	-0.14	-0.44	-0.15	-0.69
CHOCHO-	-0.17	0.77	-0.44	-0.36		0.14	-0.08	-0.59	-0.59	-0.63
CHOHCHO-		-0.03	-0.53	-0.48	0.35	-0.07	-0.50	-0.57	-0.52	-0.71
CH <sub>2</sub> OCHO-	-0.66	-0.18	-0.86	-1.08	-0.13	-0.33	-1.05	-1.07	-1.04	-0.97
CH <sub>2</sub> OHCHO-	-0.51	-0.14	-0.97	-1.01	-0.06	-0.49	-0.71	-0.88	-0.59	-1.20



**Table A.28.** (a) Panel clarification of the 6 families indicated by thicker lines cluster  $C_1$  and  $C_2$ .couplings in (b). (b) Activation energies ( $E_a$ ) in eV, zero values indicate barrier-less reactions. The connecting point between the two fragments is shown by (-) marks the direction. Void boxes denote not located transition states. Related to **Figure 4.3**.

(a) Panel instruction for the 6 families

1	2
2	3
4	5
5	6

(b)

	unfavored <span style="display: inline-block; width: 100px; height: 10px; background: linear-gradient(to right, black, purple, red, orange, yellow);"></span> favored									
	-C	-CH	-CH <sub>2</sub>	-CH <sub>3</sub>	-CO	-COH	-CHO	-CHOH	-CH <sub>2</sub> O	-CH <sub>2</sub> OH
CC-	1.02	1.45	1.46	1.33	0.82	0.95	0.51	0.38	0.24	1.23
CHC-	1.10	0.62	0.85	0.81	0.99		0.43	0.91	0.81	2.00
CH <sub>2</sub> C-	1.82	1.83	1.41	1.25	1.10	1.31	0.60	0.48	0.76	1.40
CH <sub>3</sub> C-		1.31	0.38	1.00	0.96	0.88	*0.75			0.92
CCH-	0.57	*0.85	0.50	1.82	1.51	1.13	0.41	*1.93	0.59	1.36
CHCH-	*0.69	0.94	0.70	*2.37	1.23	1.15	0.23	1.46	0.59	*2.41
CH <sub>2</sub> CH-	1.00	0.83	1.42	*0.96	0.76	1.14	0.08	*0.45	0.72	*2.00
CH <sub>3</sub> CH-	1.34	*0.87	*0.11	0.41	0.62	*1.12	0.19	0.00	0.68	*1.60
CCH <sub>2</sub> -	1.00			1.33		1.24	1.53	0.36	*0.60	*0.86
CHCH <sub>2</sub> -		1.81	1.08	1.64	0.98	1.56	0.24	0.80	0.53	*0.35
CH <sub>2</sub> CH <sub>2</sub> -		1.45	1.19	1.73	1.11	1.53	1.61	1.05	1.22	2.02
CH <sub>3</sub> CH <sub>2</sub> -	0.98	0.75	0.68	2.70	2.15	1.21		0.26	1.06	*1.11
COC-	1.38	1.34	1.54	2.09	2.07	1.73	1.81	0.74	0.98	1.58
COHC-	1.22	1.08	0.66	0.94	1.42		0.61	0.82	*0.38	0.98
CHOC-	0.98	0.63	0.52	*0.95	1.73	1.62	0.35	0.34	0.60	0.68
CHOHC-	1.24	1.34		1.62	1.35	1.71	0.80	*1.84	0.87	1.05
CH <sub>2</sub> OC-			0.39		1.09	*1.10	0.50	0.43		0.78
CH <sub>2</sub> OHC-	0.91	1.53	0.80	1.09	1.43		0.44	0.99	0.77	1.06
COCH-	2.47		1.60	1.43	1.76	1.48	1.05	2.09	0.68	*1.84
COHCH-	1.28		1.89	*2.79	2.12	0.50		*1.35	*1.09	1.24
CHOCH-	0.63	1.42	1.25	0.87	1.04		*3.12	0.70	0.71	1.39
CHOHCH-	*1.40	1.16	*0.68	1.53	1.14		0.65	0.78	0.81	*1.37
CH <sub>2</sub> OCH-		1.36		0.00	1.09	*0.73	0.00	0.34	0.40	0.63
CH <sub>2</sub> OHC-	0.97	*0.87	*1.36	*0.56	*1.72	1.37	0.16	*2.34	0.82	*1.66
COCH <sub>2</sub> -		1.48	0.86	2.37	0.65		0.78	0.84	*0.82	1.96
COHCH <sub>2</sub> -	0.99	1.87	1.17	1.90	1.18	1.30	0.71	1.13	*0.62	*1.01
CHOCH <sub>2</sub> -	2.37	1.52	1.24	2.24	1.59	1.57	*2.36	1.41	*1.04	*2.47
CHOHCH <sub>2</sub> -	1.85	2.05	1.17	1.03	1.46		2.36	0.92	0.64	1.87
CH <sub>2</sub> OCH <sub>2</sub> -	*0.67	0.77	1.24	*2.18	*2.35	*1.43	*1.71	1.37	1.63	*1.57
CH <sub>2</sub> OHC-	*0.56	*1.15	1.39	*1.65	2.36	*1.37		2.32	1.06	*0.94

Continued Table A.28.

	-C	-CH	-CH <sub>2</sub>	-CH <sub>3</sub>	-CO	-COH	-CHO	-CHOH	-CH <sub>2</sub> O	-CH <sub>2</sub> OH
CCO-			1.26	*1.60		1.87	1.56	*0.94	1.08	1.04
CHCO-		1.55	1.08	2.11			1.06	1.23	1.00	1.37
CH <sub>2</sub> CO-	0.83	0.71		0.84	0.62	0.98	*0.00	*0.00	0.00	*0.42
CH <sub>3</sub> CO-	*0.57	0.72	0.28	*1.74	*0.75	1.01	0.32	*0.73	*0.63	*1.55
CCOH-			1.53	*0.45			0.44	*0.25	*0.60	
CHCOH-		*0.96		3.09	2.62	0.68	*3.21	1.83	*1.41	*2.27
CH <sub>2</sub> COH-	2.36	*1.42	1.12	1.88	*1.14	1.45	0.52	0.41		*0.41
CH <sub>3</sub> COH-	*0.67	0.26	1.86	1.77	0.69	1.14	0.21	1.91	*0.35	*0.69
CCHO-						1.67	*0.71			*1.14
CHCHO-				2.15			0.91			*0.93
CH <sub>2</sub> CHO-			1.24	1.48	2.05	1.96	0.97	1.24	1.16	1.47
CH <sub>3</sub> CHO-	1.86	0.92	0.48	0.83	0.30	1.14	*1.25	0.58	0.50	*0.22
CCHOH-				2.02			1.06		0.59	*0.80
CHCHOH-		1.92	1.34	1.70	1.25		1.51		0.70	1.40
CH <sub>2</sub> CHOH-		1.68	1.22	1.50	0.88	1.58	1.03	0.97	0.92	1.64
CH <sub>3</sub> CHOH-	0.71	1.10	1.15	*1.15	0.99	1.45	1.18	1.28	*0.74	*1.29
COCO-				*1.41	0.92	0.96	0.73	0.41	0.79	*1.49
COHCO-	1.97	1.21	0.40	1.81	0.79		1.15	0.52		0.25
CHOCO-	2.24	1.02	*0.76	1.04	*0.95	1.23	0.29	*3.09	*0.70	*0.16
CHOHCO-	*0.82	0.14	*0.00	*0.14	0.03	0.53	*1.01	0.00	0.00	*0.70
CH <sub>2</sub> OCO-	0.55		1.04	*1.91	1.41	1.51	*0.47	0.54	1.23	*1.36
CH <sub>2</sub> OHCO-	1.69	0.84	*0.50	*1.65	*0.70		*0.13	*0.39	*1.44	*1.57
COCOH-		1.56	*0.05	0.55	0.96		1.29		0.76	1.65
COHCOH-		1.73	0.99	1.30	*1.07		*1.79	0.51	*1.77	*2.66
CHOCOH-	1.47	*0.93	1.32	1.82	3.31	*1.60	1.47	*1.91	1.40	*0.89
CHOHCOH-	*1.06	1.28	0.64	2.97	0.91	1.31	*0.54	0.81	*0.24	*1.76
CH <sub>2</sub> OCOH-	*1.85	*1.45		*0.61	1.84		0.54			
CH <sub>2</sub> OHCOH-	0.72	*0.15		*2.85	1.37	*0.93	*0.01	*0.00		*1.86
COCHO-				0.91	0.78			0.72	0.42	*0.01
COHCHO-	1.07		1.26	1.56		1.42				*0.48
CHOCHO-	*0.96	1.46	0.78	*1.64		1.65	*0.97	0.56	*0.36	1.32
CHOHCHO-			1.10	1.31	1.16		0.78	0.87	0.76	
CH <sub>2</sub> OCHO-			0.72	1.40	0.80		*1.86	0.47	0.93	*1.03
CH <sub>2</sub> OHCHO-	*0.64	*0.74	0.37	*0.77	*0.41	*0.97	0.47		*0.13	*0.65
COCHOH-		0.47	0.24	0.91	0.00	*0.84		0.00	0.00	*0.01
COHCHOH-			1.03	1.72	*0.33	1.29		0.56	*0.45	1.18
CHOCHOH-	1.62	1.33	0.68	1.47		1.25	0.61	*0.40	*0.51	*2.03
CHOHCHOH-			1.12	1.58	1.14	1.65	*0.79	0.93	0.85	*2.07
CH <sub>2</sub> OCHOH-	0.71	1.27	0.96	*1.82	0.97		*0.22			*0.99
CH <sub>2</sub> OHCHOH-	*2.41	1.56	1.19	*1.85	*1.21	1.89	*2.33	*1.60	*1.80	*1.60

**Table A.29.** (a) Panel clarification of the 6 families indicated by thicker lines cluster  $C_1$  and  $C_2$ .couplings in (b). (b) Activation energies ( $E_a$ ) in eV, zero values indicate barrier-less reactions. The connecting point between the two fragments is shown by (-) marks the direction. Void boxes denote not located transition states. Related to **Figure 4.3**.

(a) Panel instruction for the 6 families

1	2
2	3
4	5
5	6

(b)

	unfavored <span style="display: inline-block; width: 100px; height: 10px; background: linear-gradient(to right, purple, red, orange, yellow);"></span> favored									
	-C	-CH	-CH <sub>2</sub>	-CH <sub>3</sub>	-CO	-COH	-CHO	-CHOH	-CH <sub>2</sub> O	-CH <sub>2</sub> OH
CC-	0.60	0.72	0.91	0.89	0.47	0.55	0.65	0.60	0.63	0.62
CHC-	0.48	0.75	0.86	0.33	0.31	0.78	0.35	0.32	0.77	0.87
CH <sub>2</sub> C-	0.87	1.05	0.67	0.60	0.30	0.78	0.64	0.87	0.46	0.52
CH <sub>3</sub> C-	1.18	0.86	0.93	0.70	0.55	0.64	0.37	0.59	1.02	0.54
CCH-	0.25	0.27	0.53	0.38	0.38	0.53	0.10	0.29	0.21	0.23
CHCH-	0.45	0.72	0.72	0.65	0.24	0.63	0.29	0.28	0.48	0.50
CH <sub>2</sub> CH-	0.60	0.61	0.71	0.71	0.50	0.53	0.30	0.35	0.48	0.61
CH <sub>3</sub> CH-	0.90	0.99	1.16	0.63	0.12	0.70	0.51	0.80	0.45	0.51
CCH <sub>2</sub> -	0.46		0.73	0.31		0.42	0.54	0.38	0.20	0.24
CHCH <sub>2</sub> -		0.52	0.44	0.32	0.01	0.46	0.46	0.16	0.02	0.21
CH <sub>2</sub> CH <sub>2</sub> -	0.44	0.27	0.16	0.10	-0.31	0.21	0.25	-0.18	-0.05	-0.03
CH <sub>3</sub> CH <sub>2</sub> -	0.54	0.68	0.62	0.49	0.43	0.64	0.75	0.32	0.39	0.45
COC-	0.87	0.95	0.75	0.66	1.05	0.84	0.77	0.95	0.50	0.52
COHC-	0.55	1.03	0.84	0.35	0.44	0.45	0.36	0.39	0.24	0.24
CHOC-	1.01	0.94	1.05	0.43	0.72	0.71	0.57	0.70	0.36	0.31
CHOHC-	0.92	0.88	1.23	0.62	0.86	0.71	0.66	0.83	0.49	0.50
CH <sub>2</sub> OC-	0.97	1.35	0.85	1.07	0.44	0.58	0.34	0.51		0.45
CH <sub>2</sub> OHC-	1.06	1.56	1.02	0.70	0.56	0.68	0.40	0.62	0.55	0.44
COCH-	0.79	0.47	0.84	0.00	0.25	0.76	0.91	0.19	0.61	0.64
COHCH-	0.97	0.90	0.90	0.62	0.80	0.85		0.90	0.41	0.54
CHOCH-	0.74	0.76	0.88	0.63	1.15		0.70	0.99	0.52	0.53
CHOHCH-	0.73	0.54	0.72	0.72	0.22	0.90	0.78	0.29	0.52	0.56
CH <sub>2</sub> OCH-	0.65	0.75	0.86	0.38	0.65	0.41	0.31	0.52	0.22	0.24
CH <sub>2</sub> OCH <sub>2</sub> -	0.78	0.87	1.09	0.54	0.79	0.65	0.44	0.67	0.35	0.40
COCH <sub>2</sub> -		0.02	-0.14	0.07	-0.55	-0.05	-0.05	-0.48	-0.03	-0.11
COHCH <sub>2</sub> -	0.56	0.73	0.64	0.55	0.22	0.49	0.53	0.16	0.58	0.37
CHOCH <sub>2</sub> -	0.84	0.88	0.85	0.82	0.37	0.69	0.98	0.51	0.68	0.75
CHOHCH <sub>2</sub> -	0.39	0.30	0.12	0.10	-0.35	0.03	0.23	-0.31	0.49	0.32
CH <sub>2</sub> OCH <sub>2</sub> -	0.59	0.52	0.63	0.54	0.48	0.82	0.76	0.86	0.39	0.46
CH <sub>2</sub> OCH <sub>2</sub> CH <sub>2</sub> -	0.58	0.68	0.61	0.56	0.35	0.57	0.79	0.65	0.42	0.42



Continued Table A.29.

	-C	-CH	-CH <sub>2</sub>	-CH <sub>3</sub>	-CO	-COH	-CHO	-CHOH	-CH <sub>2</sub> O	-CH <sub>2</sub> OH
CCO-			0.16	0.13		0.33	0.24	0.23	0.05	0.07
CHCO-		0.16	0.05	-0.09		-0.02	-0.07	-0.06	-0.31	-0.27
CH <sub>2</sub> CO-	-0.41	-0.28	-0.29	-0.32	-0.65	-0.29	-0.52	-0.67	-0.52	-0.40
CH <sub>3</sub> CO-	0.45	0.46	0.56	0.74	0.12	0.24	0.02	0.16	0.54	0.63
CCOH-			0.52	0.43		0.53	0.34	0.24	0.25	0.20
CHCOH-		0.78	0.82	0.70	0.67	0.47	0.71	0.54	0.47	0.54
CH <sub>2</sub> COH-	0.61	0.71	0.79	0.76	0.06	0.48	0.30	0.30	0.58	0.63
CH <sub>3</sub> COH-	0.63	0.70	0.87	0.86	-0.19	0.36	0.22	0.36	0.22	0.73
CCHO-				0.19		0.35	0.29			0.01
CHCHO-				0.32		0.45	0.43			0.17
CH <sub>2</sub> CHO-			0.16	0.08		0.31	0.22	-0.15	-0.12	-0.06
CH <sub>3</sub> CHO-	-0.09	0.00	-0.08	-0.20	-0.46	0.01	0.02	-0.49	-0.34	-0.34
CCHOH-				0.22			0.35		0.08	0.06
CHCHOH-		0.39	0.28	0.24	-0.12	0.23	0.32	0.15	0.09	0.14
CH <sub>2</sub> CHOH-		0.05	0.05	-0.03	-0.38	0.06	0.12	-0.33	-0.20	-0.14
CH <sub>3</sub> CHOH-	0.46	0.61	0.57	0.52	0.09	0.56	0.47	0.15	0.33	0.37
COCO-			0.73	0.61	0.14	0.31	0.81	0.27	0.52	0.20
COHCO-	0.41	0.30	0.36	0.01	-0.41	0.16	-0.25	-0.02	-0.11	-0.26
CHOCO-	0.63	0.56	0.44	0.10	0.39	0.06	0.07	0.37	-0.09	-0.05
CHOHCO-	0.19	0.14	-0.14	-0.20	-0.58	-0.14	-0.06	-0.43	-0.35	-0.35
CH <sub>2</sub> OCO-	0.38	0.27	0.39	0.57	0.05	0.14	-0.14	0.03	0.37	0.43
CH <sub>2</sub> OHCO-	0.40	0.30	0.51	0.65	-0.27	-0.01	-0.11	0.02	0.43	0.50
COCOH-		0.95	0.45	0.09	-0.37	0.27	0.91	0.12	0.59	0.60
COHCOH-	0.91	0.65	0.77	0.54	0.16	0.65	0.64	0.62	0.37	0.39
CHOCOH-	0.98	1.14	0.85	0.65	1.07	0.89	0.69	0.97	0.50	0.49
CHOHCOH-	0.73	0.83	0.70	0.65	0.13	0.73	0.83	0.35	0.54	0.55
CH <sub>2</sub> OCOH-	0.37	0.39	0.61	0.14	0.23	0.11	-0.02	0.17		
CH <sub>2</sub> OHCOH-	0.65	0.79	1.00	0.98	0.57	0.46	0.31	0.51		0.86
COCHO-				0.24	0.10			0.06	0.14	0.09
COHCHO-	0.63	0.69	0.70	0.57		0.67	0.73	0.31		0.33
CHOCHO-	0.75	0.85	0.80	0.76		0.91	0.95	0.39	0.56	0.63
CHOHCHO-			0.31	0.14	-0.02	0.38	0.28	-0.05	0.06	
CH <sub>2</sub> OCHO-			-0.20	-0.26	-0.48		-0.09	-0.48	-0.36	-0.36
CH <sub>2</sub> OHCHO-	-0.16	-0.05	-0.12	-0.24	-0.51	-0.12	0.00		-0.34	-0.29
COCHOH-		0.05	0.01	-0.11	-0.42	-0.08		-0.38	-0.30	-0.37
COHCHOH-		0.52	0.59	0.49	0.05	0.35	0.64	0.15	0.53	0.35
CHOCHOH-	0.74	0.83	0.87	0.61		0.86	0.90	0.49	0.67	0.58
CHOHCHOH-										
CH <sub>2</sub> OCHOH-		0.41	0.16	0.04	-0.29	0.12	0.24	-0.27	-0.11	-0.10
CH <sub>2</sub> OHCHOH-	0.44	0.57	0.51	0.45	0.02	0.72	0.63	0.11	0.25	0.37
	0.41	0.61	0.56	0.47	-0.06	0.52	0.54	0.12	0.36	0.39



**Table A.30.** Reaction and activation energies,  $\Delta E$  and  $E_a$ , in eV, for crucial C<sub>1</sub>–C<sub>2</sub> condensation reactions at  $E = 0.0$  V *vs.* RHE found in **Table A.28**. DFT values without solvation are indicated with ‘DFT’ subscript. Bader charge differences upon reaction,  $\Delta\Delta Q_{B,\Delta E}$ , and from the initial to the transition state,  $\Delta\Delta Q_{B,Ea}$ . Positive values indicate an increase in electronic density, thus the given step is promoted under reductive potentials. The labels to find the respective transition states in the ioChem-BD database are indicated.<sup>[199]</sup> Four substitution reactions were also considered, where CO or CHO replaces O or OH in a concerted step. Related to **Figure 4.3**.

Reaction (top) Label ioChem-BD (bottom)	$\Delta E_{DFT}$ eV	$E_{a,DFT}$ eV	$\Delta E$ eV	$E_a$ eV	$\Delta\Delta Q_{B,\Delta E}$ e <sup>-</sup>	$\Delta\Delta Q_{B,Ea}$ e <sup>-</sup>
COCO*+CO*→COCOCO*+* i202101+i101101-i303101+i000000	0.54	0.96	-0.3	0.92	-0.14	-0.07
COCO*+CHO*→COCOCHO*+* i202101+i111101-i313101+i000000	-0.75	0.73	-0.69	0.73	-0.81	-0.12
COCHO*+CO*→COCOCHO*+* i212101+i101101-i313101+i000000	-0.1	0.81	-0.18	0.78	-0.39	-0.02
CH <sub>2</sub> CH*+CO*→CH <sub>2</sub> CHCO*+* i230102+i101101-i331102+i000000	0.3	0.78	-0.25	0.76	-0.5	-0.18
CH <sub>2</sub> CH*+CHO*→CH <sub>2</sub> CHCHO*+* i230102+i111101-i341104+i000000	-1.47	0.09	-1.52	0.08	-0.3	-0.9
CH <sub>2</sub> CH*+CH <sub>2</sub> O*→CH <sub>2</sub> CHCH <sub>2</sub> O*+* i230102+i121101-i351105+i000000	-1.11	0.71	-1.14	0.72	-0.48	-0.53
CHCH <sub>2</sub> *+CH <sub>2</sub> O*→CHCH <sub>2</sub> CH <sub>2</sub> O*+* i230102+i121101-i351106+i000000	-0.25	0.5	-0.24	0.53	-0.02	-0.46
CH <sub>2</sub> CHO*+CO*→CH <sub>2</sub> CHCO*+O* i231101+i101101-i331102+i001101	1.13	2.08	-1.06	2.05	0.42	0.26
CH <sub>2</sub> CHO*+CO*→CH <sub>2</sub> C(O)HCO*+* i231101+i101101-i332202+i000000	1.04	1.88	-1.24	1.78	-0.37	-0.08
CH <sub>2</sub> CHO*+CHO*→CH <sub>2</sub> CHCHO*+O* i231101+i111101-i341104+i001101	-0.64	0.95	-0.71	0.97	0.62	0.02
CH <sub>3</sub> CH*+CHO*→CH <sub>3</sub> CHCHO*+* i240101+i111101-i351102+i000000	-1.98	0.17	-1.98	0.19	-0.51	-0.29
CH <sub>3</sub> CH*+CH <sub>2</sub> O*→CH <sub>3</sub> CHCH <sub>2</sub> O*+* i240101+i121101-i361102+i000000	-1.15	0.68	-1.16	0.68	-0.45	-0.51
CH <sub>2</sub> CH <sub>2</sub> *+CO*→CH <sub>2</sub> CH <sub>2</sub> CO*+* i240102+i101101-i341102+i000000	0.39	1.06	-0.38	1.11	0.31	0.1
CH <sub>2</sub> CH <sub>2</sub> *+CHO*→CH <sub>2</sub> CH <sub>2</sub> CHO*+* i240102+i111101-i351103+i000000	-0.36	1.63	-0.41	1.61	-0.25	-0.26
CH <sub>2</sub> CH <sub>2</sub> *+CH <sub>2</sub> O*→CH <sub>2</sub> CH <sub>2</sub> CH <sub>2</sub> O*+* i240102+i121101-i361103+i000000	-0.39	1.21	-0.33	1.22	0.05	-0.35
CH <sub>2</sub> CHOH*+CO*→CH <sub>2</sub> CHCO*+OH* i241103+i101101-i331102+i011101	0.3	0.86	-0.32	0.88	0.53	0.48
CH <sub>2</sub> CHOH*+CHO*→CH <sub>2</sub> CHCHO*+OH* i241103+i111101-i341104+i011101	-1.47	0.97	-1.45	1.03	0.72	0.33
CH <sub>3</sub> CH <sub>2</sub> *+CH <sub>2</sub> O*→CH <sub>3</sub> CH <sub>2</sub> CH <sub>2</sub> O*+* i250101+i121101-i371101+i000000	-1.33	1.03	-1.36	1.06	0.39	0.05

**Table A.31.** Reaction and activation energies,  $\Delta E$  and  $E_a$ , in eV, for selected C–O(H) breaking reactions at  $E = 0.00$  V *vs.* RHE. DFT values without solvation are indicated with ‘DFT’ subscript. Bader charge differences upon reaction,  $\Delta\Delta Q_{B,\Delta E}$ , and from the initial to the transition state,  $\Delta Q_{B,Ea}$ . Positive values indicate an increase in electronic density, thus the given step is promoted under reductive potentials. The labels to find the respective transition states in the ioChem-BD database are indicated.<sup>[243]</sup> Related to **Figure 4.3**.

Reaction (top) Label ioChem-BD (bottom)	$\Delta E_{\text{DFT}}$ eV	$E_{a,\text{DFT}}$ eV	$\Delta E$ eV	$E_a$ eV	$\Delta\Delta Q_{B,\Delta E}$ e <sup>-</sup>	$\Delta\Delta Q_{B,Ea}$ e <sup>-</sup>
CH <sub>2</sub> CHCO*+*→CH <sub>2</sub> CHC*+O* i331102+i000000-i330102+i001101	-0.07	1.58	-0.06	1.59	1.63	1.08
CH <sub>2</sub> CHCHO*+*→CH <sub>2</sub> CHCH*+O* i341104+i000000-i340104+i001101	0.52	2.07	0.53	2.08	1.03	0.45
CH <sub>2</sub> CHCOH*+*→CH <sub>2</sub> CHC*+OH* i34110a+i000000-i330102+i011101	-0.61	1.33	-0.54	1.42	0.91	0.49
CH <sub>3</sub> CHCHO*+*→CH <sub>3</sub> CHCH*+O* i351102+i000000-i350102+i001101	0.79	2.38	0.76	2.34	0.86	0.36
CH <sub>2</sub> CHCH <sub>2</sub> O*+*→CH <sub>2</sub> CHCH <sub>2</sub> *+O* i351105+i000000-i350105+i001101	-0.01	1.25	-0.03	1.26	0.76	0.34
CH <sub>2</sub> CHCHOH*+*→CH <sub>2</sub> CHCH*+OH* i35110a+i000000-i340104+i011101	-0.06	1.28	0	1.31	0.9	0.49
CH <sub>3</sub> CHCH <sub>2</sub> O*+*→CH <sub>3</sub> CHCH <sub>2</sub> *+O* i361102+i000000-i360102+i001101	-0.28	0.95	-0.33	0.95	0.28	0.07
CH <sub>3</sub> CHCHOH*+*→CH <sub>3</sub> CHCH*+OH* i361105+i000000-i350102+i011101	-0.02	1.58	0.07	1.64	0.97	0.45
CH <sub>2</sub> CHCH <sub>2</sub> OH*+*→CH <sub>2</sub> CHCH <sub>2</sub> *+OH* i361108+i000000-i350105+i011101	-0.71	0.08	-0.63	0.17	0.87	0.7
CH <sub>3</sub> CHCH <sub>2</sub> OH*+*→CH <sub>3</sub> CHCH <sub>2</sub> *+OH* i371103+i000000-i360102+i011101	-0.59	0.86	-0.57	0.94	0.33	0.37

**Table A.32.** Hydrogenation reactions shown on **Figure A.35** from LSR benchmarked against explicit DFT-NEB; Reaction and activation energies,  $\Delta E$  and  $E_a$ , in eV, for selected C–H and O–H bond formation reactions at  $E = 0.00$  V *vs.* RHE. DFT values without solvation are indicated with the ‘DFT’ subscript. Bader charge differences upon reaction,  $\Delta\Delta Q_{B,\Delta E}$ , and from the initial to the transition state,  $\Delta Q_{B,Ea}$ . Positive values indicate an increase in electronic density, thus the given step is promoted under reductive potentials. Activation energies calculated using LSR with solvent,  $E_{a,LSR}$ . The difference between LSR and DFT values is shown as  $\text{err}(E_a)$ . The labels to find the respective transition states in the ioChem-BD database are indicated.<sup>[243]</sup> Related to **Figure 4.3**.

Reaction (top) Label ioChem-BD (bottom)	$\Delta E_{\text{DFT}}$ eV	$E_{a,\text{DFT}}$ eV	$\Delta E$ eV	$E_a$ eV	$\Delta\Delta Q_{B,\Delta E}$ e <sup>-</sup>	$\Delta\Delta Q_{B,Ea}$ e <sup>-</sup>	$E_{a,\text{LSR}}$ eV	$\text{err}(E_a)$ eV
COCHCH <sub>2</sub> *+H*→CH OCHCH <sub>2</sub> *+* i331102-i010101+ i341104+i000000	-1.19	0.11	-1.19	0.17	0.15	0.22	0.37	0.2
CHOCHCH <sub>2</sub> *+H*→C HOCHCH <sub>3</sub> *+* i341104-i010101+ i351102+i000000	-0.6	0.61	-0.55	0.67	-0.36	-0.1	0.6	-0.07
CHOCHCH <sub>3</sub> *+H*→C HOCH <sub>2</sub> CH <sub>3</sub> *+* i351102-i010101+ i361101+i000000	0.20	0.95	0.13	0.97	-0.81	-0.33	0.86	-0.11
CHOCH <sub>2</sub> CH <sub>3</sub> *+H*→C H <sub>2</sub> OCH <sub>2</sub> CH <sub>3</sub> *+* i361101-i010101+ i371101+i000000	-0.77	0.46	-0.67	0.53	0.24	0.1	0.56	-0.03
CHOCHCH <sub>2</sub> *+H*→C HOHCHCH <sub>2</sub> *+* i341104-i010101+ i35110a+i000000	0.11	0.49	0.07	0.50	-0.68	-0.11	0.93	0.01
CHOCHCH <sub>3</sub> *+H*→C HOHCHCH <sub>3</sub> *+* i351102-i010101+ i361105+i000000	0.32	1.1	0.22	1.06	-0.92	-0.43	1.02	-0.04
CHOCH <sub>2</sub> CH <sub>3</sub> *+H*→C HOHCH <sub>2</sub> CH <sub>3</sub> *+* i361101-i010101+ i371102+i000000	0.20	1.07	0.22	1.11	-0.19	-0.63	1.02	-0.08
CH <sub>2</sub> OCH <sub>2</sub> CH <sub>3</sub> *+H*→ CH <sub>2</sub> OHCH <sub>2</sub> CH <sub>3</sub> *+* i371101-i010101+ i381101+i000000	-0.06	0.89	-0.16	0.93	-0.85	-0.47	0.79	-0.14

**Table A.33.** Reaction energies,  $\Delta E$ , for decomposition of formaldehyde. DFT values without solvation are indicated with the ‘DFT’ subscript. Bader charge differences upon reaction,  $\Delta\Delta Q_{B,\Delta E}$ , are shown in  $e^-$ . Positive values indicate an increment in electronic density, thus promoting the given step under reductive potentials. The labels to find the respective transition states in the ioChem-BD database are indicated. Formaldehyde, thus, can hardly decompose into the more reactive moieties  $\text{CH}_2$  or  $\text{CHO}$ , and their production of propylene (**Figure 4.2**) can only be rationalized by aldol condensation.<sup>[182]</sup> Related to **Figure 4.3**.

Reaction (top) Label ioChem-BD (bottom)	$\Delta E_{\text{DFT}}$ eV	$\Delta E$ eV	$\Delta\Delta Q_{B,\Delta E}$ e-
$\text{CH}_2\text{O}^* + * \rightarrow \text{CH}_2^* + \text{O}^*$	0.36	0.33	0.99
$\text{CH}_2\text{O}^* + * \rightarrow \text{CHO}^* + \text{H}^*$	0.47	0.46	0.12

**Table A.34.** Faradaic efficiencies ( $FE$ ) and standard deviations (Stdev) of products detected from the electrolysis of 50 mM propionaldehyde ( $\text{C}_3$  reagent) on OD-Cu in 0.1 M PPB at  $-0.40$  V and  $-1.00$  V *vs.* RHE for 60 min. The values shown are an average taken from three experiments. Related to **Figure 4.6**.

Products	$-0.40$ V <i>vs.</i> RHE		$-1.00$ V <i>vs.</i> RHE	
	$FE$ %	Stdev -	$FE$ %	Stdev -
Hydrogen	52.49	0.28	66.14	0.58
Propylene	0.08	0.02	0.09	0.0001
Propane	0.03	0.01	0.5	0.04
1-Propanol	39.92	0.03	10.89	3.06

**Table A.35.** Faradaic efficiencies ( $FE$ ) and standard deviations (Stdev.) of products detected from the electrolysis of 50 mM allyl alcohol ( $\text{C}_3$  reagent) on OD-Cu in 0.1 M PPB at  $-0.40$  V and  $-1.00$  V *vs.* RHE for 60 min. The values shown are an average taken from three experiments. Related to **Figure 4.6**.

Products	$-0.40$ V <i>vs.</i> RHE		$-1.00$ V <i>vs.</i> RHE	
	$FE$ %	Stdev %	$FE$ %	Stdev -
Hydrogen	75.73	6.6	78.78	3.28
Propylene	3.59	0.53	9.55	2.97
Propane	0.15	0.07	0.22	0.04
1-Propanol	13.71	2.43	2	0.61

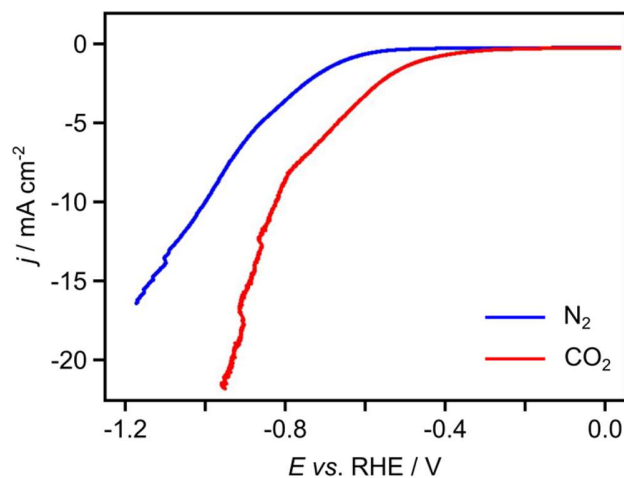


**Figure A.30.** Linear sweep voltammograms of OD-Cu in  $\text{N}_2$  (blue) and  $\text{CO}_2$  (red) purged 0.1 M  $\text{KHCO}_3$ . The scan rate used was  $5 \text{ mV s}^{-1}$ . Note that in the  $\text{CO}_2$  purged electrolyte, the electroreduction current is larger than when  $\text{N}_2$  was the purging gas. This shows the activity of OD-Cu in catalyzing  $\text{eCO}_2\text{R}$ . Related to **Figure 4.1**.

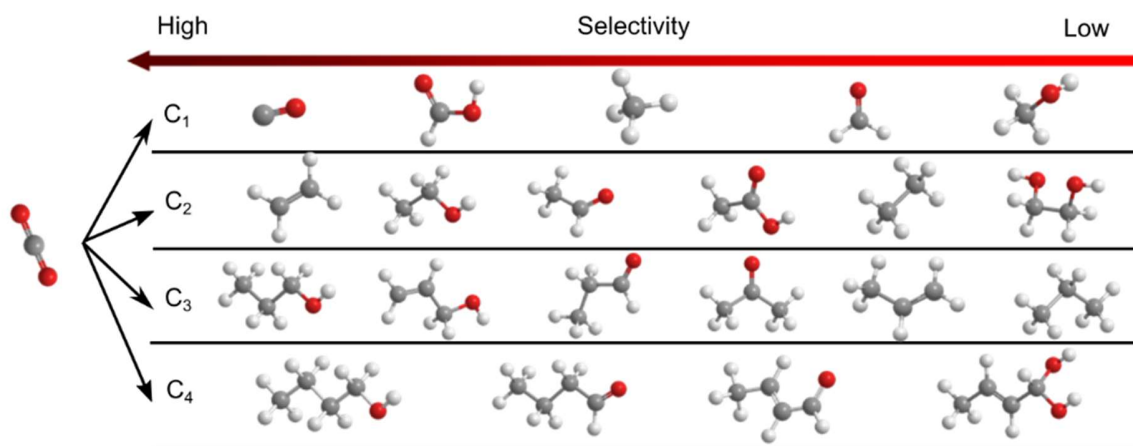


**Figure A.31.** Overview of main  $\text{C}_1$  -  $\text{C}_4$  products in  $\text{eCO}_2\text{R}$  using copper-based catalysts.<sup>[23,27,182]</sup> This is not a rigid classification, since observed selectivity trends are dependent on electrolysis conditions, especially for the case of  $\text{C}_1$  products. Related to **Figure 4.1**.

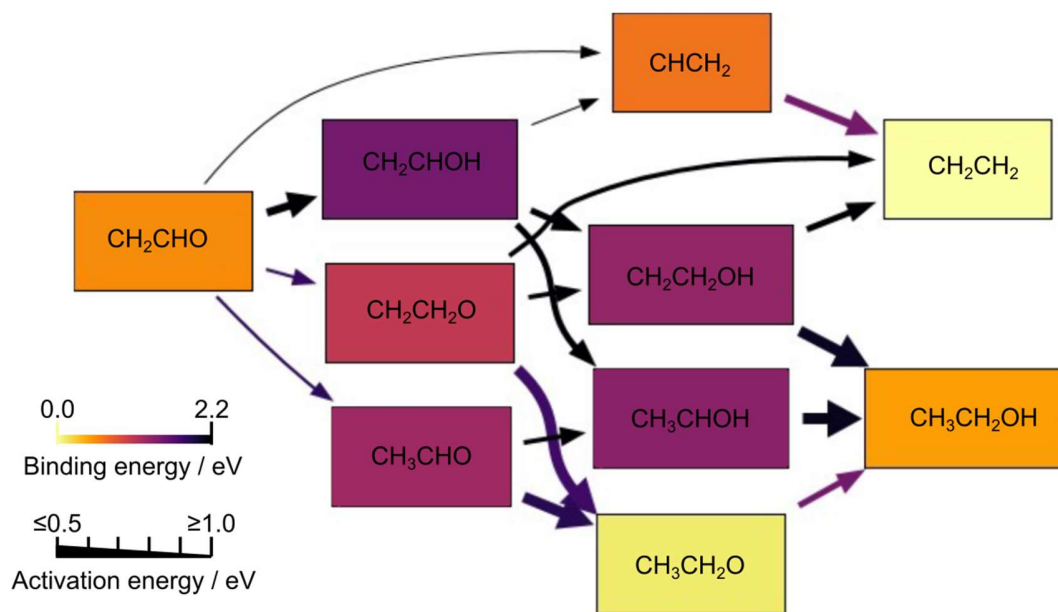


**Figure A.32.** Energy profile for  $\text{CH}_2\text{CHO}$  hydrogenation to ethanol and ethylene at  $-0.40$  V *vs.* RHE. The boxes represent intermediates with the color-code indicating their relative potential energies. The thickness of the arrows is linked to their activation energies ( $E_a$ ), estimated from LSR. Underlined intermediates can also desorb into the solution. Related to **Figure 4.4**.

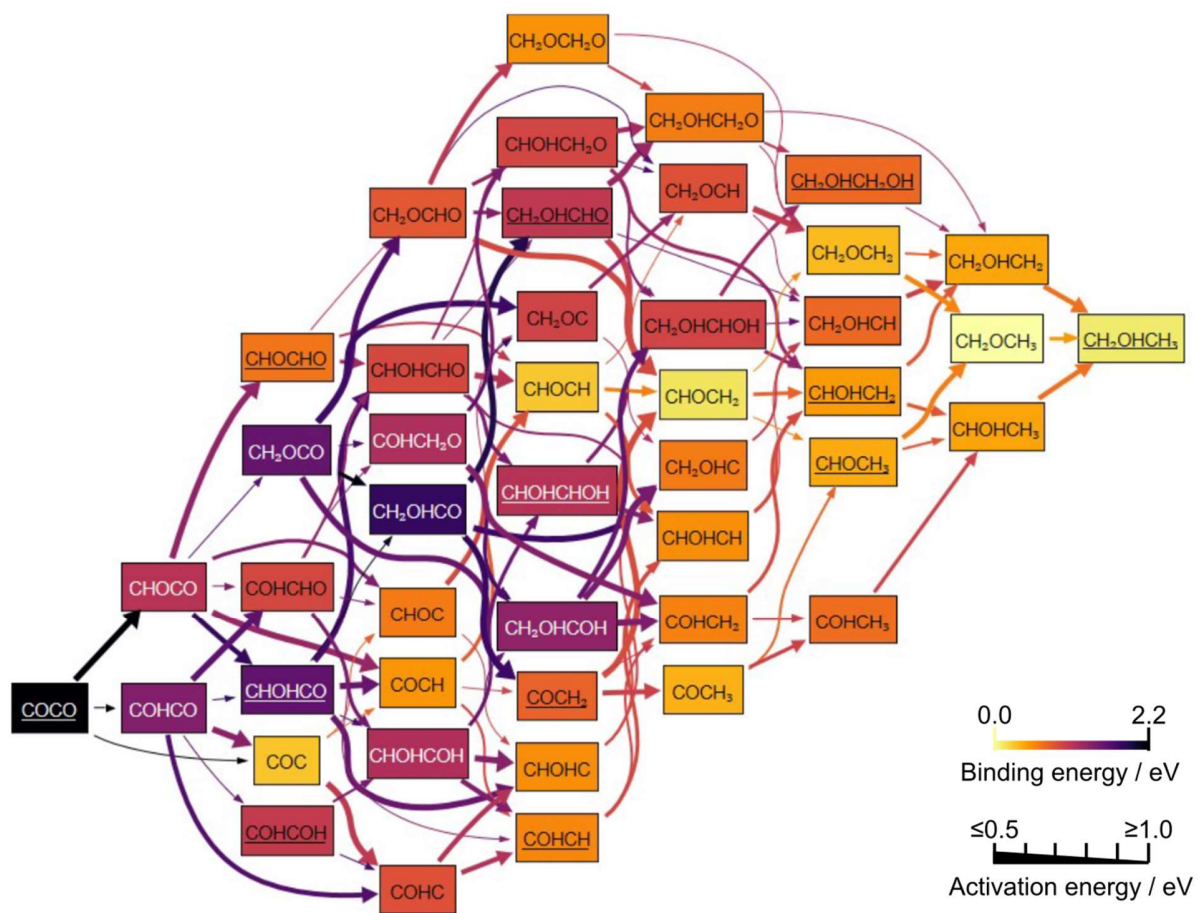


**Figure A.33.** Energy network for  $\text{OCCO}^*$  hydrogenations to main oxygenated  $\text{C}_2$  products at  $-0.40 \text{ V vs. RHE}$ . The boxes represent intermediates with the color-code indicating their relative potential energies. The thickness of the arrows is linked to their activation energies ( $E_a$ ), estimated from LSR. Underlined intermediates can also desorb into the solution. Related to **Figure 4.4**.

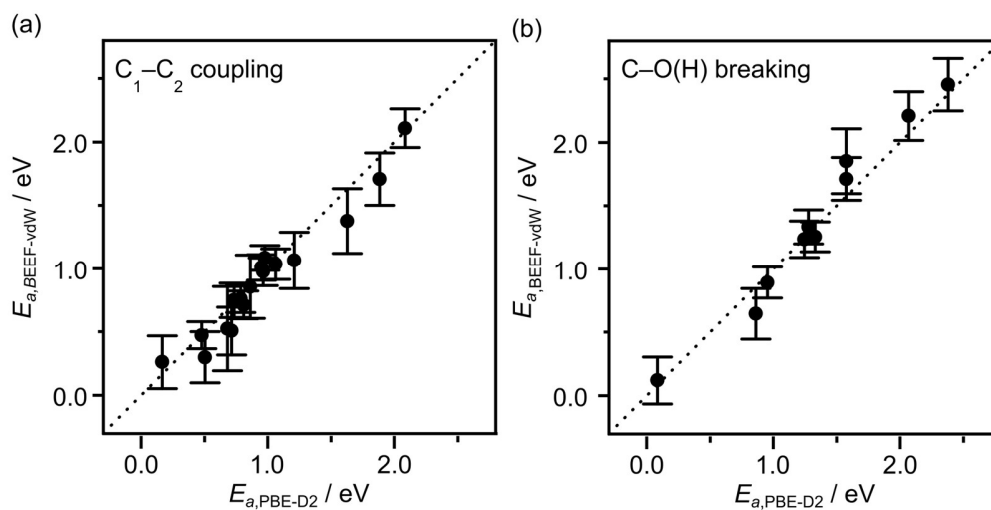


**Figure A.34.** Parity plot of activation energies calculated with PBE-D2 *vs.* the corresponding values of BEEF-vdW including error bars for a C–C coupling and b C–O(H) breakings. Related to **Figure 4.3**.

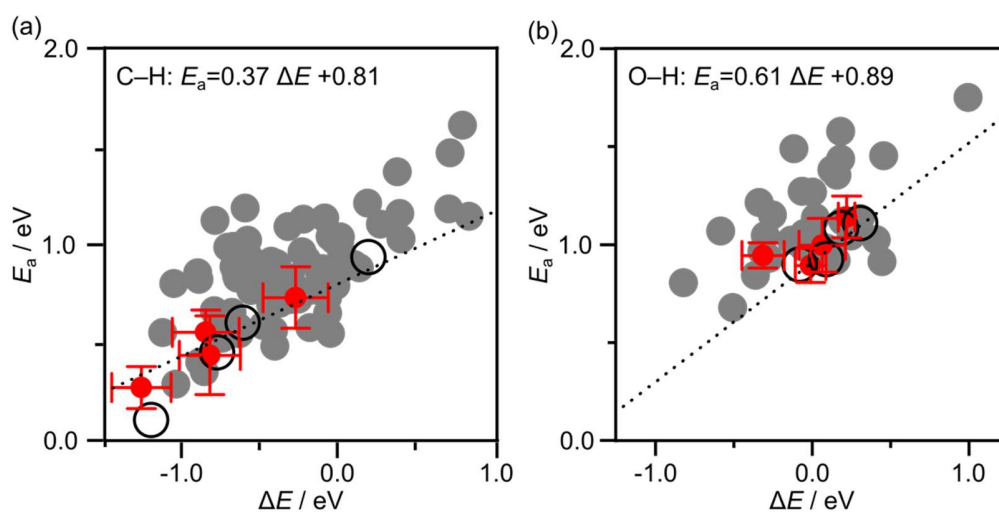


**Figure A.35.** Linear-scaling relationships<sup>[243]</sup> for C–H and O–H hydrogenations (grey) compared to selected PBE-D2 (black) and BEEF-vdW values (red). The path selected was  $\text{CH}_2\text{CHCO} \rightarrow \text{CH}_2\text{CHCHO} \rightarrow \text{CH}_3\text{CHCHO} \rightarrow \text{CH}_3\text{CH}_2\text{CHO} \rightarrow \text{CH}_3\text{CH}_2\text{CH}_2\text{O}$  and the protonation of the later four. BEEF-vdW error bars in  $\Delta E$  and  $E_a$  are included. Related to **Figure 4.3**.



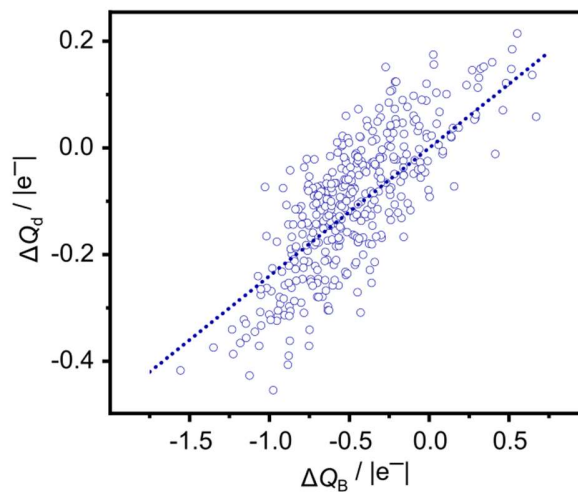


**Figure A.36.** Parity plot of Bader charges *vs.* charges deduced from increments upon adsorption in the dipole moment along  $z$ . Best linear fit without independent term added as a guide to the eye. Related to **Figure 4.3**.

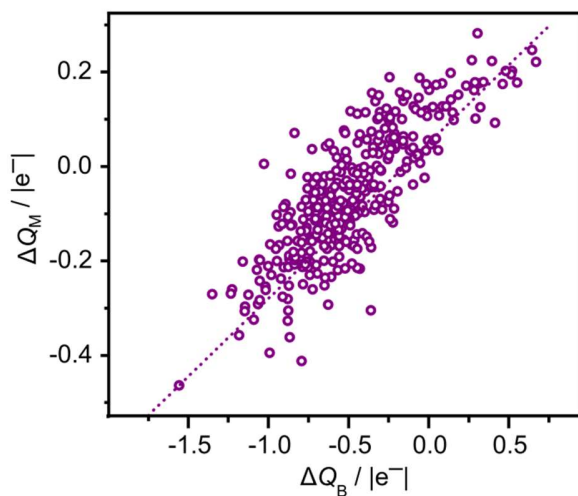


**Figure A.37.** Parity plot of Bader charges *vs.* Mulliken charges upon adsorption. Line added as a guide to the eye. Related to **Figure 4.3**.

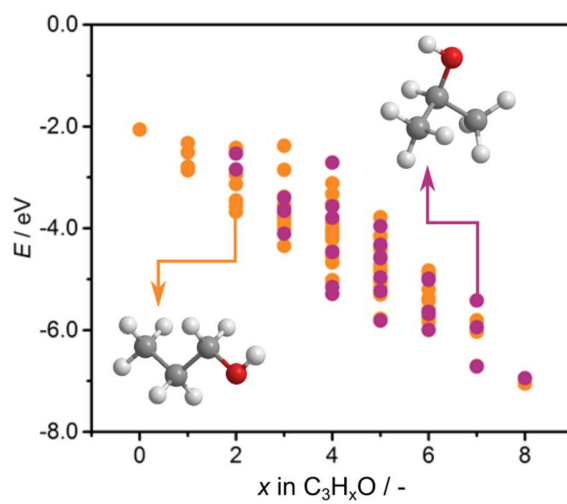


**Figure A.38.** Energy of intermediates that share 1-propanol (orange) and 2-propanol (purple) backbones as a function of the number of hydrogens of the intermediate. For a given hydrogenation degree, the most stable intermediates of both backbones are comparable in energy. Related to **Figure 4.3**.

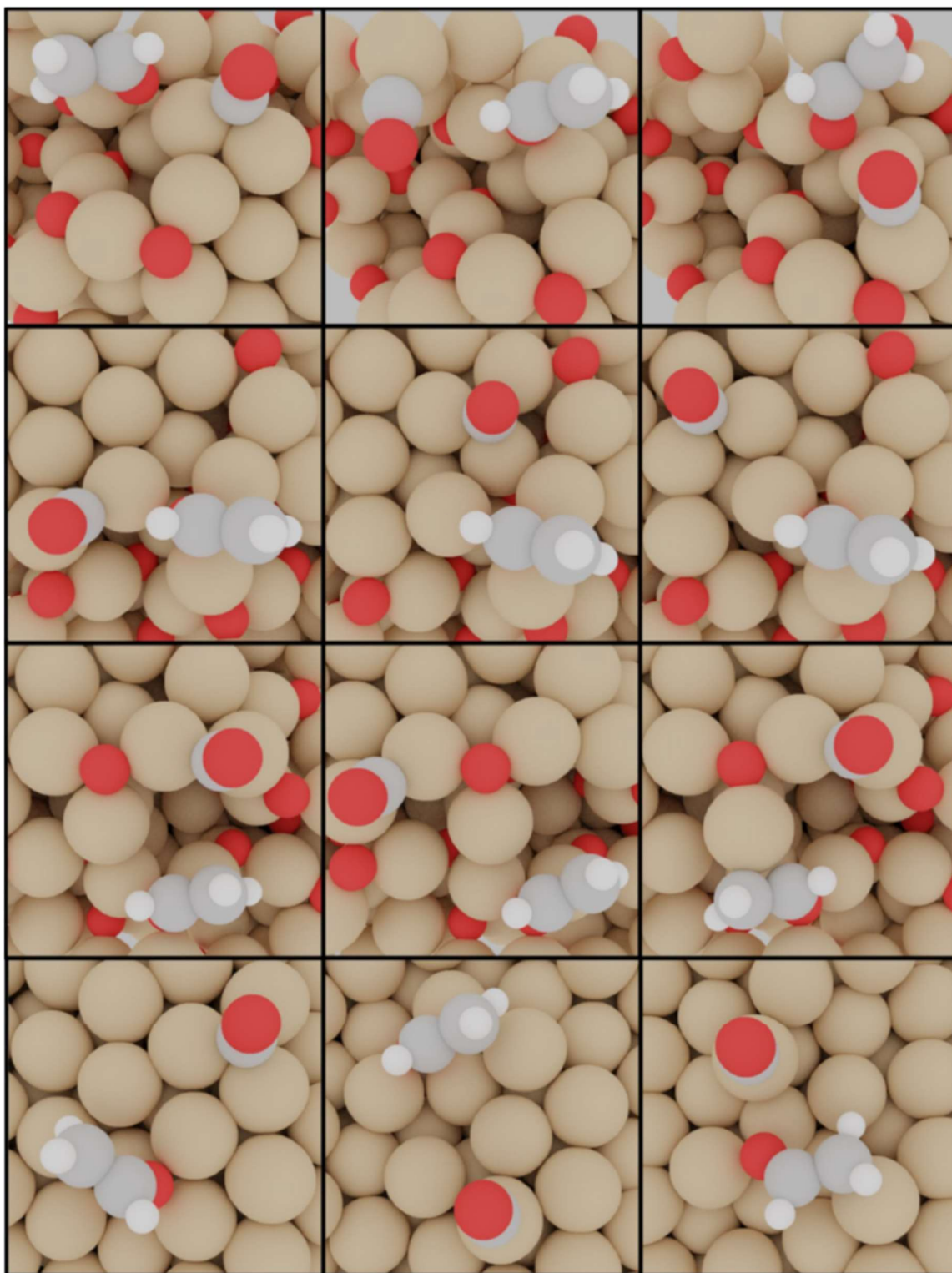


**Figure A.39.**  $\text{CH}_2\text{CHO}$   $\text{CO}$  coupling configurations on 12 structural motifs formed on oxide-derived Cu models.<sup>[201,207]</sup> The most suitable active site for promoting this step is reported in **Figure 4.4**. Related to **Figure 4.4**.

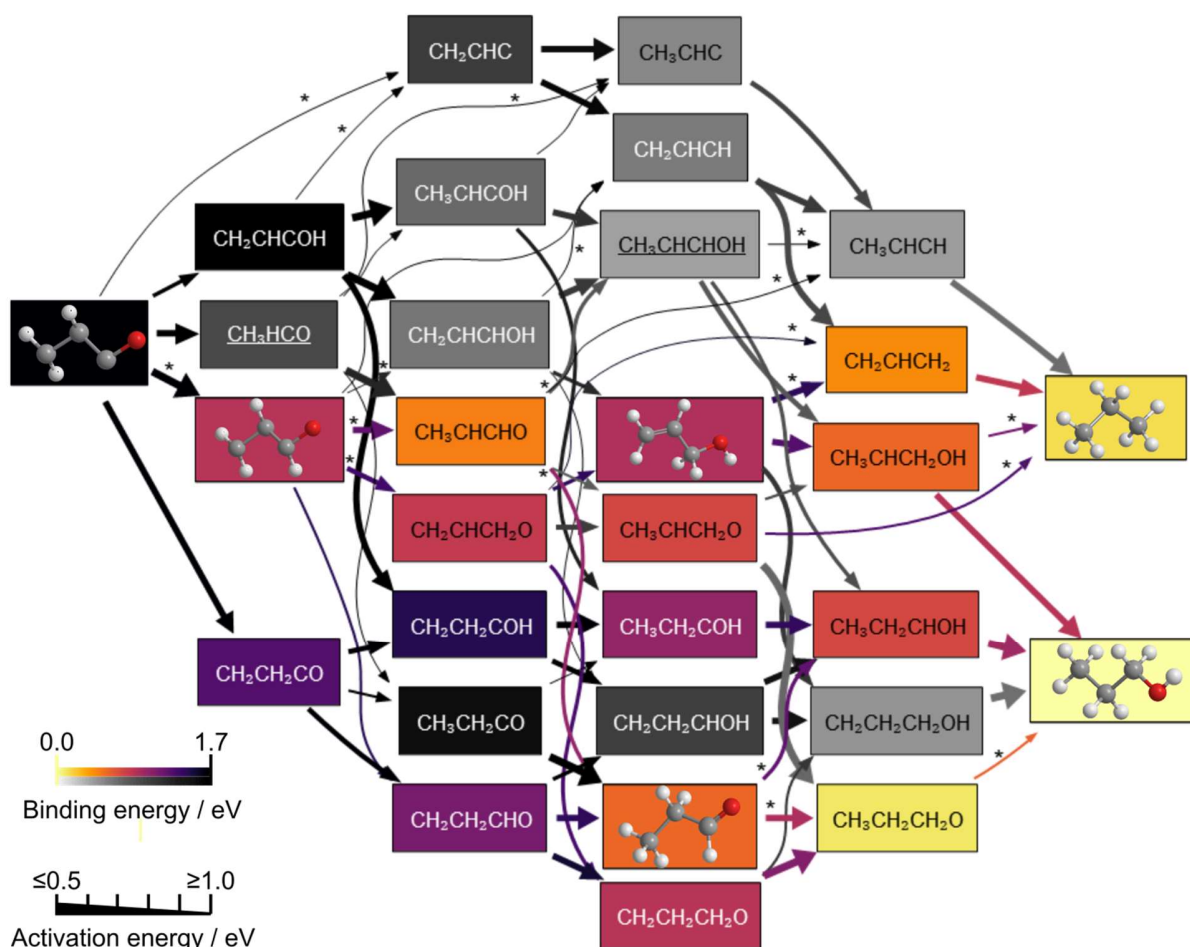


**Figure A.40.** Energy profiles for hydrogenation of  $\text{CH}_2\text{CHCO}$  and  $\text{CH}_2\text{CHCHO}$  to propylene and 1-propanol at 0.00 V *vs.* RHE. The boxes represent intermediates with the color-code indicating their relative potential energies. Grayscale was used for the paths that are overall less favored. The thickness of the arrows is linked to their activation energies ( $E_a$ ), estimated from LSR (those marked with \* correspond to explicitly calculated by DFT). Underlined intermediates can also desorb to the solution, among which, allyl alcohol and propionaldehyde were used as reactants in experiments to probe theoretical predictions (**Figure 4.6**). Related to **Figure 4.5**.

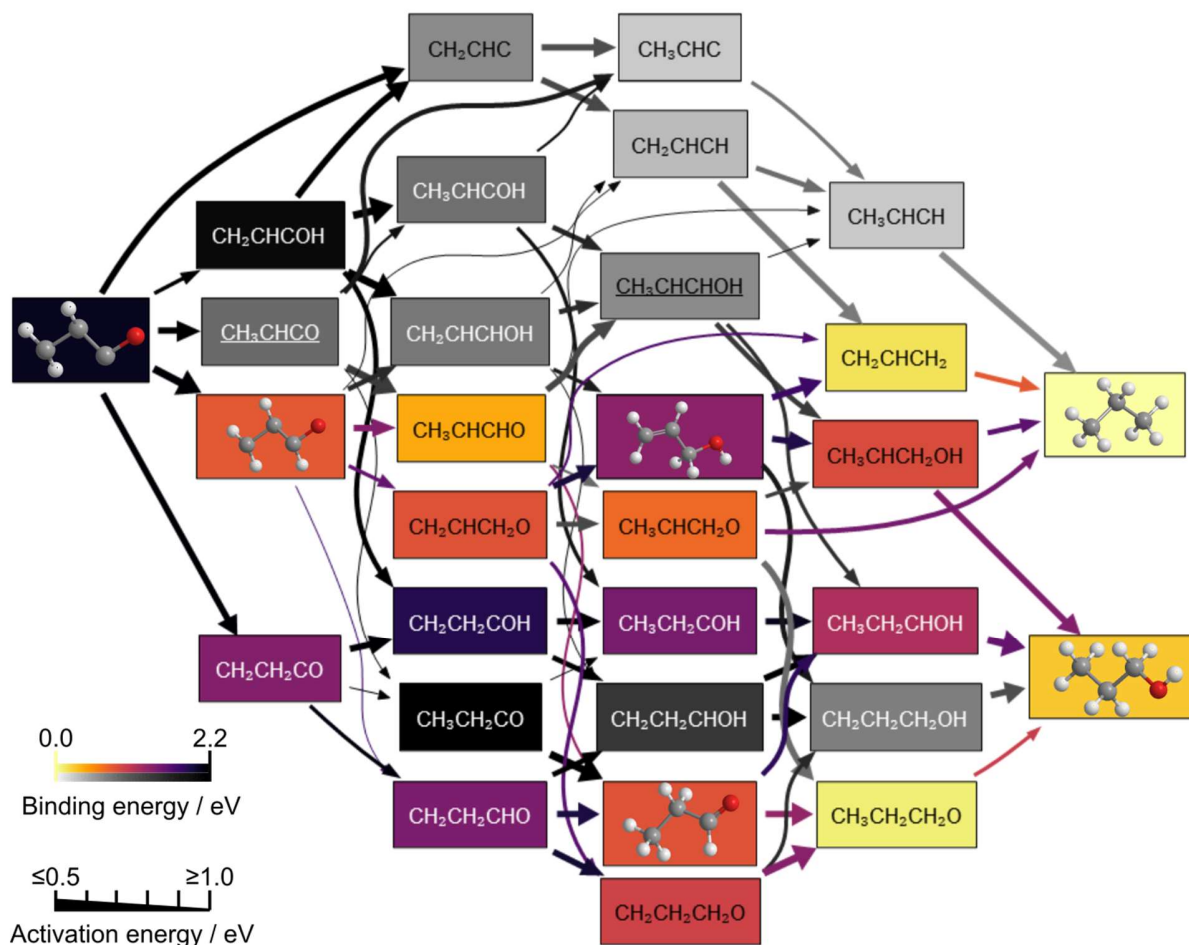


**Figure A.41.** Energy profiles for hydrogenation of  $\text{CH}_2\text{CHCO}$  and  $\text{CH}_2\text{CHCHO}$  to propylene and 1-propanol at  $-0.40$  V vs. RHE. The boxes represent intermediates with the color code indicating their relative potential energies. Grayscale was used for the paths that are overall less favored. The thickness of the arrows is linked to their activation energies ( $E_a$ ). Underlined intermediates can also desorb to the solution, among which, allyl alcohol and propionaldehyde were used as reactants in experiments to probe theoretical predictions (Figure 4.6). Related to Figure 4.5.

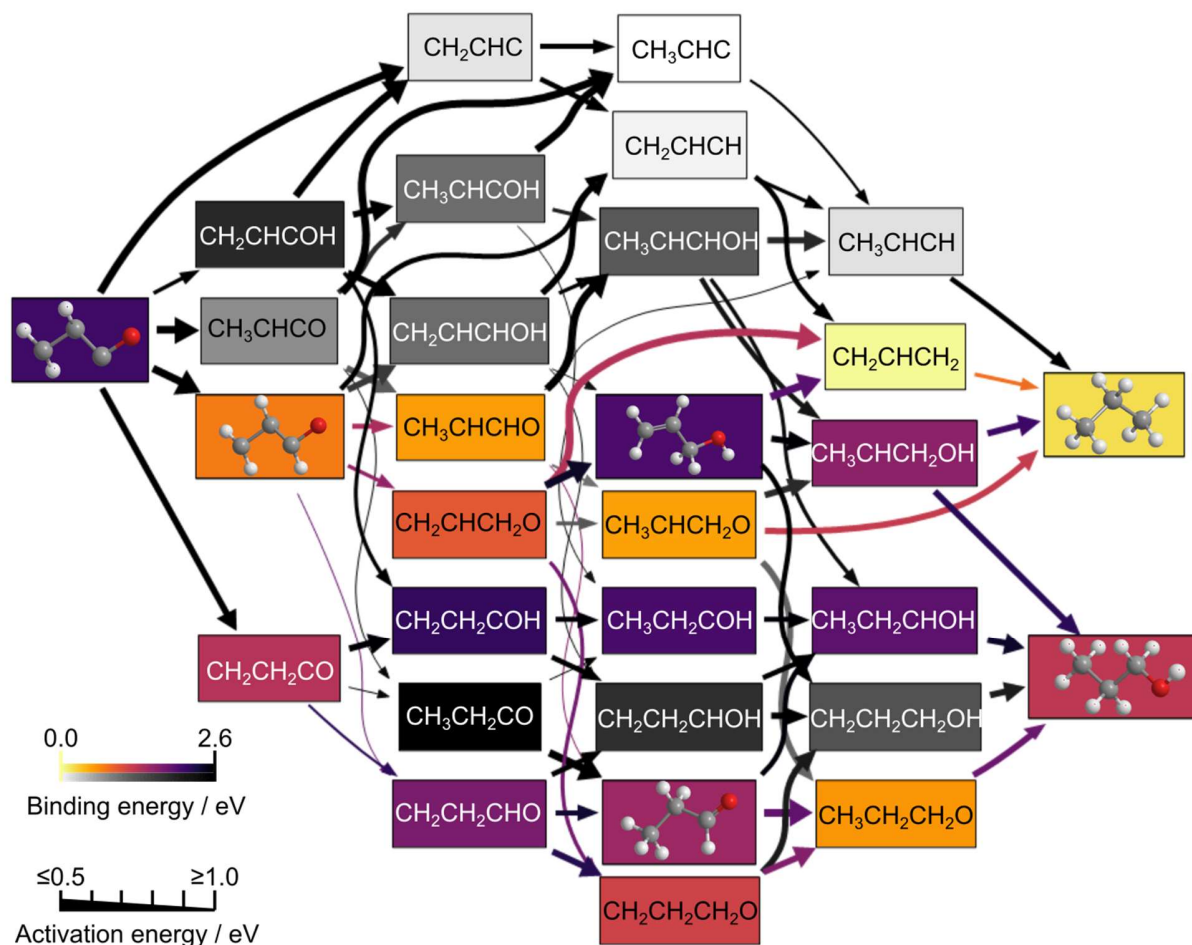


**Figure A.42.** Energy profiles for hydrogenation of  $\text{CH}_2\text{CHCO}$  and  $\text{CH}_3\text{CHCHO}$  to propylene and 1-propanol at  $-1.00$  V *vs.* RHE. The boxes represent intermediates with the color-code indicating their relative potential energies. Grayscale was used for the paths that are overall less favored. The thickness of the arrows is linked to their activation energies ( $E_a$ ). Underlined intermediates among which, allyl alcohol and propionaldehyde were used as reactants in experiments to probe theoretical predictions (**Figure 4.6**). Related to **Figure 4.5**.



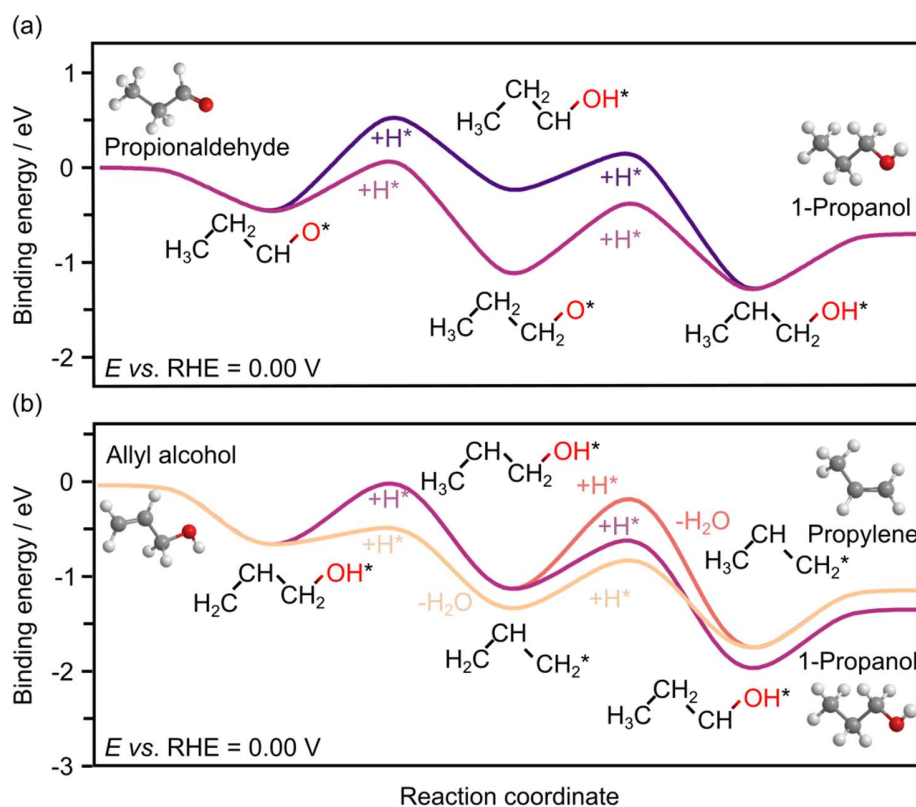


**Figure A.43.** Energy profiles for electrocatalytic reduction of (a) propionaldehyde, and (b) allyl alcohol at 0.00 V *vs.* RHE on Cu(100), using H<sub>2</sub>, CO<sub>2</sub>, and H<sub>2</sub>O as thermodynamic sinks, and shifting the energy reference to make (a) propionaldehyde and (b) allyl alcohol the zero. Lighter colors are associated with more favored reaction paths. Related to **Figure 4.6**.

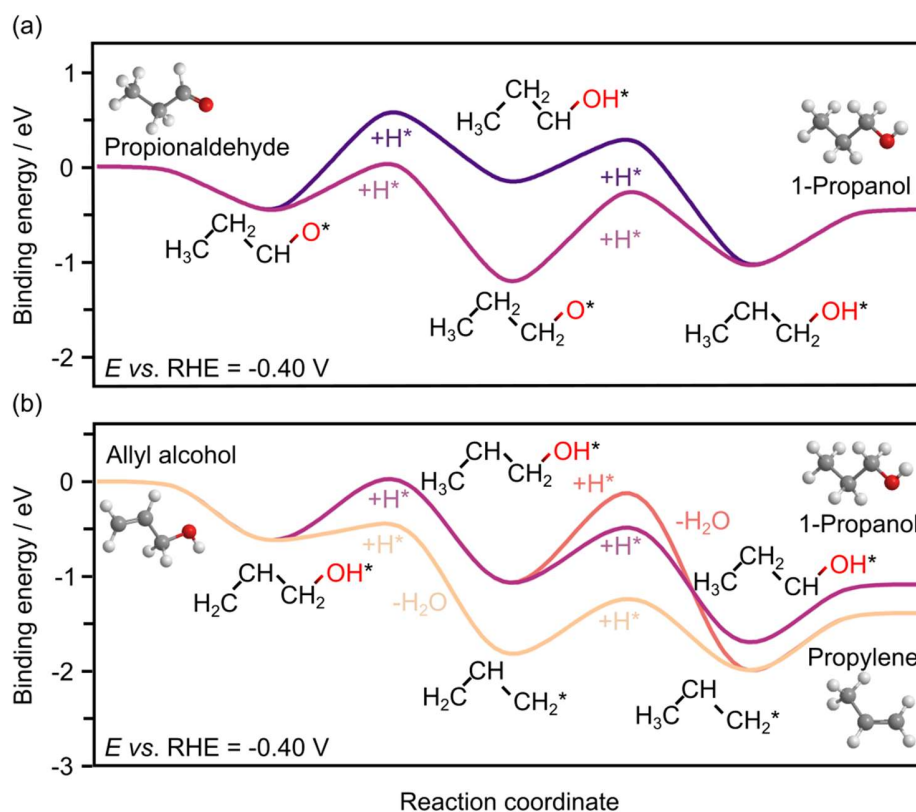


**Figure A.44.** Energy profiles for electrocatalytic reduction of (a) propionaldehyde, and (b) allyl alcohol at  $-0.40$  V *vs.* RHE on Cu(100), using  $\text{H}_2$ ,  $\text{CO}_2$ , and  $\text{H}_2\text{O}$  as thermodynamic sinks, and shifting the energy reference to make (a) propionaldehyde and (b) allyl alcohol the zero. Lighter colors are associated with more favored reaction paths. Related to **Figure 4.6**.



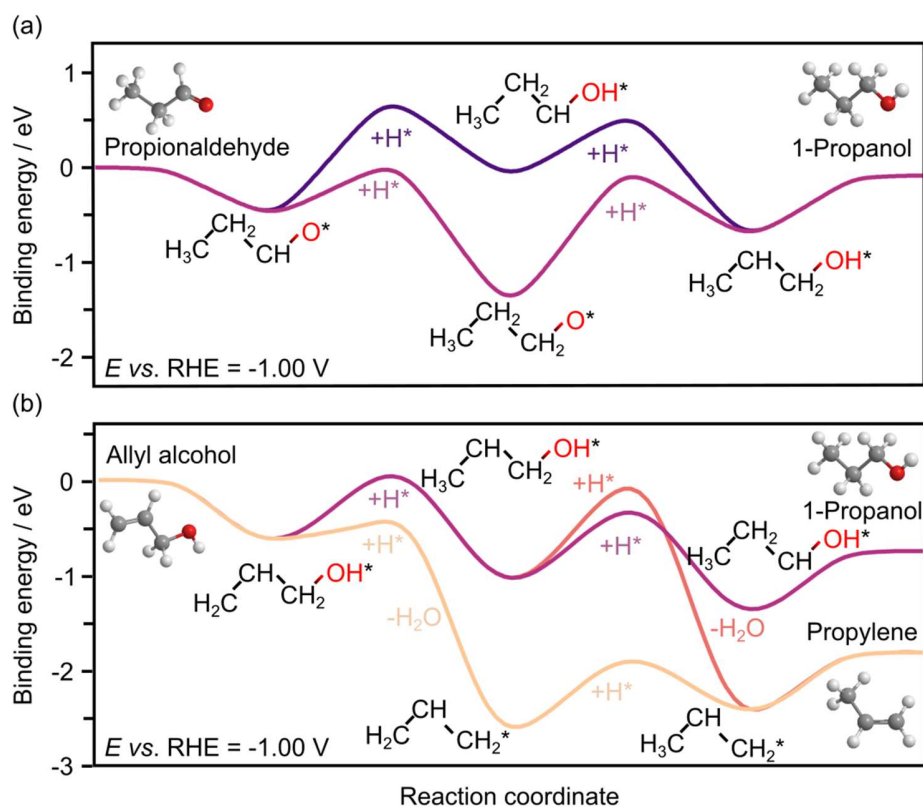


**Figure A.45.** Energy profiles for electrocatalytic reduction of (a) propionaldehyde, and (b) allyl alcohol at  $-1.00$  V *vs.* RHE on Cu(100) using H<sub>2</sub>, CO<sub>2</sub>, and H<sub>2</sub>O as thermodynamic sinks, and shifting the energy reference to make (a) propionaldehyde and (b) allyl alcohol the zero. Lighter colors are associated with more favored reaction paths. Related to **Figure 4.6**.

## Chapter 5

### Note A.8. Extended Mechanism from CO<sub>2</sub> to Crotonaldehyde via Acetaldehyde

In this section, the mechanism from CO<sub>2</sub> to 1-butanol is discussed in greater detail with emphasize to the transition of acetaldehyde to crotonaldehyde. Initially, CO<sub>2</sub> transitions into CO\* by 2 PCET steps. CO\* is dimerized with another CO\* or with HCO\*<sup>[27,77,99]</sup> in chemical steps strongly influenced by the electric potential and chemical environment. An oxygen atom in OCCO\* is protonated twice and removed as water, leaving CCO\* adsorbed on the surface, whose carbon atoms are fully hydrogenated to form <sup>[27]</sup> acetaldehyde (**Figure A.49**). There are two pathways in which the OCCO\* forms acetaldehyde, either through CHCHO\* or HCOCO\*, both having ethenyloxy (CH<sub>2</sub>CHO\*) as key intermediate. <sup>[27]</sup> Finally, the C<sub>4</sub> backbone is formed through the aldol condensation of two acetaldehyde molecules dimerizing to crotonaldehyde. An alternative pathway is envisioned through the condensation of an adsorbed ethenyloxy species bonded with an acetaldehyde molecule in the solution to produce 3-hydroxybutanal and crotonaldehyde (**Figure A.50**). This pathways is outlined for eCO<sub>2</sub>R to ethenyloxy, acetaldehyde, and eventually crotonaldehyde in **Figure A.51**. The mechanisms of eCO<sub>2</sub>R to the remaining C<sub>1</sub> and C<sub>2</sub> products have been considered in **Figure A.51**. Among the lateral paths leading to C<sub>1</sub> products,<sup>[27,77,99]</sup> the carbon atom of CO<sub>2</sub> can be hydrogenated to produce formate. CO can also be hydrogenated to produce methanol, or stripped of its oxygen atom to produce CH<sub>x</sub>. While CH<sub>x</sub> species mostly evolve towards methane, CH<sub>2</sub> may dimerize (producing ethylene) or be combined with CO to produce ketene (CH<sub>2</sub>CO).<sup>[99]</sup> Ketene in turn, can be hydrogenated to acetaldehyde,<sup>[169]</sup> potentially opening a third pathway towards crotonaldehyde and subsequently 1-butanol. The remaining C<sub>2</sub> products can be derived from the above-mentioned intermediates. <sup>[27,77]</sup> CH<sub>2</sub>CH<sub>2</sub> and CH<sub>3</sub>CHO can be further reduced to ethane (C<sub>2</sub>H<sub>6</sub>) and ethanol (C<sub>2</sub>H<sub>5</sub>OH) respectively, while OCCHO can be reduced to acetic acid via OCCHOH.<sup>[27]</sup> The mechanism for CO<sub>2</sub> reduction to C<sub>3</sub> products is still under discussion, though it has been proposed that the C<sub>3</sub> backbone may be formed via the coupling of CO with C<sub>2</sub> intermediates, like COCOH or CCH<sub>2</sub>,<sup>[103]</sup> akin to a Flory–Schulz oligomerization. <sup>[27]</sup>

**Note A.9. Acetaldehyde Electroreduction in Neutral PPB**

The electrolysis of acetaldehyde was investigated in 0.1 M PPB. The performance ( $FE$  and  $j$ ) towards 1-butanol was significantly poorer compared to the performance in 0.1 M KOH. The applied potentials required to generate 1-butanol were also more negative when compared to the required potentials in 0.1 M KOH. During electrochemical reduction reactions, the local pH at the electrode surface is higher than that of the bulk electrolyte.<sup>[93]</sup> Therefore, an increase in local pH was expected to facilitate the aldol condensation and improve the production of 1-butanol. To investigate the effects of local pH on acetaldehyde reduction to 1-butanol, the electrolysis was performed under a constant applied geometric current density of  $-30 \text{ mA cm}^{-2}$  in different PPB concentrations for 1 h.

**Note A.10. Acetaldehyde and Crotonaldehyde Electrolysis on Transition Metal Discs**

The ability of a series of transition metal discs to catalyze acetaldehyde reduction to 1-butanol was studied. The discs were polished sequentially with SiC paper (1200  $\mu\text{m}$ , Struers) followed by 15  $\mu\text{m}$  and 3  $\mu\text{m}$  Diapro slurries (Struers). They were sonicated in ultrapure water and dried using nitrogen gas. Galvanostatic electrolyses (1 h) were performed at  $-10 \text{ mA cm}^{-2}$  in 50 mM acetaldehyde in 0.1 M KOH. The constant-current electrolysis helps to minimize the differences in local pH between the different metals used. Nonetheless, some electrolysis products like ethanol are weak acids, and the difference in their production rates among the different metals may potentially result in small differences on local pH between metals. This would impact the actual amounts of crotonaldehyde present (and further reduced) at the electrode surface. Thus, the  $FE$  ratio of 1-butanol to  $C_4$  products ( $FE_{1\text{-butanol}} / FE_{C_4}$ ) was included as a fair basis of comparison between the different metals. crotonaldehyde electrolysis of 1 h was performed on the metal discs in 0.1 M PPB at  $-10 \text{ mA cm}^{-2}$ . The PPB was used as a supporting electrolyte to retard the hydration of crotonaldehyde to an unreactive diol.

**Table A.36.** Product distribution of eCO<sub>2</sub>R in 1.0 M KOH on OD-Cu GDE over a variety of cathodic potentials ( $E$  vs. RHE) denoted in V. Related to **Figure 5.3**.

Products	-0.38 V		-0.48 V		-0.58 V		-0.68 V	
	<i>FE</i> %	<i>j</i> mA cm <sup>-2</sup>	<i>FE</i> %	<i>j</i> mA cm <sup>-2</sup>	<i>FE</i> %	<i>j</i> mA cm <sup>-2</sup>	<i>FE</i> %	<i>j</i> mA cm <sup>-2</sup>
Hydrogen	47.80	-15.9	23.90	-35.5	31.50	-131	72.30	-608
Formate	10.10	-3.36	24.20	-29.3	7.50	-24.2	1.90	-14.4
Carbon monoxide	27.20	-9.05	10.30	-15.9	8.70	-36.7	5.30	-45.7
Methane	-	-	0.02	-0.02	0.21	-0.83	1.50	-13.5
Methanol	-	-	0.07	-0.1	0.06	-0.25	0.11	-0.98
Ethylene	7.90	-2.60	16.80	-27.4	34.80	-152	18.50	-162
Ethanol	3.90	-1.31	9.80	-15.8	13.20	-56.7	8.30	-74.8
Ethane	0.10	-0.03	0.06	-0.1	0.03	-0.14	0.01	-0.05
Acetaldehyde	0.10	-0.06	0.10	-0.16	0.08	-0.34	0.04	-0.41
Propylene	-	-	0.27	-0.44	0.61	-2.55	0.18	-1.56
1-Propanol	2.64	-0.88	5.43	-13.2	3.25	-13.2	0.74	-6.47
Propionaldehyde	0.15	-0.05	0.10	-0.14	0.04	-0.19	0.02	-0.21
Allyl alcohol	0.16	-0.05	0.63	-1.00	0.60	-2.34	0.20	-1.74
1-Butanol	-	-	0.056	-0.08	0.007	-0.026	0.002	-0.013
1-Butanal	-	-	0.003	-0.004	0.004	-0.013	0.001	-0.01
Total	100.2	-33.3	91.6	-147	100.7	-418.0	109.0	-850.0

– Product not detected or process not applicable.

**Table A.37.** Product distribution of eCO<sub>2</sub>R in 0.1 M KHCO<sub>3</sub> on OD-Cu discs at -0.95 V *vs.* RHE. Related to **Figure 5.3**.

<b>Products</b>	<i>FE</i> %	<i>j</i> mA cm <sup>-2</sup>
Hydrogen	33.5	-9.54
Formate	8.2	-2.29
Carbon monoxide	1.6	-0.43
Methane	2.5	-0.69
Methanol	-	-
Ethylene	28.5	-8.09
Ethanol	9.8	-2.83
Ethane	0.2	-0.04
Acetaldehyde	0.7	-0.2
Acetic acid	0.8	-0.22
Propylene	-	-
1-Propanol	5	-1.41
Propionaldehyde	1.5	-0.42
Allyl alcohol	1.7	-0.48
1-Butanol	-	-
1-Butanal	-	-
Total	94.1	-28.3

- Product not detected or process not applicable.

**Table A.38.** Comparison of CO<sub>2</sub> reduction activity to C<sub>2</sub> and C<sub>3</sub> products between OD-Cu GDE and other Cu-loaded carbon GDEs reported in the literature. Related to **Figure 5.3**.

Conditions	$FE_{C_2}$ %	$j_{C_2}$ mA cm <sup>-2</sup>	Major C <sub>2</sub> product	$FE_{C_3}$ %	$j_{C_3}$ mA cm <sup>-2</sup>	Major C <sub>3</sub> product	Ref.
-0.58 V <i>vs.</i> RHE <sup>A</sup>	48.1	201	Ethylene	4.5	-18.8	1-propanol	This work
-0.79 V <i>vs.</i> RHE <sup>A</sup>	65.5	197	Ethylene	4.5	-13.5	1-propanol	[247]
-0.60 V <i>vs.</i> RHE <sup>A</sup>	65.3	131	Ethylene	5.1	-10.2	1-propanol	[248]
-0.80 V <i>vs.</i> RHE <sup>A</sup>	72	186	-	-	-	-	[249]
-300 mA cm <sup>-2</sup> <sup>B</sup>	40.1	120	Ethylene	5.1	-15.3	1-propanol	[250]
-400 mA cm <sup>-2</sup> <sup>A</sup>	45.9	184	Ethanol	6.9	-27.6	1-propanol	[174]
-275 mA cm <sup>-2</sup> <sup>C</sup>	83	228	Ethylene	-	-	-	[141]
-200 mA cm <sup>-2</sup> <sup>A</sup>	68.3	137	Ethylene	-	-	-	

A in 1.0 M KOH      B in 1.0 M KHCO<sub>3</sub>  
C in 10.0 M KOH      - Product not detected or process not applicable.

**Table A.39.** Product distribution of acetaldehyde electroreduction in 0.1 M KOH on OD-Cu. Related to **Figure 5.4**.

Product molecule	Reaction equation	Number of electrons transferred
Ethanol	$CH_3CHO + 2H^+ + 2e^- \rightarrow C_2H_5OH$	2
1-Butanal	$2 CH_3CHO + 2H^+ + 2e^- \rightarrow C_3H_7CHO + H_2O$	2
Crotyl alcohol	$2 CH_3CHO + 2H^+ + 2e^- \rightarrow CH_3CH=CHCH_2OH + H_2O$	3
1-Butanol	$2 CH_3CHO + 4H^+ + 4e^- \rightarrow CH_3(CH_2)_3OH + H_2O$	4
Crotonaldehyde	$2 CH_3CHO \rightarrow CH_3CH=CHCHO + H_2O$	0

**Table A.40.** Product distribution of acetaldehyde electroreduction in 0.1 M PPB on OD-Cu over a variety of cathodic potentials ( $E$  vs. RHE) denoted in V. Crotyl alcohol and 1-butanal have not been detected. Related to **Figure 5.4**.

Products	-0.80 V		-0.85 V		-1.00 V		-1.05 V	
	<i>FE</i> %	<i>j</i> mA cm <sup>-2</sup>	<i>FE</i> %	<i>j</i> mA cm <sup>-2</sup>	<i>FE</i> %	<i>j</i> mA cm <sup>-2</sup>	<i>FE</i> %	<i>j</i> mA cm <sup>-2</sup>
Hydrogen	26.3	-3.0	32.6	-4.6	53.6	-15.3	92.1	-38.1
Ethane	0.25	-0.03	0.87	-0.12	1.23	-0.35	1.08	-0.68
Ethanol	68.3	-7.7	61.8	-8.8	41.9	-11.9	27.9	-17.4
1-Butanol	-	-	-	-	0.01	-0.003	0.10	-0.072
Total	94.8	-11.2	95.6	-14.1	96.8	-28.5	92.1	-61.2

- Product not detected or process not applicable.

**Table A.41.** Product distributions of acetaldehyde electrolysis on OD-Cu in buffering solutions at -30 mA cm<sup>-2</sup>. Related to **Figure 5.4**.

Products	0.01 M PPB		0.01 M PPB		1.0 M PPB	
	<i>FE</i> %	<i>j</i> mA cm <sup>-2</sup>	<i>FE</i> %	<i>j</i> mA cm <sup>-2</sup>	<i>FE</i> %	<i>j</i> mA cm <sup>-2</sup>
Hydrogen	53.3	-16.0	55.2	-16.6	82.4	-24.7
Ethane	0.08	-0.02	0.27	-0.08	0.09	-0.03
Ethanol	37.1	-11.2	39.7	-11.9	13.4	-4.0
Crotyl alcohol	0.17	-0.049	0.02	-0.005	-	-
1-Butanal	0.07	-0.002	-	-	-	-
1-Butanol	0.20	-0.061	0.01	-0.003	-	-
Total	90.9	-30	95.3	-30	95.9	-30

- Product not detected or process not applicable.

**Table A.42.** Half equations for relevant products obtained from crotonaldehyde reduction. Related to **Figure 5.4**.

Product molecule	Half equation	Number of electrons transferred
1-Butanal	$\text{CH}_3\text{CH}=\text{CHCHO} + 2\text{H}^+ + 2\text{e}^- \rightarrow \text{C}_3\text{H}_7\text{CHO} + \text{H}_2\text{O}$	2
Crotyl alcohol	$\text{CH}_3\text{CH}=\text{CHCHO} + 2\text{H}^+ + 2\text{e}^- \rightarrow \text{CH}_3\text{CH}=\text{CHCH}_2\text{OH} + \text{H}_2\text{O}$	2
1-Butanol	$\text{CH}_3\text{CH}=\text{CHCHO} + 4\text{H}^+ + 4\text{e}^- \rightarrow \text{CH}_3(\text{CH}_2)_3\text{OH} + \text{H}_2\text{O}$	4

**Table A.43.** Product distributions of crotonaldehyde, 1-butanal and crotyl alcohol electrolyses on OD- Cu over a variety of cathodic potentials ( $E$  vs. SHE) denoted in V. Related to **Figure 5.4**.

Products	Crotonaldehyde						1-Butanal				Crotyl alcohol	
	-1.20 V <sup>a</sup>		-0.90 V <sup>c</sup>		-1.20 V <sup>b</sup>		-1.20 V <sup>a</sup>		-1.20 V <sup>b</sup>		-1.20 V <sup>a</sup>	
	<i>FE</i> %	<i>j</i> mA cm <sup>-2</sup>	<i>FE</i> %	<i>j</i> mA cm <sup>-2</sup>	<i>FE</i> %	<i>j</i> mA cm <sup>-2</sup>	<i>FE</i> %	<i>j</i> mA cm <sup>-2</sup>	<i>FE</i> %	<i>j</i> mA cm <sup>-2</sup>	<i>FE</i> %	<i>j</i> mA cm <sup>-2</sup>
Hydrogen	52.9	-7.08	0.5	-0.03	31.1	-8.04	70.3	-5.36	45.7	-6.89	88.4	3.96
Ethanol	4.5	-0.76	-	-	-	-	-	-	-	-	-	-
Crotyl alcohol	1.1	-0.12	3.2	-0.18	5.4	1.33	-	-	-	-	-	-
1-Butanal	0.3	-0.05	77.9	-4.29	7.0	1.72	-	-	-	-	-	-
1-Butanol	14.8	-2.55	3.9	-0.22	46.9	-11.7	17.3	-1.61	45.8	-6.87	-	-
Total	72.2	-18.5	85.6	-5.51	90.3	-25.4	87.6	-7.58	91.6	-14.9	88.4	-4.50

a 0.1 M KOH (pH 13.0) -0.44 V vs. RHE

b 0.1 M PPB (pH 7.0) -0.79 V vs. RHE

c 0.1 M PPB (pH 7.0) -0.44 V vs. RHE

- Product not detected or process not applicable.

**Table A.44.** Total C<sub>4</sub> Faradaic efficiency and relative Faradaic selectivity toward C<sub>4</sub> products from electrolysis of acetaldehyde and crotonaldehyde on OD-Cu in 0.1 M KOH at -0.44 V vs. RHE. Related to **Figure 5.4**.

Reactant	All C <sub>4</sub> products	Crotyl alcohol	1-Butanal	1-Butanol
	<i>FE</i> %	<i>FE</i> %	<i>FE</i> %	<i>FE</i> %
Acetaldehyde	10.2	3.3	2.0	94.7
Crotonaldehyde	16.2	6.6	1.9	91.4



**Table A.45.** Product distribution of 50 mM acetaldehyde electrolysis in 0.1 M KOH on metal discs at  $-10 \text{ mA cm}^{-2}$ . Related to **Figure 5.4**.

	<b>Cu</b>	<b>Fe</b>	<b>Co</b>	<b>Ni</b>	<b>Ag</b>	<b>Au</b>	<b>Pt</b>	<b>Pd</b>	<b>Zn</b>	<b>Ti</b>	<b>Cr</b>	<b>Mo</b>
<b>Products</b>	<i>FE</i>	<i>FE</i>	<i>FE</i>	<i>FE</i>	<i>FE</i>	<i>FE</i>	<i>FE</i>	<i>FE</i>	<i>FE</i>	<i>FE</i>	<i>FE</i>	<i>FE</i>
	%	%	%	%	%	%	%	%	%	%	%	%
Hydrogen	70.1	71.0	73.0	76.3	75.1	75.0	89.3	4.7	63.9	93.7	98.6	95.1
Ethane	0.4	0.7	0.5	0.2	1.2	0.5	0.3	-	0.2	0.1	0.02	-
Ethanol	18.6	19.0	15.6	11.5	10.5	10.4	1.9	2.1	26.9	2.1	0.7	1.0
Crotyl alcohol	1.4	0.4	0.4	0.6	1.3	0.1	0.2	0.5	0.2	0.1	0.04	0.2
1-Butanal	0.2	0.2	0.4	0.4	0.1	0.02	0.1	0.4	0.01	0.08	0.02	0.1
1-Butanol	1.7	4.0	2.7	1.4	0.5	0.1	-	-	0.2	-	-	-
Total	92.3	95.2	92.7	90.2	88.8	86.1	91.8	7.7	91.4	96.2	99.4	96.3
1-Butanol / C <sub>4</sub>	0.52	0.88	0.76	0.59	0.26	0.41	-	-	0.50	-	-	-

- Product not detected or process not applicable.

**Table A.46.** Product distribution of 50 mM crotonaldehyde electrolysis in 0.1 M PPB on metal discs at  $-10 \text{ mA cm}^{-2}$ . Related to **Figure 5.4**.

	<b>Cu</b>	<b>Fe</b>	<b>Co</b>	<b>Ni</b>	<b>Ag</b>	<b>Au</b>	<b>Pt</b>	<b>Pd</b>	<b>Zn</b>	<b>Ti</b>	<b>Cr</b>	<b>Mo</b>
<b>Products</b>	<i>FE</i>	<i>FE</i>	<i>FE</i>	<i>FE</i>	<i>FE</i>	<i>FE</i>	<i>FE</i>	<i>FE</i>	<i>FE</i>	<i>FE</i>	<i>FE</i>	<i>FE</i>
	%	%	%	%	%	%	%	%	%	%	%	%
Hydrogen	40.7	35.9	45.7	41.3	29.6	39.1	81.0	2.2	38.9	54.6	72.1	87.0
Crotyl alcohol	5.6	5.3	5.1	5.4	25.2	5.9	1.6	2.7	1.3	1.9	0.8	0.8
1-Butanal	22.5	13.0	19.9	38.9	16.3	16.5	7.9	21.9	2.5	7.0	5.5	2.2
1-Butanol	12.4	26.3	6.8	6.0	4.1	3.9	1.6	1.4	0.8	0.7	0.5	0.1
Total	81.1	80.4	77.5	91.6	75.1	65.4	92.1	28.2	43.5	64.3	79.9	90.1
1-Butanol / C <sub>4</sub>	0.31	0.59	0.21	0.12	0.09	0.24	0.15	0.05	0.18	0.07	0.06	0.04

- Product not detected or process not applicable.

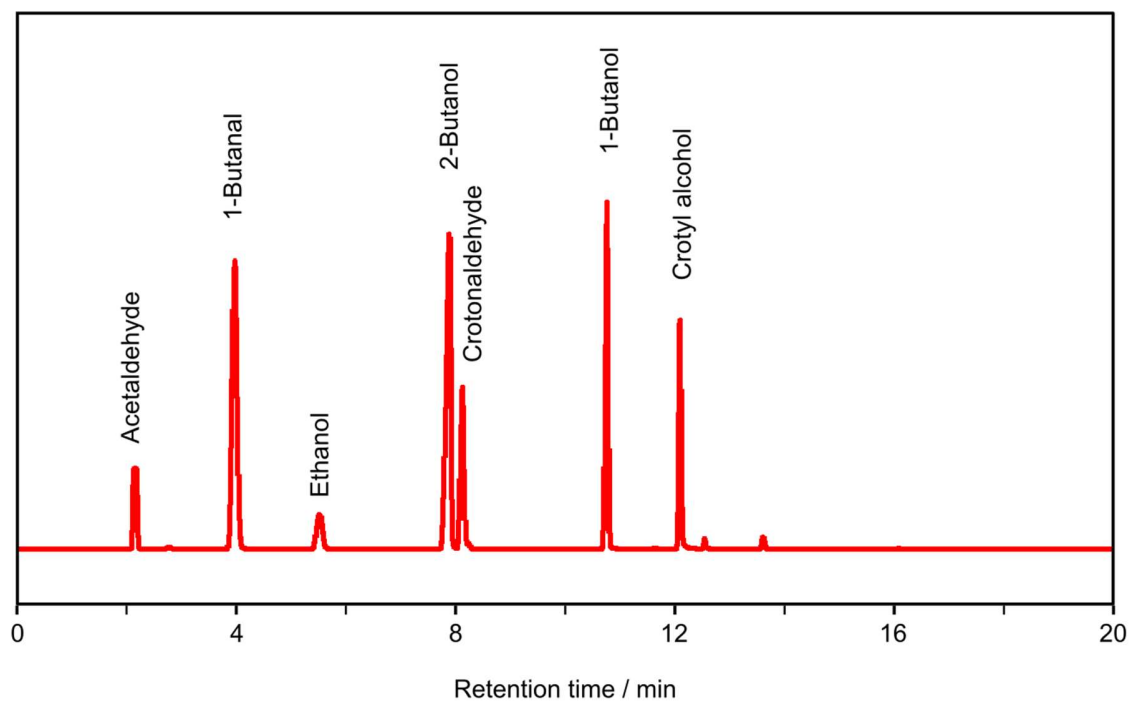


**Figure A.46.** Headspace GC of standard compounds in 0.1 M KOH after neutralization with 4 M H<sub>2</sub>SO<sub>4</sub>. The concentration of each compound is 5 mM. Related to **Figure 5.2**.

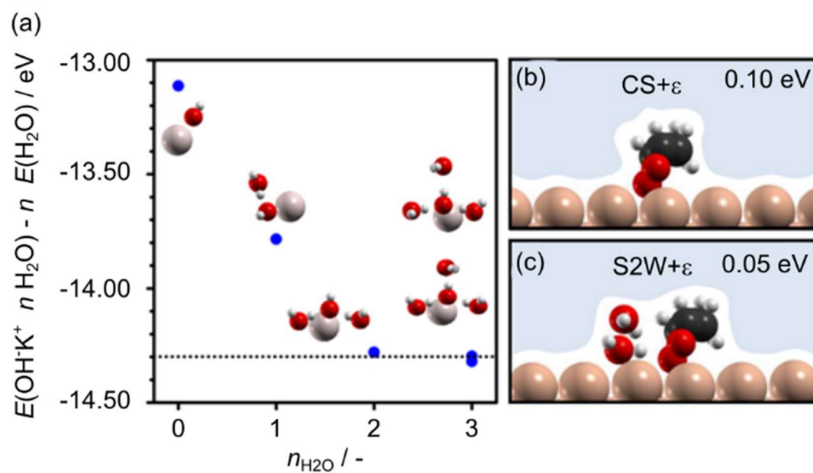


**Figure A.47.** (a) Potential energy of a solvated  $\text{OH}^-\text{K}^+ \cdot n \text{H}_2\text{O}$  cluster, with respect to  $\text{H}_2\text{O}$  in implicit<sup>[189]</sup> solvent. For the remaining anionic species, only a water molecule and a  $\text{K}^+$  counteraction were needed. Solvation models derived from Ref <sup>[190]</sup>: (b)  $\text{CS}+\epsilon$ , clean surface (CS) plus implicit solvation ( $\epsilon$ ); and (c)  $\text{S2W}+\epsilon$ , Two explicit water molecules (S2W) plus implicit solvation ( $\epsilon$ ). In the mixed schemes represented in (b) and (c) the white region corresponds to the cavities left by the adsorbates, explicit molecules, and metal surface, while the shadowed blue region represents the volume substituted by the implicit solvent (characterized by the relative permittivity,  $\epsilon$ ). The typical error bars (0.10 eV and 0.05 eV) with respect to fully explicit solvent are indicated. Related to **Figure 5.4**.

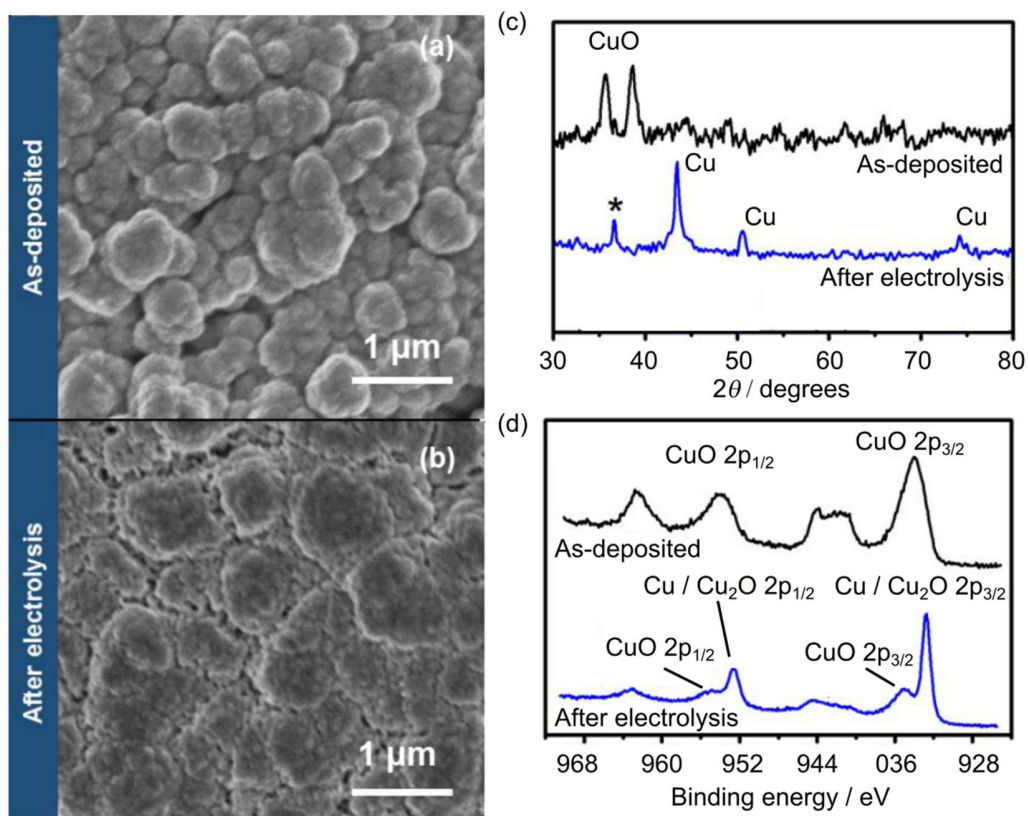


**Figure A.48.** SEM images of (a) as-deposited CuO GDE and (b) OD-Cu after eCO<sub>2</sub>R in 1.0 M KOH at  $-0.48 \text{ V vs. RHE}$ . (c) XRD patterns of as-deposited CuO GDE and OD-Cu GDE after eCO<sub>2</sub>R. Cu<sub>2</sub>O (111) signals (indicated by \*) were detected due to the surface oxidation of the catalyst. (d) Cu 2p XPS spectra of as-deposited CuO GDE and OD-Cu GDE after eCO<sub>2</sub>R. Related to **Figure 5.4**.

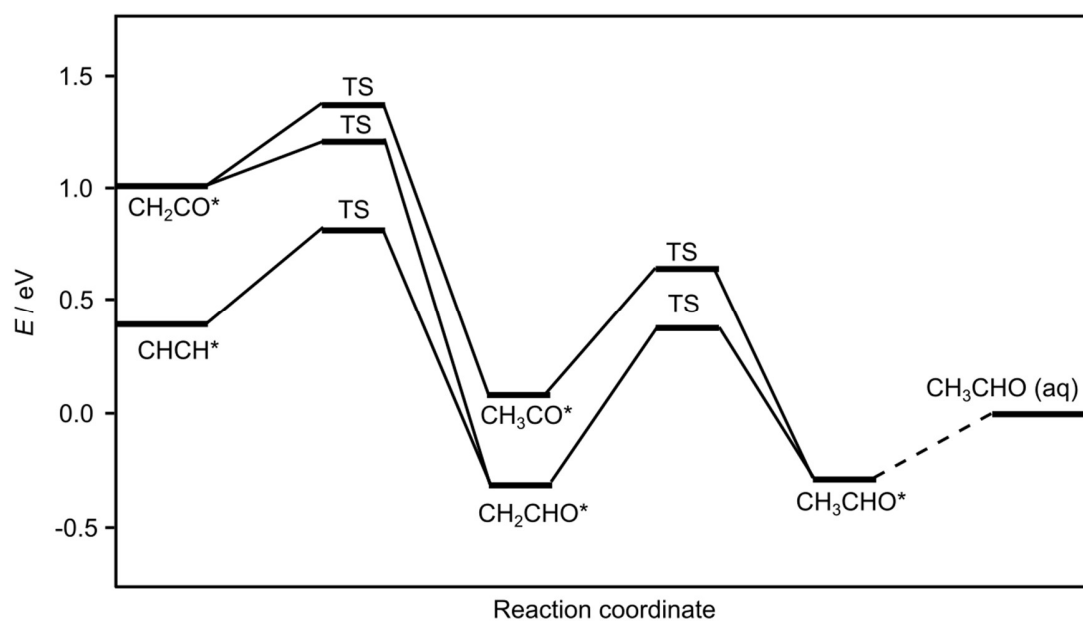


**Figure A.49.** Potential energy diagram for acetaldehyde formation from  $\text{CHCHO}^*$  and  $\text{CH}_2\text{CO}^*$ . The dashed line represents the desorption of acetaldehyde. The formation of precursors  $\text{CHCHO}^*$  and  $\text{CH}_2\text{CO}^*$ , as well as other lateral paths, have been investigated in detail by earlier works.<sup>[27,77,99,169]</sup> Related to **Figure 5.4**.

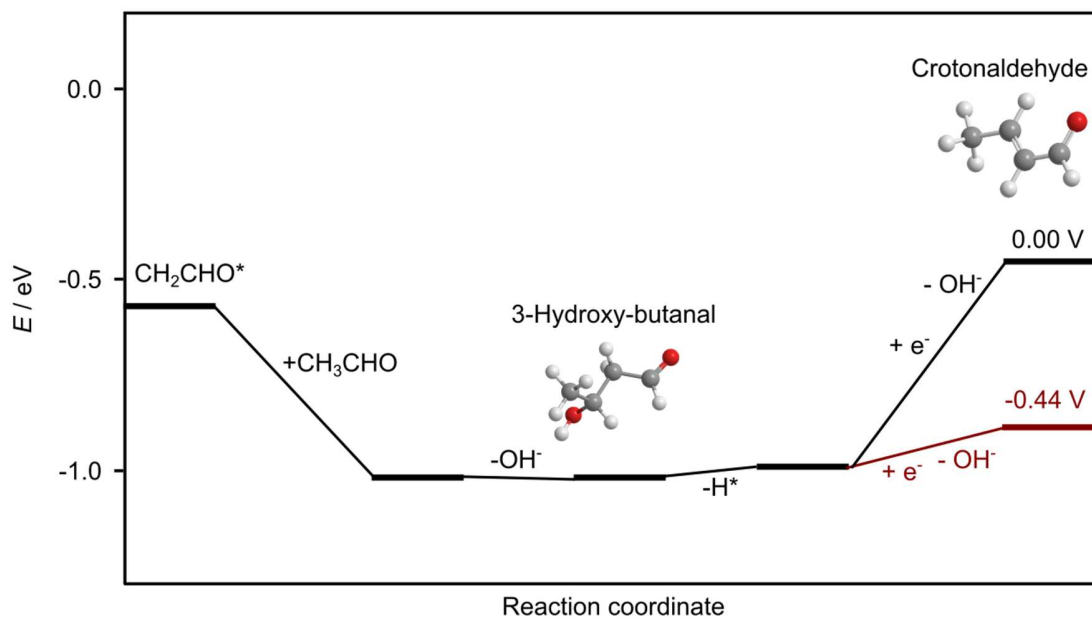


**Figure A.50.** Potential energy diagram for the condensation of ethenyloxy with acetaldehyde to crotonaldehyde on the Cu surface (black). The final  $\text{OH}^-$  removal can be assisted by one electron donated by the surface and stabilized under reductive potentials (dark red). Water molecules were omitted for clarity. The energy references of **Figure 5.4** are preserved, thus the energy of aqueous acetaldehyde corresponds to exactly 0.0 eV. Related to **Figure 5.4**.

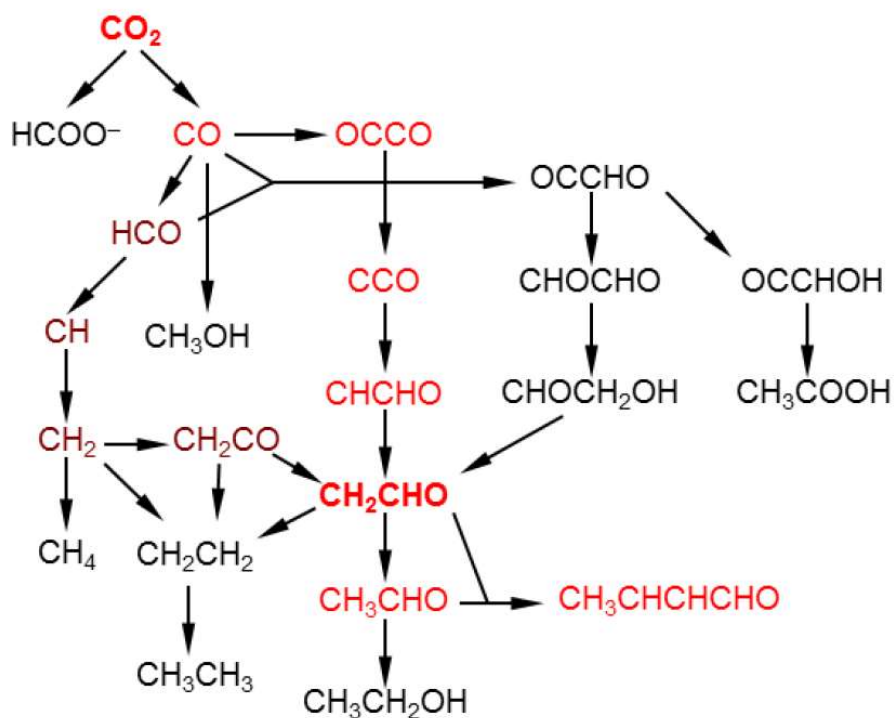


**Figure A.51.** Main pathways from  $\text{CO}_2$  to the key ethenyloxy intermediate ( $\text{CH}_2\text{CHO}$ , **bold**) and acetaldehyde, as reported in literature,<sup>[27,77,99]</sup> leading eventually to crotonaldehyde. Routes going through  $\text{CHCHO}$ <sup>[27]</sup> and ketene ( $\text{CH}_2\text{CO}$ )<sup>[169]</sup> are highlighted in red and dark red respectively. Routes involving glyoxal and glycolaldehyde were omitted as these molecules were not detected. Paths to detected  $\text{C}_1$  and  $\text{C}_2$  side products are shown for completeness. Routes to crotonaldehyde from  $\text{CO}_2$  and acetaldehyde shown in **Figure A.50** and **Figure 5.4**, respectively. Related to **Figure 5.1**.

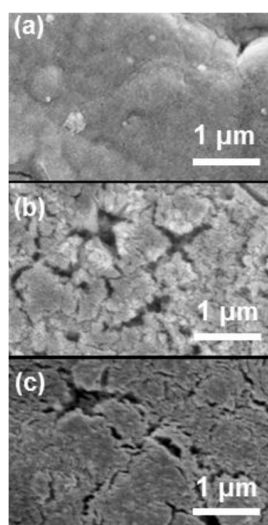


**Figure A.52.** SEM images of the (a) as-deposited CuO, (b) OD-Cu, obtained after pre-reduction of the electrodeposited CuO, and (c) OD-Cu after 1 h of acetaldehyde electrolysis in 0.1 M KOH at  $-0.44$  V *vs.* RHE. Related to **Figure 5.2**.

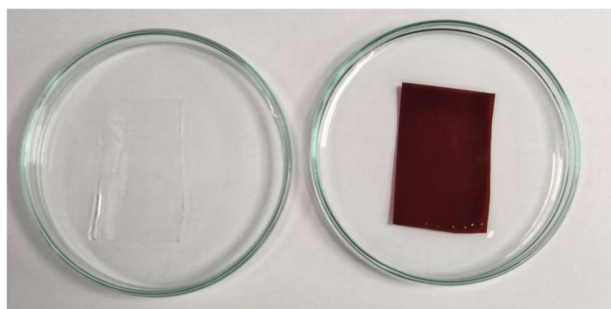


**Figure A.53.** Photographs of Selemion AMVN anion exchange membrane in solution A (left) and solution B (right) after 3 h. Related to **Figure 5.2**.



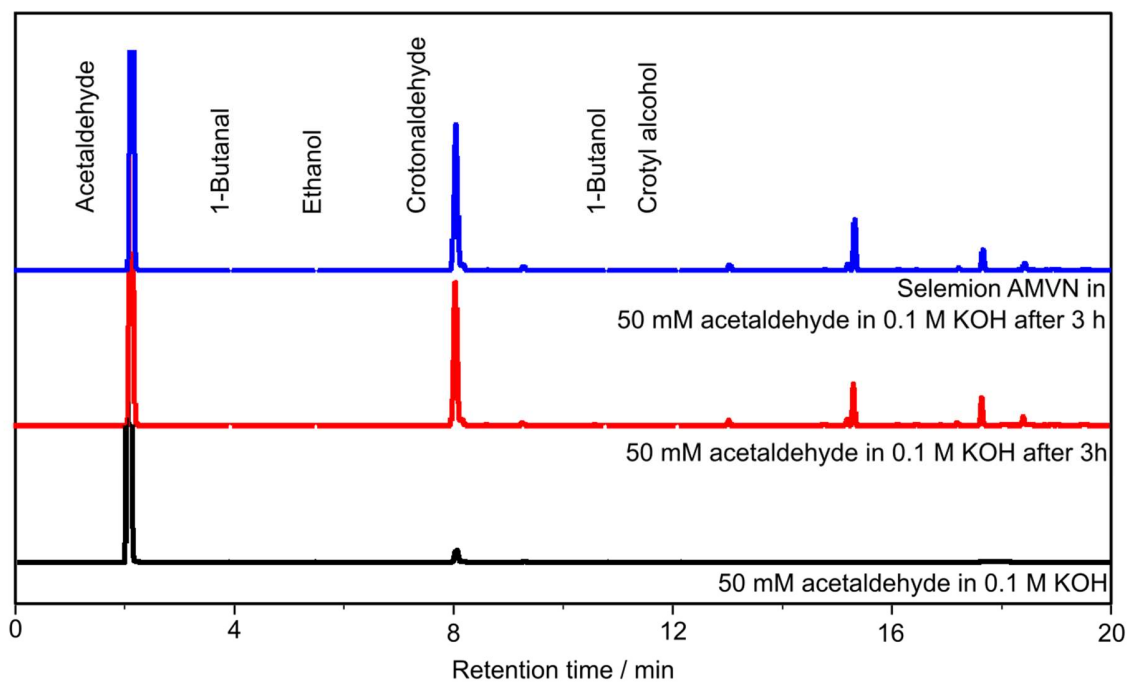


**Figure A.54.** Headspace gas chromatogram of solution B after membrane immersion for 3 h (blue), compared to 50 mM acetaldehyde in 0.1 M KOH aged for 3 h (red) and 50 mM acetaldehyde in 0.1 M KOH, neutralized and analyzed immediately (black). The retention times of acetaldehyde reduction products are indicated. Related to **Figure 5.2**.

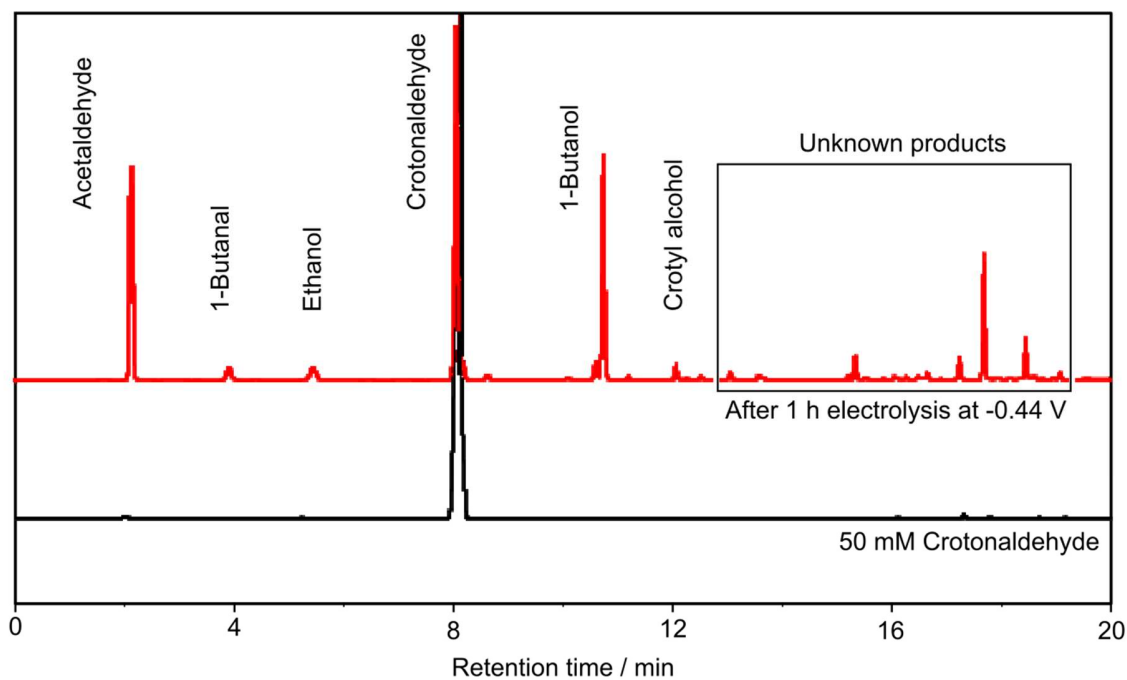


**Figure A.55.** Headspace gas chromatogram of 50 mM crotonaldehyde in 0.1 M KOH (black) and the electrolyte mixture after 1 h electrolysis at  $-0.44$  V *vs.* RHE (red). Both samples were neutralized with 4 M  $\text{H}_2\text{SO}_4$  prior to analysis. Related to **Figure 5.2**.

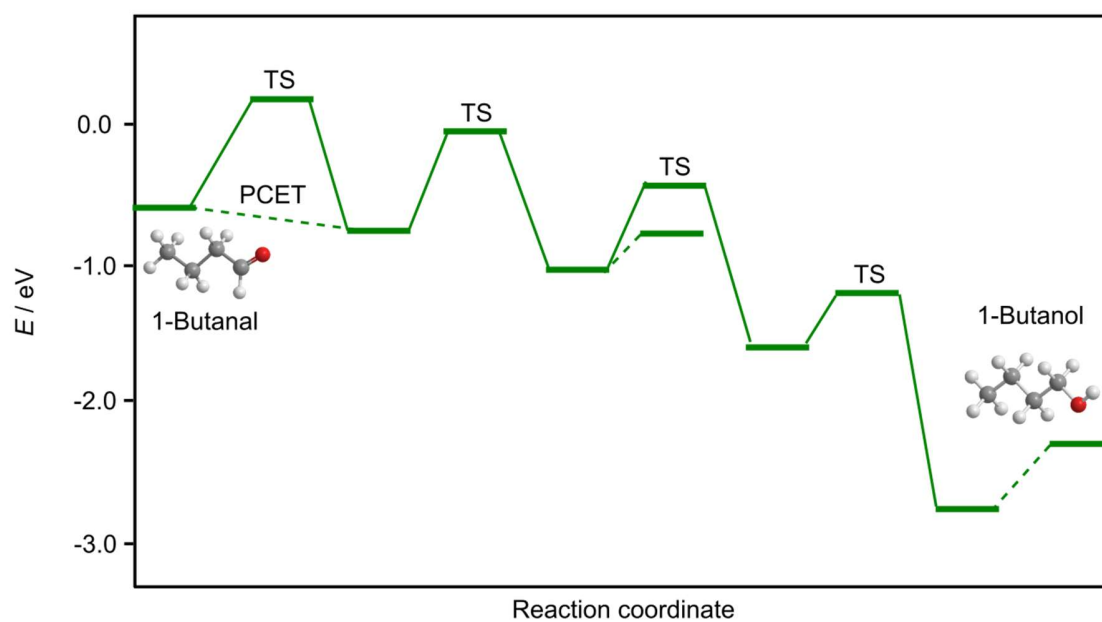


**Figure A.56.** Potential energy diagram for the reduction of crotonaldehyde to 1-butanol via crotyl alcohol. The dashed lines represent desorption processes. The dotted lines represent PCET. Under negative potentials, the O atom of crotonaldehyde can be hydrogenated via PCET. The remaining reactions are chemical steps. Once formed, crotyl alcohol would desorb rather than react. Related to **Figure 5.5**.

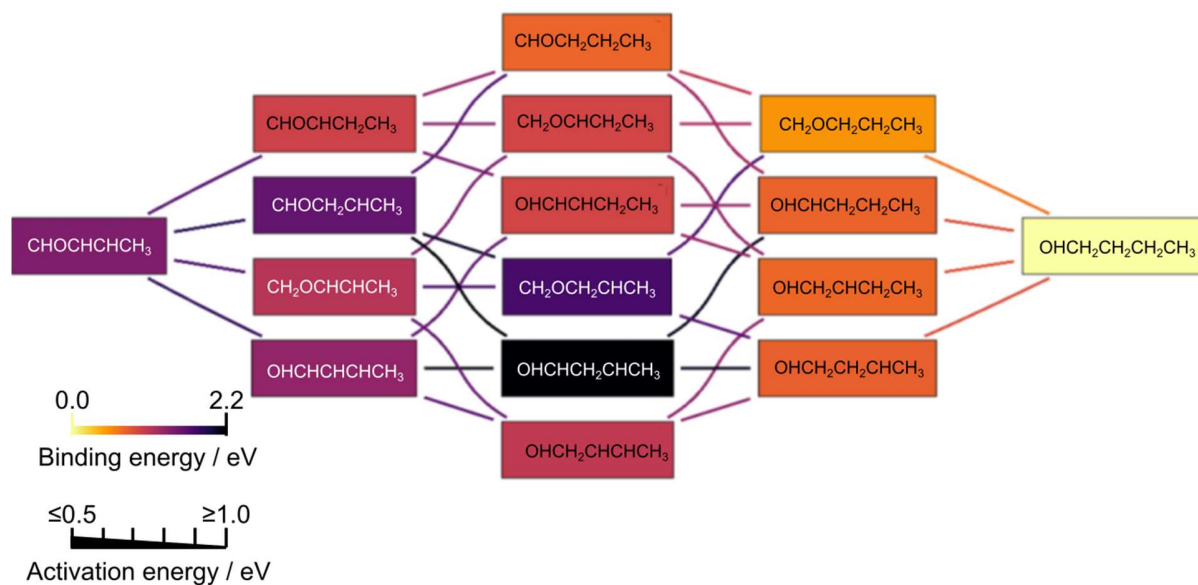


**Figure A.57.** Energy profile of crotonaldehyde reduction to 1-butanol via chemical steps. The color of each box, with reference to the scale on the right, represents the energy of each intermediate. Lines represent transition state energies between the connected intermediates. 1-Butanol ( $\text{CHO-CH}_2\text{-CH}_2\text{-CH}_3$ ) is the most favored intermediate both thermodynamically and kinetically. Adsorbed hydrogen species ( $\text{H}^*$ ) have been omitted for simplicity. Related to **Figure 5.6**.

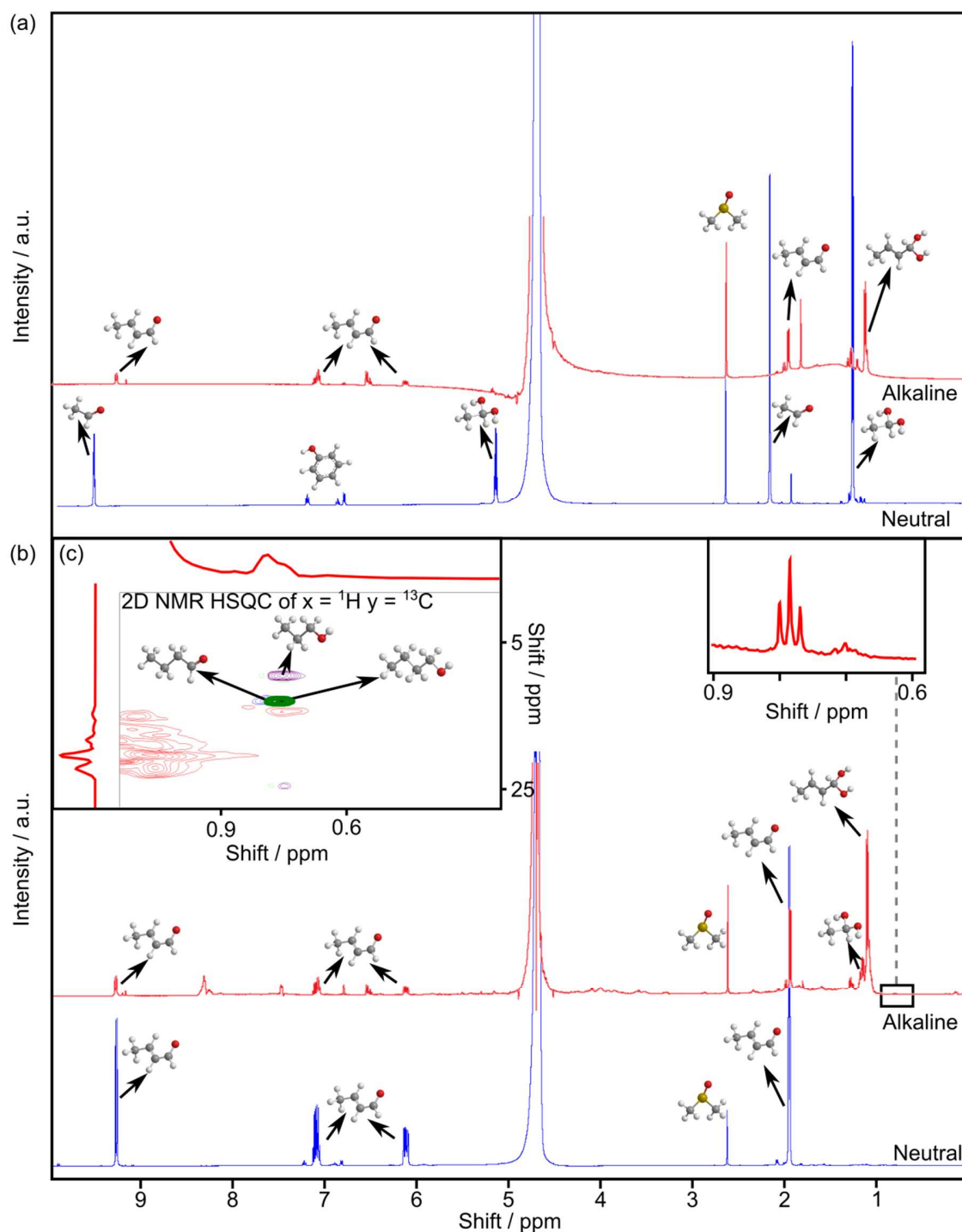


**Figure A.58.** Nuclear magnetic resonance (NMR) spectroscopic analyses ( $\delta$  refers to the chemical shift). (a)  $^1\text{H}$  NMR spectra of fresh (< 2 min) solutions of 10 mM acetaldehyde in ultrapure deionized water (blue) and 0.1 M KOH (red). The conversion of acetaldehyde to hydrated acetaldehyde in water is evidenced by the  $\sim 1:1$  ratio of their respective peaks. In alkaline conditions, crotonaldehyde and hydrated crotonaldehyde are the predominant compounds, consistent with the aldol condensation of acetaldehyde to crotonaldehyde,

followed by its hydration. **(b)** NMR spectra of 10 mM crotonaldehyde in 0.1 M KOH after 50 min. The chemical reactions of crotonaldehyde in the alkaline environment led to multiple unidentified peaks, including the  $\text{CH}_3$  triplet peak at 0.8 ppm which suggests the formation of  $\text{C}_4$  alcohols or aldehydes. (Inset i) Two-dimensional heteronuclear single quantum coherence (HSQC) spectra of 10 mM 1-propanol, 1-butanal and 1-butanol in 0.1 M KOH overlaid with the spectrum of 10 mM crotonaldehyde in 0.1 M KOH. The non-overlap of the signals at 0.8 ppm indicates that neither 1-propanol, 1-butanal nor 1-butanol were formed through a chemical route. Related to **Figure 5.6**.

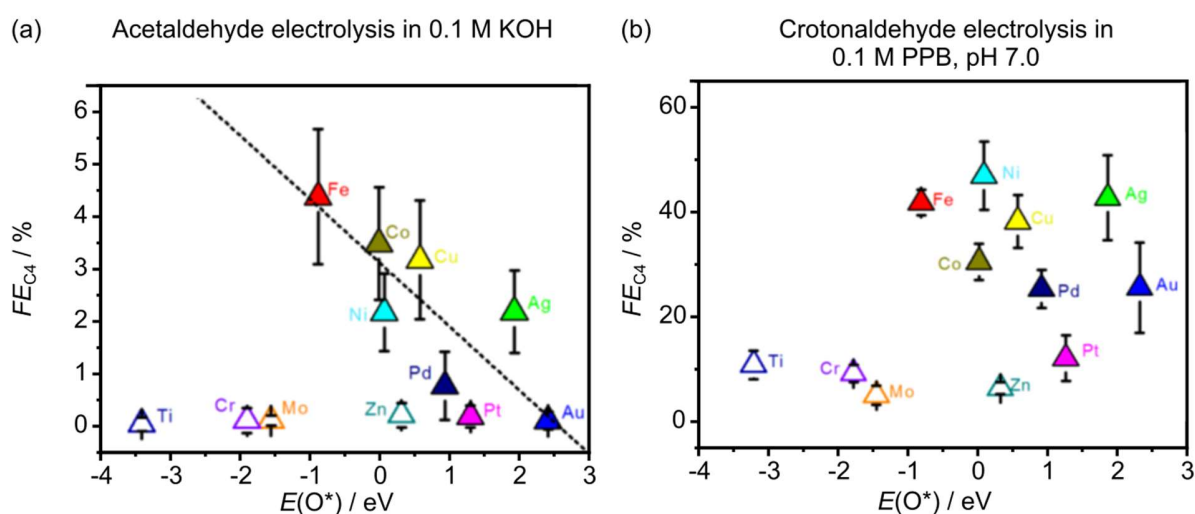


**Figure A.59.** Faradaic efficiency of  $\text{C}_4$  oxygenates from  $-10 \text{ mA cm}^{-2}$  constant-current electrolysis of **(a)** acetaldehyde and **(b)** crotonaldehyde on selected metals as a function of the DFT-computed adsorbed oxygen stability on these metals with respect to water and hydrogen. Metals that are typically oxides at  $0.00 \text{ V vs. RHE}$  at the pH of the supporting electrolyte are shown as hollow symbols. The oxide layer present on the surface of these metals might have prevented the adsorption of acetaldehyde and crotonaldehyde, which resulted in poor  $\text{C}_4$  selectivity. Related to **Figure 5.7**.



## Appendix B

### List of Publications and Presentations

#### Doctoral Publications

S. Pablo-García, F.L.P. Veenstra, L.R.L. Ting, R. García-Muelas, A.J. Martín, F. Dattila, B.S. Yeo, J. Pérez-Ramírez, N. López

Mechanistic routes toward C<sub>3</sub> products in copper-catalysed CO<sub>2</sub> electroreduction

*Catal. Sci. Technol.* **2022**, *12*, 409-417 ([doi:10.1039/D1CY01423D](https://doi.org/10.1039/D1CY01423D))

L.R.L. Ting, R. García-Muelas, A.J. Martín, F.L.P. Veenstra, S.T.-J. Chen, Y. Peng, E.Y.X. Per, S. Pablo-García, N. López, J. Pérez-Ramírez, B.S. Yeo

Electrochemical reduction of carbon dioxide to 1-butanol on oxide-derived copper

*Angew. Chem. Int. Ed.* **2020**, *59*, 21072-21079 ([doi:10.1002/anie.202008289](https://doi.org/10.1002/anie.202008289))

*Angew. Chem.* **2020**, *132*, 21258-21265 ([doi:10.1002/ange.202008289](https://doi.org/10.1002/ange.202008289))

F.L.P. Veenstra, N. Ackerl, A.J. Martín, J. Pérez-Ramírez

Selectivity patterns in the electrocatalytic reduction of CO<sub>2</sub> revealed by laser-microstructured copper

*Chem* **2020**, *6*, 1707-1722 ([doi:10.1016/j.chempr.2020.04.001](https://doi.org/10.1016/j.chempr.2020.04.001))

F.L.P. Veenstra, A.J. Martín, J. Pérez-Ramírez

Nitride-derived copper modified with indium as a selective and highly stable catalyst for the electroreduction of carbon dioxide

*ChemSusChem* **2019**, *12*, 3501-3508 ([doi:10.1002/cssc.201901309](https://doi.org/10.1002/cssc.201901309), very important paper, cover feature)



## Other publications

A.J. Martín, F.L.P. Veenstra, J. Lüthi, R. Verel, J. Pérez Ramírez

Toward reliable and accessible ammonia quantification in the electrocatalytic reduction of nitrogen  
*Chem Catal.* **2021**, *1*, 1505-1518 ([doi:10.1016/j.checat.2021.10.002](https://doi.org/10.1016/j.checat.2021.10.002), front cover)

M.S. Frei, F.L.P. Veenstra, D. Capeder, J.A. Stewart, D. Curulla-Ferré, A.J. Martín, C. Mondelli,  
J. Pérez-Ramírez

Microfabrication enables quantification of interfacial activity in thermal catalysis  
*Small Methods* **2021**, *5*, 2001231 ([doi:10.1002/smt.202001231](https://doi.org/10.1002/smt.202001231), inside back cover)

## Pre-doctoral publications

I.M. Denekamp, F. L. P. Veenstra, P. Jungbacker, G. Rothenberg

A simple synthesis of symmetric phthalocyanines and their respective perfluoro and transition -  
metal complexes

*Appl. Organometal Chem.* **2019**, *33*, 4872 ([doi:10.1002/aoc.4872](https://doi.org/10.1002/aoc.4872))

J.O. Taylor, F.L.P. Veenstra, A.M. Chippindale, M.J. Calhorda, F. Hartl

Group 6 Metal Complexes as Electrocatalysts of CO<sub>2</sub> Reduction: Strong Substituent Control of  
the Reduction Path of [Mo( $\eta^3$ -allyl)(CO)<sub>2</sub>(x,x'-dimethyl-2,2'-bipyridine)(NCS)] (x = 4 - 6)

*Organometallics* **2019**, *38*, 1372-1390 ([doi:10.1021/acs.organomet.8b00676](https://doi.org/10.1021/acs.organomet.8b00676))

**Doctoral presentations**

F.L.P. Veenstra, S. Pablo-García, L.R.L. Ting, R. García-Muelas, F. Dattila, A.J. Martín, B.S. Yeo, N. López, J. Pérez-Ramírez

Talk: Expanding the mechanistic understanding on the electrocatalytic CO<sub>2</sub> reduction: routes toward C<sub>3</sub> and C<sub>4</sub> compounds

**Division of Catalysis Science and Technology (CATL) American Chemical Society**, Online, U.S.A., April 2021

F.L.P. Veenstra, A.J. Martín, J. Lüthi, R. Verel, Javier Pérez-Ramírez

Poster: Toward reliable and accessible ammonia quantification in the electrocatalytic reduction of nitrogen

**Fall Meeting of the Swiss Chemical Society**, Online, Switzerland, September 2021

F.L.P. Veenstra, N. Ackerl, A.J. Martín, J. Pérez-Ramírez

Poster: Laser-microstructured copper reveals selectivity patterns in the electrocatalytic reduction of CO<sub>2</sub>

**Fall Meeting of the Swiss Chemical Society**, Online, Switzerland, August 2020

F.L.P. Veenstra, A.J. Martín, J. Pérez-Ramírez

Poster: In<sub>2</sub>O<sub>3</sub>/Cu<sub>3</sub>N as a selective and highly stable catalyst for the electroreduction of carbon dioxide

**Fall Meeting of the Swiss Chemical Society**, Lausanne, Switzerland, September 2019



# Appendix C

## Curriculum Vitae

Maiden name      Florentine Louise Petronella Veenstra  
Married name     Mrs. Strudwick (since October 2021)  
Date of Birth     November 22<sup>nd</sup> 1990  
Place of Birth    Amsterdam, The Netherlands  
Nationality       Netherlands

### Education

2018 – 2022      Doctoral studies under the supervision of Prof. Dr. Javier Pérez-Ramírez, Institute for Chemical and Bioengineering, Department of Chemistry and Applied Biosciences, ETH Zürich, Switzerland  
2016 – 2018      MSc. in Chemistry, University of Amsterdam, The Netherlands (GPA. 7.57)  
2015 – 2016      Premaster in Chemistry, University of Amsterdam, The Netherlands  
2011 – 2015      BSc. in Chemie, Hogeschool Inholland, The Netherlands

### Experience

2021 - 2022      President of the Association of Scientific Staff at ETH (AVETH), ETH Zürich, Switzerland (on voluntary basis)  
2022              Jury member in the [Kite award](#) committee for innovation in learning and teaching , ETH Zürich, Switzerland (on voluntary basis)  
2021              Member in organization of [MaP symposium](#) and MaP awards, ETH Zürich, Switzerland (on voluntary basis)  
2021              Member in organization of mentorship program, organized by [ETH Circle](#) with support from [AVETH](#), ETH Zürich, Switzerland (on voluntary basis)  
2019 - 2021      Coordinator of Counselling of the Association of Scientific Staff at ETH (AVETH), ETH Zürich, Switzerland (on voluntary basis)  
2017              Master thesis: “Converting Carbon Dioxide into Fuel on Modified Electrode Surfaces.” Under the supervision of Prof. Dr. Frantisek Hartl, Reading University, United Kingdom

- 2017 Master thesis (minor): "Unsymmetrically Substituted Phthalocyanine Complex Covalently Bond to Porous Support." Under the supervision of Prof. Dr. Gadi Rothenberg, University of Amsterdam, The Netherlands
- 2015 Bachelor thesis: "Influence of electron donor groups in perylene diimide-probes to observe glass transition in polymer films." Under the supervision of Prof. Dr. Fred Brouwer, University of Amsterdam, The Netherlands.
- 2013 Bachelor thesis (minor): "Passerini-type reactions for the Green synthesis of pharmaceuticals." Under the supervision of Dr. Eelco Ruijter, Vrije Universiteit Amsterdam, The Netherlands.

